Designing and simulating a micro-robot for transporting filamentous cargos in Newtonian and viscoelastic fluids

by

Sepehr Ghadami

A thesis
presented to the University of Waterloo
in fulfillment of the
thesis requirement for the degree of
Doctor of Philosophy
in Applied Mathematics

Waterloo, Ontario, Canada, 2024

© Sepehr Ghadami 2024

Examining Committee Membership

The following served on the Examining Committee for this proposal.

External Examiner:	Sarah Olson Professor, Dept. of Mathematical Sciences, Worcester Polytechnic Institute
Supervisor(s):	Henry Shum Associate Professor, Dept. of Applied Math, University of Waterloo
Internal Members:	Hans De Sterck Professor, Dept. of Applied Math, University of Waterloo
	Sander Rhebergen Associate Professor, Dept. of Applied Math, University of Waterloo
Internal-External Member:	Zhao Pan Assistant Professor, Dept. of Mechanical and Mechatronics Engineering, University of Waterloo

Author's Declaration

I hereby declare that I am the sole author of this thesis. This is a true copy of the thesis, including any required final revisions, as accepted by my examiners.

I understand that my thesis may be made electronically available to the public.

Abstract

In recent years, there has been a notable surge in interest within the medical field towards minimally invasive procedures, with magnetic micro-robots emerging as a promising avenue. These micro-robots exhibit the capability to traverse various mediums, including viscoelastic and non-Newtonian fluids, facilitating targeted drug delivery and medical interventions. Many current designs, drawing inspiration from micro-swimmers found in biological systems such as bacteria and sperm, utilize a contact-based approach for transporting payloads. However, adhesion between the cargo and the carrier can complicate release at the intended site. In this thesis, our primary aim was to investigate the potential of a helical micro-robot for non-contact delivery of drugs or cargo. We conducted an extensive examination of the shape and geometrical parameters of the helical micro-robot, with a specific focus on its ability to transport passive filaments. Based on our analysis, we propose a novel design comprising three sections with alternating handedness, incorporating two pulling and one pushing microhelices, to improve the capture and transportation of passive filaments in Newtonian fluids using a non-contact approach. Subsequently, we simulated the process of capturing and transporting the passive filament and evaluated the functionality of the newly designed micro-robot. Initially concentrating on naturally straight filaments, we also demonstrated the micro-robot's capability to capture filaments with intrinsic curvature and those with a spherical payload attached at one end. Our findings provide valuable insights into the mechanics of helical micro-robots and their potential applications in medical procedures and drug delivery. Furthermore, the proposed non-contact delivery method for filamentous cargo could pave the way for the development of more efficient and effective micro-robots for medical purposes.

In the second phase of our project, recognizing that most biological fluids exhibit viscoelastic properties due to the presence of protein fibers, we proposed a viscoelastic model. Inspired by the viscoelastic structure of bovine vaginal fluid, we developed and initially characterized this model using creep and strain tests. Subsequently, in the proposed viscoelastic model, we investigated the functionality of the designed micro-robot in the viscoelastic fluid and compared its performance with that of the conventional single-handed helical micro-robot. It was observed that although the designed micro-robot is highly effective in transporting filamentous microcargo without contact

in Newtonian fluid, its unique structure presents challenges when moving in viscoelastic fluid.

Acknowledgements

I would like to express my deepest gratitude to my supervisor, Prof. Henry Shum, for his invaluable guidance and support throughout the development of this thesis. His insights and encouragement have been crucial to my work.

I also wish to extend my heartfelt thanks to my family and friends, whose unwavering support has been a constant source of strength and motivation.

Table of Contents

List of Figures x

List of Tables xx

1 Introduction 1

1.1 Motivation 1

1.2 Micro-robot overview 4

1.3 Understanding sperm morphology and structure 8

1.4 Classification of fluid behaviour 10

1.4.1 Time-independent non-Newtonian fluids 11

1.4.2 Time-dependent non-Newtonian fluids 12

1.4.3 Viscoelastic fluids 14

1.5 Micro-swimmer motion in a viscoelastic fluid 23

1.5.1 Helical locomotion 28

1.5.2 Non-continuum effects 30

1.5.3 Numerical methods for modeling micro-swimmer motion in viscoelastic fluids 32

1.6 Outline of the thesis 35

2 Regularized stokeslet method 37

2.1 Modeling rigid objects 40

2.2 Modeling flexible objects 42

3 Designing micro-robot for transporting filamentous cargo 45

3.1 Introduction . . . 45

3.2 Geometric model and mechanical properties . . . 47

3.3 Governing equations . . . 49

3.4 Model validation . . . 52

3.4.1 Validation of the model developed for flexible filament 52

3.4.2 Validation of the model developed for rigid object . . 56

3.4.3 Mesh independency . . . 58

3.5 Fluid transport due to prescribed rotation of the helical micro-robot . . . 59

3.6 The instantaneous flow field around a helical micro-robot in a rotating magnetic field . . . 61

3.7 Coupling between a passive filament and a helical micro-robot 64

3.7.1 The impact of helical pitch of the micro-robot 65

3.7.2 The impact of flexibility of the passive filament . . . 67

3.7.3 The impact of cross-sectional radius of the micro-robot 69

3.8 Improved design with multiple helical sections . . . 69

3.8.1 Micro-robot with two helical sections . . . 69

3.8.2 Micro-robot with three helical sections . . . 72

3.9 Capture and transport of filaments with different resting shapes 75

3.10 Capture and transport of a filament with a head . . . 77

3.11 Analytical study on the possibility of coupling . . . 81

3.12 Conclusions . . . 86

4 Developing and characterizing viscoelastic fluid 88

4.1 Numerical method and verification . . . 93

4.2 Characterization of the developed viscoelastic network . . . 95

4.3 Modifying the developed viscoelastic network . . . 107

5 Motion of micro-robot in a viscoelastic fluid **117**

5.1 Introduction 117

5.2 Geometry and mechanical/viscoelastic properties of the helical micro-robot and viscoelastic network fluid 119

5.3 Locomotion of helical magnetic micro-robot in a viscoelastic network 121

5.3.1 Behaviour of helical micro-robots passing through a viscoelastic network 122

5.3.2 Studying the effect of viscoelastic properties on the performance of the helical micro-robots 134

5.3.3 Studying the effect of breakpoints for links in the viscoelastic network on the performance of helical micro-robots 151

5.4 Summary and conclusion 156

6 Summary and conclusions **160**

6.1 Recommendations for future works 163

Appendix I: Detailed Calculations for Deriving the Analytical Equation of Developed Viscoelastic Network **165**

Appendix II: Genetic Algorithm **173**

References **177**

List of Figures

1.1 Schematic of complex geometry that sperm swim through to fertilize the egg [1, 2]. 2

1.2 Schematic and SEM image of the developed magnetic microrobot, featuring a helical tail and tubular head, illustrating its fluidic trapping and object transport abilities. Adapted from Huang et al., 2014.[3] 5

1.3 Depiction of a sperm-carrying micromotor in the process of capturing, transporting, and attempting to release a sperm cell near an oocyte for fertilization assistance. Adapted from Medina-Sanchez et al., 2016.[4] 6

1.4 Motion control of the micro-helix with respect to the rotation of the magnetic field. [5] 7

1.5 Experimental results for the rotational frequency of the magnetic field versus the velocity of the helix, obtained by Qiu & Nelson in 2015 [5]. 8

1.6 Schematic of Sperm structure. [6] 9

1.7 Graphical representation of shear stress versus shear rate(strain rate) for various types of Time-Independent non-Newtonian fluids. [7] 12

1.8 Graphical representation of shear stress versus shear rate for thixotropic and rheopectic substances, illustrating the distinctive hysteresis patterns emblematic of each fluid type. [7] . . 14

1.9 (a) Creep and Recovery Tests: (1) stress step, (2) response of an ideal viscous liquid (3) response of an ideal elastic solid (4) response of two different viscoelastic materials, both demonstrating a lag in deformation recovery. (b) Stress Relaxation Tests: (1) strain step (2) ideal viscous liquid relaxation curve (3) ideal elastic solid relaxation curve (4) stress relation curves of two viscoelastic materials, each exhibiting prolonged stress relaxation. (c) (1) Diagram of the Maxwell liquid model and (2) its behavior during a creep recovery test, (3) followed by a stress relaxation test.[8] 17

1.10 Diagram illustrating material responses at different frequencies and strain rates, depicting transitions from Newtonian viscous to nonlinear viscoelastic behaviors as strain rates increase [7]. 20

1.11 Diagrammatic representations and relaxation modulus for various linear viscoelastic models, adapted from [9]. 22

1.12 Solving for the microstructure of complex fluids during cell swimming. (a) Distribution of long polymer dumbbells around a rotating helical filament (adapted from Ref. [10, 11]). (b) Bacteria swim faster in a dense solution of semi-flexible polymers than in a dilute solution (adapted from Ref. [12, 11]). (c) Model flagellated swimmer moving through a viscoelastic network (adapted from Ref. [13, 11]). 31

1.13 Schematic of a Maxwell fluid element. 34

2.1 Structure of the flexible filament. The surface of the object is discretized into multiple nodes, with the nodes interconnected by springs to provide the necessary stiffness. 43

2.2 Flowchart of the algorithm implemented for simulating the motion of a flexible object 44

3.1 schematic of the shape of filament and helical micro-robot. . 49

3.2 Schematic representation of the filament with Hookean springs connecting the filament nodes within each cross-section to neighboring cross-sections. Each node is connected to 26 adjacent nodes. 50

3.3 Comparison of the numerically obtained results for the filament position at four corresponding times in the cycle with the experimental results. 54

3.4 Relationship between the applied force and the terminal setting velocity. The markers are data points from simulations as given in Table 3.1 and the line shows the analytical linear relationship from Equation (3.8). 55

3.5 The deformed shape of the filament after reaching terminal setting velocity compared with the analytical formula. 57

3.6 The influence of r and λ on the maximum distance D between the pathline of the point and the axis of the micro-robot. The radius of the helical micro-robot for all simulations is set to $R = 0.1$. 61

3.7 Pathline of the point represented in 3D views with a close-up view of a portion in (b). The blue curve illustrates the trajectory of the point, while the red points depict the nodes situated on the surface of the micro-robot at one instant in time. 62

3.8 Streamlines of the fluid in the X–Z plane around a helical micro-robot in a rotating magnetic field. The color scale shows the velocity of the fluid in the Z direction relative to the translational velocity of the micro-robot in the Z direction ($V_z = 0.29$). 63

3.9 Velocity profile of the fluid in the Z direction versus Z position in the X–Z plane at a) $X = 0$ (on the axis) b) $X = 0.02$ (between the axis and the surface of the micro-robot) c) $X = 0.0375$ (close to the surface of the micro-robot) and d) $X = 0.1$ (beyond the surface of the micro-robot). The helix parameters are $\lambda = 0.15$, $R = 0.06$, and $r = 0.015$. The top and bottom of the micro-robot are located at $Z = 0.6$ and $Z = -0.6$, respectively. 64

3.10 Snapshots of the motion of a helical micro-robot and a passive filament with different ratios of helical pitch to radius; a) $\lambda/R = 1.6$, b) $\lambda/R = 3.3$, c) $\lambda/R = 5$, d) $\lambda/R = 6.6$. 67

3.11 Snapshots of the motion of the helical micro-robot and the passive filament with different flexibility (Hookean spring constant between mesh nodes of the filament); a) $k = 1000$, b) $k = 300$, c) $k = 50$, d) $k = 5$. 68

3.12 A micro-robot consisting of a pushing (black) and pulling (red) microhelix. Fluid streamlines around the rotating micro-robot are shown on the right, with the color scale indicating the Z-component of the velocity relative to the Z-velocity of the micro-robot. 70

3.13 A micro-robot with two microhelices initially containing a passive filament. The pushing section at the front of the micro-robot has the same axial length as the filament and pushes the filament out of the micro-robot. t1, t2, ..., t5, corresponding to times 0, 120, 240, 360 and 480, respectively. 72

3.14 A helical micro-robot with two microhelices approaching a passive filament. t1, t2, ..., t7, corresponding to times 0, 380, 760, 1140 and 1520, respectively. 73

3.15 A micro-robot consisting of three microhelices: a pushing (black) section between two pulling (red) sections. Fluid streamlines around the rotating micro-robot are shown on the right, with the color scale indicating the Z-component of the velocity relative to the Z-velocity of the micro-robot. 74

3.16 The effect of length ratio ξ of the middle (pushing) length to the combined front and middle lengths on the coupling between the three-section helical micro-robot and the passive filament. 76

3.17 Integration and carrying the passive filament with the designed helical micro-robot with three microhelices. The pushing microhelix is highlighted in blue, while the pulling microhelices are depicted in red. The values of the dimensionless times t1, t2, ..., and t7 are 0, 160, 320, 480, 640, 720, and 960, respectively. 77

3.18 Integration and transport of a passive, flexible filament with a sinusoidal shape having an amplitude equal to the filament radius. The pushing microhelix is highlighted in blue, while the pulling microhelices are depicted in red. t1, t2, ..., t7, corresponding to times 0, 120, 240, 360, 480, 600, and 640, respectively. 78

3.19 Integration and transport of a passive, flexible filament with a circular shape featuring an arc angle of 60 degrees. The pushing microhelix is highlighted in blue, while the pulling microhelices are depicted in red. t1, t2, ..., t7, corresponding to times 0, 80, 160, 240, 320, 480, and 560, respectively. . . . 79

3.20 Integration and transport of a passive, flexible filament with a head over time. The positions of the micro-robot, filament, and head are illustrated at seven different instances, t_1, t_2, ..., t_7, corresponding to times 0, 87.5, 254, 420, 588, 754, and 920, respectively. The pushing microhelix is highlighted in blue, while the pulling microhelices are depicted in red. . . . 80

3.21 Velocity profile of the fluid computed using the Regularized Stokeslet method along the axis of a right-handed helix in the axial direction when the microhelix moves with prescribed speed $U = 1$ and $\Omega = 0$. The back and front of the micro-robot are located at $Z = -4$ and $Z = 0$, respectively. The velocity at the central plateau corresponds to the parameter α. 83

3.22 Velocity profile of the fluid computed using the Regularized Stokeslet method along the axis of a right-handed helix in the axial direction when the microhelix moves with prescribed speed $U = 0$ and $\Omega = 1$. The back and front of the micro-robot are located at $Z = -4$ and $Z = 0$, respectively. The velocity at the central plateau corresponds to the parameter β. 84

3.23 Impact of λ/R and r/R on η^*. (desired η to have the same velocity for the filament and the micro-robot) 85

4.1 (a) Photomicrograph of bovine spermatozoa in a vaginal fluid sample [14]. (b) Model of a micro-swimmer moving through a viscoelastic network, adapted from Ref [13]. 90

4.2 Schematic of the element connecting two nodes in the viscoelastic network. 90
4.3 A cube within the viscoelastic network, where the nodes are connected by the elements shown in Figure 4.2. 91
4.4 Viscoelastic network. This is an infinite network. All connected nodes are connected with a Maxwell component. . . . 93
4.5 Creep functions for the viscoelastic network whose top surface is subjected to a unit stress, with results compared to the study by Wróbel et al. [13], to verify our model. 95
4.6 Creep functions for the viscoelastic network with the top surface subjected to a stress of 0.1 from time 0 to 1, while varying the spring constant of the Maxwell element. The dashed line represents the exponential curve fitted to the decreasing section of the plot to estimate the relaxation time. 97
4.7 Creep functions for the viscoelastic network whose top surface is subjected to a 0.1 stress from time 0 to 1, while the dash-pot constant of the Maxwell element is varied. The dashed line represents the exponential curve fitted to the decreasing section of the plot to estimate the relaxation time. 98
4.8 Creep functions for the viscoelastic network whose top surface is subjected to a 0.1 stress from 0 to 1, while the spacing between the viscoelastic nodes is varied. The dashed line represents the exponential curve fitted to the decreasing section of the plot to estimate the relaxation time. 99
4.9 Stress functions for the viscoelastic network in the strain test while the spring constant of the Maxwell element is varied. . 101
4.10 Stress functions for the viscoelastic network in the strain test while the dash-pot constant of the Maxwell element is varied. 102
4.11 Stress functions for the viscoelastic network in the strain test while the spacing between the viscoelastic nodes is varied. . 103
4.12 Comparison of the creep functions obtained from the simulation of the viscoelastic network and those derived from the analytical equation 4.3. The comparison includes sinusoidal stress functions with frequencies of 1, 2, 4, and 8, as well as linear and constant stress functions. 106

4.13 a) Scanning electron micrograph of a freeze-dried bovine vaginal fluid sample. Scale bar = $5\mu m$. b) Scanning electron micrograph of a freeze-dried bovine vaginal fluid sample considered to be an artifact. Scale bar = $25\mu m$, and insert $7.5\mu m$. Both figures adapted from Ref [14]. 108

4.14 Viscoelastic network with 50% of the links removed, showing the heterogeneity of the network from two different views. . 109

4.15 Creep functions for the viscoelastic network whose top surface is subjected to a 0.1 stress while the spring constant of the Maxwell element is varied. The dashed line represents the exponential curve fitted to the decreasing section of the plot to estimate the relaxation time. 111

4.16 Creep functions for the viscoelastic network whose top surface is subjected to a 0.1 stress while the dashpot constant of the Maxwell element is varied. The dashed line represents the exponential curve fitted to the decreasing section of the plot to estimate the relaxation time. 112

4.17 Creep functions for the viscoelastic network whose top surface is subjected to a 0.1 stress while the concentration of the viscoelastic network is varied by changing the fraction of links removed. The dashed line represents the exponential curve fitted to the decreasing section of the plot to estimate the relaxation time. 113

4.18 Creep functions for a viscoelastic network with $K = 0.625$ and $\eta = 10$ under a cyclic force $\sin(2\pi t)$ applied to the top surface: (a) fully connected network and (b) heterogeneous network with 40% of the links randomly removed. 116

5.1 Helical micro-robots used in the simulation: (a) Micro-robot with single handedness, (b) Micro-robot with three helices of alternating handedness. 120

5.2 Two views of the initial configuration of the viscoelastic network and location of the micro-robot before entering the viscoelastic network. 123

5.3 Normalized velocity of the micro-robot with single handedness in a viscoelastic fluid compared to its velocity in a Newtonian fluid versus time. Red vertical lines indicate where the micro-robots enter and exit the viscoelastic network. 125

5.4 Normalized velocity of the micro-robot with three helices and two different handedness in a viscoelastic fluid compared to its velocity in a Newtonian fluid versus time. Red vertical lines indicate where the micro-robots enter and exit the viscoelastic network. 126

5.5 Streamline of the fluid around the micro-robot with single handedness while the micro-robot is at the middle of the viscoelastic network. 127

5.6 Streamline of the fluid around the micro-robot with three helices and two different handedness while the micro-robot is at the middle of the viscoelastic network. 128

5.7 Helical micro-robot with single handedness a) inside the viscoelastic network and b) while it is exiting the network. . . . 129

5.8 Helical micro-robot with three helices and two different handedness a) inside the viscoelastic network and b) while it is exiting the network. 130

5.9 Normalized density of the viscoelastic nodes around the micro-robot with single handedness. 132

5.10 Normalized density of the viscoelastic nodes around the pushing micro-helix of the micro-robot with three helices and two different handedness. 133

5.11 Viscoelastic network around the micro-robot with three helices and a pushing micro-helix at the center, with Maxwell element stiffness of a) 0.625 and b) 160. 138

5.12 Normalized density of the viscoelastic nodes around the micro-robot close to the a) pushing micro-helix and b) back pulling micro-helix when the stiffness of the Maxwell element is 160. 139

5.13 Streamline of the fluid around the micro-robot with three helices where the stiffness of the Maxwell element is 160. . . . 140

5.14 Normalized density of the viscoelastic nodes around the micro-robot with single handedness where the stiffness of the Maxwell element is 160. 141

5.15 Viscoelastic network around a micro-robot with single handedness during its motion where the viscosity of the Maxwell element is 20. 143

5.16 Viscoelastic network around a micro-robot with three helices during its motion where the viscosity of the Maxwell element is 20. 144

5.17 Normalized velocity of the micro-robot inside the viscoelastic fluid for different values of the stiffness (K) of the Maxwell element. The concentration is represented by 100 minus the percentage of removed links. The plot compares the performance of single-handedness micro-robots and micro-robots with three helices. 146

5.18 Normalized velocity of the micro-robot inside the viscoelastic fluid for different values of the viscosity (η) of the Maxwell element. The concentration is represented by 100 minus the percentage of removed links. The plot compares the performance of single-handedness micro-robots and micro-robots with three helices. 147

5.19 Normalized velocity of the micro-robot with three helices in the forward direction over time within a viscoelastic network with a concentration of 40%, Maxwell element stiffness of 160, and Maxwell element viscosity of 10. 149

5.20 Normalized density of viscoelastic nodes around the micro-robot during the time robot has negative velocity and stuck inside the network (a) and after the viscoelastic links have been pushed away (b), where the micro-robot achieves a normalized speed greater than 1. 150

5.21 Viscoelastic network around a micro-robot with three helices during its motion. The viscosity of the Maxwell element is 20, the stiffness of the Maxwell element is 0.625, and breakpoints for the Maxwell element are considered. 153

5.22 Viscoelastic network around a micro-robot with single handedness during its motion. The viscosity of the Maxwell element is 20, the stiffness of the Maxwell element is 0.625, and breakpoints for the Maxwell element are considered. 154

1 Schematic of the element connecting two nodes in the viscoelastic network. 165

2 A cube within the viscoelastic network, where the nodes are connected by the elements shown in Figure 1. 167

List of Tables

3.1 Comparison of obtained velocity and analytical formula in sedimentation test. The radius of the filament a is 0.022, and half the length of the filament l is 0.1. 55

3.2 Comparison of propulsive velocity of a helix in a rotating magnetic field for different geometrical parameters between the developed model and the BEM model by Shum et al. [15]. R is the radius of the helix of the micro-robot and λ is the pitch of the helix. The frequency for all cases is 1 and the cross-section radius r is 0.015. 58

3.3 Mesh independency study. The radius of the helix of the micro-robot R is 0.06, the radius of the cross-section r is 0.015, the pitch of the helix λ is 0.2, and the winding is 6 for all cases. 59

4.1 Relaxation time obtained in the creep test for different cases where the stiffness of the spring and the dashpot constant in the Maxwell element and the spacing between the nodes in the viscoelastic network is varied. 100

4.2 Characterizing the fluid and obtaining the apparent solvent and solution viscosities and the elasticity of the viscoelastic network using the oscillation test and comparing the results with the formula derived in Equation 4.3. 104

4.3 Relaxation time (τ) for different cases with varying spring stiffness (K), dashpot constant (η), and fraction of removed links in the viscoelastic network. 114

5.1 Effect of viscoelastic properties on the normalized velocity of the micro-robot with single handedness. (Velocity is normalized with the velocity of the micro-robot in Newtonian fluid.) 135

5.2 Effect of viscoelastic properties on the normalized velocity of the micro-robot with three helices. (Velocity is normalized with the velocity of the micro-robot in Newtonian fluid.) . . 136

5.3 Effect of having breakpoints for the Maxwell elements in the viscoelastic fluid on the performance of the three-helix micro-robot with 60% removed links. 155

5.4 Effect of having breakpoints for the Maxwell elements in the viscoelastic fluid on the performance of the single handedness micro-robot with 60% removed links. 155

Chapter 1

Introduction

The development of magnetic micro-robots marks a significant advance in minimally invasive medical technology. These micro-robots, inspired by biological micro-swimmers, are increasingly used in various biomedical applications including drug delivery[16, 17, 18, 19, 20, 21, 22, 23], surgery[24, 25, 26], bio-sensing[27], and therapies involving chemicals and radiation[28]. Compared to traditional methods, micro-robots offer the potential for less invasive procedures and more precise drug delivery, which can reduce infection risks and side effects[24, 25, 26].

1.1 Motivation

The primary objective of this thesis is to design an innovative micro-robot capable of transporting filamentous micro cargo for drug delivery purposes, as well as aiding in the transportation of infertile sperm. To comprehend the rationale behind initiating this project, let us delve into an overview of the fertilization process, the associated challenges, and explore how micro-robots can address these issues. Fertilization entails the fusion of male and female gametes, resulting in the fertilization of the egg by the sperm[6]. In humans, fertilization occurs within the fallopian tube inside the female body. Sperm must traverse considerable distances within the complex environment of the female reproductive tract to reach the egg, encountering various chemical, rheological, and thermal properties along the way[1, 29, 30, 31]. Figure

1.1 illustrates the intricate geometry of the path that sperm must navigate to reach the egg. Approximately one in six couples in Canada and

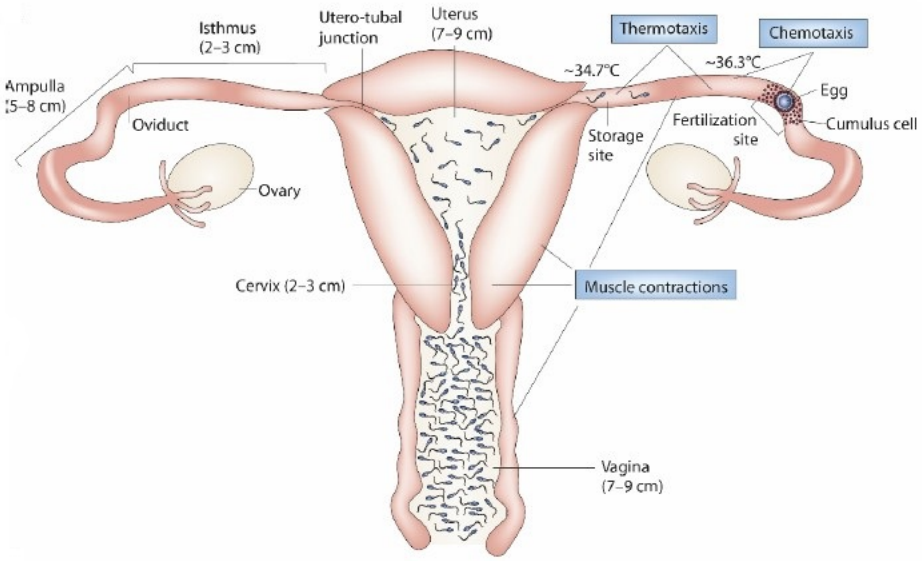


Figure 1.1: Schematic of complex geometry that sperm swim through to fertilize the egg [1, 2].

the UK face challenges conceiving, despite engaging in unprotected sexual intercourse for over a year[32]. Clinical studies indicate that 50% of these cases are attributable to male infertility[33]. Male infertility may stem from factors such as low sperm count, poor sperm motility, and DNA damage. Notably, low sperm motility is a prevalent cause of infertility. Most techniques employed to address sperm motility issues are invasive, expensive, and pose significant health risks to patients. Presently, assisted reproductive technologies (ARTs) have been developed and deployed to tackle male infertility problems[34, 35, 36]. These methods involve selecting sperm and either placing them adjacent to or injecting them into the egg to facilitate fertilization. In vitro fertilization (IVF)[37], intrauterine insemination (IUI), and intracytoplasmic sperm injection (ICSI) represent various ART methods utilized to address male infertility issues[38]. In IVF, sperm are placed in a petri dish alongside an egg to facilitate fertilization in vitro. In IUI, sperm are directly injected into the uterus via an insemination syringe. In ICSI, an egg is held while a sperm is injected through a needle into the egg.

The success rates of ART methods are suboptimal, necessitating numerous cycles, which are time-consuming and costly[39]. Sperm selection stands out as a pivotal step influencing the success of ART methods. Recently, various microfluidic methods have been developed to enhance sperm selection processes[40, 41]. However, these methods primarily serve as auxiliary approaches to traditional ART methods, aiming to enhance their success rates. A novel technique has emerged to aid the fertilization process for low motility sperm. Due to their poor motility, certain sperm may struggle to fertilize the egg. In 2015, Mariana et al. [4] introduced a magnetic micro-helix to enhance sperm motility. In this approach, sperm are housed within the micro-robot, where the sperm head surpasses the diameter of the helical micro-robot. Consequently, as the micro-robot rotates and advances, it propels the sperm forward. Upon reaching the egg, the micro-robot reverses rotation to release the sperm. However, Mariana et al. reported incomplete sperm release due to helix-sperm adhesion. This adhesion arises from the contact-based method employed for sperm transport. During micro-robot movement, close proximity or direct contact between the micro-robot and sperm leads to adhesion. This study is centered on the design of a magnetic helical micro-robot using a non-contact method to transport passive filaments along its axis. The primary application considered is the transport of immotile sperm for assisted fertilization, although the design concept has broader potential for other filamentous cargo.

The research begins by addressing the challenges associated with the helical geometry of the micro-robot and its effect on the transport process. A key focus is on overcoming the limitations of simple helical micro-robots in effectively transporting filaments. To address these challenges, we propose innovative design modifications aimed at enhancing the micro-robot's ability to capture and transport passive filaments effectively. Furthermore, since biological fluids like cervical mucus are viscoelastic, we also explore the behavior of the designed micro-robot in such complex environments.

Subsequent chapters will delve into these challenges in detail, presenting the developed models, numerical methods, and proposed solutions to optimize the micro-robot's design for various applications.

1.2 Micro-robot overview

The increasing application of micro-robots within the biomedical field is well-documented across numerous studies, highlighting their roles in drug delivery, surgical procedures, bio-sensing, and therapeutic practices[16, 17, 18, 19, 20, 21, 22, 23, 24, 25, 26, 27, 28]. These diminutive robots present a less invasive alternative to traditional surgical techniques, offering precise drug targeting capabilities that reduce both infection risks and side effects[24, 25, 26]. Typically, micro-robots' propulsion methods fall into three categories: chemical, physical, and bio-hybrid[42, 43, 44, 45, 46, 47, 48, 49].

Chemically propelled micro-robots, which generate movement through chemical reactions, face challenges regarding the safe release of materials in vivo. Bio-hybrid variants, integrating motile organisms for movement, also raise concerns about potential bio-contamination. Consequently, physical propulsion, especially magnetic-based mechanisms, has emerged as a preferable choice for internal body applications[50, 51, 4, 52].

Magnetic micro-robots, guided by external magnetic fields, stand out for their precision and minimal interaction with biological tissues[50, 51, 4, 52]. Their ability to navigate through diverse internal environments, such as the vitreous of the eye, knee tissue, and blood vessels, is particularly noted[50, 53, 54, 55, 56, 57]. Helical designs, driven by rotating magnetic fields and leveraging asymmetric drag for propulsion, have shown great efficacy in these roles[57, 58, 59].

Such helical micro-robots are adept at both direct cargo delivery and passive manipulation of cells, offering options for contact and non-contact transport methods. Direct contact can result in cargo adhesion and stress, while non-contact approaches utilize surrounding flow for gentle and selective transport[4, 3]. The study by Huang et al. (2014) exemplifies the capabilities of non-contact magnetic micro-robots in fluid environments, showcasing their selective trapping, stable transport, and delivery of microscale objects through flow and vortex generation, even under low-frequency magnetic control[3]. Medina-Sanchez et al. (2016) further advanced this field with sperm-carrying micromotors, showcasing a novel solution to male infertility by facilitating sperm delivery to oocytes[4]. These micromotors, crafted from metal-coated helices, promise controlled 3D movement within fluidic channels that simulate biological conditions necessary for fertilization.

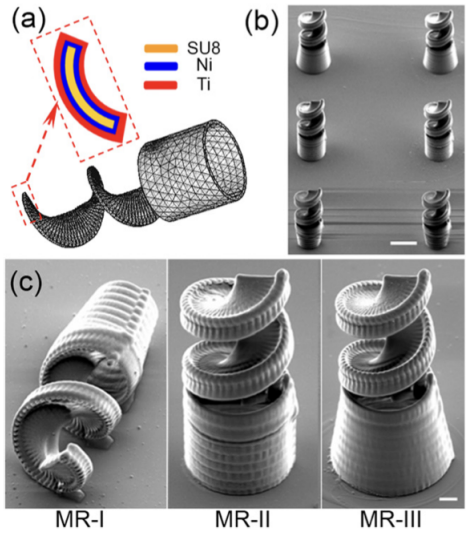


Figure 1.2: Schematic and SEM image of the developed magnetic micro-robot, featuring a helical tail and tubular head, illustrating its fluidic trapping and object transport abilities. Adapted from Huang et al., 2014.[3]

This pioneering approach, despite current limitations in achieving successful fertilization, signifies a major leap in assisted reproductive technologies, potentially enabling in vivo fertilization[4]. However, the release of sperm post-transport remains a challenge due to adhesion issues. Despite significant advancements, challenges in the effective release of cargo due to adhesion remain, underscoring the necessity for continued research into magnetic micro-robot applications in biomedicine. This study focuses on the design of a helical magnetic micro-robot that utilizes a non-contact approach to transport passive filaments, including immotile sperm. It is essential to understand how various geometrical parameters of the helical magnetic micro-robot, along with its underlying physics, influence its effectiveness in carrying passive filaments using this non-contact method. The primary geometry of the helix is described by the equations:

$$\begin{aligned} x(t) &= a\cos t, \\ y(t) &= a\sin t, \\ z(t) &= bt, \end{aligned} \tag{1.1}$$

where $t \in [0, T]$, a and $2\pi b$ denote the radius and pitch of the helix, re-

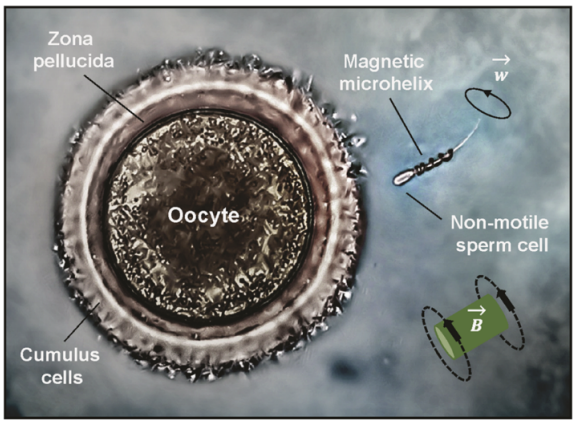


Figure 1.3: Depiction of a sperm-carrying micromotor in the process of capturing, transporting, and attempting to release a sperm cell near an oocyte for fertilization assistance. Adapted from Medina-Sanchez et al., 2016.[4]

spectively. The arc length of the helix is given by $T\sqrt{a^2+b^2}$. Variations in the total length of the helix, its windings, and pitch are explored to optimize performance. The circular cross-section of the helix is discretized into four nodes around its circumference, with equal spacing maintained between adjacent nodes both in the cross-section and along the length of the helix.

To induce rotation of the micro-helix, an external rotating magnetic field with a specific frequency is applied. The magnetization vector of the micro-helix, denoted by $\vec{M}$, interacts with the magnetic field vector $\vec{B}$. In hard magnetic materials, such as those employed in this project, the magnetization $\vec{M}$ is fixed relative to the micro-helix and does not change in response to variations in the external magnetic field. The torque, T_M, exerted on the micro-helix is given by:

$$T_M = \alpha \vec{M} \times \vec{B}, \tag{1.2}$$

where α represents the magnetic volume of the object. This torque acts to align the magnetization direction of the micro-helix with the magnetic field. The externally imposed magnetic field takes the form

$$\vec{B}(t) = B_0 \begin{pmatrix} \cos(2\pi f t) \\ 0 \\ \pm \sin(2\pi f t) \end{pmatrix}, \tag{1.3}$$

where f is the rotational frequency, B_0 is the constant magnitude of the magnetic field, and the direction of rotation is determined by the sign in the Z-component of (1.3). The magnetic field rotates around the $\pm Y$-direction, which is parallel to the axis of the micro-robot in its initial configuration. The control of motion relative to the rotating magnetic field is illustrated in Figure 1.4. The object attempts to rotate at the same frequency as the magnetic field, but there is a threshold known as the step-out frequency, beyond which the object's rotational frequency cannot keep up. Figure 1.5

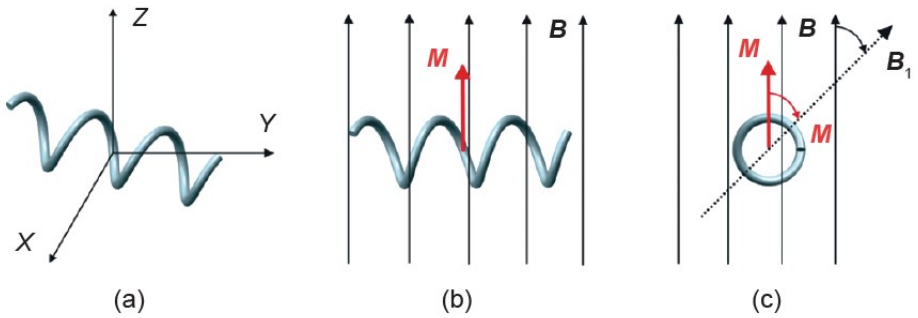


Figure 1.4: Motion control of the micro-helix with respect to the rotation of the magnetic field. [5]

illustrates how the forward velocity of the micro-helix varies with the rotational frequency of the magnetic field. The plot is divided into three regions: the wobbling, corkscrew, and step-out regions. In the wobbling region, the rotation frequency is minimal and the micro-helix oscillates around its axis. As the frequency increases, reaching the corkscrew region, the helix stabilizes and moves in a corkscrew pattern without wobbling. Here, the velocity of the micro-helix increases linearly with the frequency until reaching the step-out frequency. Beyond this point, in the step-out region, the velocity declines sharply as the rotational frequency becomes too high for the micro-helix to follow.

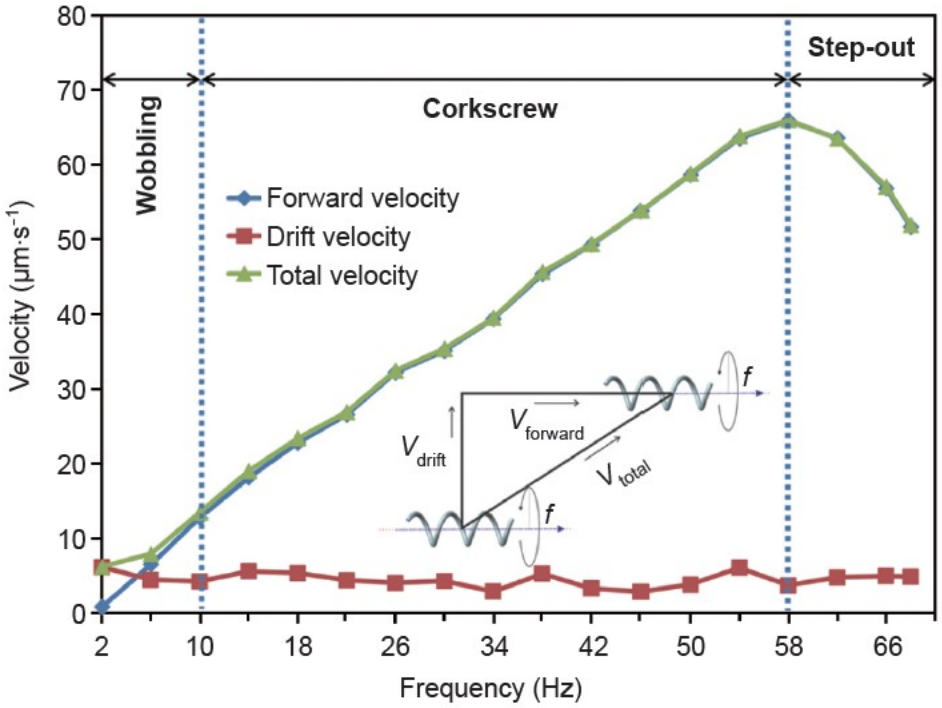


Figure 1.5: Experimental results for the rotational frequency of the magnetic field versus the velocity of the helix, obtained by Qiu & Nelson in 2015 [5].

1.3 Understanding sperm morphology and structure

As part of our efforts to design a micro-robot capable of transporting immotile sperm, it is imperative to thoroughly understand the morphology and structure of sperm. Sperm, also known as spermatozoon, is the male reproductive cell known for carrying the densest genetic material ever discovered [60]. The DNA crystal, housing genetic information and the sex-determining chromosome, is encapsulated within the head of the sperm. The sperm is essentially composed of two main parts: the head and the flagellum or tail. The head has a smooth oval shape, typically measuring 5-6 μm in length and 2.5-3.5 μm in width [6].

The flagellum is segmented into three distinct regions: the midpiece, the principal piece, and the end piece [6]. These regions differ primarily in their

internal structures. The entire flagellum spans an average length of 50-60 μm, with the midpiece measuring 4 μm, the principal piece 50 μm, and the end piece 3 μm.

A schematic representation of the sperm structure is shown in Figure 1.6. Details such as the cross-sectional structure of the midpiece are depicted in Figures 1.6b and 1.6e. The flagellum tapers along its length, with the radius decreasing from the midpiece to the endpiece [61]. The midpiece consists of nine dense outer fibers surrounded by mitochondria, which provide the necessary energy for sperm motility [6, 62]. Additionally, the passive stiffness of the flagellum decreases along its length due to structural variations in its composition. However, for the purposes of this study, we assume a fixed radius and uniform stiffness along the flagellum, although in reality it tapers [61]. The central axoneme structure, which extends through the entire flagellum, comprises nine microtubule doublets arranged around two central microtubules.

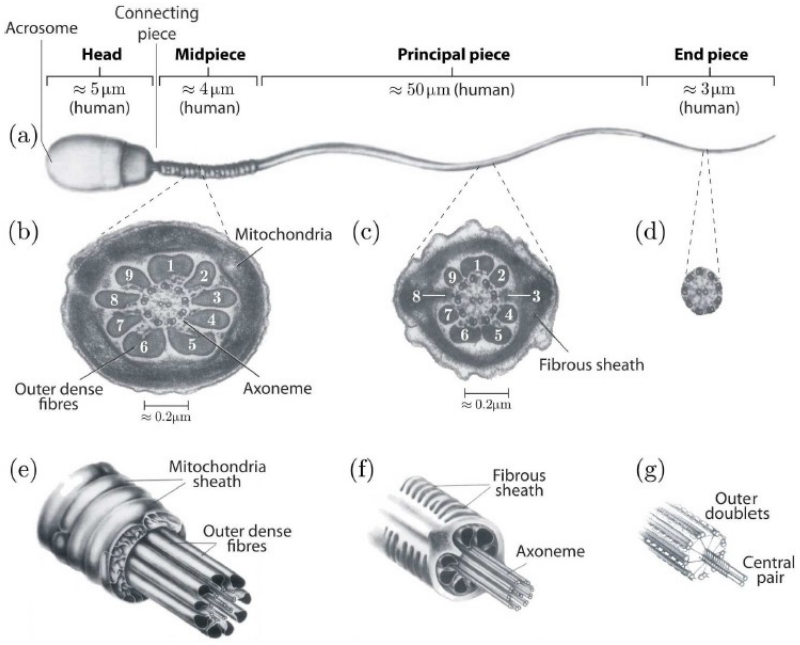


Figure 1.6: Schematic of Sperm structure. [6]

1.4 Classification of fluid behaviour

Fluids can be broadly categorized based on their rheological behavior into Newtonian and non-Newtonian types. Newtonian fluids exhibit a constant viscosity regardless of the applied shear rate, exemplified by substances like water and air. The response of a Newtonian fluid is characterized by a linear relationship between the applied shear stress and the strain rate,

$$\sigma = \eta\dot{\gamma}. \tag{1.4}$$

where σ is the stress tensor (Pa), η is the viscosity $(Pa.s)$ and $\dot{\gamma}$ is the strain rate (s^{-1}). The most basic deviation from Newtonian fluid behavior can be observed when the shear data does not originate from zero or fail to maintain a linear relationship between shear stress and strain rate. The apparent viscosity, denoted as $\mu = \tau/\dot{\gamma}$, is not constant but varies with shear rate or shear stress. Under certain conditions, the apparent viscosity of some materials not only changes with flow conditions such as geometry and shear rate but also depends on the fluid's previous motion history.

Materials exhibiting these traits can be arbitrarily categorized into three groups:

1. Substances for which the stress at a point is solely dependent on the instantaneous shear rate at that point. These are known as purely viscous, inelastic, time-independent, or generalized Newtonian fluids including shear thinning, shear thickening and viscoplastic fluids.

2. Materials where the stress-shear rate relationship varies with the duration of shear and past shear history, referred to as time-dependent fluids.

3. Materials that show characteristics of both viscous fluids and elastic solids, such as partial elastic recovery and creep. These are recognized as viscoelastic or elastico-viscous fluids.

This classification, while convenient, is somewhat arbitrary since many real materials often exhibit combinations of these behaviors under certain conditions. For instance, a polymer melt may simultaneously display shear-thinning and viscoelastic properties, while a china clay suspension might show characteristics of both shear-thinning and thixotropic behavior at specific concentrations and shear rates.[63]

1.4.1 Time-independent non-Newtonian fluids

In this category, the fluids demonstrate a viscosity that is not constant but varies according to the shear rate(strain rate), while it does not depend on the duration of shear application. This indicates that the immediate shear stress determines their behavior without regard to their past conditions, illustrating an absence of time-dependent memory. The description of their response under steady shear can be mathematically represented by the following relationship:

$$\dot{\gamma} = g(\sigma). \tag{1.5}$$

or by its corresponding reciprocal relationship:

$$\sigma = g^{-1}(\dot{\gamma}). \tag{1.6}$$

The behavior of these fluids under different conditions can be categorized in one of three forms:

- **Shear-Thinning Behavior:** These fluids experience a reduction in viscosity with an increase in shear rate, a phenomenon typically seen in polymer mixtures.
- **Shear-Thickening Behavior:** In this case, the viscosity augments in response to an increased shear rate, which is commonly observed in suspensions with high particulate concentrations.
- **Bingham Plastic Behavior:** These materials exhibit solid-like characteristics up to a certain stress threshold (yield stress) and flow like fluids when this threshold is exceeded.

Figure 1.7 showcases the variation in shear stress relative to shear rate for the aforementioned fluid types, thereby depicting their unique behaviors.

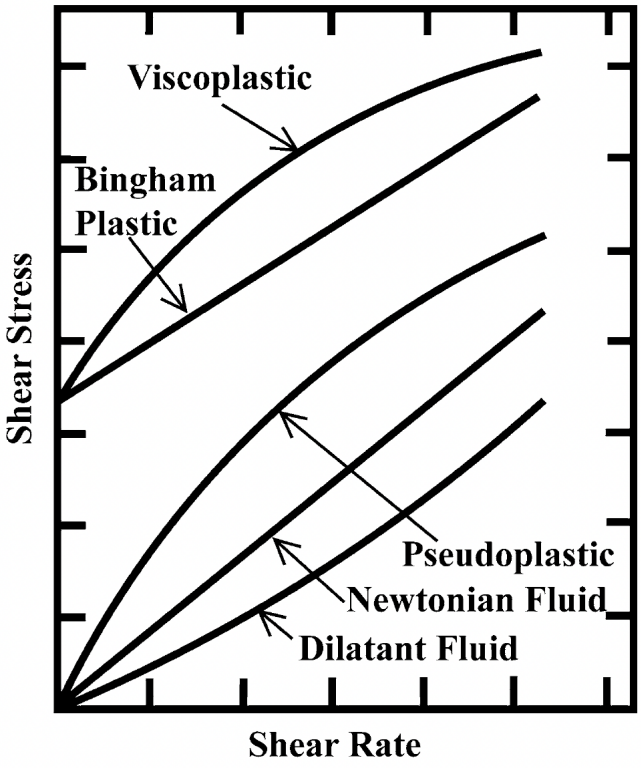


Figure 1.7: Graphical representation of shear stress versus shear rate(strain rate) for various types of Time-Independent non-Newtonian fluids. [7]

1.4.2 Time-dependent non-Newtonian fluids

The rheological properties found in several industrial domains, such as food production, pharmaceuticals, and cosmetology, often diverge from the behaviors predicted by conventional Newtonian frameworks, which are depicted in Equations 1.5 and 1.6. The apparent viscosities of these fluids are not solely determined by their immediate shear stress or rates; they are also substantially influenced by how long and in what manner shear has been historically applied. For instance, the manner in which a sample is introduced for viscometry can substantially alter the observed shear stress or rate. Fluids like bentonite-water mixtures and red mud suspensions, alongside everyday products such as hand lotions, usually show a reduction in viscosity under consistent shear, indicating a temporal breakdown of structure. On the other

hand, certain substances exhibit a shear-induced increment in viscosity over time.

Specifically, time-dependent non-Newtonian fluids fall into two principal categories, thixotropic and rheopectic fluids. Thixotropic fluids are recognized by their diminishing apparent viscosity under constant shearing. This decline points to a reliance on the shear's duration, typically represented by a hysteresis loop in a plot of shear stress versus shear rate under variable shear conditions. Intriguingly, thixotropic fluids can revert structurally, restoring their initial viscosity after the cessation of shear. This behavior is notably demonstrated by materials such as red mud suspensions, where an escalation in shear rate markedly reduces the time needed to stabilize the viscosity. Rheopectic behavior, also known as anti-thixotropy, is less commonly observed and characterizes fluids whose viscosity increases with the duration of constant-rate shear. This suggests an internal structure enhancement due to ongoing shearing. It's noteworthy that the same fluid can manifest both thixotropic and rheopectic properties depending on their concentration and the applied shear rate, exhibiting a unique dual nature in their rheological behavior.

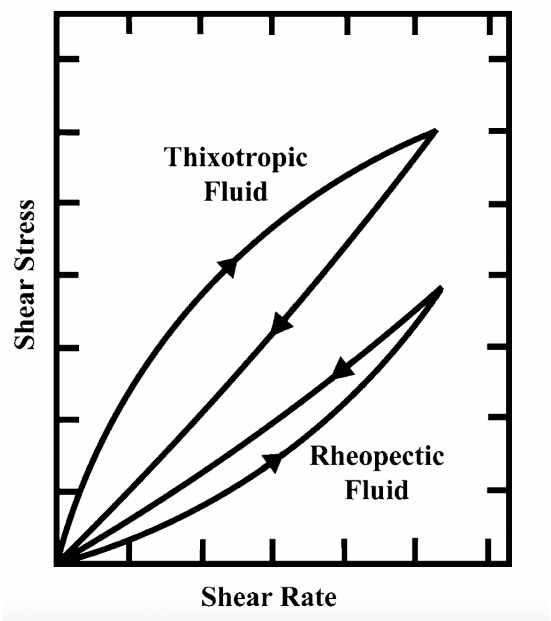


Figure 1.8: Graphical representation of shear stress versus shear rate for thixotropic and rheopectic substances, illustrating the distinctive hysteresis patterns emblematic of each fluid type. [7]

1.4.3 Viscoelastic fluids

When a force is applied to an elastic solid, it deforms immediately and returns to its original state as soon as the force is removed. By contrast, the deformation of a viscous fluid accumulates over time under the influence of an applied force, and although it stops deforming when the force is withdrawn, the changes it underwent remain permanent. Viscoelastic materials, which embody properties of both elastic solids and viscous fluids, behave in a more complex manner. Upon the application of a force, these materials exhibit an immediate deformation followed by a gradual increase in deformation, a process known as creep. Once the force is removed, a viscoelastic material quickly recovers some, but not all, of its deformation. The recovery continues over time, but typically, the material does not regain its original form completely.

The unique characteristics of viscoelastic materials arise from their internal structure, which can model the behavior of complex polymers and

biological tissues that exhibit both solid and fluid-like properties. The molecular chains within these materials can stretch and reorient under stress and gradually return to their original state, a process governed by the material's relaxation time. This time parameter is crucial as it dictates how quickly the material responds to stress and how effectively it can dissipate the energy absorbed from external forces. The behavior of viscoelastic materials under various conditions can be further described by rheological models, which help predict how these materials react under different loading rates. For instance, under a high frequency or rapid loading, viscoelastic materials may appear more solid-like, exhibiting minimal deformation and higher energy storage. Conversely, under low-frequency or sustained loading, they may behave more like viscous fluids, showing significant permanent deformation.

Thus, the response of viscoelastic materials is not only dependent on the force applied but also on the duration and frequency of the application, making them suitable for a wide range of applications from industrial polymers to biomedical devices, where tailored mechanical properties are crucial. Simple experimental methods such as creep and recovery, and stress relaxation tests, effectively demonstrate viscoelasticity.

Creep and recovery tests

When a Newtonian fluid is subjected to stress from a starting point $t = t_0$, as depicted in Figure 1.9a(1), the strain $\epsilon(t)$ rises linearly over time, as illustrated in Figure 1.9a(2). Once the stress is withdrawn at $t = t_s$, the strain maintains the level it reached at that moment, $\epsilon(t_s)$. In contrast, when a Hookean solid is subjected to stress, its strain $\epsilon(t)$ immediately increases in proportion to the stress, reaching $\epsilon(t_0)$, as shown in Figure 1.9a(3). This strain remains constant until the stress is removed at $t = t_s$, after which the strain fully reverts to zero. A viscoelastic material behaves differently under a constant stress; the strain $\epsilon(t)$ exhibits a delayed response, as seen in Figure 1.9a(4). Upon removal of the stress at $t = t_s$, a viscoelastic material only partially recovers its original shape immediately, with some deformation potentially remaining permanent. For viscoelastic solids, however, deformation recovery is relatively quicker, with nearly complete recovery achievable over an extended period.

Stress relaxation test

As shown in Figure 1.9b(1), when a material undergoes a sudden strain step at $t = t_0$ and maintains this strain for a prolonged period, different responses are observed. In Newtonian fluids, stress $\tau(t)$ spikes sharply with the abrupt increase in strain but drops to zero almost immediately, as depicted in Figure 1.9b(2), leading to immediate and total stress relaxation. Conversely, a Hookean solid maintains a constant stress level following the strain step at $t = t_0$, indicating no stress relaxation. For both viscoelastic liquids and solids, stress relaxation exhibits a nonlinear delay relative to their viscoelastic properties, as illustrated in Figure 1.9b(4). In viscoelastic liquids, if observed long enough, stress relaxation completes, albeit delayed. In viscoelastic solids, stress relaxation is both delayed and partial, persisting even after prolonged periods.

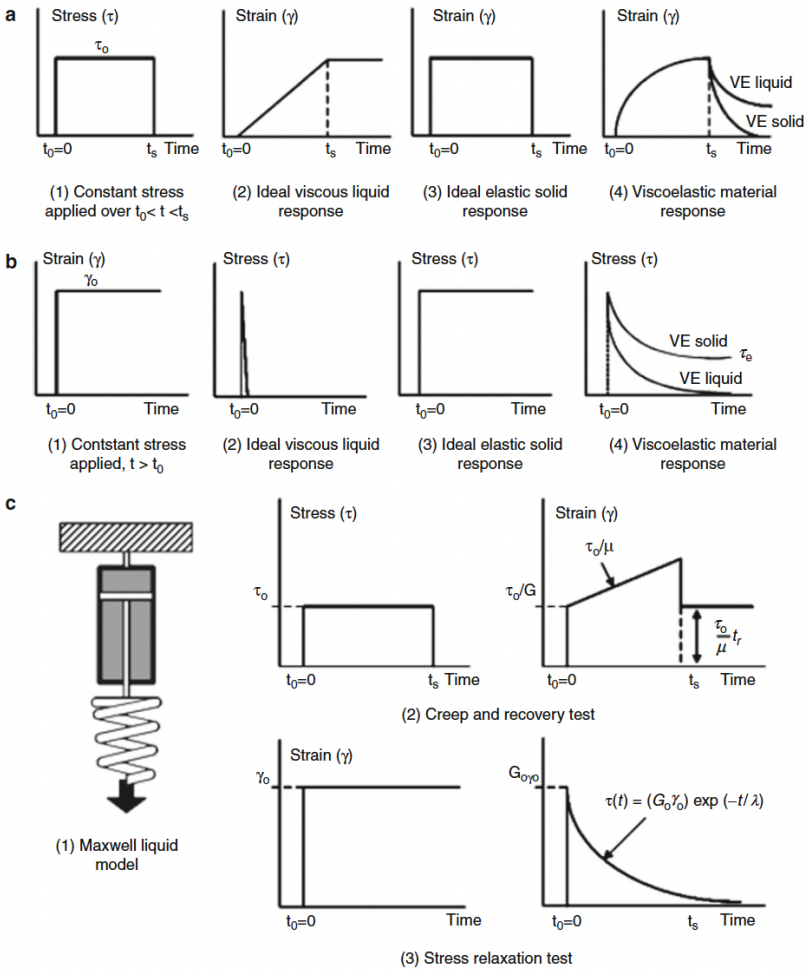


Figure 1.9: (a) Creep and Recovery Tests: (1) stress step, (2) response of an ideal viscous liquid (3) response of an ideal elastic solid (4) response of two different viscoelastic materials, both demonstrating a lag in deformation recovery. (b) Stress Relaxation Tests: (1) strain step (2) ideal viscous liquid relaxation curve (3) ideal elastic solid relaxation curve (4) stress relation curves of two viscoelastic materials, each exhibiting prolonged stress relaxation. (c) (1) Diagram of the Maxwell liquid model and (2) its behavior during a creep recovery test, (3) followed by a stress relaxation test.[8]

Parameters Characterizing Viscoelastic Behavior

The relaxation time λ_p indicates how long it takes for a polymer coil to revert from a deformed state back to its equilibrium configuration. It is therefore

a pivotal parameter for delineating the characteristics of a viscoelastic fluid. In fluids with a large λ_p, stresses dissipate slowly, allowing elastic behaviors to manifest even under low deformation rates. Conversely, fluids with a smaller λ_p may still exhibit significant elastic behaviors if the rate of deformation is sufficiently high. For polymeric liquids, where λ_p typically ranges from seconds in dilute solutions to much shorter times in more concentrated solutions. Moreover, λ_f denotes the characteristic time scale of the flow or deformation process.

Deborah Number: The importance of elasticity in flow dynamics is frequently quantified by the Deborah number (De). It reflects the ratio of the material or polymer's relaxation time λ_p to the characteristic time scale of the flow λ_f, and is defined as:

$$De = \frac{\lambda_p}{\lambda_f}. \tag{1.7}$$

This dimensionless number is crucial because it describes how the fluid behaves under various flow conditions. A high Deborah number ($De \gg 1$) suggests that elastic effects dominate the fluid behavior, meaning the material behaves more like an elastic solid during the flow. This is typical in many polymer processing operations where viscoelastic effects significantly influence the material's response. Conversely, a low Deborah number ($De \ll 1$) indicates that viscous effects dominate, and the fluid behaves more like a Newtonian liquid.

Weissenberg Number (Wi) The Weissenberg number (Wi) is a dimensionless quantity that characterizes the dominance of elastic forces over viscous forces in a flow. It is defined as:

$$Wi = \lambda_f \dot{\gamma}. \tag{1.8}$$

where $\dot{\gamma}$ is the shear rate. High Weissenberg numbers suggest that elastic effects profoundly influence the flow behavior of viscoelastic fluids. This insight is pivotal for deciphering flow instabilities and the material's response to deformation.

Hysteresis effect A defining characteristic of viscoelastic fluids is the hysteresis effect. Hysteresis in these fluids manifests as a divergence in the stress-strain curve during loading versus unloading cycles. This phenomenon,

indicative of energy dissipation and the time-dependent nature of the material's response to external forces, is typically observed in cyclic loading tests. It plays a critical role in understanding the memory effects and non-linear behavior of viscoelastic materials.

Comprehending the Weissenberg and Deborah numbers, along with the hysteresis effect, significantly enriches the analysis of viscoelastic fluid behavior. These concepts highlight the critical role of time-dependent properties and the interplay between elastic and viscous forces in determining how the fluid reacts to deformation. Integrating these considerations into models of viscoelastic fluids improves the accuracy of predictions for both linear and nonlinear responses under varied conditions.

Viscoelastic fluids, including polymer solutions and melts, biological fluids, and some suspensions, play a critical role in various applications, from industrial processes to biological systems. Understanding their complex rheological behavior is essential for designing processes and materials that effectively utilize their unique properties. Viscoelastic materials combine the properties of viscous fluids and elastic solids, leading to unique behaviors under applied stress or strain. To describe these behaviors, models are classified into linear and nonlinear categories based on the material's response to the applied load. Linear models are applicable under small deformations, assuming a proportional response to stress or strain, while nonlinear models are necessary for large deformations or complex loading conditions, capturing the material's behavior more accurately.

In the context of rheology, the response of materials is classified as linear if the change in input results in a proportional change in output, adhering to the superposition principle. For example, in small amplitude oscillatory shear (SAOS), altering the strain amplitude proportionately alters the stress amplitude. Thus, material functions like the storage and loss moduli remain independent of the strain amplitude, denoting a linear viscoelastic behavior up to a certain strain amplitude limit. Beyond this limit, materials exhibit a nonlinear response characterized by larger deformations, structural changes, or phase transitions, complicating the analysis due to their complex interplay and mathematical representation. Several methods such as creep and recovery, stress relaxation, and oscillatory shear are utilized to investigate these nonlinear behaviors. These techniques help in emphasizing certain structural-property relationships or are selected based on their relevance to specific applications. The development and application of comprehensive

models to describe these behaviors continue to evolve, significantly aided by advancements in experimental and theoretical tools over recent decades. The graph presented in Figure 1.10 delineates the behavior of a viscoelastic fluid subject to different frequencies and amplitudes of applied strain. Notably, at minimal strain amplitudes, the fluid's response adheres to linear viscoelasticity, characterized by a constant strain rate amplitude that is independent of the frequency. This region is indicative of a linear, proportionate relationship between stress and strain, signifying predictable viscoelastic behavior. As the amplitude of deformation intensifies, the fluid departs from linear behavior, manifesting nonlinear viscoelastic characteristics where both the amplitude and frequency of the strain influence its response. The extremes of the frequency spectrum reveal the fluid's tendency to mimic Newtonian viscous behavior at low frequencies, while at high frequencies, it resembles the behavior of an elastic solid. This demonstrates the intricate balance between viscous and elastic properties in viscoelastic fluids, contingent on the conditions of the mechanical stress they encounter.

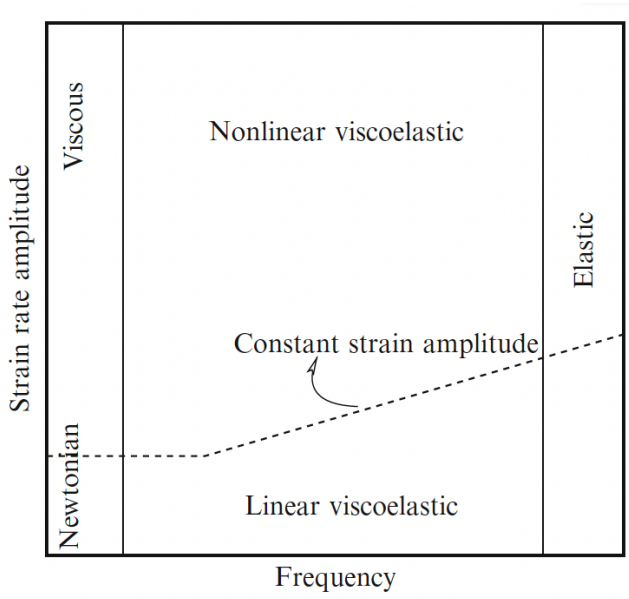


Figure 1.10: Diagram illustrating material responses at different frequencies and strain rates, depicting transitions from Newtonian viscous to nonlinear viscoelastic behaviors as strain rates increase [7].

Linear viscoelastic models

Linear viscoelasticity assumes a direct proportionality between stress and strain, suitable for small deformations where material properties remain constant.

Maxwell Model

The Maxwell model, representing a viscous damper and an elastic spring in series, is described by:

$$\frac{d\sigma}{dt} = \frac{K}{\eta}\left(\frac{d\epsilon}{dt} - \frac{\sigma}{K}\right)$$

where σ is stress, ϵ is strain, K is the elastic modulus, and η is the viscosity.

Kelvin-Voigt Model The Kelvin-Voigt model, combining a damper and a spring in parallel, follows:

$$\sigma = K\epsilon + \eta\frac{d\epsilon}{dt}$$

capturing creep behavior but not stress relaxation effectively.

Standard Linear Solid Model (Zener Model) This model integrates the features of the Maxwell and Kelvin-Voigt models, offering:

$$\sigma + \frac{\eta_1}{E_1}\frac{d\sigma}{dt} = E_2\epsilon + (\eta_1 + \eta_2)\frac{d\epsilon}{dt} + \frac{\eta_1\eta_2}{E_1}\frac{d^2\epsilon}{dt^2}$$

where E_1 and E_2 are the moduli of springs, and η_1 and η_2 are viscosities.

Burgers Model The Burgers model, a series combination of Maxwell and Kelvin-Voigt elements, is governed by:

$$\sigma + \left(\frac{\eta_1 + \eta_2}{E_1}\right)\frac{d\sigma}{dt} + \frac{\eta_1\eta_2}{E_1E_2}\frac{d^2\sigma}{dt^2} = (E_1 + E_2)\,\epsilon + (\eta_1 + \eta_2)\,\frac{d\epsilon}{dt}$$

Nonlinear viscoelastic models

Nonlinear viscoelastic models account for non-proportional stress-strain relationships, essential for describing behaviors under large deformations or complex loading.

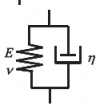
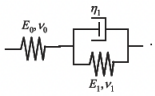
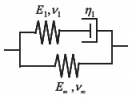
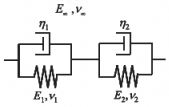
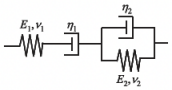
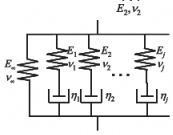
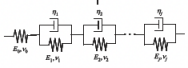
Viscoelastic models	Relaxation moduli			
	Diagrammatic sketches	Young's relaxation modulus $E(t)$	Bulk relaxation modulus $K(t)$	Shear relaxation modulus $G(t)$
Hooke model		E	K	G
Newton model		$9Ke^{-\frac{t}{\tau_K}}$	K	$\eta\delta(t)$
Maxwell model		$Ee^{-\frac{t}{\tau_E}}$	K	$Ge^{-\frac{t}{\tau_G}}$
Voigt model		$9Ke^{-\frac{t}{\tau_0}} + E\bar{e}^{-\frac{t}{\tau_0}}$	K	$G + \eta\delta(t)$
Boltzmann model		$E_0^{\times}e^{-\frac{t}{\tau_1^{\times}}} + E^{\times}\bar{e}^{-\frac{t}{\tau_1^{\times}}}$	$K^{\times}$	$G_0e^{-\frac{t}{\tau_G^{\times}}} + G^{\times}\bar{e}^{-\frac{t}{\tau_G^{\times}}}$
Zener model		$E^{+}e^{-\frac{t}{\tau_1^{+}}} + E_{\infty}^{+}\bar{e}^{-\frac{t}{\tau_1^{+}}}$	K^{+}	$G^{+}e^{-\frac{t}{\tau_1^{+}}} + G_{\infty}\bar{e}^{-\frac{t}{\tau_1^{+}}}$
Tsay model		$9K^{+}\left[a_1^E e^{-\frac{t}{\tau_1^E}} + a_2^E e^{-\frac{t}{\tau_2^E}}\right] + E_{\times}^{+}\left[a_1^E \bar{e}^{-\frac{t}{\tau_1^E}} + a_2^E \bar{e}^{-\frac{t}{\tau_2^E}}\right]$	K^{+}	$G^{\times} + \eta^{\times}\delta(t) + \frac{(G_1\eta_2 - G_2\eta_1)^2}{(G_1+G_2)(\eta_1+\eta_2)^2}e^{-\frac{t}{\tau_{12}}}$
Burgers model		$E_1^{\times}\left[a_1^E e^{-\frac{t}{\tau_1^E}} + a_2^E e^{-\frac{t}{\tau_2^E}}\right]$	$K^{\times}$	$G_1\left[a_1^G e^{-\frac{t}{\tau_1^G}} + a_2^G e^{-\frac{t}{\tau_2^G}}\right]$
Weichert model		$E_0\sum_{n=1}^{N_G} a_n^E e^{-\frac{t}{\tau_n^E}} + E_{\infty}\sum_{n=1}^{N_G} a_n^E \bar{e}^{-\frac{t}{\tau_n^E}}$	K	$G_0\sum_{n=1}^{N_G} a_n^G e^{-\frac{t}{\tau_n^G}} + G_{\infty}\sum_{n=1}^{N_G} a_n^G \bar{e}^{-\frac{t}{\tau_n^G}}$
Kelvin model		$E_0\sum_{n=1}^{N_J} a_n^E e^{-\frac{t}{\tau_n^E}} + E_{\infty}\sum_{n=1}^{N_J} a_n^E \bar{e}^{-\frac{t}{\tau_n^E}}$	K	$G_0\sum_{n=1}^{N_J} a_n^G e^{-\frac{t}{\tau_n^G}} + G_{\infty}\sum_{n=1}^{N_J} a_n^G \bar{e}^{-\frac{t}{\tau_n^G}}$

Figure 1.11: Diagrammatic representations and relaxation modulus for various linear viscoelastic models, adapted from [9].

Oldroyd-B Model The Oldroyd-B model, useful for viscoelastic fluids, combines fluid viscosity with elastic elements, described by:

$$\tau + \lambda_1 \frac{D\tau}{Dt} = \eta\left(\nabla v + (\nabla v)^T\right) + \lambda_2 \frac{D}{Dt}\left(\nabla v + (\nabla v)^T\right)$$

where τ is the stress tensor, $\frac{D}{Dt}$ is the material derivative, and λ_1, λ_2 are time constants.

Phan-Thien and Tanner (PTT) Model The PTT model incorporates

shear-thinning behavior:

$$\tau + \lambda \frac{D\tau}{Dt} = \eta(\dot{\gamma}) \left(\nabla v + (\nabla v)^T \right) - \epsilon \tau (\nabla v + (\nabla v)^T)$$

where $\eta(\dot{\gamma})$ represents a shear-dependent viscosity, and ϵ is a model parameter related to shear thinning.

Giesekus Model The Giesekus model introduces anisotropic drag contributions:

$$\tau + \lambda \frac{D\tau}{Dt} = \eta_0 \left(\nabla v + (\nabla v)^T \right) + \alpha \frac{\tau^2}{\eta_0}$$

where η_0 is the zero-shear viscosity, α is the mobility factor influencing material anisotropy.

These equations provide a mathematical foundation for understanding and modeling the viscoelastic behavior of materials under various conditions, highlighting the diversity and complexity of these phenomena. In summary, the distinction between linear and nonlinear viscoelastic models is fundamental in understanding and predicting the behavior of materials under various loading conditions. Linear models, ideal for small deformations, offer simplicity and analytical tractability. In contrast, nonlinear models, essential for large deformations or complex loading conditions, provide a more accurate representation of the material's behavior by incorporating the dependence of the material's response on the magnitude of applied stress or strain.

1.5 Micro-swimmer motion in a viscoelastic fluid

The movement of microorganisms and sperm cells within viscoelastic fluids plays a pivotal role in numerous biological functions, including fertilization, infection, and the development of biofilms. The response of these microswimmers to the complexities of the fluid environment varies based on their propulsion strategies. Changes may include alterations in their swimming speed and efficiency, adaptations in their propulsion kinematics and swimming patterns, and varied hydrodynamic interactions with the environment. Within their complex biological environments, microorganisms

and spermatozoa frequently navigate through non-Newtonian fluids. For instance, mammalian sperm navigate viscoelastic mucus within the cervix or the fallopian tubes [64, 65, 66, 67]. Similarly, the bacterium *Helicobacter pylori* travels through the mucus layers that coat the stomach, contributing to ulcer formation [68, 69]. The Lyme disease-causing spirochete, *Borrelia burgdorferi*, moves through the connective tissues of the skin [70, 71]. An additional significant example of biological flow involving complex fluids at the micron scale involves the movement of cilia. These cilia transport mucus layers that envelop the epithelium of various organs and glands. Such motion is vital for several functions: it aids in the expulsion of foreign materials within the mammalian respiratory tracts, facilitates the movement of mucus and ovum through the fallopian tubes, and contributes to transcervical processes. Spermatozoa migration in reproductive tracts is notable [72]. Additionally, ependymal cilia, present in specialized brain cells, play a role in the small-scale transport of cerebrospinal fluid [73]. For micro-scale locomotion, which is central to this discussion, $\mathrm{Re} \equiv \frac{\rho U_c l_c}{\mu}$, where l_c and U_c are the characteristic length and swimming speed of the microorganism, and ρ and μ are the mass density and dynamic viscosity of the fluid, respectively. In the low-Reynolds number domain of cells, $\mathrm{Re} \ll 1$, meaning cells swimming in Newtonian fluids must utilize non-reversible strokes to circumvent the limitations set by Purcell's scallop theorem and achieve self-propulsion [74].

Various swimming strategies are utilized by motile cells in nature [75]. For example, certain protozoa like *Paramecium*, and algae such as *Volvox*, employ metachronal waves triggered by collective cilia beating. Many bacteria, including the model organism *Escherichia coli* (*E. coli*), swim by rotating helical flagellar filaments attached to their bodies, whereas spirochete bacteria like *Spiroplasma* move through the propagation of rotational waves or shape kinks along their spiral cell structures. In contrast, most spermatozoa and some nematodes, such as *Caenorhabditis elegans*, navigate using a planar waving deformation of their flagella or slender bodies. The non-Newtonian rheology of complex fluids generally disrupts the time-reversal symmetry inherent in the Newtonian Stokes equations, facilitating self-propulsion under reciprocal motion as demonstrated with artificial swimmers [76, 77]. Importantly, complex fluids can significantly alter the swimming kinematics and motility of individual micro-swimmers and their collective behaviors. *E. coli*, for instance, swims faster and follows straighter trajectories with re-

duced cell body wobbling in a polymer solution compared to a Newtonian setting; this is due to the rotation of its flagellar filaments, which substantially stretches polymers within the fluid and generates local elastic stresses that prevent flagellar filament unbundling, thus affecting its run-and-tumble behavior [78]. The algal cell *C. reinhardtii* experiences alterations in the wave envelope of its beating flagella due to the viscoelasticity of the fluid, limiting flagellar displacement near the cell body and reducing swimming speed despite higher frequency flagellar beats in a polymer solution [79]. Similar phenomena are observed in swimming spermatozoa, whose flagella beat at higher frequencies with smaller amplitude near the cell body in viscoelastic cervical mucus compared to Newtonian fluids [64, 80, 81, 82]; however, their swimming speed is surprisingly less impacted [64]. Bovine spermatozoa exhibit disorganized individual swimming in Newtonian fluids, yet form dynamic clusters in viscoelastic fluids, with cluster sizes and cell–cell alignments increasing with fluid viscoelasticity. This collective behavior is attributed to the elastic properties of the fluid, which generate normal stress differences and promote interactions between nearby sperm cells. Tung *et al.* (2017) demonstrated that viscoelasticity enhances the formation of sperm clusters by inducing elastic stresses that align neighboring cells, facilitating cooperative swimming and increasing overall motility efficiency. They also observed that the presence of polymers in the fluid leads to changes in the flow field around the sperm, effectively mediating cell–cell interactions through elastic stresslets [83].

These instances illustrate how complex fluids' effects on micro-swimming vary significantly depending on the type of swimming cells and the interplay between their swimming gait and the fluid's rheology. Numerous non-Newtonian biological fluids, such as biofilm and mucus, are hydrated polymeric gels composed of 90% water by weight; the remaining constituents, typically a mix of extracellular polysaccharides, proteins, and lipids, contribute to the fluid's elasticity and shear-thinning viscosity. The rheological properties of biofilms are highly variable; their elastic modulus G ranges from 10 to 10^3 Pa for most biofilms and can reach up to 10^5 Pa in biofilms from natural hot springs [84, 85, 86, 87]; the viscosity of biofilms generally lies between $\mu \approx 10^2$ to 10^5 Pas, while their relaxation time $\lambda_p \approx 10$ s for *S. epidermidis* biofilm and around 10^3 s for a broad spectrum of environmental biofilms [88]. For mucus, $\mu \approx 10^{-2}$ to 10^2 Pas, $G \approx 0.1$ to 10^2 Pa, and $\lambda_p \approx 1$ to 10 s [89, 90]. Given that the relevant timescale for micro-swimming along-

side the swimmer size is $l_f/U \approx 0.1$ to 1 s and the flagellum beating period $T \approx 10^{-2}$ to 0.1 s, the relaxation time of these complex fluids is comparable to, or much longer than, the timescales of micro-swimming. Thus, micro-swimmers are expected to be profoundly influenced by the elastic stresses in a complex fluid, thereby experiencing the full spectrum of non-Newtonian effects, including stress relaxation, strain retardation, and normal stress differences. Although numerous studies depict complex fluids as homogeneous continuum media, it is essential to acknowledge that most biological samples exhibit considerable heterogeneity at the microscale [91]. Microorganisms frequently navigate through environments consisting of entangled fibers approximately 10–100 nm in diameter and pores ranging from 0.1 to 1 μm [92]. For instance, an aerobic biofilm forms a porous matrix where polymer clusters are interspersed with voids and channels about 10–100 μm across, facilitating enhanced oxygen and nutrient transport across the colony [93]. This microscale heterogeneity significantly influences micro-swimmer motility. In semi-dilute polymer solutions, the bacterium E.coli moves faster than in Newtonian fluids, as its rotating flagella intensely stretch nearby polymer molecules, effectively creating a low-viscosity pathway devoid of polymers around the flagellum, thereby increasing the flagellar motor's rotation rate and consequently the cell's speed. Conversely, in cervical mucus, "following" spermatozoa exhibit slower movement compared to "vanguard" ones, even though their flagellar beating frequencies and shapes are identical. This discrepancy in propulsive efficiency results from changes in the local mucus properties caused by ongoing sperm permeation [66]. To enhance understanding of the effects of microscale heterogeneity, recent investigations have suggested employing coarse-grained polymer models [10, 12]. Now let's introduce the classical dimensionless numbers that define the dynamics of fluids within a viscoelastic (polymeric) medium and the associated governing equations relevant for microswimming. The polymer relaxation time is denoted by λ_p, while λ_f, $\dot{\gamma}$, and l_f represent the characteristic time, shear rate, and length scales, respectively, for fluid motion around a microswimmer. The fluid's mass density is ρ, and the total viscosity μ is the sum of the solvent and polymer viscosities, μ_f and μ_p, respectively.

Key dimensionless quantities, including the Reynolds number Re, the Deborah number De, and the Weissenberg number Wi, which are explained in equations 1.7 and 1.8 respectively, are crucial for characterizing fluid flow in this context. The Reynolds number Re represents the ratio of inertial

forces to viscous forces and is defined as:

$$\mathrm{Re} = \frac{\rho U_f l_f}{\mu}$$

where U_f is the velocity of the fluid. The Reynolds number helps in determining whether the flow is laminar or turbulent, with lower values indicating viscous-dominated flow and higher values signifying inertia-dominated flow. These include the elasticity number El, the dimensionless viscosities of the polymer and solvent $\hat{\mu}_p$ and $\hat{\mu}_f$, and the suspension Knudsen number Kn_f. These quantities are mathematically expressed as:

$$\mathrm{El} = \mathrm{Wi}/\mathrm{Re} = \frac{\mu\lambda_f}{\rho l_f^2}, \tag{1.9}$$

$$\hat{\mu}_p = \frac{\mu_p}{\mu}, \quad \hat{\mu}_f = 1 - \hat{\mu}_p, \tag{1.10}$$

$$\mathrm{Kn}_f = \frac{l_d}{l_f}, \tag{1.11}$$

As explained also before in equation 1.7,the Deborah number De signifies the ratio between the polymer relaxation time and the observational time scale of the fluid flow. When considering a swimming microorganism, the flow time scale is often set as $t_f = 1/\dot{\gamma} = l_f/U$ or $t_f = 1/\omega$, where U represents the swimming speed and ω the frequency of any periodic motion of the swimmer, such as the undulating motion of the flagella. The Weissenberg number Wi also as explained before, representing the product of the polymer relaxation time and the effective shear rate, also serves as a measure of the ratio between the elastic force and the viscous force. In certain types of motion like steady squirming, $\mathrm{Wi} \approx \mathrm{De}$, but these dimensionless numbers can differ substantially in other contexts. For example, in viscoelastic flows prompted by oscillatory shear on a squirmer surface, De and Wi may assume different values. The Deborah number De and Weissenberg number Wi are particularly crucial, indicating the ratio of polymer relaxation to the characteristic flow time and the product of polymer relaxation time with the shear rate, respectively. The elasticity number El, independent of the swimming kinematics, relates to the polymer's momentum diffusion, crucial for understanding microswimmers in biologically relevant media like biofilms and mucus. In the context of viscoelastic polymer solutions, Kn_f captures the non-continuum aspects of the medium, considering the size of dispersed

phases such as polymers (l_d) relative to the swimming flow length scale(l_f), which is essential for recognizing local non-uniformities that influence microswimmer dynamics. For instance, $\mathrm{Kn}_s \ll 1$ indicates that the fluid can be modeled as a continuum; otherwise, the microstructural details become significant.

1.5.1 Helical locomotion

Helical locomotion, propelled by the rotation of slender helical structures, is prevalent among bacteria equipped with flagellar filaments and spirochetes. Research indicates that numerous bacteria not only navigate through polymer solutions but also exhibit enhanced speeds compared to those in pure solvents, despite higher viscosities of the solutions [94, 95]. The speed variation among different bacterial species does not follow a simple pattern with viscosity changes but instead peaks at a specific viscosity level [94, 96, 97]. Berg and Turner [95] observed that for *E. coli* anchored in a branched polymer solution, the angular velocity of its body inversely correlates with fluid viscosity, aligning with expected Newtonian dynamics. However, this effect is diminished in unbranched polymer solutions, indicating pronounced non-Newtonian behaviors. They proposed that bacteria navigate through a complex, quasi-rigid network of microscale pores in unbranched polymers, facing dual frictional forces—lower inside the pores and higher against the network structure, leading to unique motility patterns. Conversely, branched polymer solutions exhibit more uniform behavior, resembling that of Newtonian fluids. Helical locomotion, propelled by the rotation of slender helical structures, is prevalent among bacteria equipped with flagellar filaments and spirochetes. Research indicates that numerous bacteria not only navigate through polymer solutions but also exhibit enhanced speeds compared to those in pure solvents, despite higher viscosities of the solutions [94, 95]. The speed variation among different bacterial species does not follow a simple pattern with viscosity changes but instead peaks at a specific viscosity level [94, 96, 97]. *Berg* and *Turner* [95] observed that for *E. coli* anchored in a branched polymer solution, the angular velocity of its body inversely correlates with fluid viscosity, aligning with expected Newtonian dynamics. However, this effect is diminished in unbranched polymer solutions, indicating pronounced non-Newtonian behaviors. They proposed that bacteria navigate through a complex, quasi-rigid network of microscale pores in un-

branched polymers, facing dual frictional forces—lower inside the pores and higher against the network structure, leading to unique motility patterns. Conversely, branched polymer solutions exhibit more uniform behavior, resembling that of Newtonian fluids. Similarly, studies on artificial helical micro-robots in fibrous environments, such as those conducted by *Ullrich* et al. [98], have demonstrated that these micro-robots also exhibit enhanced propulsion in viscoelastic fluids. Specifically, they found that a peak in swimming velocity occurs at an optimal collagen concentration, where the micro-robot can effectively exploit the fibrous network for propulsion. This mirrors the enhanced swimming speeds observed in bacteria navigating fibrous polymer solutions, further supporting the concept that such environments can facilitate helical propulsion by providing a structured medium that reduces drag and improves motility.

Magariyama and *Kudo* [99] enhanced this understanding by empirically adjusting the classical resistive-force theory, introducing variable apparent viscosities for motion tangential and normal to a body surface, which effectively replicated observed experimental outcomes. A subsequent investigation [100] reevaluated these findings, confirming that the differential rotation rates between the cell body and its flagellum in unbranched polymer solutions are primarily due to viscosity differences, where polymers near the rapidly rotating flagellum transition from a coiled to an elongated state, thereby reducing local viscosity and boosting swimming speed. This emphasizes the significant role of microscale fluid rheology over macroscopic properties typically assumed in standard fluid models.

Further studies [101, 102] on helical motion within viscoelastic fluids analyzed how an infinitely long filament emitting a helical wave of small amplitude shows a reduction in swimming speed with increasing Deborah number (De). Specifically, *Li* and *Spagnolie* [102] demonstrated that for helices of any cross-section within a viscoelastic medium, the speed of each wave mode correlates directly with the real component of the complex viscosity, a phenomenon consistent even when confined within a cylindrical space.

Contrastingly, experiments with helical filaments having large pitch angles revealed that their swimming speeds vary non-monotonically with De [103, 104]. It was found that macro-scale, force-free helical rotations in viscous and viscoelastic *Boger* fluids achieve maximal speed enhancements around $\mathrm{De} \sim O(1)$, with numerical simulations confirming that helices with higher pitch angles and thinner structures benefit more from this effect due

to interactions with their self-generated viscoelastic wakes, particularly when the helical motion's timescale aligns with the fluid's polymer relaxation time [103].

1.5.2 Non-continuum effects

Most studies on viscoelastic micro-swimming thus far have treated the fluid as a homogeneous, single-phase continuum. However, complex fluids are usually chemically and mechanically heterogeneous on the length scales relevant to biological swimmers, so non-continuum effects are therefore expected to be important.

In dilute and semi-dilute polymer solutions, micro-swimmers encounter individual and interlaced polymer coils with radii of gyration ranging from 10 to 100 nm. Numerous studies have employed discrete spring network models to investigate how the rotating flagellar filaments of bacteria induce local shear flows that significantly stretch the polymers. This stretching leads to a reduction in fluid viscosity around the flagellum and consequently enhances the swimming speed by increasing flagellar rotation and reducing the body's rotation [10, 12].

Brownian dynamics simulations of a helix rotating in a polymer dumbbell suspension demonstrate that, at a constant Deborah number, longer polymers deform less under shear than shorter ones, due to a diminished first normal stress difference (Fig. 1.12 a) [10]. Additionally, the impact on swimming speed alterations is more pronounced when the polymer length is less than that of the swimmer [10].

Investigations by *Balin* et al. [105] tracked a single polymer chain near a rotating helix, showing that polymers are propelled along the helical flagellum, migrating radially towards it, stretching, and ultimately accumulating at the flagellum's rear before returning to their equilibrium state. This dynamic creates a depletion zone of long polymer chains around the cell body, leading to an apparent slip velocity that increases swimming speed [12]. This study challenges previous models by suggesting that flagella rotate slower in polymer solutions than in Newtonian fluids, contrary to earlier viscosity-based predictions [100], necessitating further experimental verification of flagellar rotation speeds.

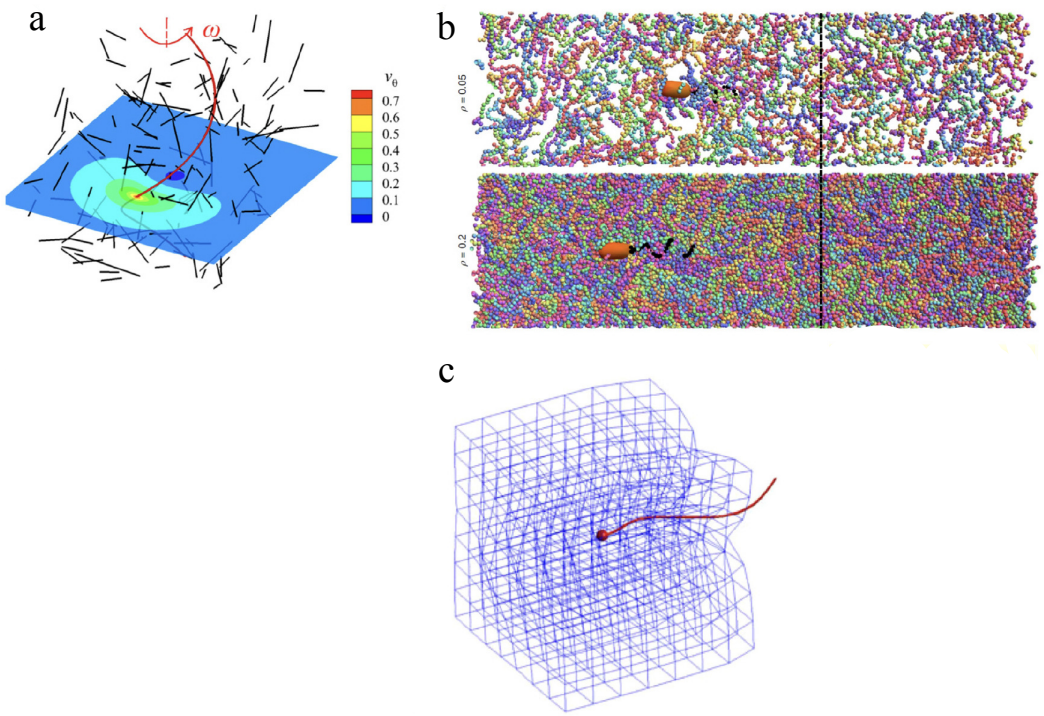


Figure 1.12: Solving for the microstructure of complex fluids during cell swimming. (a) Distribution of long polymer dumbbells around a rotating helical filament (adapted from Ref. [10, 11]). (b) Bacteria swim faster in a dense solution of semi-flexible polymers than in a dilute solution (adapted from Ref. [12, 11]). (c) Model flagellated swimmer moving through a viscoelastic network (adapted from Ref. [13, 11]).

At elevated polymer concentrations, crosslinking causes polymer molecules to overlap and entangle, forming gel-like networks. *Leshansky* [106] demonstrated that in fluids with fixed microstructures, pronounced anisotropy in hydrodynamic resistance significantly boosts microswimming speed and efficiency for specific propulsion techniques. Research utilizing two-fluid models, which conceptualize the polymer network and solvent as interconnected elastic and viscous phases, indicates that the flexibility of the network and its interaction dynamics with the swimmer crucially affect microswimming speeds [107, 108]. Notably, the most substantial speed enhancements occur within sparse networks of rigid polymers, where interactions are primarily

solvent-mediated [107]. Simulations of a discrete viscoelastic network submerged in a viscous fluid confirm these findings [13].

1.5.3 Numerical methods for modeling micro-swimmer motion in viscoelastic fluids

The dynamics of micro-swimmers in non-Newtonian fluids are influenced by the interplay of low-Reynolds number hydrodynamics, as described by the Cauchy momentum equation, the swimmer's own kinematics or internal actuation mechanisms (which define the fluid's boundary conditions), and the fluid's rheological characteristics (i.e. the constitutive equation for the complex fluid). The standard equations that govern continuum viscoelastic fluids are presented below:

$$\nabla p = \nabla \cdot \tau, \tag{1.12}$$

$$(1 + A)\tau + M(\tau, \mu) = \mu(1 + B)\dot{\gamma} + N(\dot{\gamma}, \mu), \tag{1.13}$$

where p denotes the dynamic pressure and τ is the deviatoric part of the stress tensor, which incorporates both Newtonian and non-Newtonian contributions to the stress. The Cauchy momentum in the absence of inertia, equation 1.12, states therefore simply that the divergence of the total stress tensor, $\sigma = -pI + \tau$, is zero. In equation 1.13, μ is the total zero-shear rate viscosity of the fluid, $\dot{\gamma} = \nabla u + (\nabla u)^T$ is the shear rate tensor, while A and B are two linear differential operators in time that capture the polymer relaxation and retardation. In contrast, the symmetric nonlinear operators M and N represent convection, stretching and nonlinear relaxation; they include in particular all terms arising from the objective derivatives of the deviatoric stress and of the shear rate tensor. The constitutive relationship stated in Eq. (2b) describes all the classical differential constitutive relationship for polymeric fluids, including all Oldroyd models. The equations above are then to be solved with kinematic and/or stress boundary conditions provided by the swimmer; in parallel, the dynamics of a microswimmer is subject to instantaneous force-free and torque-free conditions, allowing to determine in a quasi-steady fashion its linear and angular swimming velocities.

To simulate viscoelastic fluids, these governing equations must be solved using various numerical methods, such as the finite difference method, finite element method, and lattice Boltzmann method[109, 110, 111, 112, 113]. As noted earlier, treating the fluid as continuous may not adequately capture the

interactions between microorganisms or robots designed to navigate through viscous fluids containing suspended microstructures such as elastic polymers and filamentous networks, especially when the size of the polymeric network is of the same scale as the micro-robot or cargo. For instance, mammalian sperm navigate through such heterogeneous networks within the female reproductive tract, facing various configurations and spacings between mucin fibers that alter throughout the menstrual cycle [14, 114]. Moreover, recent experiments have demonstrated that organisms like *C. elegans* can achieve enhanced velocities in concentrated solutions compared to semi-dilute solutions when moving through viscous fluids embedded with polymeric networks [115]. Similarly, the propulsion of engineered micropropellers has been improved in gels when the size of the swimmer corresponds to the mesh size of the polymer network [116]. These studies illustrate that when a micro-object traverses a viscoelastic network where the spacing between network elements is comparable to the size of the object, continuous models and equations, such as the Oldroyd-B model, may not be sufficiently precise. Recent advancements in modeling have led to approaches that consider viscoelastic behavior as discrete rather than continuous properties. Developing a model that accurately represents the discrete properties of viscoelastic behavior is crucial for precisely simulating the interaction between filamentous cargo and the surrounding fluid. To model the non-continuum behavior of the viscoelastic fluid, as depicted in Fig 1.12, various methods have been proposed. As illustrated in Fig 1.12c, Wróbel et al. proposed a model in which an immersed object swims through a compliant viscoelastic network immersed in a viscous Newtonian fluid [13, 117]. This network, structured as nodes connected by springs and dashpot elements to neighboring nodes, dynamically responds to the forces exerted by the swimming object. The viscoelastic properties of the network, which mimic the behavior of polymers and fibers, significantly influence the overall dynamics of the fluid environment.

In this model, the regularized Stokeslet method, as will be discussed in chapter 2, is employed to resolve the fluid dynamics at the microscopic level, focusing on the interactions between the swimmer and the viscoelastic network. The viscoelastic network is modeled using Maxwell elements, effectively capturing the rheological behavior of fluids found in cervical and vaginal environments. The forces within the viscoelastic network are calcu-



Figure 1.13: Schematic of a Maxwell fluid element.

lated using the following equation:

$$f_s(x_1) = -f_s(x_2) = l_0^2 K \left(\frac{||x_2 - x_1||}{l(t)} - 1 \right) \frac{x_2 - x_1}{||x_2 - x_1||.} \tag{1.14}$$

where $l(t)$ represents the element's resting length, K is the spring stiffness constant, and l_0 is the initial resting length. The resting length dynamically changes, and its time evolution is given by:

$$\frac{dl(t)}{dt} = \frac{K l_0}{\eta} \left(\frac{||x_2 - x_1||}{l(t)} - 1 \right). \tag{1.15}$$

Another method, employed by Zhang et al. [10], attempted to simulate the motion of a bacterium through a non-continuum viscoelastic fluid. In their computational model, the bacterial flagellum is represented as an endlessly long helix that rotates at a uniform angular velocity within a viscous polymeric fluid. The model simplifies polymer molecules as bead-spring dumbbells, where a spring connects two beads representing the ends of the polymer molecule (refer to Fig. 1.12a). It is important to note that the bead-spring dumbbell model simplifies actual polymer structures by not accounting for resistance to bending or twisting. This model is a basic representation of a Kramers chain, which depicts a polymer chain. [118] The spring component behaves as Hookean when the end-to-end distance of the Kramers chain is below half the total length of the chain; beyond this, the spring exhibits nonlinear characteristics [118].

The fluid dynamics are resolved using the three-dimensional incompressible Stokes equations, augmented with body forces in the momentum equation. These additions account for the hydrodynamic forces exerted by the flagellum and the polymer beads, derived using a distributed Lagrange multiplier technique. The next and final method, illustrated in Fig. 1.12b, was proposed by Zöttl et al. [12]. In their study, they simulated the motion of a bacterium in a macromolecular polymer solution. The fluid in which the bacterium moves is comprised of a Newtonian fluid characterized by a viscosity

μ_0 and a temperature T_0, simulated using multiparticle collision dynamics (MPCD). This fluid is integrated with coarse-grained polymers, represented by N spherical beads of specific diameter. These beads are interconnected via quasi-rigid springs with a default length l_0 and a defined bending stiffness k_b. In summary, two distinct approaches have been utilized to solve the motion of micro-swimmers in non-continuum viscoelastic fluids: the method proposed by Wróbel et al. [13, 117] using the Regularized Stokeslet, and the approach by Zöttl et al. [12] employing the MPCD method. The Regularized Stokeslet method is highly accurate in modeling interactions within a viscoelastic network, offering precise force-velocity coupling that is essential for understanding micro-robot dynamics in these environments. However, this accuracy comes with significant computational costs, especially when solving large 3D systems, and the method does not naturally account for thermal fluctuations, which can be critical at the microscale. Conversely, the MPCD method provides greater computational efficiency, particularly for large-scale simulations, by using a coarse-grained approach that models the fluid as a collection of particles. This approach naturally includes thermal fluctuations, making MPCD suitable for mesoscale simulations. Nonetheless, the coarse-grained nature of MPCD may lead to less precise hydrodynamic interactions, especially in dense polymer solutions, and requires careful tuning of parameters such as cell size and time step. Ultimately, the choice between these methods depends on the specific simulation requirements, balancing the need for detailed viscoelastic modeling against computational efficiency and the inclusion of thermal effects. Inspired by the model proposed by Wróbel et al. [13, 117], a new model is proposed and characterized in this thesis.

1.6 Outline of the thesis

This thesis is comprised of six chapters. In Chapter 1, the motivation behind the study and the overarching goals of designing an innovative micro-robot for transporting filamentous microcargo, with applications in drug delivery and assisted fertilization, are explained. An overview of previously designed micro-robots, different types of micro-robots, and various methods for propelling micro-robots is provided. One of the primary goals of this thesis is to design a micro-robot for transporting filamentous microcargo, including

sperm; hence, sperm morphology and structure are explained. The classification of fluid behavior is discussed, including explanations of Newtonian and non-Newtonian fluids and their differences. The chapter further explores viscoelastic fluids, discussing different models proposed over recent decades for simulating the behavior of viscoelastic fluids. Finally, different numerical models proposed for simulating the locomotion of microswimmers in viscoelastic fluids are explained.

In Chapter 2, we delve into the numerical methods used in this thesis for modeling the motion of rigid and flexible objects in a fluid. The Regularized Stokeslet Method (RSM) is explained in detail, and the method used for simulating the motion of flexible and rigid objects in this thesis is described.

Chapter 3 begins with a summary of the governing equations. The model developed in this thesis for simulating flexible and rigid objects is validated, and mesh independence is studied. The physics of the rotating helical magnetic micro-robot is examined, leading to an improved design. A novel helical micro-robot is designed, and its performance in carrying filamentous microcargo is studied, demonstrating its success in non-contact transport.

In Chapters 4 and 5, a viscoelastic model inspired by the viscoelastic structure of bovine vaginal fluid is proposed to simulate the motion of the designed helical micro-robot in a viscoelastic fluid with polymer fiber sizes comparable to the size of the micro-robot. The performance of the designed helical micro-robot and a conventional helical micro-robot in the viscoelastic fluid is tested, investigating their effectiveness in biological fluids with viscoelastic properties.

The final chapter summarizes the findings of the thesis and discusses the broader implications of the research. It reflects on the success of the designed micro-robot in achieving non-contact transport of filamentous cargo in Newtonian fluid and its challenges in moving through viscoelastic fluids. The chapter also outlines potential future directions for research in this field.

Chapter 2

Regularized stokeslet method

The Navier-Stokes equations, which serve as the foundational equations for fluid motion, consist of two primary components: the momentum equation and the continuity equation. For an incompressible fluid, these equations are formulated as:

$$\nabla \cdot \vec{u} = 0,$$
$$\mathrm{Re}\left(\frac{\partial \vec{u}}{\partial t} + (\vec{u} \cdot \nabla)\vec{u}\right) = -\nabla p + \nabla^2 \vec{u} + \vec{f}, \tag{2.1}$$

where Re, the Reynolds number, is defined as $\frac{\rho U D}{\mu}$, highlighting the relationship between inertial and viscous forces. The external force acting on the fluid is denoted by $\vec{f}$. In situations where a moving object is involved, ρ and μ represent the fluid's density and viscosity, respectively, while U and D indicate the object's characteristic velocity and length. However, for small-scale objects moving at low velocities within the fluid, the Reynolds number becomes negligible, rendering the inertia and convection terms in the second equation irrelevant. This simplification leads us to the Stokes equation for low Reynolds number flows:

$$\nabla \cdot \vec{u} = 0, \tag{2.2}$$
$$-\nabla p + \mu \nabla^2 \vec{u} + \vec{f} = \vec{0}, \tag{2.3}$$

where $\vec{f}$ represents the external forces acting on the fluid, and μ denotes the fluid's viscosity. The Stokes equation is well-regarded for its tractability, often providing an exact solution under specific conditions. To solve the

Stokes equations, the Regularized Stokeslet method is employed[119, 120]. This method avoids singularities by distributing forces over a small volume rather than applying them at points. Specifically, the force is distributed using a radially symmetric smoothing function, $\phi_\epsilon(x)$, which has the property that $\int \phi_\epsilon(x)\, dx = 1$. The force is distributed over a finite region, centered at $\vec{x}_0$, with the parameter ϵ controlling the spread of the force. Therefore, a single regularized force distributed as:

$$\vec{f}(x) = \vec{f_0}\phi_\epsilon(\vec{x} - \vec{x_0}), \tag{2.4}$$

where $\vec{f_0}$ is the applied force and $\phi_\epsilon(\vec{x})$ is the radially symmetric smoothing function. The solution to the Stokes equations for this distributed force in three-dimensional free space, with the far-field boundary condition that the velocity decays to zero at infinity, can be obtained using the Green's functions $G_\epsilon(x)$ and $B_\epsilon(x)$. These functions represent the fluid's response to the applied forces and satisfy the following equations [119]:

$$\nabla^2 G_\epsilon(x) = \phi_\epsilon(\vec{x}), \quad \nabla^2 B_\epsilon(x) = G_\epsilon(x). \tag{2.5}$$

The function $G_\epsilon(x)$ is a regularized approximation of the Green's function for the Stokeslet, and $B_\epsilon(x)$ is the corresponding biharmonic function. Taking the divergence of 2.3 and using 2.2 we find that the pressure satisfies $\Delta p = \nabla \cdot \vec{f}(x)$ which results in the particular solution for p [119]:

$$p(\vec{x}) = \vec{f_0} \cdot \nabla G_\epsilon(\vec{x} - \vec{x}_0). \tag{2.6}$$

Substituting the obtained pressure into equation 2.3 results in the equation:

$$\mu \Delta \vec{u} = (\vec{f_0} \cdot \nabla)\nabla G_\epsilon(\vec{x} - \vec{x}_0) - \vec{f_0}\phi_\epsilon,$$

whose particular solution is [119]

$$\vec{u}(\vec{x}) = \vec{U_0} + \frac{1}{\mu}[(\vec{f_0} \cdot \nabla)\nabla B_\epsilon(\vec{x} - \vec{x}_0) - \vec{f_0} G_\epsilon(\vec{x} - \vec{x_0})]. \tag{2.7}$$

Here, $\vec{U_0}$ represents a constant flow that can be introduced to satisfy boundary conditions. This solution is referred to as the Regularized Stokeslet solution, and it smoothly approximates the fluid's behavior in response to the applied force $\mathbf{f}_0$. To extend this solution to multiple forces, we apply the principle of superposition. For N forces applied at different points $\mathbf{x}_k$, each

force $\mathbf{f}_k$ is regularized using the same smoothing function $\phi_\epsilon(\vec{x} - \vec{x}_k)$. The total pressure and velocity fields due to these forces are given by[119]:

$$p(\vec{x}) = \sum_{k=1}^{N} \vec{f}_k \cdot \nabla G_\epsilon(\vec{x} - \vec{x}_k), \tag{2.8}$$

$$\vec{u}(\vec{x}) = \vec{U}_0 + \frac{1}{\mu} \sum_{k=1}^{N} \left[(\vec{f}_k \cdot \nabla) \nabla B_\epsilon(\vec{x} - \vec{x}_k) - \vec{f}_k G_\epsilon(\vec{x} - \vec{x}_k) \right]. \tag{2.9}$$

This formulation accounts for the effects of multiple forces distributed at various locations in the fluid, providing a tractable method for numerical simulations. In the context of an immersed object interacting with the fluid, the forces exerted by the object can be modeled using this Regularized Stokeslet approach. A body force field $\vec{F}$ is distributed around the object, representing the stresses it imposes on the surrounding fluid. Specifically, we distribute N nodes over the surface of the object, with each node applying a regularized force:

$$\vec{F}(\mathbf{x}) = \sum_{i=1}^{N} \mathbf{f}_i \phi_\epsilon(\vec{x} - \vec{x}_i),$$

where $\mathbf{f}_i$ represents the force at node $\vec{x}_i$. This approach allows for the calculation of the velocity and pressure fields throughout the fluid domain, incorporating the effects of the object in a smooth and numerically stable manner. By distributing the forces over a small region rather than concentrating them at singular points, the Regularized Stokeslet method enables accurate and stable numerical simulations of low Reynolds number flows, even in the presence of complex boundaries and immersed objects. To describe the fluid flow influenced by an immersed object, a body force field $\vec{F}$ is concentrated near the object. This force field symbolizes the stresses exerted on the fluid by the immersed objects. Specifically, we distribute N nodes over the surface of the immersed objects, and following the method of Regularized Stokeslets, a regularized force is placed at each node. The total body force field evaluated at a point $\vec{x}$ is the sum of contributions from each node:

$$\vec{F}_i(\vec{x}) = \vec{f}_i \phi_\epsilon(\vec{x} - \vec{x}_i)\,, \tag{2.10}$$

where $\vec{f_i}$ is the force applied at the ith node, located at $\vec{X_i}$. The regularization function is chosen to be[119]:

$$\phi_\epsilon(\vec{r}) = \frac{15\epsilon^4}{8\pi(r^2+\epsilon^2)^{7/2}}\,, \tag{2.11}$$

where $r = ||\vec{r}||$, and ϵ is the regularization parameter, determining the spatial extent of the force distribution. The velocity at a point $\vec{x}$, resulting from N regularized forces $\vec{f_i}$ applied at positions $\vec{x_i}$, is given by[121]:

$$\vec{u}(\vec{x}) = \frac{1}{8\pi}\sum_{i=1}^{N}\frac{(r^2+2\epsilon^2)\vec{f_i} + [\vec{f_i}\cdot(\vec{x}-\vec{x_i})](\vec{x}-\vec{x_i})}{(r^2+\epsilon^2)^{3/2}}\,, \tag{2.12}$$

where $r_i = ||\vec{x}-\vec{x_i}||$.

This thesis utilizes the Regularized Stokeslet method to simulate the dynamics of specially designed micro-robots and cargos within both Newtonian and viscoelastic fluids. We differentiate between simulating rigid and flexible objects by discretizing each object's surface into points. For flexible objects, these points are interconnected with linear springs to enable flexibility. We conduct various tests to determine the stiffness of these objects, with details provided in subsequent sections. For rigid objects, it is assumed that all points on the object's surface share the same rotational frequency and translational velocity. We elaborate on the methodology for simulating the motion of both rigid and flexible objects, focusing on spherical cargos, micro-robots, and the heads and tails of filamentous cargos. Notably, the tail of the filamentous cargo, being flexible, contrasts with the other objects, which are modeled as rigid.

2.1 Modeling rigid objects

A rigid object is defined by the invariant distance between any two points on its surface. This constancy necessitates that, upon discretizing a rigid object's surface into multiple points, the distance between each pair of points remains unchanged. To ensure that any two points maintain their distance throughout their motion, they must exhibit identical angular velocity relative to an origin and the same translational velocity. Thus, at each timestep in

simulating the motion of a rigid object, it suffices to determine the vectors of translational and angular velocity with respect to an origin.

In the context of Stokes flow simulation, where the Reynolds number is significantly low and inertial forces are negligible, the sum of forces and torques acting on an object is nullified. Initially selecting one point as the reference and origin ($\vec{Y}$), at each timestep, if a point force f_j acts upon point y_j, the resulting forces are governed by the following equations:

$$\sum_j \vec{f_j} = \vec{F}_{\text{external}}, \tag{2.13}$$

$$\sum_j (\vec{y_j} - \vec{Y}) \times \vec{f_j} = \vec{T}_{\text{external}}, \tag{2.14}$$

$$\vec{U} + \vec{\Omega} \times (\vec{y_i} - \vec{Y}) = \frac{1}{8\pi\mu} \sum_j \frac{({r_j}^2 + 2\epsilon^2)\vec{f_j} + [\vec{f_j} \cdot (-\vec{y_j} + \vec{y_i})](-\vec{y_j} + \vec{y_i})}{({r_j}^2 + \epsilon^2)^{3/2}}. \tag{2.15}$$

Given the negligible inertia, objects in Stokes flow experience no acceleration, implying in Equation 2.13 that the net force exerted on the object equals the external forces applied. To propel objects forward in our simulations, a magnetic field applies a net torque to the micro-robot, while other objects are moved by the drag force from the fluid, rendering the external force in the right-hand side (RHS) of Equation 2.13 effectively zero. Equation 2.14 asserts that the total torque on the object matches the external torque. For the micro-robot, this external torque arises from the interaction with a rotational magnetic field, further detailed in subsequent sections. It's noteworthy that $\vec{Y}$ in Equations 2.14 and 2.15 represents the position of the chosen reference point, which is arbitrary.

Furthermore, the left-hand side (LHS) of Equation 2.15 calculates the velocity of point i at position y_i, where $\vec{U}$ denotes the translational velocity of the rigid body, and $\vec{\Omega}$ signifies its rotational velocity about the origin located at $\vec{Y}$. The RHS of Equation 2.15 derives the velocity of point $\vec{y_i}$ using the Stokeslet formula attributable to the forces exerted on the fluid. Collectively, Equation 2.13 encompasses three equations for the net force in the x, y, and z directions; Equation 2.14 includes three equations for net torque in the x, y, and z directions; and Equation 2.15 consists of $3N$ equations, where N is the number of surface points, accounting for velocity in the x, y, and

z directions. Hence, Equations 2.13, 2.14, and 2.15 together form a system of $3N + 6$ equations with $3N + 6$ unknown parameters, including the components of N forces, and the translational ($\vec{U}$) and rotational ($\vec{\Omega}$) velocities. Solving this system yields the forces applied to the object and its velocity. With the translational velocity $\vec{U}$ and rotational velocity $\vec{\Omega}$ determined at each timestep, the object's position can be updated, facilitating continuous tracking of its motion. Moreover, calculating the forces exerted on the object helps track the motion of other objects, as Equation 2.15 necessitates considering all forces applied to the fluid.

2.2 Modeling flexible objects

The sole flexible object examined in this thesis is the filamentous cargo. Analogous to the approach for rigid bodies, the surface of the flexible object is discretized into multiple points, resulting in a point cloud covering the flexible filament's surface. Mesh nodes are strategically distributed across the filament by segmenting it into numerous cross-sections along their central axes and further subdividing each cross-section's circumference into multiple nodes. The number of cross-sections is determined based on the filament's length and cross-sectional diameter to ensure uniform spacing between adjacent cross-sections and nodes within a single cross-section. These cross-sections are oriented along and perpendicular to the filament's centerline.

To simulate the flexibility of the filament, nodes within the same and adjacent cross-sections are interconnected via Hookean springs, each characterized by a spring constant k, to impart the desired structural rigidity. The stiffness of the filament is assessed using the following formulations:

$$\epsilon = \frac{1}{2} \sum_j k_j l_j \left(\frac{\|\vec{x}_{j_1} - \vec{x}_{j_2}\|}{l_j} - 1 \right)^2, \tag{2.16}$$

$$EI = \frac{2\epsilon}{\kappa^2 L}. \tag{2.17}$$

where Equation 2.16 defines ϵ as the dimensionless elastic energy and k_j as the stiffness of a spring of resting length l_j connecting nodes j_1 and j_2. This equation sums over all springs. In Equation 2.17, EI denotes the bending stiffness of the spring system, and κ represents the curvature of the filament

when it is bent into a curved shape. Thus, to ascertain the bending stiffness of a specific filament, it is first bent into a curved shape; subsequently, the total energy stored in the springs is calculated. Using the known curvature of the bent filament and Equation 2.17, the filament's bending stiffness is determined.

To simulate and monitor the motion of the filament, elastic forces attributable to the springs are calculated at each timestep based on the instantaneous arrangement of the nodes. Forces exerted on the fluid by rigid bodies, as described in the preceding section, are also evaluated. Then, utilizing Equation 2.12, the velocities of the nodes on the filament's surface are determined. Employing a fourth-order Runge-Kutta method, the filament's new position is updated according to $\frac{d\mathbf{X}_j}{dt} = \mathbf{v}_j$, where $\mathbf{X}_j$ denotes the position of node j, t is the time, and $\mathbf{v}_j$ is the calculated velocity for point j. With the updated positions of the surface nodes, the filament is repositioned, and the cycle of recalculating the elastic and fluid forces continues, thereby tracking the motion of both the flexible filament and rigid bodies. A flowchart illustrating the simulation workflow, including the application of the RK4 method for updating node positions, is presented in Figure 2.2.

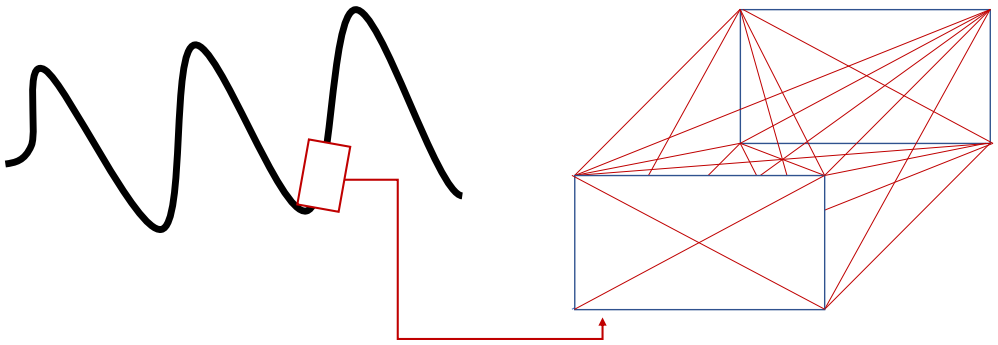


Figure 2.1: Structure of the flexible filament. The surface of the object is discretized into multiple nodes, with the nodes interconnected by springs to provide the necessary stiffness.

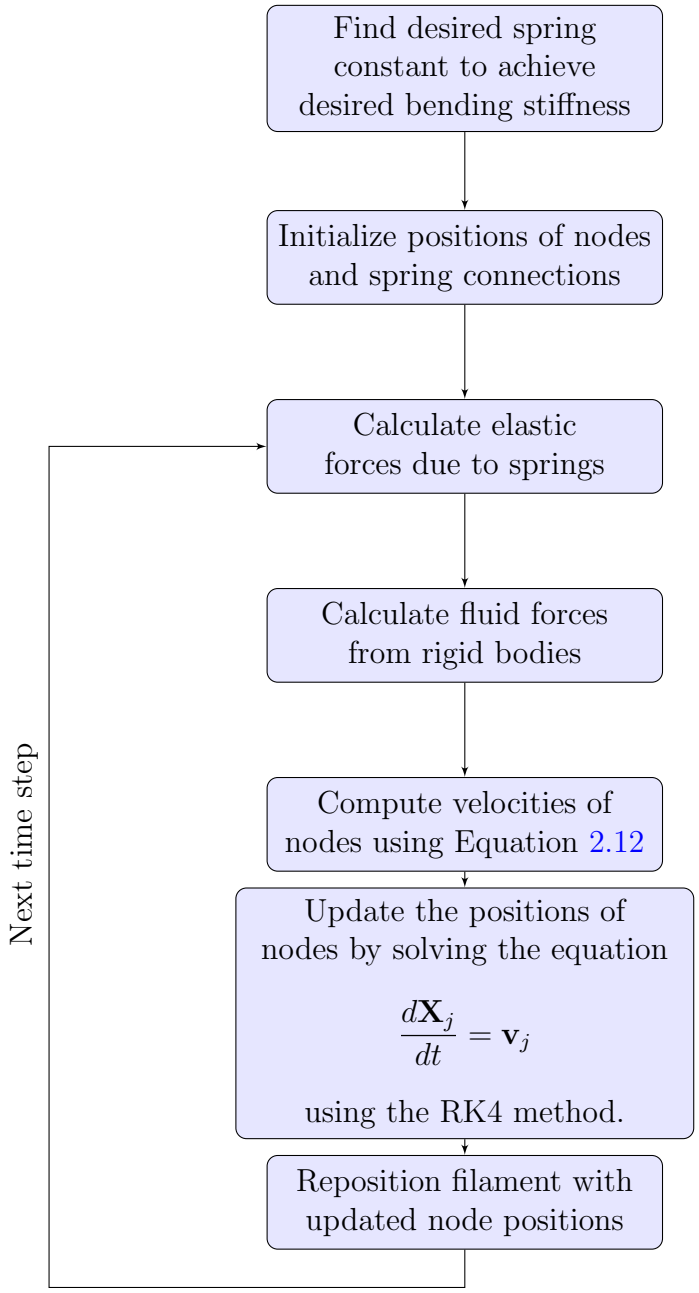


Figure 2.2: Flowchart of the algorithm implemented for simulating the motion of a flexible object

Chapter 3

Designing micro-robot for transporting filamentous cargo

3.1 Introduction

Micro-robots are gaining considerable attention across numerous biomedical fields, such as targeted drug delivery [16, 17, 18, 19, 20, 21, 22, 23], surgical procedures [24, 25, 26], bio-sensing [27], and both chemical and radiation treatments [28]. The introduction of micro-robots, particularly in surgical applications, presents a less invasive alternative to traditional approaches, enhancing precision in drug delivery while minimizing infection risks and adverse effects [24, 25, 26]. These micro-robots are categorized into three main groups based on their propulsion and manipulation mechanisms: chemical-driven [42, 43], physical-driven [44, 45, 46, 47], and bio-hybrid [48, 49]. Chemical micro-robots employ in-situ chemical reactions to generate motion, which, however, poses potential safety risks due to the release of chemical substances within the body. Bio-hybrid micro-robots, which utilize motile organisms for movement, similarly face challenges due to the potential for residual organisms within the body post-operation. Consequently, physical micro-robots, especially those driven by magnetic forces, are deemed more appropriate for internal biomedical applications [50, 51, 4, 52].

Magnetic micro-robots, controlled externally via magnetic fields, are notably advantageous in terms of controllability and tissue compatibility. They are designed to penetrate various tissues and have been effectively employed

in environments as diverse as the vitreous of the eye [50], knee joint tissues, and vascular systems [53, 54]. These robots are activated through magnetic torques [55] or forces [56]. Force-actuated micro-robots are propelled by magnetic field gradients, whereas torque-actuated robots utilize rotating, oscillating, or stepping magnetic fields to achieve motion. The pioneering helical magnetic micro-robot, devised by Bell et al. [57], was driven by rotating magnetic fields, harnessing asymmetric drag forces induced by helical rotation to propel itself in a direction determined by the helix's handedness and rotation direction [58, 59].

Helical magnetic micro-robots have found applications in cargo delivery and passive cellular manipulation. These micro-robots typically employ either a direct contact method, pushing cargo particles via physical contact, or a non-contact approach, manipulating cargo through fluid flows generated around the micro-robot. The direct contact method, while straightforward, often results in adhesion issues between the micro-robot and the cargo, posing challenges in cargo release upon reaching the target and potentially causing mechanical stress and deformation to the cargo [4]. Conversely, the non-contact method involves generating micro-vortices with a specially designed tubular head at the micro-robot's tip, a technique demonstrated by Huang et al. in 2014 [3]. This method, though effective with spherical cargo, might not suit elongated or filamentous materials.

A notable application of these helical micro-robots involves the transport of viable but immotile sperm, utilizing the micro-robot's helical structure to encase the sperm's flagellum while preventing the sperm's body from passing through, thus facilitating controlled transport albeit with occasional adhesion issues [4]. In our current research, we aim to design a magnetic helical micro-robot that leverages a non-contact approach to transport passive filamentous materials along its axis. This design is intended not only for assisted fertilization applications by transporting sperm but could also be adapted for other filamentous cargoes. Our study begins with a detailed description of the model and numerical methods employed, followed by an analysis of how helical geometry influences the trajectory and velocity field around the micro-robot, especially when it is allowed to both translate and rotate under a rotating magnetic field. Despite initial findings indicating suboptimal transport efficiency for filaments using a simple helical design, we propose modifications incorporating alternating helical sections to optimize filament capture and transport. The new design involves two pulling microhelices at

the ends and a central pushing microhelix, facilitating effective coupling of the filament to the micro-robot's motion. By adjusting the length ratios of these sections, we explore the optimal configurations

3.2 Geometric model and mechanical properties

In the previous chapter, we explained about the regularized stokeslet method and how we used this technique to simulate and track flexible and rigid objects. In this chapter, as we are going to design a micro-robot for transporting filamentous cargo, both methods are utilized. For simulating filament, the method developed for flexible object is utilized and for the micro-robot and head of filament, method developed for rigid object is used. It is worth noting that, based on our objective of carrying a filament of length 45–50 µm (corresponding to the length of a human sperm flagellum, for example) suspended in an aqueous medium, we non-dimensionalize all variables throughout this thesis using the characteristic length scale $\hat{l} = 45$ µm, the viscosity of water $\mu = 0.001$ Pa s, and the density scale $\rho = 1000\ \mathrm{kg\,m^{-3}}$, which corresponds to the density of the water.[5] To determine whether Brownian motion and fluctuations in the shape of the filament due to thermal forces are important, we estimate the Péclet number and the persistence length of the filament. The persistence length, defined by the formula $l_p = \frac{EI}{K_b T}$, where EI represents the bending stiffness, characterizes the length scale below which thermal effects produce negligible changes in the shape of a flexible filament from its resting shape. Based on the bending stiffness of the flagella of human sperm, $EI = 4 \times 10^{-21}\ \mathrm{N\,m^2}$,[122] the persistence length is $l_p \approx 1$ m at a temperature of $T = 300$ k. Thus, we expect that naturally straight filaments of length $L = 45$ µm would remain approximately straight in the presence of thermal fluctuations but in the absence of other external forces and hydrodynamic stresses; that is, they are rigid rods with respect to thermal forces. The Péclet number $\mathrm{Pe} = \frac{Lu}{D}$ represents the ratio of the rate of convective transport u/L to the rate of diffusive transport D/L^2, where D is the diffusion coefficient of the object in water. For a rod-like object, the diffusion coefficient is defined as $D = \frac{k_B T \ln(L/a)}{2\pi\mu L}$,[123] where k_B denotes Boltzmann's constant, T stands for temperature, μ represents the dynamic viscosity of water, and $a = 1.2$ µm and $L = 45$ µm signify the thickness and the length of

the rod. For our filament, we estimate the translational diffusion coefficient at room temperature to be 5.1×10^{-14} m^2 s^{-1}. Taking the characteristic convective speed to be the typical speed of a helical micro-robot $u = 45$ µm s^{-1} from previous experiments, the Péclet number is approximately 4×10^4, indicating that Brownian motion is negligible compared with motion due to convection. Since Pe and L/l_p are both large, we do not include thermal effects in our model.

Now lets look at the helical shape of micro-robot used in this project. The centerline equation of the helical micro-robot in the initial configuration is defined as:

$$\begin{aligned} x(s) &= R\cos s, \\ y(s) &= \pm R\sin s, \\ z(s) &= bs. \end{aligned} \tag{3.1}$$

where $0 \leq s \leq s_{\max}$, and the radius and pitch of the helix are R and $\lambda = 2\pi b$, respectively. The positive sign in the equation for y is used for right-handed helices and the negative sign is used for left-handed helices. The arc length of the helical micro-robot is equal to $s_{\max}\sqrt{R^2 + b^2}$. For the filament, we consider different initial configuration coinciding with the rest configuration including sinusoidal, circular and straight. We will discuss further there reason of using different configuration for the filament in the next sections. A schematic of the shape of filament and helical micro-robot used in this project is illustrated in the Figure 3.1. Mesh nodes are distributed over the filament and the micro-robot by discretizing the objects into many cross-sections along their respective centerlines and further dividing the circumference of each cross-section into multiple nodes (three for the helix and four for the filament). We choose the number of cross-sections of the helix and filament depending on their lengths and cross-sectional radii to ensure that the spacing between neighboring cross-sections and the spacing between nodes at a cross-section are equal. The cross-sections are placed along and perpendicular to the centerline of the filament and the axis of the helical micro-robot. To model the flexible filament, as illustrated in the Figure 3.2, each filament node is connected to the other nodes at the same cross-section and at neighboring cross-sections by Hookean springs with a spring constant of k, which provide the desired rigidity to the overall structure.

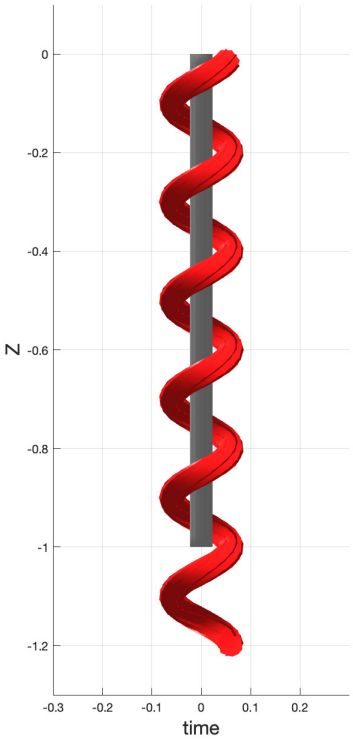


Figure 3.1: schematic of the shape of filament and helical micro-robot.

3.3 Governing equations

As noted in the previous chapter, regularized stokeslet method is used to solve the stokes equation and find velocity of the fluid. To obtain the velocity of each point in the fluid using equation 2.12, forces exerted into the fluid must be calculated. Different forces are applied to the fluid including elastic forces and repulsive forces. As we discussed before, the flexible filament is constructed from different nodes connected with Hookean linear spring. The elastic force exist due to the hookean spring used in the structure of the flexible filament, can be calculated using the following equations

$$F_{\text{Elastic}} = -k_t \left(|\vec{X_1} - \vec{X_2}| - L_{\text{eq}} \right) \left(\frac{\vec{X_1} - \vec{X_2}}{L_{\text{eq}}} \right). \tag{3.2}$$

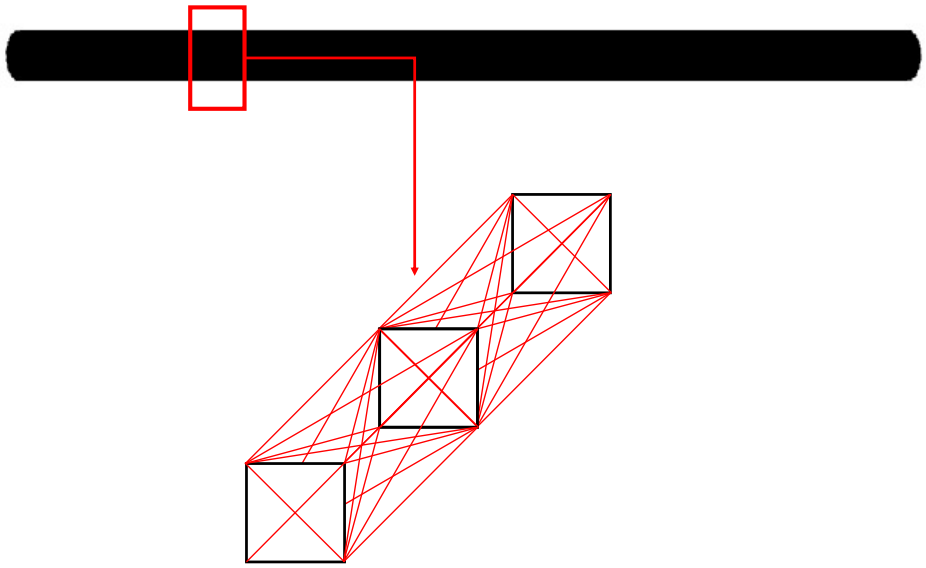


Figure 3.2: Schematic representation of the filament with Hookean springs connecting the filament nodes within each cross-section to neighboring cross-sections. Each node is connected to 26 adjacent nodes.

where $\vec{X_1}$ and $\vec{X_2}$ are the position of two points which are connected with the linear spring, L_{eq} is the equilibrium length of spring connecting those two points and k_t is the spring constant of the linear spring. Therefore, this elastic force is applied to the point X_1 and a force with the same magnitude and opposite direction is applied to the point X_2. In addition to the elastic forces, a repulsive steric force is introduced to prevent collisions between the filament and the micro-robot. When the nodes of the filament and the micro-robot are in close proximity, a truncated Lennard-Jones potential is employed to exert this repulsive force [124]:

$$E_{LJ}(\vec{r_s}) = \frac{\sigma F_s}{6}\left[\left(\frac{\sigma}{|\vec{r_s}|}\right)^{12} - \left(\frac{\sigma}{|\vec{r_s}|}\right)^{6}\right] H(2^{\frac{1}{6}}\sigma - \vec{r_s}). \tag{3.3}$$

where H is the Heaviside step function, $\vec{r_s}$ is the vector connecting the two nearby points, σ is the cutoff distance, and F_s sets the repulsion strength. Then, the repulsive force can be computed by

$$\begin{cases} \vec{F}^{steric} = -\nabla E_{LJ}, & |\vec{r_s}| < \sigma, \\ \vec{F}^{steric} = \vec{0}, & |\vec{r_s}| \geq \sigma. \end{cases} \tag{3.4}$$

We compute the hydrodynamic force $\vec{f}_i$ at filament nodes by applying a force balance condition, namely, that the hydrodynamic force balances the steric and elastic forces. The hydrodynamic force is the force applied to the fluid. At each point, a hydrodynamic force is computed and after finding all the hydrodynamic forces applied to the fluid, using equation 2.12, the velocity of the fluid can be obtained.The helical micro-robot, in contrast to the filament, is simulated as a rigid body; the forces applied at the helix nodes are determined so that the nodal velocities, computed via equation 2.15, are consistent with a rigid body translation and rotation. Additionally, the total hydrodynamic force exerted by the helix balances the steric repulsion force and the total hydrodynamic torque balances the magnetic torque $\vec{T}_M$ applied to the micro-robot, which is given by

$$\vec{T}_M = \vec{m} \times \vec{B}. \tag{3.5}$$

where $\vec{B}$ is the magnetic field and $\vec{m}$ is the magnetic dipole moment of the micro-robot, which we assume to be fixed in the (rotating) reference frame of the micro-robot. In the initial position, the magnetic moment of the micro-robot is aligned with the magnetic field in the X-direction. The rotating magnetic field is given by

$$\vec{B}(t) = B_0 \begin{pmatrix} \cos(2\pi f t) \\ \pm \sin(2\pi f t) \\ 0 \end{pmatrix}. \tag{3.6}$$

where f is the rotational frequency, B_0 denotes a constant magnitude of the magnetic field, and the direction of rotation is determined by the sign in the Y-component of (3.6). The magnetic field rotates around the $\pm Z$-direction, which is parallel with the axis of the micro-robot in the initial configuration.

In general, a magnetic torque acts to rotate a magnetic dipole to be aligned with the magnetic field. Since the magnetic field continuously rotates, the micro-robot rotates to follow the magnetic field, provided that the magnetic field rotates below a threshold known as the step-out frequency.[125] In all simulations performed in this paper, the rotational frequency, as represented by Equation 3.6, is fixed at $f = 0.1$. With our non-dimensionalization, this corresponds to 50 Hz, which is a frequency used in past experiments by Medina-Sánchez et al.[4] We fix the maximum magnitude of the non-dimensional magnetic torque at $T|\vec{m}| = 65$, equivalent to 3×10^{-12} N m,

which we chose based on the structure and material of micro-helices and experimentally feasible magnetic field strengths.

Once all of the hydrodynamic forces on the micro-robot and filament nodes are determined, the velocities at the filament nodes are evaluated using equation 2.12. These velocities, along with the rigid body translational and rotational velocity of the micro-robot, are used to update the node positions by the fourth-order Runge-Kutta method.

3.4 Model validation

In Chapter 2 and the previous section, the model developed for simulating flexible and rigid objects using regularized stokeslets was explained in detail. As previously mentioned, the filament is flexible, so the model developed for flexible objects is used for simulating the motion of passive flexible filaments, while the head of the flexible filament is considered a rigid object for which the rigid model is used. To validate the developed models, we first validate the model developed for the flexible object (passive filament) and then validate the model developed for the rigid object. It is worth noting that to calculate the bending stiffness of the filament, as explained in Chapter 2, Section 2, we bend the filament into a curved shape and calculate the energy stored in the springs constructing the filament structure. Using Equations 2.16 and 2.17, the bending stiffness of the filament is determined.

3.4.1 Validation of the model developed for flexible filament

To validate the numerical methods developed for simulating the dynamics of a flexible filament, two different simulations were conducted. In the first simulation, a filament is pivoted at one end, which remains fixed without any momentum resisting its rotation. To perform the simulation, the filament was discretized into 64 cross-sections, with each cross-section constructed from 4 distinct nodes, resulting in a total of 256 nodes. The filament is actuated by prescribing a periodically oscillating angle to the direction normal to the cross-section at the pivoting end, given by $\theta(t) = a_0 \sin \omega t$ at $s = 0$. A time step of 10^{-6} was employed to ensure numerical stability and

accuracy. Additionally, the bending stiffness was calibrated to determine the desired spring constant, as detailed in the previous chapter on the model used for simulating flexible objects. The simulation results were then compared with the experiments presented by [126]. In the second simulation, a sedimentation test is simulated. In the sedimentation test, a uniform force density along the length of the filament is applied to a flexible filament, and the shape of the filament after reaching terminal settling velocity and the terminal velocity itself is compared with the analytical solutions [127].

For the first test, the obtained numerical result is compared with the experimental results reported by Yu et al. [126]. In this study, the length of the filament is 20 cm, and the diameter is $b = 0.5\,\mathrm{mm}$. The angular amplitude and the oscillation frequencies are $a_0 = 0.435\,\mathrm{rad}$ and $\omega = 5.24\,\mathrm{rad\,s^{-1}}$, respectively. The sperm number based on the bending stiffness of the filament is 3.11.

The sperm number (Sp) is a dimensionless parameter that quantifies the balance between elastic forces and viscous drag forces acting on the sperm flagellum. It is defined as

$$\mathrm{Sp} = L\left(\frac{\xi_\perp \omega}{E}\right)^{1/4}. \tag{3.7}$$

where L is the characteristic length of the flagellum, $\xi_\perp$ is the perpendicular fluid dynamic resistance coefficient, ω is the angular frequency of flagellar beating, and E is the flagellum bending stiffness. The sperm number provides insight into how elastic forces (due to bending stiffness) compare to viscous forces (due to fluid resistance) in the motion of the sperm flagellum.

A passive filament with the same sperm number as the experimental results was simulated. In the first step, the stiffness of the linear spring in the structure was calculated to ensure the sperm number matches that in the experiments. Then, snapshots of the filament positions at four points in the cycle of the obtained results were compared with the experimental results reported by Yu et al. [126]. The comparison is shown in Figure 3.3. The close agreement between the numerical and experimental results demonstrates the accuracy of the developed model in capturing the dynamic behavior of the flexible filament. Overall, the validation confirms that the model can reliably simulate the motion of passive flexible filaments in viscous fluids under oscillatory conditions.

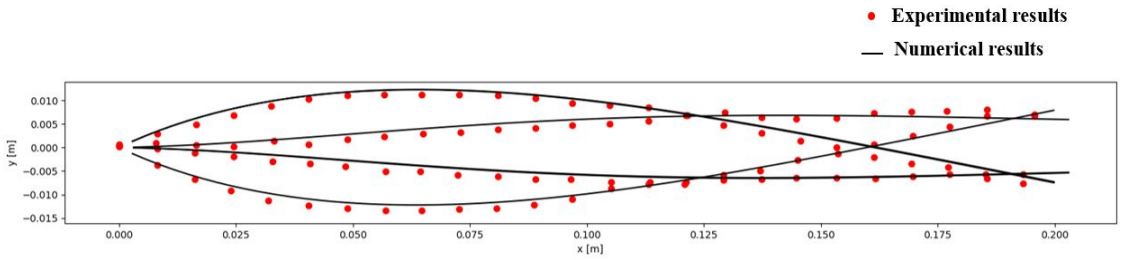


Figure 3.3: Comparison of the numerically obtained results for the filament position at four corresponding times in the cycle with the experimental results.

In the second (sedimentation) test, we apply a uniform force density along the length of the filament acting in the transverse direction within a three-dimensional free space environment. The simulation is conducted under far-field boundary conditions, where the fluid velocity decays to zero at infinity, corresponding to the scenario where the filament is far away from any boundaries or walls. Initially, the filament is at rest, meaning the initial velocity $U_0 = 0$. According to the study conducted by Xu and Nadim [127], the filament should reach a steady settling velocity and bend depending on its bending stiffness. The terminal settling velocity U is given by

$$U = F\frac{\ln(4/\kappa) - \frac{1}{2}}{8\pi\mu l}, \tag{3.8}$$

where F is the total force applied to the filament, μ is the viscosity of the fluid, l is half of the length of the filament, and κ is the ratio a/l where a is the radius of the cross-section of the filament. Therefore, as can be interpreted from Equation 3.8, the relationship between the terminal settling velocity and the applied force is linear. For a filament with a length of 0.2 and a radius of 0.022, three different forces, as illustrated in the Table 3.1, are applied, and the obtained value for terminal settling velocity is compared with the analytical solution. The error of the calculation is summarized in the Table 3.1. Moreover, as shown in Figure 3.4, the relationship between the force and the velocity is linear.

Moreover, for a flexible filament with a Hookean spring constant of 1000, as used in the paper, and a bending stiffness of $EI = 4.6 \times 10^{-21}$ N m^2, the sedimentation test described above for force 1 is conducted, and the shape

Case	F	Obtained Velocity	Analytical Formula	Error %
1	1	0.9548	0.9556	0.0818
2	2	1.9099	1.9112	0.0661
3	3	2.865	2.8667	0.0609

Table 3.1: Comparison of obtained velocity and analytical formula in sedimentation test. The radius of the filament a is 0.022, and half the length of the filament l is 0.1.

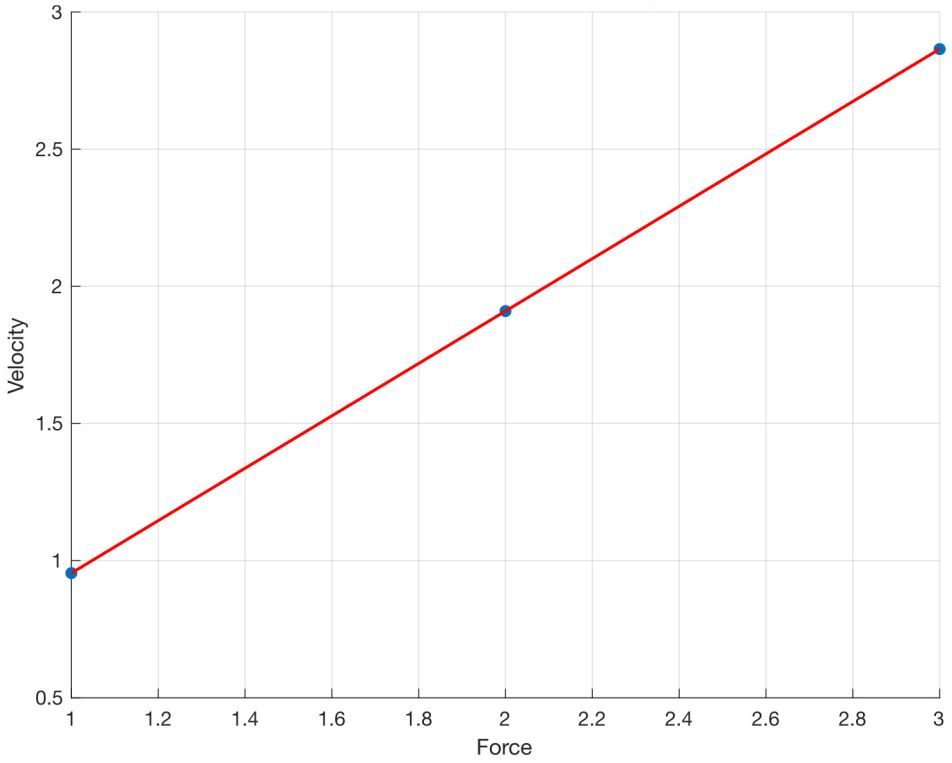


Figure 3.4: Relationship between the applied force and the terminal setting velocity. The markers are data points from simulations as given in Table 3.1 and the line shows the analytical linear relationship from Equation (3.8).

of the filament after reaching terminal settling velocity is compared with the formula derived by Xu et al. [127]. According to their study, if we scale the position x along the length of the filament with l, and the curve of the filament in the y direction, assuming that a/l and the filament's deflection

are very small, we have:

$$D = \frac{2\pi\mu U l^4}{EI(\ln\kappa)^2},$$

the relationship between y and x which shows the curve of the filament after bending would be [128]:

$$y(x) = -\frac{1}{24}\left[(1+x)^4\ln(1+x) + (1-x)^4\ln(1-x) - \left(\frac{13}{16} + 2\ln 2\right)x^4 - (1+12\ln 2)x^2\right]. \tag{3.9}$$

This curve is compared with the curve of our filament in our simulation and illustrated in Figure 3.5 for three different values of D: 0.02, 0.04, and 0.2. By changing the flexibility of the filament, it was observed that, independent of the D parameter, after nondimensionalizing y with D, the deformed shape of the filament after reaching the settling velocity has good agreement with Equation 3.9.

3.4.2 Validation of the model developed for rigid object

To validate the model developed for rigid body motion, a micro-robot with a single handedness and varying geometrical parameters is modeled. A rotating magnetic field propels the micro-robot, causing it to move forward due to the drag force applied in the forward direction. Initially, the velocity of the robot changes, but it eventually reaches a steady value. This steady velocity is calculated and compared with other verified results to validate the developed model.

Since there is no exact formula for the velocity of a helical magnetic micro-robot of arbitrary dimensions, we used the boundary element method (BEM) code developed by Shum et al.[15] to calculate the velocity of the micro-robot with the desired geometry. This code was previously used to simulate the locomotion of model bacteria propelled by rotating helical flagella. Removing the cell body, we consider only the helical structure rotating due to a rotating magnetic field. The results from this code were then compared with those from the model developed in this study.

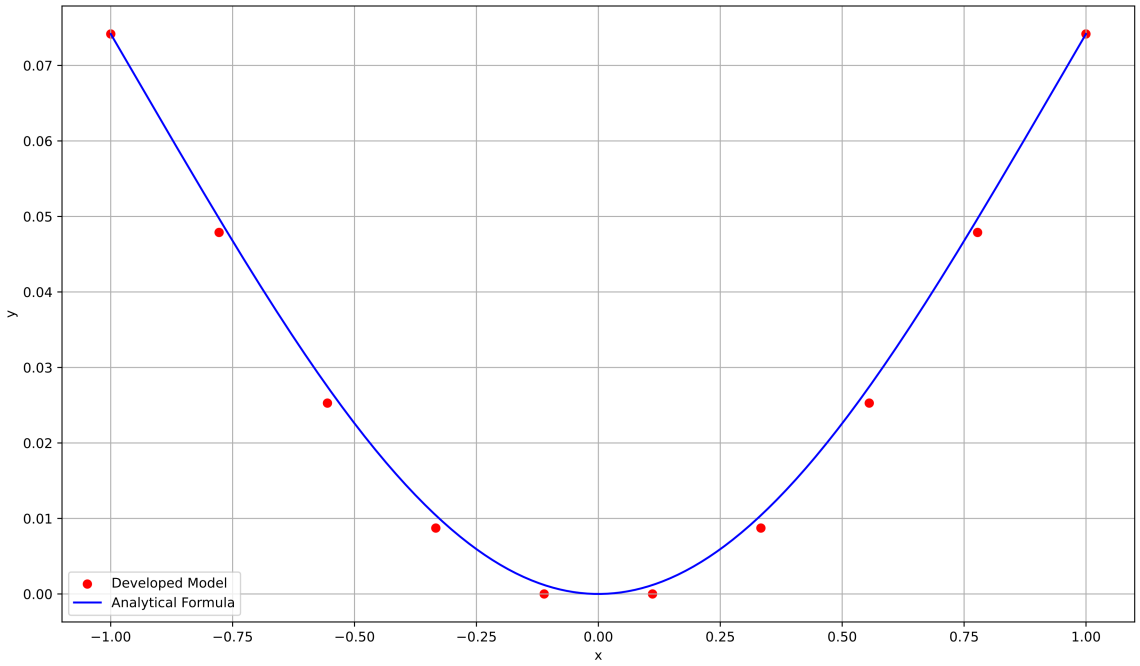


Figure 3.5: The deformed shape of the filament after reaching terminal setting velocity compared with the analytical formula.

Table 3.2 summarizes the geometrical parameters and the obtained steady velocity based on our regularized stokeslet method model and the code developed by Shum et al. For these regularized Stokeslet simulations, we used three nodes per cross-section of the helix.

Case	R	λ	Winding	Velocity (developed model)	Velocity (BEM)
1	0.06	0.1	10	0.0158	0.0155
2	0.06	0.15	8	0.0337	0.0333
3	0.06	0.2	6	0.0523	0.0548
4	0.08	0.15	8	0.0324	0.0316

Table 3.2: Comparison of propulsive velocity of a helix in a rotating magnetic field for different geometrical parameters between the developed model and the BEM model by Shum et al. [15]. R is the radius of the helix of the micro-robot and λ is the pitch of the helix. The frequency for all cases is 1 and the cross-section radius r is 0.015.

3.4.3 Mesh independency

As discussed in the main text, we use the regularized Stokeslet method to simulate the motion of the micro-robot and the filament. In the regularized Stokeslet method, the surfaces of objects are discretized. The spacing Δs between mesh nodes on these surfaces and the regularization parameter ϵ determine the discretization error and the regularization error, which are of order $O(\Delta s^2/\epsilon^3)$ and $O(\epsilon)$, respectively for evaluating the velocity field close to the discretized surface [121]. There is typically an optimal choice of ϵ for a given node spacing Δs.

To assess mesh independence, we varied the number of nodes on the object's surface and compared the resulting simulated steady speeds. We used a helical micro-robot with single-handedness, rotating a magnetic field of the same magnitude as described in our paper, with a rotational frequency of 1, then calculated the micro-robot's steady-state velocity. We compared meshes with three, four, and five nodes per cross-section, adjusting the number of cross-sections for each case such that the minimum distance between nodes on each cross-section matches the distance between cross-sections along the micro-robot's axis. The regularization parameter for all simulations was set to the minimum distance between nodes. The geometrical parameters of the micro-robots and the obtained velocities for each case are summarized in the Table 3.3. The table compares the errors for cases 1 and 2, with three and four nodes respectively, with respect to case 3 with five nodes in the cross-section, showing that the error is small and the results are independent of

mesh size.

Case	Number of Nodes per Cross-section	Steady Velocity of the Robot	Error (%)
1	3	0.0523	1.506
2	4	0.0528	0.564
3	5	0.0531	—

Table 3.3: Mesh independency study. The radius of the helix of the micro-robot R is 0.06, the radius of the cross-section r is 0.015, the pitch of the helix λ is 0.2, and the winding is 6 for all cases.

3.5 Fluid transport due to prescribed rotation of the helical micro-robot

In the first step, our objective is to gain a deeper understanding of the motion of the fluid near a rotating helical micro-robot. Two crucial ratios influence the flow field and movement of these robots: (1) λ/R and (2) r/R. Here, λ, R, and r denote the pitch, radius of the helical micro-robot, and the radius of its cross-section, respectively. We analyze the impact of the two ratios individually on pathlines in the fluid around the micro-robot. This knowledge will aid us in designing a helical micro-robot capable of efficiently transporting cargoes with flexible filaments. In section 3.6, we delve into studying the fluid's streamline.

To examine the effects of λ/R and r/R, we maintain a constant helical micro-robot radius $R = 0.1$ while varying λ and r. Subsequently, we plot the pathline of the fluid. To mitigate any potential end effects caused by the helical micro-robot, we generate a long micro-robot with $N_\lambda = 10$ windings. A point is selected along the axis of the micro-robot, situated one quarter of the way down from the top of the helix. We apply a prescribed motion to the micro-robot so that it rotates around its axis without any translational velocity. The reason for considering this prescribed motion rather than allowing free motion under the force-free and prescribed torque conditions is

that we will later connect the helix to another helical section of opposite handedness, which will alter the translational velocity.

We track and plot the pathline of the chosen point resulting from the rotation of the helix over time, using the velocity field given by equation 2.15. The fluid pathline gives an indication of the motion of a point on a passive filament located along the axis of the micro-robot. Ensuring a strong coupling between the filament and the micro-robot is crucial for retaining the filament inside the micro-robot, as we will discuss in subsequent sections.

Since our main focus is investigating how well a filament can be confined inside the micro-robot, we calculate the maximum distance (D) of the point from the axis of the micro-robot along its pathline as the point traverses from the top quarter plane to the bottom quarter plane (one quarter of the axial length of the helix from the bottom). The influence of r and λ on D is shown in Figure 3.6. It can be observed that reducing the pitch of the micro-robot leads to a more confined pathline for the point, regardless of the value of r. However, no specific increasing or decreasing trend is observed for D as r increases. Nonetheless, it is evident that D depends on both r and λ. Figure 3.7 showcases the 3D pathline of a point where the pitch of the micro-robot is $\lambda = 0.4$ and the radius of the cross section is $r = 0.0232$.

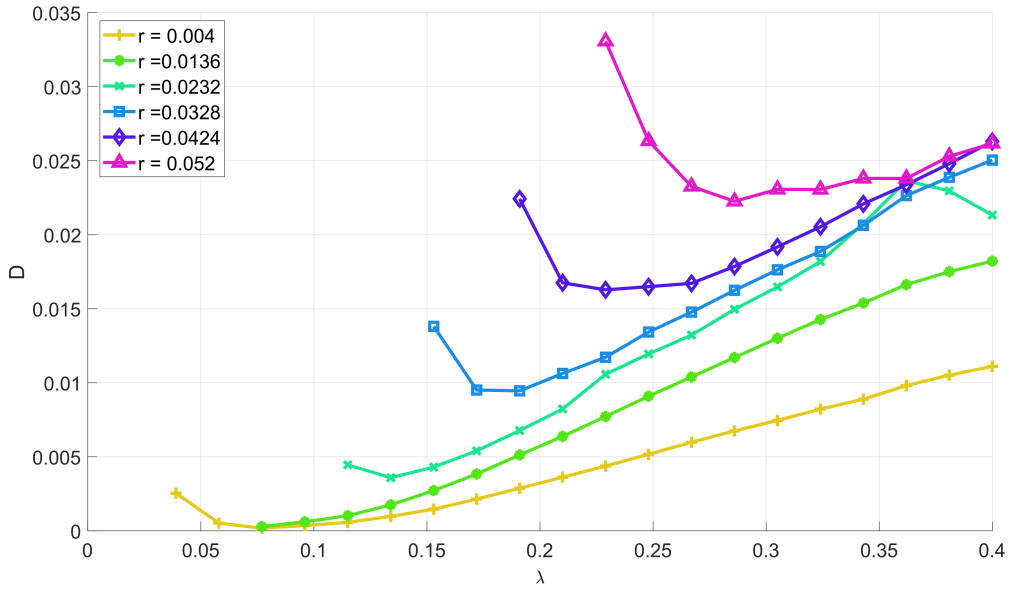


Figure 3.6: The influence of r and λ on the maximum distance D between the pathline of the point and the axis of the micro-robot. The radius of the helical micro-robot for all simulations is set to $R = 0.1$.

3.6 The instantaneous flow field around a helical micro-robot in a rotating magnetic field

To complement the pathlines for prescribed motion of the micro-robot, we now consider a force-free helical micro-robot driven by a rotating magnetic field and plot the fluid streamlines in the X–Z plane (Figure 3.8). We use $N_\lambda = 8$ windings, pitch $\lambda = 0.15$, radius $R = 0.06$, and cross-sectional radius $r = 0.015$ for the helix. The instantaneous streamlines have a complex pattern with significant lateral motion, which is expected to cancel out on average over a revolution of the micro-robot. The vertical velocity is almost everywhere negative (in the backward direction) relative to the micro-robot, and most negative between the turns of the microhelix at distances $\approx R$ from the helical axis. Therefore, in order to improve the coupling between the cargo and the micro-robot, it is crucial to keep the cargo inside the micro-robot. The ability to keep the pathline of a point inside the micro-

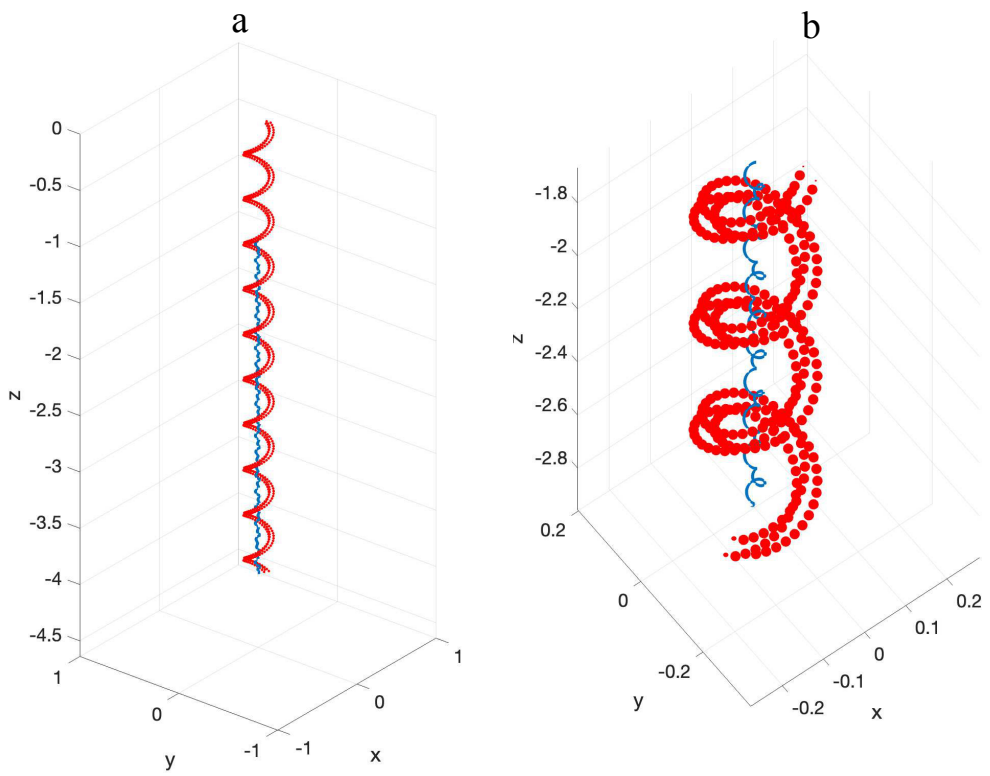


Figure 3.7: Pathline of the point represented in 3D views with a close-up view of a portion in (b). The blue curve illustrates the trajectory of the point, while the red points depict the nodes situated on the surface of the micro-robot at one instant in time.

robot, as discussed in the previous section, depends on the geometry of the micro-robot. Additionally, it is demonstrated in the section 3.7.2 that the flexibility of the filament is another parameter that affects the behavior of the passive filament inside the micro-robot.

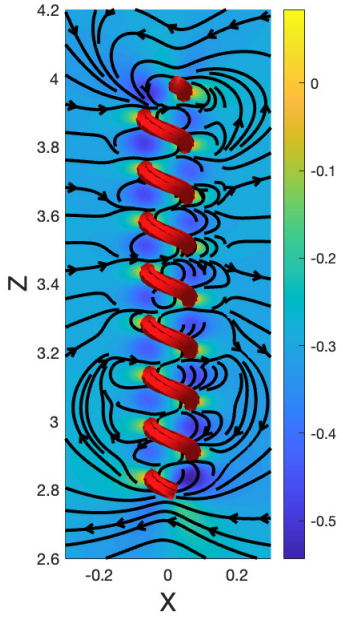


Figure 3.8: Streamlines of the fluid in the X–Z plane around a helical micro-robot in a rotating magnetic field. The color scale shows the velocity of the fluid in the Z direction relative to the translational velocity of the micro-robot in the Z direction ($V_z = 0.29$).

To better understand the flow around the micro-robot, we also plot the Z-component of the velocity field as a function of Z along four lines at different distances from the Z axis in the X–Z plane (Figure 3.9). The Z-velocity of the fluid on the Z-axis ($X = 0$) is mostly positive, i.e., in the forward direction, but with a low speed $U_z \sim 0.04$ compared with the non-dimensional translational speed of the micro-robot $V_z = 0.29$. However, as one moves away from the axis, the Z-velocity of the fluid oscillates along Z with a larger amplitude and alternates between forward and backward directions. To prevent decoupling between the filament and the micro-robot, it is imperative for the filament to remain within a region where the fluid moves forward at a comparable speed to the helix. Based on our analysis of the flow field within the rotating helix, it should be beneficial for the filament to be close to the axis of the micro-robot.

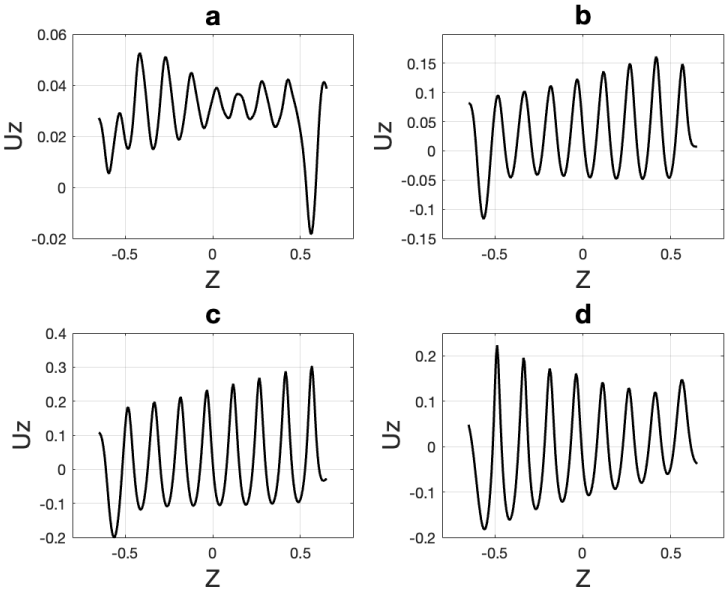


Figure 3.9: Velocity profile of the fluid in the Z direction versus Z position in the X–Z plane at a) $X = 0$ (on the axis) b) $X = 0.02$ (between the axis and the surface of the micro-robot) c) $X = 0.0375$ (close to the surface of the micro-robot) and d) $X = 0.1$ (beyond the surface of the micro-robot). The helix parameters are $\lambda = 0.15$, $R = 0.06$, and $r = 0.015$. The top and bottom of the micro-robot are located at $Z = 0.6$ and $Z = -0.6$, respectively.

3.7 Coupling between a passive filament and a helical micro-robot

In this section, we examine the motion of a passive flexible filament, of length $L_f = 1$ and radius $r_f = 0.014$, located along the axis of a rotating magnetic helical micro-robot. Our objective is to investigate the coupling between the micro-robot and the passive filament in such an arrangement. In the preceding sections, we studied the streamlines and the pathlines of the fluid surrounding the helical micro-robot. Based on the obtained streamlines, it is critical to confine the filament inside the micro-robot to apply hydrodynamic drag force in the forward direction and establish good coupling between the filament and the micro-robot. Moreover, based on the pathline studied in the previous section, selecting the r/R and λ/R ratios carefully is crucial

to confine the pathline of fluid inside the micro-robot. We consider the baseline parameter values of helical radius $R = 0.06$, axial length of the micro-robot $L = 1.2$, cross-sectional radius of the micro-robot $r = 0.015$, helical pitch $\lambda = 0.2$ (corresponding to six windings), and spring constant between filament mesh nodes $k = 1000$. This value, based on our bending stiffness tests, results in a bending stiffness of $EI = 4.6 \times 10^{-21}$ N m^2, which closely matches the bending stiffness of the sperm tail previously mentioned. From these values, we separately vary λ, k, and r. To characterize how well the micro-robot and filament move together, we initialize the micro-robot and filament so that their top ends are at the same Z position. We then track their relative displacement,

$$\Delta Z = Z_{helix} - Z_{filament}. \tag{3.10}$$

until the micro-robot overtakes the filament or they reach a steady-state position relative to each other. Although it is possible to transport the filament with any displacement ΔZ as long as it becomes steady at long times, we aim for $\Delta Z = 0$ so that the filament is at the top of the micro-robot (which may help with releasing the cargo at the destination) without protruding from the microhelix. We anticipate that keeping the filament confined within the micro-robot will allow the micro-robot to be turned to a different swimming direction without losing the filament.

We note that our chosen initial conditions, with the straight filament placed along the axis of the helix and with their tops aligned, is not representative of a typical situation one would encounter in an experiment. However, the flow field and motion of the helix immediately break this special configuration and we do not expect the precise details of the initial configuration to be influential. In any case, we will see that the filament is always left behind by the micro-robot so the conclusion is that even if we start the filament in the center, where we showed that the average fluid velocity is most positive, this micro-robot design is not able to transport the filament over long distances.

3.7.1 The impact of helical pitch of the micro-robot

The motion of the micro-robots and filaments are presented visually in Figure 3.10 for four values of λ/R. In all cases, the micro-robot moves faster than

the filament so the two objects decouple. Using the relative displacement ΔZ as an indication of coupling, we found that performance was similarly poor with all helical pitches and there was no clear trend with λ/R. In terms of the absolute motion, for small λ/R, the filament moves in the forward direction whereas for large pitches ($\lambda/R = 3.3$ and greater), the filament has a net downward displacement. For larger λ/R, the helix is not able to confine the filament, which bends significantly and moves laterally to the exterior of the micro-robot. We note that the Z-velocities of the fluid at these larger distances from the helical axis are more negative (Figure 3.9), which explains why the filament moves backward in these cases. Therefore, careful selection of the geometry of the helix is necessary to achieve good coupling.

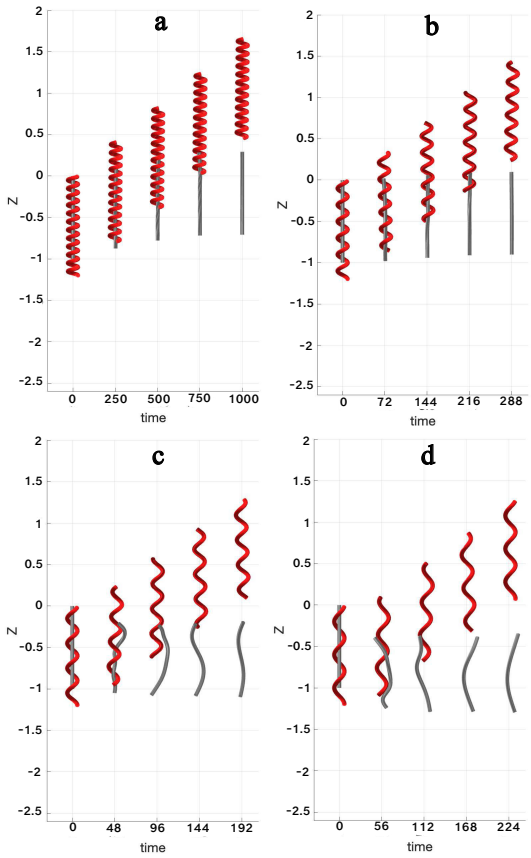


Figure 3.10: Snapshots of the motion of a helical micro-robot and a passive filament with different ratios of helical pitch to radius; a) $\lambda/R = 1.6$, b) $\lambda/R = 3.3$, c) $\lambda/R = 5$, d) $\lambda/R = 6.6$.

3.7.2 The impact of flexibility of the passive filament

We now vary the flexibility of the filament to study its effect on the coupling between the filament and the micro-robot. As shown in Figure 3.11, when the filament is very flexible, it undergoes high deformation, causing some parts to extend beyond the surface of the micro-robot. As previously discussed, this results in the filament being pushed backwards. On the other hand, stiff filaments are confined closer to the axis where they are driven forward by the flow field. Hence, coupling is best for stiffer filaments.

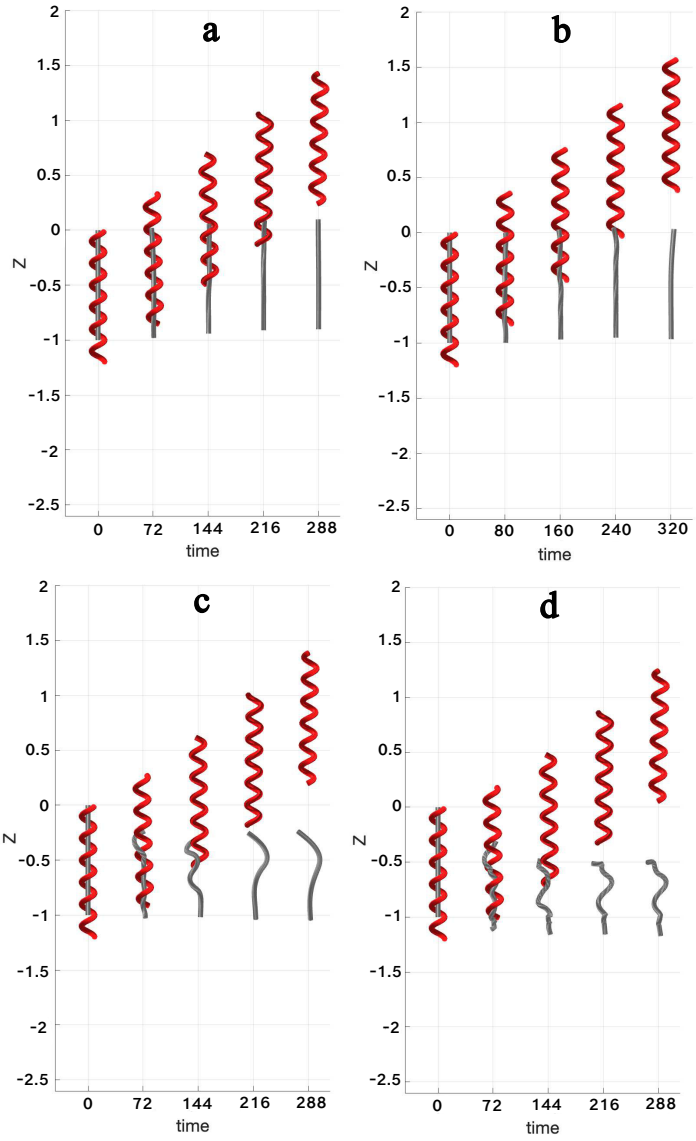


Figure 3.11: Snapshots of the motion of the helical micro-robot and the passive filament with different flexibility (Hookean spring constant between mesh nodes of the filament); a) $k = 1000$, b) $k = 300$, c) $k = 50$, d) $k = 5$.

3.7.3 The impact of cross-sectional radius of the micro-robot

In this section, the ratio of r/R is varied, for constant helical radius $R = 0.06$, to investigate its impact on the motion of the helical micro-robot and the filament. Four different values for r/R are tested: 0.25, 0.2, 0.16, and 0.13. The obtained results indicate that when r/R is set to 0.25, the value of ΔZ is approximately 1.05. This means that at time 192, the top of the micro-robot is positioned approximately 1.05 units (almost the full axial length of the micro-robot) ahead of the top of the filament. For r/R values of 0.2, 0.16, and 0.13, the corresponding ΔZ values are 1.15, 1.24, and 1.25, respectively. We remark that increasing r/R reduces the space available within the helix, forcing the filament to be in closer proximity to the micro-robot. Viscous effects then drag the filament with a velocity closer to that of the micro-robot, leading to a better coupling between the filament and the micro-robot. However, $\Delta Z \approx L$ in all cases, indicating that the micro-robot eventually overtakes the filament, and the coupling is lost. In the next section, we will attempt to redesign the micro-robot to achieve complete coupling between the filament and the micro-robot.

3.8 Improved design with multiple helical sections

3.8.1 Micro-robot with two helical sections

As demonstrated in the preceding sections, the simple helical micro-robot is able to propel the filament forward if the geometrical parameters are suitably chosen. However, the average speed of the filament is always lower than that of the micro-robot, hence, the micro-robot eventually overtakes the filament and leaves it behind. The objective of this project is to devise a novel design that enhances the coupling between the micro-robot and the filament. To achieve this, we must decrease the velocity difference between the micro-robot and the filament. As an initial approach, two microhelices, one pushing and one pulling, as depicted in Figure 3.12, are connected in series. Model parameters are as in Section 3.7.

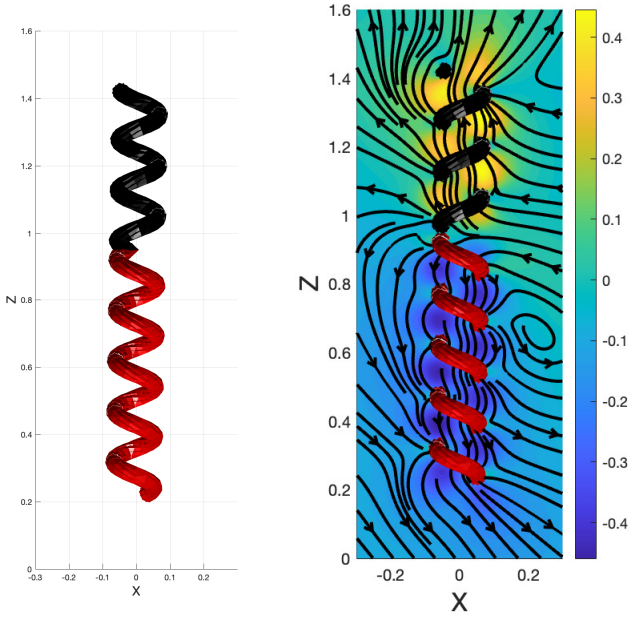


Figure 3.12: A micro-robot consisting of a pushing (black) and pulling (red) microhelix. Fluid streamlines around the rotating micro-robot are shown on the right, with the color scale indicating the Z-component of the velocity relative to the Z-velocity of the micro-robot.

The presence of a pushing helix at the front of the micro-robot reduces the speed of the micro-robot while simultaneously increasing the speed of the filament by driving forward the section of the filament within the pushing section.

Thus, we can improve the coupling between the filament and the micro-robot, while maintaining a positive swimming speed, by adjusting two parameters: the length ratio of the pulling section to the pushing section and the proportion of the filament in the pushing section compared with that in the pulling section.

Figure 3.13 demonstrates that if the pushing microhelix is long enough to contain the filament, then the filament can move faster than the micro-helix. Thus, by varying the length ratio between the pushing and pulling microhelix, along with the length of the section of the filament within the pushing microhelix, the coupling can be significantly improved compared to

a helical micro-robot with a single type of microhelix.

However, the initial step for carrying the filament is integrating (capturing) it with the micro-robot and this step has different requirements from the steady transportation step. Therefore, this study investigates the capability of the micro-robot to integrate with the filament by simulating the motion starting from a configuration in which the filament is aligned with but ahead of, and fully outside, the micro-robot, as shown in Figure 3.14. This is a reasonable initial configuration to consider as it has been demonstrated experimentally that magnetic helical micro-robots (of a single chirality) can be accurately manoeuvered and, indeed, sperm have been captured by such robots.[4, 129, 130]

Figure 3.14 shows that when the micro-robot approaches the filament, the filament is pushed forward, making it difficult for the micro-robot to catch it. This can be expected since the fluid moves forward in the Z-direction relative to the micro-robot, as shown in Figure 3.12.

In contrast, the fluid velocity in front of the pulling helix is in a downward direction (Figure 3.8). This means that objects in front of the helix are drawn in, rather than being pushed away. To solve the integration issue in the current design, a pulling helix is added to the front of the micro-robot. Thus, the final design, which is studied in the next section, is constructed from two pulling and one pushing helix. The pushing helix is located in the middle of the micro-robot between the two pulling helices with different lengths. Its length is carefully determined to optimize the coupling between the micro-robot and the filament.

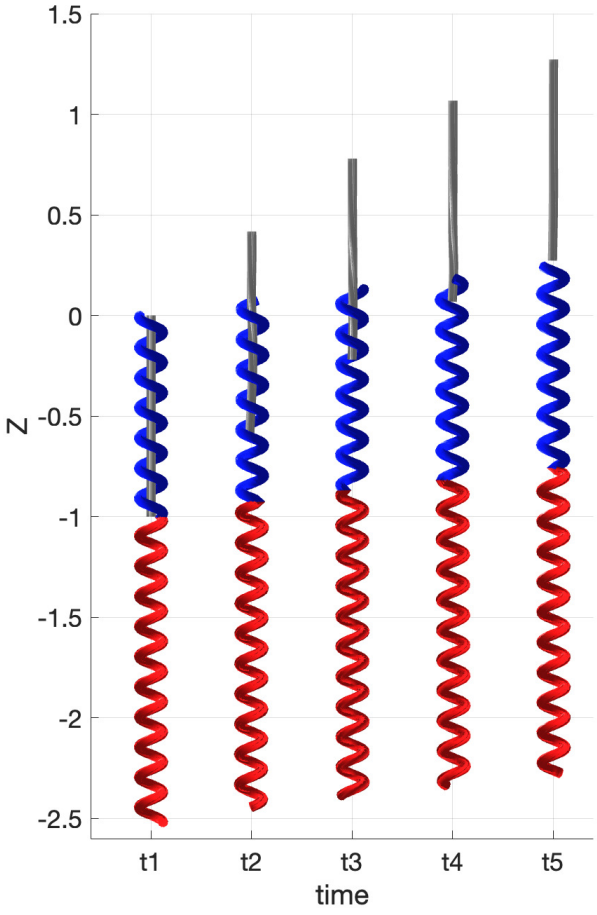


Figure 3.13: A micro-robot with two microhelices initially containing a passive filament. The pushing section at the front of the micro-robot has the same axial length as the filament and pushes the filament out of the micro-robot. t1, t2, ..., t5, corresponding to times 0, 120, 240, 360 and 480, respectively.

3.8.2 Micro-robot with three helical sections

To improve the integration process of micro-robot and the filament, a pulling helix is added to the front of the micro-robot discussed in Section 3.8.1. A schematic of the new micro-robot, and the generated flow field, is presented in Figure 3.15. The middle section of the micro-robot generates the necessary

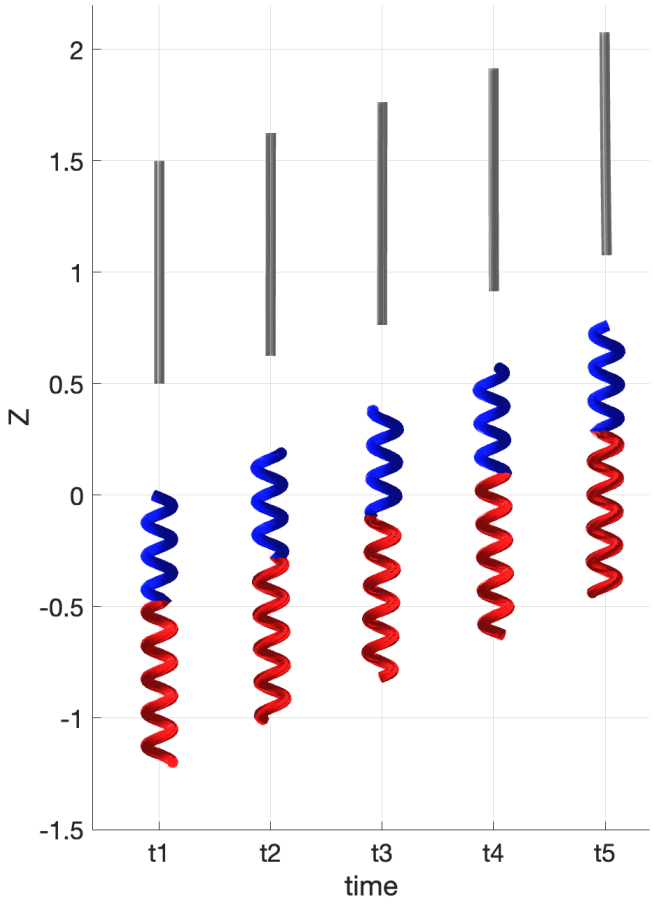


Figure 3.14: A helical micro-robot with two microhelices approaching a passive filament. t1, t2, ..., t7, corresponding to times 0, 380, 760, 1140 and 1520, respectively.

drag force to propel the filament forward, while the front section draws the filament into the helix to aid the integration process. The back part of the micro-robot generates most of the driving force required for the micro-robot to move forward. The length ratio between the middle, front, and back sections of the micro-robot must be carefully chosen to maximize the coupling between the filament and the micro-robot while providing forward propulsion for the coupled structures.

In Section 3.11, we use a simplified analytical model to estimate the

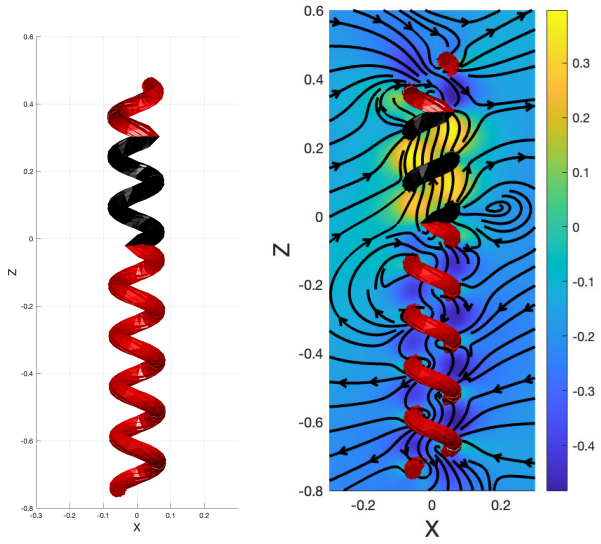


Figure 3.15: A micro-robot consisting of three microhelices: a pushing (black) section between two pulling (red) sections. Fluid streamlines around the rotating micro-robot are shown on the right, with the color scale indicating the Z-component of the velocity relative to the Z-velocity of the micro-robot.

swimming speeds and show that full coupling can be achieved for many combinations of helical pitch and cross-sectional radius. It is important to note that various design criteria must be considered when designing the micro-robot. Firstly, increasing the total length of the micro-robot may enhance the speed of the filament and the micro-robot, but also reduces the robot's manoeuvrability as it will be unable to pass through narrow channels with sharp bends. Thus, the total length of the micro-robot must be specified based on its intended application. The second criterion to consider is the position of the end part of the filament, which should be located inside the middle (pushing) part of the micro-robot for stability of the coupled configuration. These two considerations are also discussed in Section 3.11.

With these considerations in mind, we fix the total length of the micro-robot $L = 2.5$ and let the sum of the lengths of the front and middle microhelices be 1.125, which is slightly greater than the length of the filament $L_f = 1$. The ratio of the middle (pushing) length to the combined front and middle length, denoted ξ, is varied from 0.3 to 0.6. Simulations are started

with the tops of the filament and micro-robot at the same Z position and run up to a fixed time, after which we compare the relative Z positions.

As shown in Figure 3.16, when the pushing length ratio is $\xi = 0.3$, the filament falls behind the micro-robot ($\Delta Z > 0$). However, as the ξ parameter increases, more of the filament becomes enclosed within the pushing microhelix, leading to accelerated filament movement. When ξ exceeds 0.5, we find that the filament is pushed ahead of the micro-robot ($\Delta Z < 0$). By interpolating the nearly linear trend depicted in Figure 3.16, the optimal length ratio ξ for full coupling ($\Delta Z = 0$) was estimated to be approximately 0.52.

Using the length ratio $\xi = 0.52$, the processes of integration and coupling for the micro-robot are simulated by initializing the filament ahead of the micro-robot. As shown in Figure 3.17, both of these steps are successful. In summary, the design's advantage lies in the pulling microhelix as the front microhelix, which causes the filament to be pulled toward the micro-robot during the integration phase and prevents the filament from moving ahead of the micro-robot, facilitating coupling. Furthermore, by choosing the lengths of the front and middle sections so that part of the pushing microhelix is below the bottom of the filament, we prevent the filament from falling behind. Therefore, not only can coupling and integration be achieved with the current design, but the coupled configuration is stable.

3.9 Capture and transport of filaments with different resting shapes

In the previous sections, we evaluated the designed micro-robot's capability to capture and transport a flexible filament that was naturally straight. To determine whether the same micro-robot could be used to capture and carry non-straight filaments, two different shapes were considered: a sinusoidal curve and a circular arc. In each case, the filaments were initialized in their respective resting configurations.

For the sinusoidal filament, we considered a fixed wavelength $\lambda_f = 0.25$ and performed simulations with the amplitude of the sinusoidal curve equal to 0.5, 0.75, and 1.0 times the radius of the filament, $r_f = 0.014$. The micro-

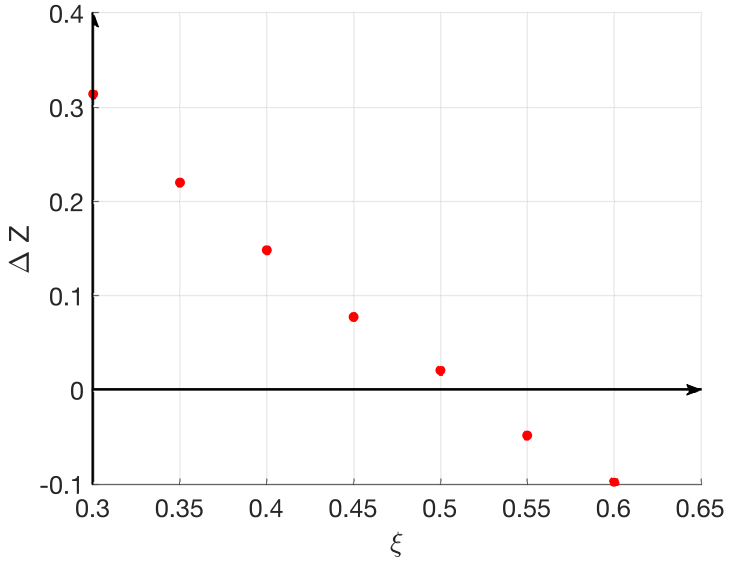


Figure 3.16: The effect of length ratio ξ of the middle (pushing) length to the combined front and middle lengths on the coupling between the three-section helical micro-robot and the passive filament.

robot was able to capture and transport all three sinusoidal filaments; the case with the largest amplitude is presented in Figure 3.18.

For the circular arc, we considered three different curvatures such that the central angle subtended by the arcs were 30, 40, and 60 degrees, respectively, and found that the micro-robot could capture and transport all of these filaments. Figure 3.19 depicts results for a circular filament with a central angle of 60 degrees. To assess the micro-robot's capability in capturing and transporting filaments of varying flexibility and stiffness, simulations were conducted with different spring constants for the filaments. Previously, a spring constant of 1000 was employed, resulting in a bending stiffness of $EI = 4.6 \times 10^{-21}$ N m^2. This value closely mirrors the rigidity of a sperm tail and was utilized in simulations. However, simulations were repeated with spring constants of 500 and 1500 to explore the feasibility of capturing and transporting filaments with different stiffness levels. We found that the micro-robot effectively captures and transports both curvilinear and sinusoidal filaments with any of these stiffnesses.

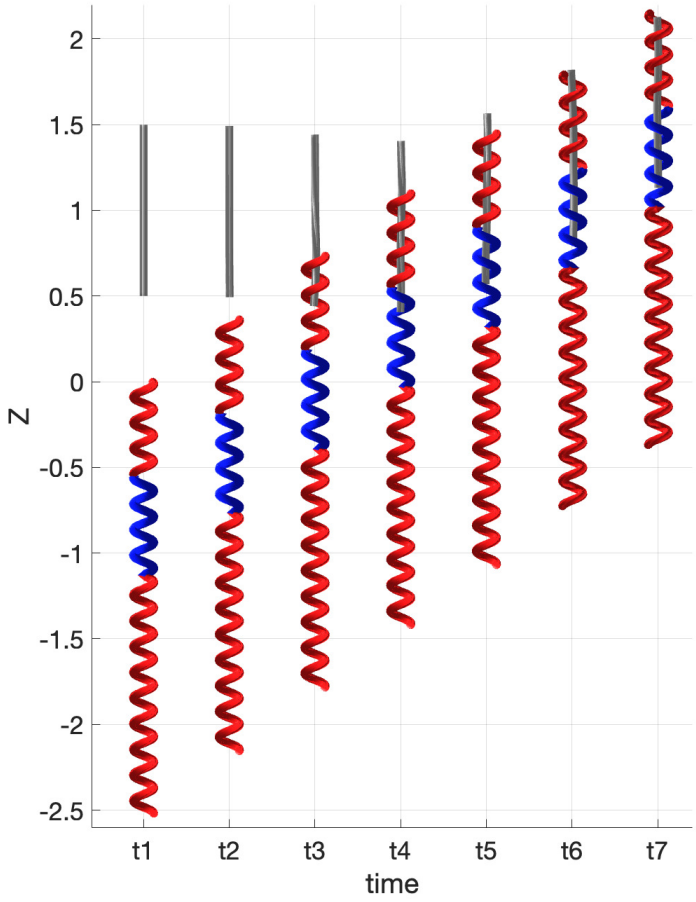


Figure 3.17: Integration and carrying the passive filament with the designed helical micro-robot with three microhelices. The pushing microhelix is highlighted in blue, while the pulling microhelices are depicted in red. The values of the dimensionless times t1, t2, ..., and t7 are 0, 160, 320, 480, 640, 720, and 960, respectively.

3.10 Capture and transport of a filament with a head

In human spermatozoa, the flagellum is attached to a head that has a diameter larger than that of the flagellum. Other microorganisms, as well as micro-robotic designs, follow a similar structure; namely, a long motile

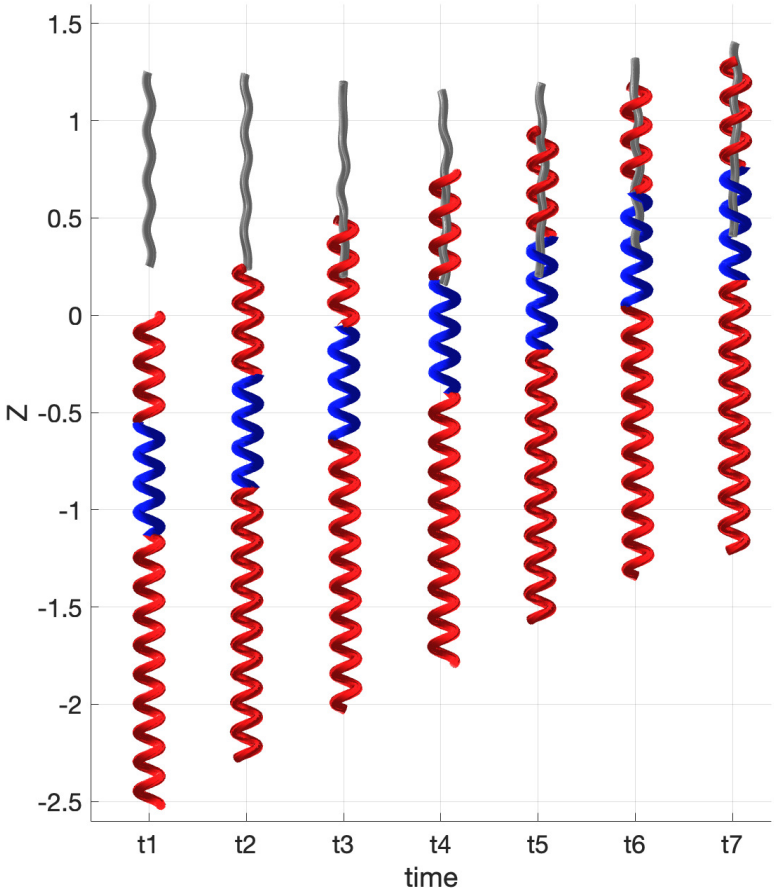


Figure 3.18: Integration and transport of a passive, flexible filament with a sinusoidal shape having an amplitude equal to the filament radius. The pushing microhelix is highlighted in blue, while the pulling microhelices are depicted in red. t1, t2, ..., t7, corresponding to times 0, 120, 240, 360, 480, 600, and 640, respectively.

filament is used to propel an attached payload. This section explores the functionality of a micro-robot when a spherical head is attached to one end of the filament structure. A rigid spherical head, consisting of 162 nodes, with a radius of 0.055 is attached to the filament, chosen to match the larger diameter of the human sperm head.[131] The connection between the head and the filament involves 16 springs, linking the four nodes of the first cross-section of the filament to four nodes on the head. The spring constant of

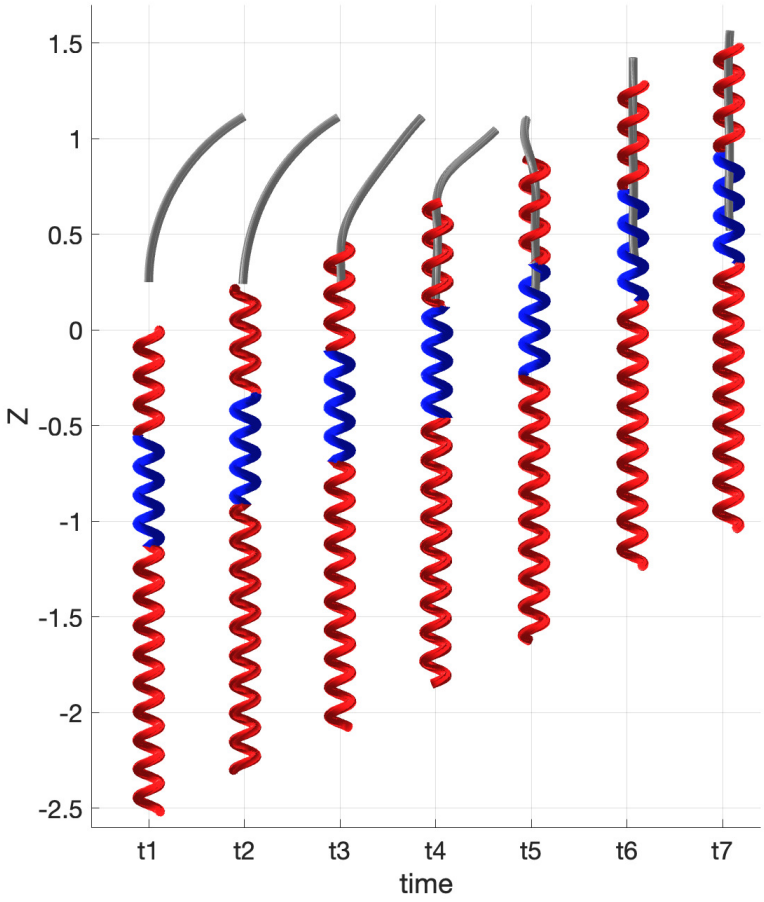


Figure 3.19: Integration and transport of a passive, flexible filament with a circular shape featuring an arc angle of 60 degrees. The pushing microhelix is highlighted in blue, while the pulling microhelices are depicted in red. t1, t2, ..., t7, corresponding to times 0, 80, 160, 240, 320, 480, and 560, respectively.

these connecting springs is set to be four times stiffer than the filament's structural springs, which have a spring constant of 1000. The micro-robot used in Section 6.2 is employed here, operating at a non-dimensionalized frequency of 0.1, to capture and transport the filament with the head. As depicted in Figure 3.20, the micro-robot initially approaches the filament to capture it. Subsequently, the filament is successfully captured, and at times t_6 and t_7, the efficient transportation of the filament by the micro-robot is ev-

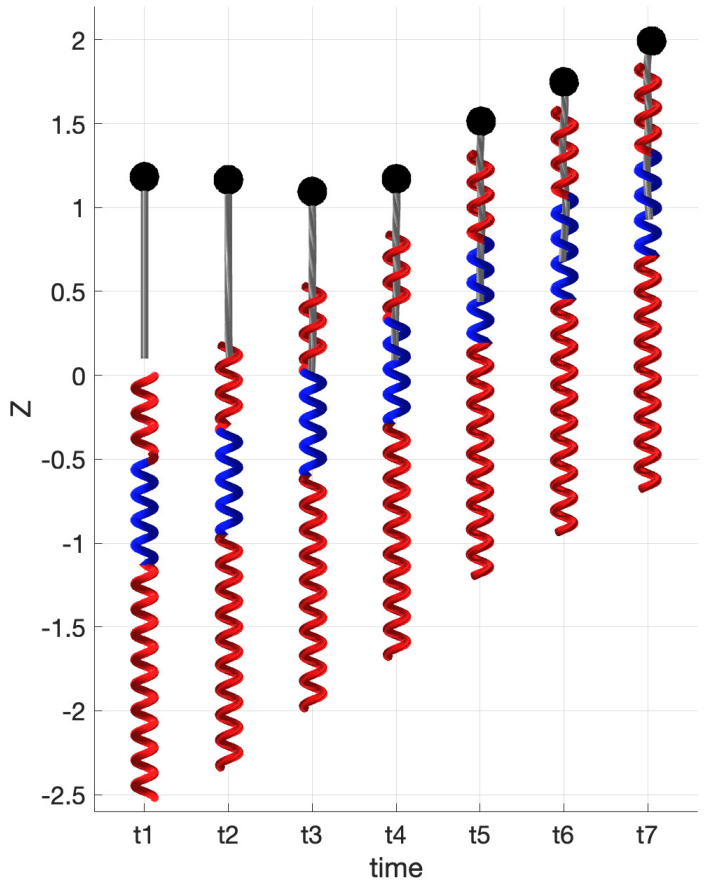


Figure 3.20: Integration and transport of a passive, flexible filament with a head over time. The positions of the micro-robot, filament, and head are illustrated at seven different instances, t_1, t_2, ..., t_7, corresponding to times 0, 87.5, 254, 420, 588, 754, and 920, respectively. The pushing microhelix is highlighted in blue, while the pulling microhelices are depicted in red.

ident, demonstrating the stability of this coupling and transportation. From our discussion in Section 3.8, we expect that the parameter ξ (the length ratio between the pushing and front pulling microhelices) can influence the gap between the head and the micro-robot. We found that using the value $\xi = 0.52$, which was chosen in Section 3.8 without consideration of a head, the micro-robot and the head came within range of the steric repulsion in-

teraction. Increasing the ratio to $\xi = 0.59$ resulted in a minimum distance of 0.15 between the head and micro-robot, ensuring no contact occurs.

3.11 Analytical study on the possibility of coupling

We develop a reduced analytical model to demonstrate, with a small number of parameters that must be determined numerically, that full coupling between the micro-robot and passive filament is generically achievable by changing the proportions of pushing and pulling helices. Consider a long right-handed microhelix. Adopting a resistive force theory approach (in particular, ignoring end effects), the relationships between the axial velocity U of the helix, the rotational rate Ω of the helix, the thrust force per unit length F applied to the fluid, and torque per unit length T (in the forward axial direction) applied to the fluid, can be expressed as[132, 133]

$$\begin{cases} A_{11}U + A_{12}\Omega = F, \\ A_{21}U + A_{22}\Omega = T. \end{cases} \tag{3.11}$$

where the resistance matrix per unit length $\begin{pmatrix} A_{11} & A_{12} \\ A_{21} & A_{22} \end{pmatrix}$ is a symmetric matrix that depends only on the cross-sectional radius, helical radius, and pitch of the microhelix. A left-handed microhelix with the same geometric parameters would have the same resistance coefficients except for a change in signs for the off-diagonal elements.[132] For motion driven by an external torque T, we set $F = 0$ and express the translational velocity of the helix as

$$U = -\frac{A_{12}}{A_{11}}\Omega. \tag{3.12}$$

It should be noted that A_{12}/A_{11} is negative for a right-handed helix so that $U > 0$ (pulling) if $\Omega > 0$. In our proposed geometry, the micro-robot comprises both a pulling microhelix and a pushing microhelix, which are of opposite handedness. Denoting the ratio of the pushing microhelix length to the total length by η, the forward swimming speed of the compound micro-robot is

$$U = -\frac{A_{12}}{A_{11}}\Omega(1 - 2\eta). \tag{3.13}$$

To estimate the velocity of the passive filament, we formulate equations analogous to 3.11 for the passive filament, where the force and torque densities are interpreted as the hydrodynamic force and torque densities that would act on a stationary filament in the flow field generated by the helical micro-robot. In general, these quantities depend on all of the geometric parameters of the problem as well as the position of the filament relative to the helix. For long helices, we find that the fluid velocity in the axial direction is roughly uniform along the axis of a rotating or translating helix, away from the ends (Figures 3.21 and 3.22). Hence, we assume that the filament lies along the helical axis and is nested within the axial bounds of the micro-robot. We then make the approximation that the force per unit length and the torque per unit length on the filament are proportional to the uniform fluid velocity along the axis of the helix, which is in turn linearly related to the rotational rate and translational velocity of the helix. The system of equations governing the passive filament inside the right-handed helix can be expressed as

$$\begin{cases} B_{11}U_f + B_{12}\Omega_f = (C_{11}U + C_{12}\Omega), \\ B_{21}U_f + B_{22}\Omega_f = (C_{21}U + C_{22}\Omega). \end{cases} \tag{3.14}$$

Assuming that the filament is almost straight, the effect of Ω on the axial force on the passive filament is negligible, so $B_{12} \approx 0$. Therefore, the translational velocity of the filament is approximated by

$$U_f = \alpha U + \beta\Omega. \tag{3.15}$$

where $\alpha = C_{11}/B_{11}$ and $\beta = C_{12}/B_{11}$ are only functions of the cross-sectional radius, the helical pitch, and the helical radius of the micro-robot, which we determine numerically using the regularized Stokeslet method for a long helix (20 windings) with fixed helical radius $R = 0.1$ and various combinations of cross-sectional radius r and helical pitch λ. We expect that α takes values between 0 and 1, because the fluid should be dragged in the same direction as a translating helix but not faster than the helix. We expect $\beta < 0$ for right-handed helices, as demonstrated in Sections 3.5 and 3.6. For a left-handed helix, we would have the same values for C_{11} and B_{11}, and hence α. The coefficient C_{12}, and hence also β, would have the same magnitudes but opposite signs.

For a micro-robot with both left- and right-handed sections, the velocity of the filament is estimated by taking the average of the velocities of the

portions of the filament in the right- and left-handed sections of the micro-robot, weighted by the lengths of these two portions. Suppose that the fraction of the filament contained in the left-handed section of the micro-robot is ξ and the fraction in the right-handed section is $(1-\xi)$. In general, ξ and η may be different if the filament is shorter than the helix. If the filament runs through all of the left-handed portion of the micro-robot, then $\xi = \eta L/L_f$. For simplicity, we will assume that this is the case. The estimated velocity of the filament is

$$U_f = \alpha U + \beta\Omega(1 - 2\eta L/L_f). \tag{3.16}$$

Coupling is achieved when the velocities of the micro-robot and the filament,

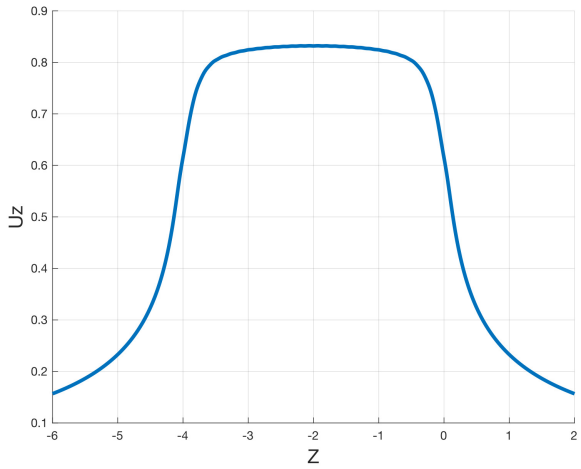


Figure 3.21: Velocity profile of the fluid computed using the Regularized Stokeslet method along the axis of a right-handed helix in the axial direction when the microhelix moves with prescribed speed $U = 1$ and $\Omega = 0$. The back and front of the micro-robot are located at $Z = -4$ and $Z = 0$, respectively. The velocity at the central plateau corresponds to the parameter α.

respectively given by (3.13) and (3.16), are equal. For nonzero rotation rate Ω, there is a unique ratio

$$\eta^* = \frac{1}{2}\left[1 - \frac{\left(\frac{L}{L_f} - 1\right)\beta}{\frac{A_{12}}{A_{11}}(1-\alpha) + \beta\frac{L}{L_f}}\right]. \tag{3.17}$$

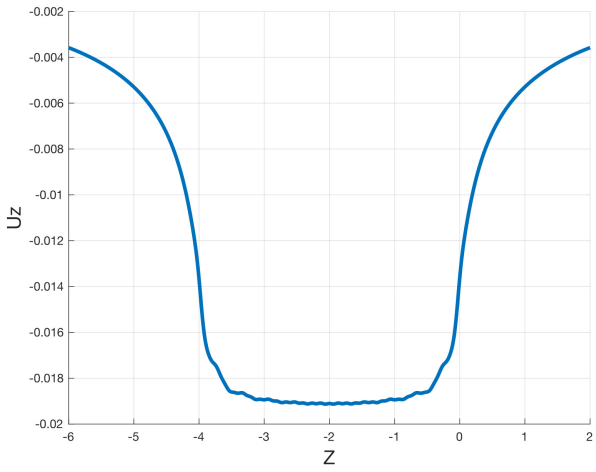


Figure 3.22: Velocity profile of the fluid computed using the Regularized Stokeslet method along the axis of a right-handed helix in the axial direction when the microhelix moves with prescribed speed $U = 0$ and $\Omega = 1$. The back and front of the micro-robot are located at $Z = -4$ and $Z = 0$, respectively. The velocity at the central plateau corresponds to the parameter β.

at which $U = U_f$ for given helical parameters.

We now present results from simulations used to determine numerical values for the coefficients. The total length of the micro-robot was fixed at $L = 1$, while the length of the filament was fixed at $L_f = 0.5$. Our analytical model does not explicitly account for the thickness of the filament. However, to allow a straight filament to fit inside the micro-robot, the ratio r/R is constrained to take values between 0 and $(1-r_f/R) < 1$. We consider pitches $\lambda > 4r$ so that successive turns of the helix are not too close together. In Figure 3.23, we show η^* for various values of r/R between 0.04 and 0.71, and for λ/R up to 4. Except for the smallest values of r/R and λ/R, we find that η^* increases with λ/R. In addition, we tested larger values of λ/R up to 400 for $r/R = 0.3$. Across all tested parameter combinations, the values of η^* remained in a narrow range, between 0.23 and 0.275. This suggests that $\eta \approx 0.25$ should be suitable for most helical geometries. For comparison, the optimum value for ξ was found to be 0.52 in Section 3.8.2, corresponding to $\eta = 0.234$. In Section 3.8.2, we mentioned two design considerations for the three-section micro-robot. To explain why the speed of the micro-

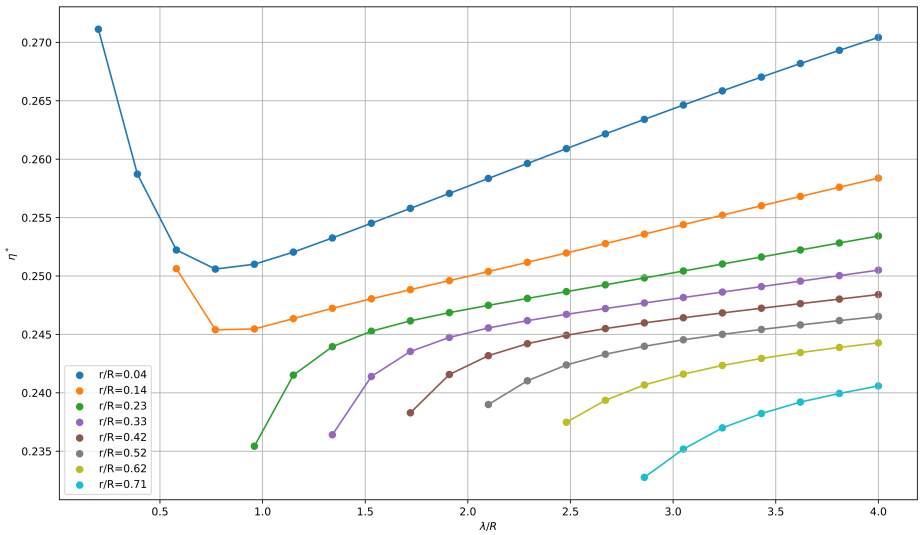


Figure 3.23: Impact of λ/R and r/R on η^*. (desired η to have the same velocity for the filament and the micro-robot)

robot increases with the total length, note that η^*, given by (3.17), is a decreasing function of L/L_f if as anticipated, $L > L_f$, $\beta < 0$, $0 < \alpha < 1$, and $A_{12}/A_{11} < 0$. Additionally, the swimming speed, given by (3.13), is a decreasing function of η. Hence, the swimming speed for micro-robots designed with $\eta = \eta^*$ increases with the total length L.

The second consideration was that the bottom of the filament should be within the middle section of the micro-robot. To illustrate the benefit of this, suppose that the filament is straight and consider a vertical perturbation ΔZ of the micro-robot relative to the filament. If $\Delta Z < 0$ (the filament protrudes out of the micro-robot slightly), then the portion of the filament in the middle, pushing, section of the micro-robot is shorter while the portion in the front, pulling, section is the same. Hence, the filament will be pulled back into the micro-robot. If $\Delta Z > 0$, then the portion of the filament in the pulling helices becomes shorter while the portion in the pushing helix is longer. The filament is pushed forward and ΔZ decreases. Hence, this design stabilizes the fully coupled configuration $\Delta Z = 0$, as demonstrated in Figure 3.17.

3.12 Conclusions

Recent advancements in micro-robot design have led to the development of robots capable of carrying cargo in vivo/in-vitro using a magnetic fields. However, many of these methods involve contact-based cargo transportation, which can make it difficult to release the cargo after reaching their target. In this study, we sought to provide a non-contact method for carrying cargo using a rotating helical micro-robot.

To design the helical micro-robot for capturing and carrying a passive filament, we first studied the streamline and pathline of fluid around the rotating helical micro-robot. To achieve a good coupling between the passive filament and the micro-robot, the filament must be located where the fluid flows in the forward direction. Our calculations showed that confining the filament inside the micro-robot close to its axis maximized the forward hydrodynamic drag force. We found that the geometrical parameters r/R and λ/R affect the pathline of the fluid significantly. Unsuitable choices for r/R and λ/R cause the pathline of the fluid to escape the radial confinement of the micro-robot, which according to the streamline of the fluid, the velocity of the fluid is in the backward direction.

Next, we simulated the motion of the helical micro-robot and the passive filament and examined the effects of three parameters: the flexibility of the filament, r/R, and λ/R. Our results indicated that increasing the flexibility of the filament and the ratio of r/R led to better coupling, while reducing λ/R improved the coupling as well. However, we found that the forward velocity of the filament for the designed helical micro-robot was lower than that of the micro-robot, causing the micro-robot to surpass the filament and lose the coupling. To address this issue, we added a pushing helix to the front of the micro-robot to apply a larger hydrodynamic thrust force to the filament and enhance its forward velocity.

Despite this improvement, we encountered another issue with the second design: the flow field on the front of the micro-robot was in the forward direction, causing the filament to push forward during the capturing process and making it difficult to capture. Thus, we proposed a third design, which consisted of three helical sections: one pushing microhelix located between two pulling microhelices of different lengths. The pulling helix located at the back provided the main thrust for the micro-robot to push forward, while

the front helix pulled fluid into the micro-robot to assist with capturing the filament. By changing the length ratio between the pushing and pulling microhelices and selecting the helix's parameters of r/R and λ/R, we were able to manipulate the coupling between the filament and the micro-robot. Using the optimal length ratio for coupling, our simulations demonstrated that the micro-robot with three sections was also effective at capturing a filament.

Since biological and synthetic filaments are often curved, we conducted simulations with two different non-straight resting shapes: sinusoidal and circular arcs. We demonstrated that our micro-robot can capture and transport such filaments over a range of curvatures and amplitudes. Furthermore, we showed that our micro-robot can transport a straight filament with an attached head, similar in proportion to that of human sperm. By tuning the length ratio of the helical sections, we could push the filament enough to maintain a gap between the head of the cargo and the micro-robot. Thus, we assert that our novel micro-robot not only facilitates non-contact transport of micro-swimmers with a head but also offers the flexibility to regulate the gap between the head and the micro-robot, mitigating any potential contact or adhesion issues.

Finally, we developed a theoretical model to estimate the length ratios that allow complete coupling between a filament without a head and a micro-robot and found a low sensitivity to geometrical parameters. The optimal length ratio from the model was in close agreement with the numerically determined optimum. In addition, the model supports our recommendation that the combined length of the front and middle sections be slightly longer than the length of the intended filament cargo.

We anticipate that the micro-robot we have designed would be suitable for transporting immotile sperm cells. If the helical micro-robot configuration and the lengths of the first, second, and first helices are carefully designed according to the criteria discussed in Section 3.8.2, then the sperm can be carried without relying on direct contact with the micro-robot to push the cell forward. This could reduce the chance of adhesion and damage due to shear stresses applied to the head.

Chapter 4

Developing and characterizing viscoelastic fluid

In the preceding chapter, a helical magnetic micro-robot was developed to transport filamentous micro-cargo in a Newtonian fluid. However, as previously discussed, most biological microorganisms navigate through viscoelastic fluids. The movement of microorganisms within viscoelastic fluids is crucial for various biological processes, including fertilization, infection, and biofilm formation. Thus, it is essential to also simulate the motion of a helical micro-robot in a viscoelastic fluid.

To date, most studies on viscoelastic micro-swimming have treated the fluid as a homogeneous, single-phase continuum. However, complex fluids are typically chemically and mechanically heterogeneous at the length scales relevant to biological swimmers, meaning that non-continuum effects are expected to be significant. As mentioned earlier, treating the fluid as continuous may not sufficiently capture the interactions between microorganisms or robots navigating through viscous fluids containing suspended microstructures, such as elastic polymers and filamentous networks. This is especially true when the size of the polymeric network is comparable to that of the micro-robot or cargo. For instance, mammalian sperm navigate through such heterogeneous networks within the female reproductive tract, encountering various configurations and spacings between mucin fibers that change throughout the menstrual cycle [14, 114]. Given that the size of the micro-robot designed in the previous chapter was based on the size of sperm, the size of heterogeneous networks within the female reproductive tract or the

vitreous humour is comparable to the size of the micro-robot. Therefore, to simulate the motion of the micro-robot in the viscoelastic fluid, it is required to consider the fluid as a non-continuum fluid.

Therefore, in this chapter and the subsequent one, we will simulate the motion of a helical micro-robot in a viscoelastic fluid. To accomplish this, we must first define and characterize the viscoelastic model. This chapter will explain the proposed model for the viscoelastic fluid and provide its characterization. In chapter 5, the motion of the micro-robot within the viscoelastic fluid will be simulated.

The model used in this chapter is based on the one proposed by Wróbel et al. [13]. As illustrated in Figure 4.1b, the viscoelastic network consists of multiple nodes arranged in a cubic structure, with each node connected to its 26 neighboring nodes via springs and dashpots, as shown in Figure 1.13. This configuration forms the foundation of the viscoelastic network used in this study. First, we will characterize this network, and then subsequently introduce modified viscoelastic networks to better mimic the behavior of the vaginal fluid sample, drawing inspiration from Figure 4.1a. To begin, we aim to analytically predict the behavior of the viscoelastic network using a simple ODE model characterized by a small number of parameters with physical interpretations. The nodes are connected by a spring and dashpot in series, and because they are immersed in a Newtonian fluid, a more accurate representation of the behaviour of the whole viscoelastic fluid, is a spring and dashpot in series, parallel to another dashpot, as illustrated in Figure4.2.

The relationships between the forces, strains, and the velocity of nodes x_1 and x_2 are given by

$$\frac{\eta}{K}\dot{F} + F = (\eta + \eta_2)\dot{\epsilon} + \frac{\eta\eta_2}{K}\ddot{\epsilon}. \tag{4.1}$$

where F and ϵ are the forces and strain applied between nodes x_1 and x_2 which are connected. The detailed derivations and further analysis of this model are provided in the Appendix I. By defining $\alpha = \frac{\eta}{K}$, $\beta = \eta + \eta_2$, and $\gamma = \frac{\eta\eta_2}{K}$, we obtain the following ODE relationship between F and ϵ:

$$\alpha\dot{F} + F = \beta\dot{\epsilon} + \gamma\ddot{\epsilon}. \tag{4.2}$$

To characterize the viscoelastic fluid, several tests can be conducted, including the creep test and strain test, where a strain or force is applied to

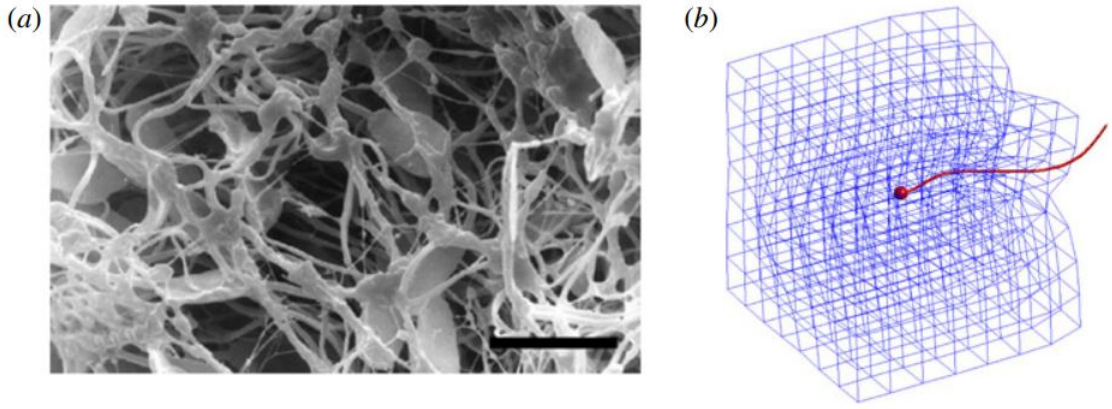


Figure 4.1: (a) Photomicrograph of bovine spermatozoa in a vaginal fluid sample [14]. (b) Model of a micro-swimmer moving through a viscoelastic network, adapted from Ref [13].

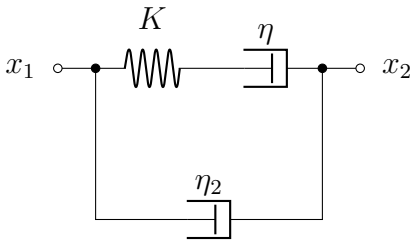


Figure 4.2: Schematic of the element connecting two nodes in the viscoelastic network.

the viscoelastic fluid and the system's behavior is observed. Assume the previously described network, consisting of multiple nodes arranged within a cubic lattice where each node is connected to its 26 neighboring nodes, extends infinitely in the x, y, and z directions. To analyze the system, we focus on a single representative cube containing eight nodes, which forms one unit of the periodic lattice. Since the network is periodic, all cubes are assumed to be identical, with edges and nodes shared between adjacent cells. By studying the behavior of a single cube, we can infer the behavior of the entire infinite viscoelastic network. Applying a shear force in the x-direction to the top surface ABCD, as shown in Figure 4.3, and an equal and opposite force to the bottom surface OPMN allows us to calculate the displacement of

the nodes in the x-direction. The ODE equation relating the displacement of the nodes in the x direction to the force applied to the ABCD surface is derived, providing a general formula for the viscoelastic fluid's behavior. The strain parameter is defined as follows:

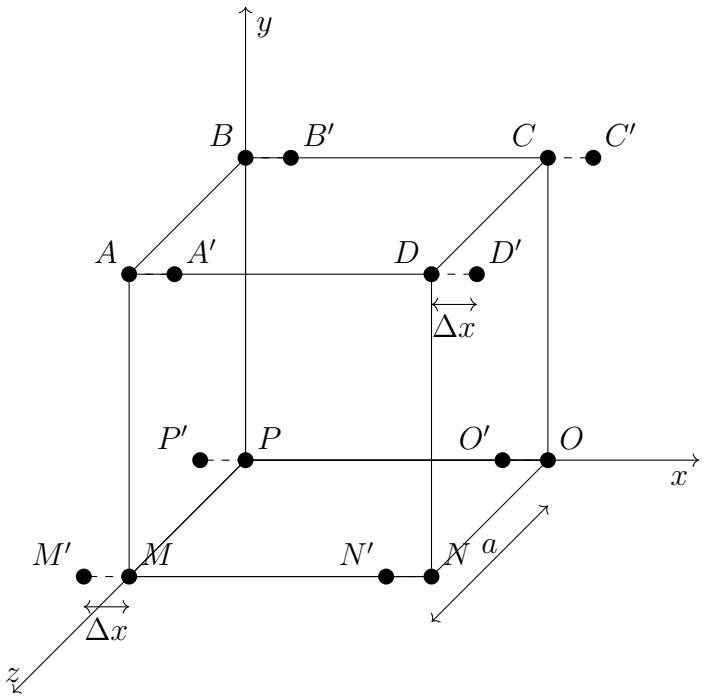


Figure 4.3: A cube within the viscoelastic network, where the nodes are connected by the elements shown in Figure 4.2.

$$\epsilon = \frac{2\Delta x}{a}.$$

Based on the diagram provided and considering that a shear force is applied to the cube, it is observed that the top vertices A, B, C, and D are displaced by a magnitude of Δx to the right, while the bottom vertices M, N, O, and P are displaced by the same magnitude Δx to the left. The relationships between force, strain, and the velocity of the nodes are examined, leading to the derivation of the following equation that relates the force F and the strain ϵ:

$$F + \alpha\dot{F} = \beta(1.4769\dot{\epsilon} + 1.5332\epsilon^2\dot{\epsilon}) + \gamma(1.4769\ddot{\epsilon} + 3.8782\dot{\epsilon}^2\epsilon + 1.8261\epsilon^2\ddot{\epsilon}). \tag{4.3}$$

This equation characterizes the behavior of the viscoelastic fluid. Detailed derivations and further analysis of this model are provided in Appendix I. Equation 4.3 illustrates the relationship between the force and strain in the viscoelastic network. However, since stress is defined as force per unit area, the equation can also be rewritten to describe the relationship between stress and strain as follows:

$$\sigma + \alpha\dot{\sigma} = (\beta/a)(1.4769\dot{\epsilon} + 1.5332\epsilon^2\dot{\epsilon}) + (\gamma/a)(1.4769\ddot{\epsilon} + 3.8782\dot{\epsilon}^2\epsilon + 1.8261\epsilon^2\ddot{\epsilon}), \tag{4.4}$$

where σ is the stress applied to the viscoelastic network. This equation is derived for one cube of the viscoelastic network shown in Figure 4.4. It must be noted that, according to Equation 4.3, the relationship between the force and strain is non-linear. As discussed in Section 1.4, "Classification of Fluid Behaviour," simulating the behaviour of a fluid using dashpots and springs typically only captures the linear behaviour of the system. However, as demonstrated, when multiple Maxwell components are used to connect the nodes of a cube's vertices, located in a Newtonian fluid, the overall behaviour of the viscoelastic fluid becomes non-linear. Furthermore, it is important to note that the positions of the nodes are influenced by the fluid, indicating that the viscoelastic properties are convected within the fluid. This is consistent with the behavior observed in non-linear viscoelastic fluids rather than in linear viscoelastic fluids. We believe the derived Equation 4.3 can also describe the behaviour of the viscoelastic fluid created with the network shown in Figure 4.4. Therefore, we first simulate the oscillation test, as described in section 4.2, and then compare the results with those predicted by Equation 4.3. Using a genetic optimization algorithm [134, 135](briefly described in Appendix II), implemented via MATLAB's genetic algorithm function(GA), we determine the values of α, β, and γ to ensure that the predicted results align well with the simulated results using regularized stokeslet methods. Then, using the formulas $\alpha = \frac{\eta}{K}$, $\beta = \eta + \eta_2$, and $\gamma = \frac{\eta\eta_2}{K}$, we can find the equivalent viscosities for the solvent and solution as well as the elasticity of the viscoelastic fluid. Subsequently, using the creep and strain tests, we will calculate the relaxation time for both strain and stress of the viscoelastic fluid. Before delving into these tests, it is essential to explain the numerical methods used for simulating the viscoelastic network and validate the model. Finally, we apply the oscillation, creep and strain tests to the developed viscoelastic network, which will be used in the next chapter to study the behaviour of a magnetic micro-robot in a viscoelastic fluid.

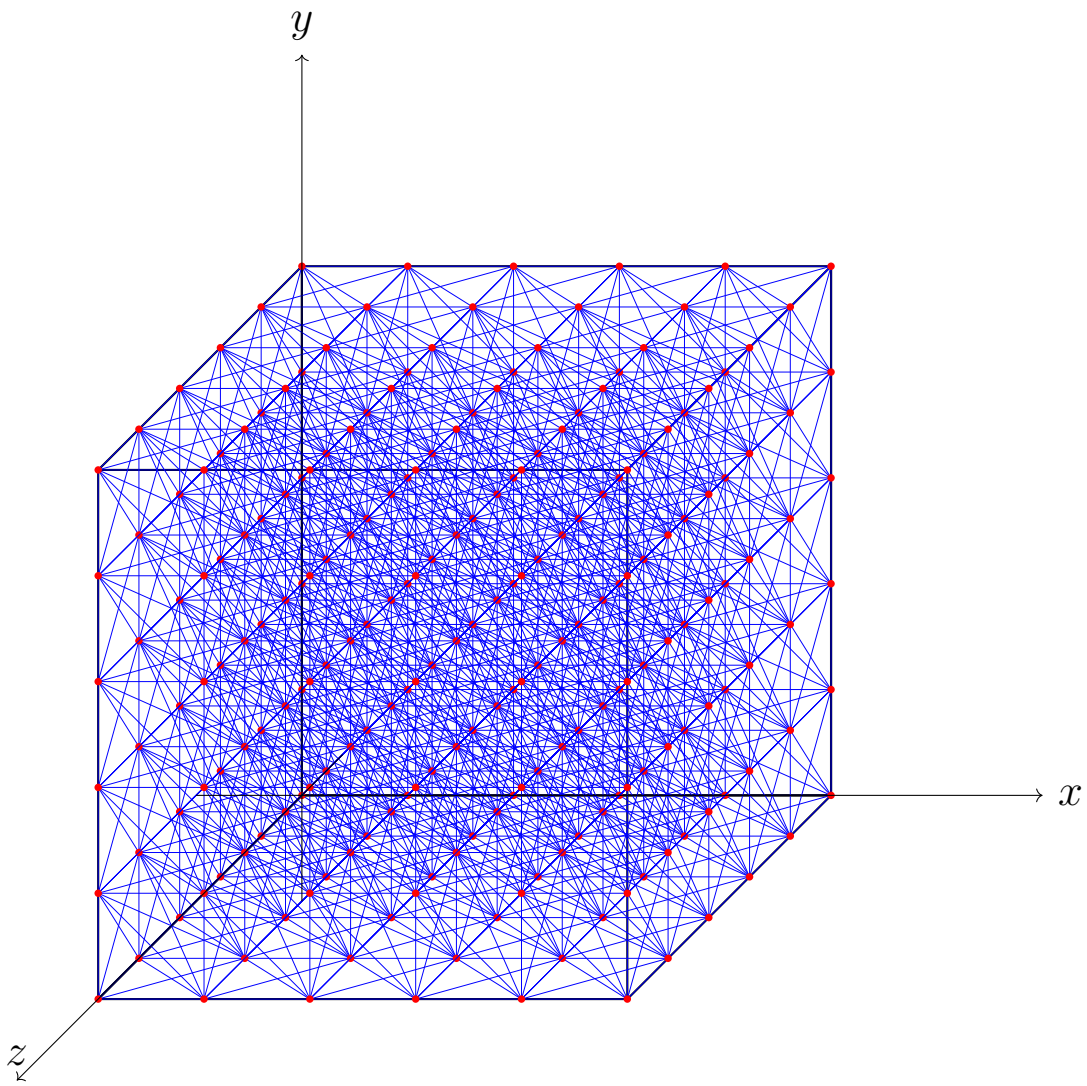


Figure 4.4: Viscoelastic network. This is an infinite network. All connected nodes are connected with a Maxwell component.

4.1 Numerical method and verification

In the previous section, we derived a formula relating the stress and strain applied to a viscoelastic network containing a single cube where viscoelastic nodes are located at the vertices. All vertices are connected via Maxwell

elements, and the viscoelastic network is embedded in a Newtonian fluid. This derivation aids in developing a ODE equation to better understand the relationship between strain and stress in such viscoelastic fluids.

We now describe the numerical method employed for this simulation. As previously explained, the regularized Stokeslet method is utilized to resolve the fluid dynamics. Within the Stokes fluid, multiple nodes represent the viscoelastic nodes, and the viscoelastic network is modeled using Maxwell elements. Due to the relative motion of these nodes, forces are applied to the viscoelastic nodes. Subsequently, using the regularized Stokeslet method, the velocity field within the fluid is obtained. Therefore, this simulation method is based on the regularized Stokeslet method, as explained in Chapter 2, where the forces are derived from the viscoelastic network. The viscoelastic nodes and network introduce viscoelastic behavior into the system to mimic the characteristics of biological fluids, such as cervical mucus, due to the presence of polymer chains.

As explained in the introduction section, the forces within the viscoelastic network are calculated using the following equation [13]:

$$f_s(x_1) = -f_s(x_2) = l_0^2 K \left(\frac{||x_2 - x_1||}{l(t)} - 1 \right) \frac{x_2 - x_1}{||x_2 - x_1||}. \tag{4.5}$$

where $l(t)$ represents the element's resting length, K is the spring stiffness constant, and l_0 is the initial resting length. The resting length dynamically changes, and its time evolution is given by:

$$\frac{dl(t)}{dt} = \frac{K l_0}{\eta} \left(\frac{||x_2 - x_1||}{l(t)} - 1 \right). \tag{4.6}$$

To validate the numerical method and the developed model, we considered a regular unit cubic network constructed of an $8 \times 8 \times 8$ grid, with nodes equally spaced and connected to their neighboring nodes, as illustrated in Figure 4.4. The creep functions for the viscoelastic network, whose top surface is subjected to a unit stress, were then obtained. The response of the network was plotted as a function of time and compared with the results presented in the study by Wróbel et al. [13]. As shown in the figure 4.5, the obtained results has a good agreement with the study by Wróbel et al. [13], to verify our model.

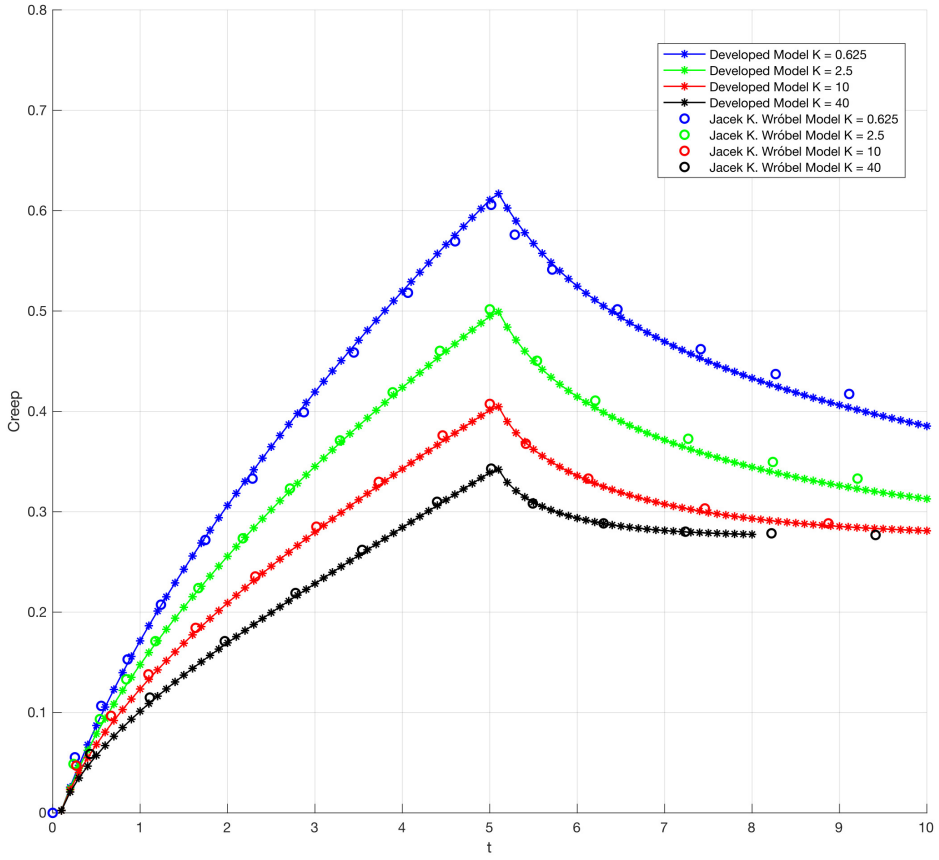


Figure 4.5: Creep functions for the viscoelastic network whose top surface is subjected to a unit stress, with results compared to the study by Wróbel et al. [13], to verify our model.

4.2 Characterization of the developed viscoelastic network

Now we characterize the viscoelastic network we will use in the next section to test the functionality of the designed micro-robot. To examine the effect of different parameters on the characteristics of the network, three parameters were varied. The viscosity of the Newtonian fluid was kept constant and equal to one, normalized to the viscosity of water as explained in the previous chapter for nondimensionalization of the parameters. The elasticity of the

spring used in the Maxwell element and the constant of the dashpot were then varied. Additionally, the number of nodes used in the viscoelastic network cube was also changed. The non-dimensional sides of the cube were set to one. A non-dimensional stress with a magnitude of 0.1 was applied to the top surface of the network, while the bottom surface of the cube was fixed. The resulting creep was plotted as a function of time. The creep function was determined by measuring the average displacement of the nodes on the top surface of the cube relative to the nodes on the bottom surface, in the direction of the applied stress. The strain relaxation time for each case was then determined by fitting an exponential function of the form $a\exp(bt)+c$ to the decreasing section of the curve. The relaxation time was calculated as $\frac{1}{|b|}$.

The simulations were conducted separately for the strain test. In this test, a displacement equal to a quarter of the distance between two adjacent nodes in the viscoelastic network was applied to the nodes at the top surface, while the bottom surface, like in the stress test, was fixed. The average force applied to the nodes at the top surface of the network was then measured. It is worth noting that the force and strains were applied and measured in the x direction as shown in Figure 4.4. The relaxation time of the stress was then calculated. It is important to note that each interior node of the viscoelastic network in both tests is connected to all 26 neighboring nodes with a Maxwell element. Figures 4.6, 4.7, and 4.8 show the effect of the stiffness of the spring, dash-pot constant in the Maxwell element, and the spacing between the viscoelastic nodes on the creep function in the creep test, respectively.

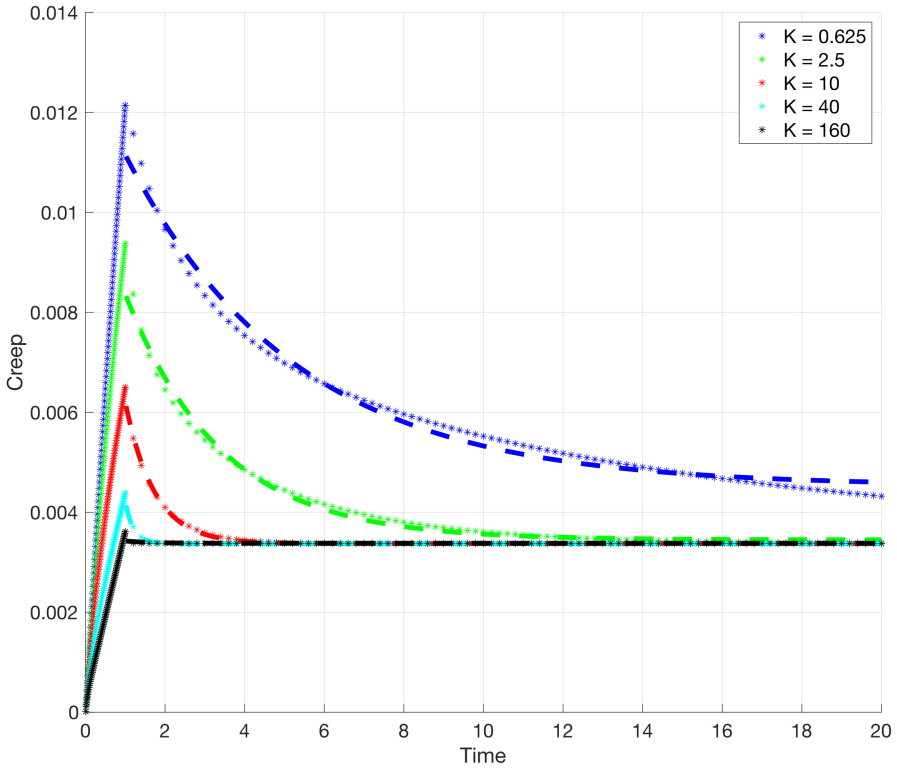


Figure 4.6: Creep functions for the viscoelastic network with the top surface subjected to a stress of 0.1 from time 0 to 1, while varying the spring constant of the Maxwell element. The dashed line represents the exponential curve fitted to the decreasing section of the plot to estimate the relaxation time.

As shown in Figures 4.6, 4.7, and 4.8, a stress is applied for a duration of 1 non-dimensional time, after which it is removed, allowing the cube to reach a steady-state condition. During the application of stress, the creep function increases non-linearly, and after the stress is removed, the creep function decreases. As previously mentioned, to estimate the relaxation time in the viscoelastic network, an exponential function $a\exp(bx) + c$ was fitted to the descending portion of the curve. The relaxation time was then determined as $\frac{1}{|b|}$. Dashed lines in all figures represent these exponential fits, highlighting the relaxation time τ for the strain. It is important to note that when either the stiffness or viscosity of the Maxwell element was varied, the exponential function fit the descending part of the creep curve

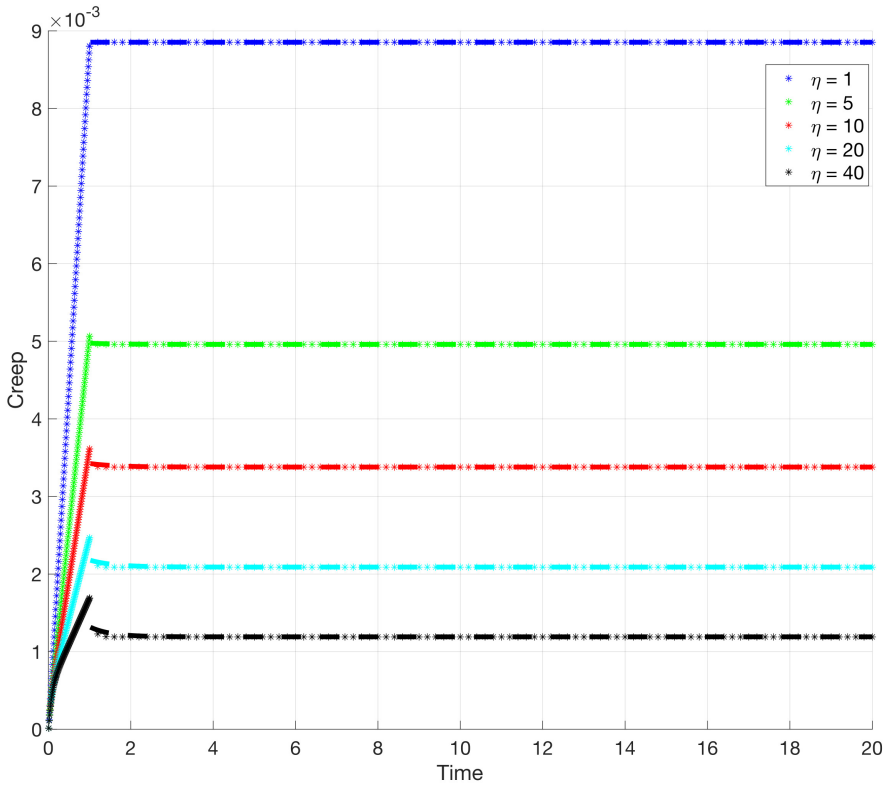


Figure 4.7: Creep functions for the viscoelastic network whose top surface is subjected to a 0.1 stress from time 0 to 1, while the dash-pot constant of the Maxwell element is varied. The dashed line represents the exponential curve fitted to the decreasing section of the plot to estimate the relaxation time.

well, and the relaxation time could be calculated accordingly. However, as seen in Figure 4.8, where the spacing between the viscoelastic nodes was altered, the exponential function does not fit the descending portion of the curve accurately. Consequently, estimating the relaxation time from this fit is not reliable. Therefore, for this figure, a rough estimation based on the percentage of change in the curve over time was employed to approximate the relaxation time. Table 4.1 presents the relaxation time for all the cases discussed above. As interpreted from Table 4.1, increasing the stiffness of the spring results in a decrease in relaxation time, while increasing the dash-pot constant in the Maxwell element results in a decrease in relaxation time.

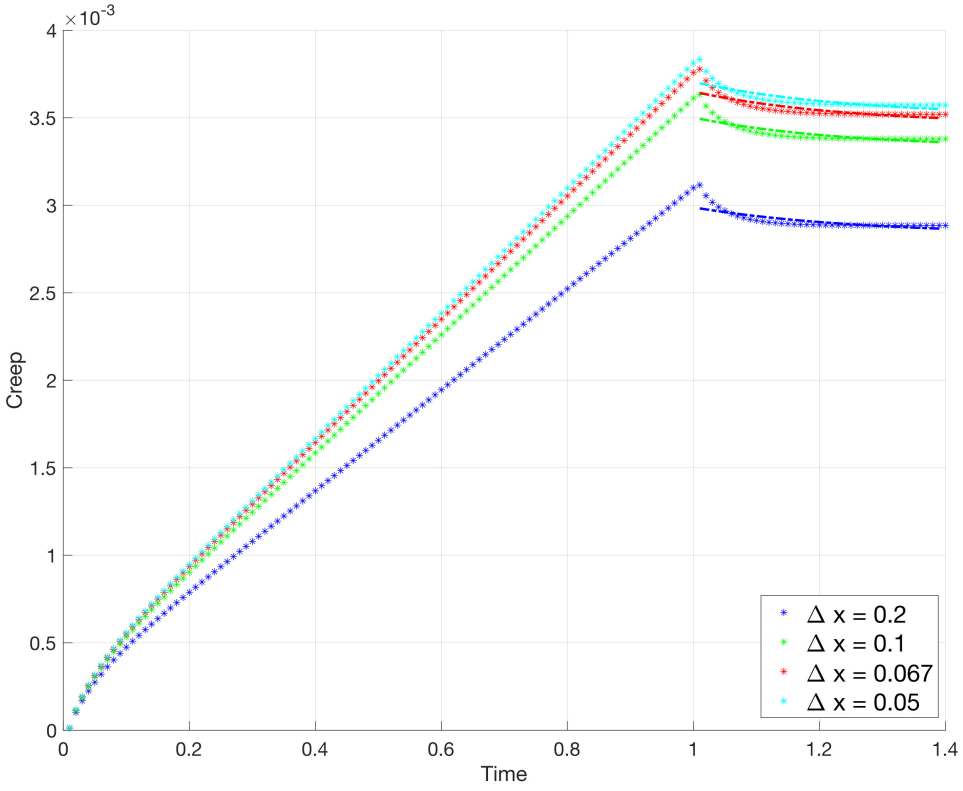


Figure 4.8: Creep functions for the viscoelastic network whose top surface is subjected to a 0.1 stress from 0 to 1, while the spacing between the viscoelastic nodes is varied. The dashed line represents the exponential curve fitted to the decreasing section of the plot to estimate the relaxation time.

Additionally, changing the spacing between the nodes in the viscoelastic network does not significantly affect the relaxation time. The next step is to calculate the relaxation time of the stress in the strain test. Figures 4.9, 4.10, and 4.11 show the effect of the stiffness of the spring, dash-pot constant in the Maxwell element, and the spacing between the viscoelastic nodes on the stress function in the strain test.

Case	K	η	ΔX	ΔY	ΔZ	Relaxation time (τ)
1	0.625	10	0.1	0.1	0.1	4.26
2	2.5	10	0.1	0.1	0.1	2.4
3	10	10	0.1	0.1	0.1	0.75
4	40	10	0.1	0.1	0.1	0.2
5	160	10	0.1	0.1	0.1	0.1
6	160	1	0.1	0.1	0.1	0.02
7	160	5	0.1	0.1	0.1	0.03
8	160	10	0.1	0.1	0.1	0.1
9	160	20	0.1	0.1	0.1	0.5
10	160	40	0.1	0.1	0.1	0.58
11	160	10	0.2	0.2	0.2	0.21
12	160	10	0.1	0.1	0.1	0.22
13	160	10	0.067	0.067	0.067	0.23
14	160	10	0.05	0.05	0.05	0.23

Table 4.1: Relaxation time obtained in the creep test for different cases where the stiffness of the spring and the dashpot constant in the Maxwell element and the spacing between the nodes in the viscoelastic network is varied.

As observed in Figures 4.9, 4.10, and 4.11, increasing the stiffness of the spring increases the relaxation time of the stress, while increasing the dash-pot constant in the Maxwell element does not significantly change the relaxation time. Furthermore, it can be understood that increasing the spacing between the nodes in the viscoelastic network increases the relaxation time of the stress in the strain test.

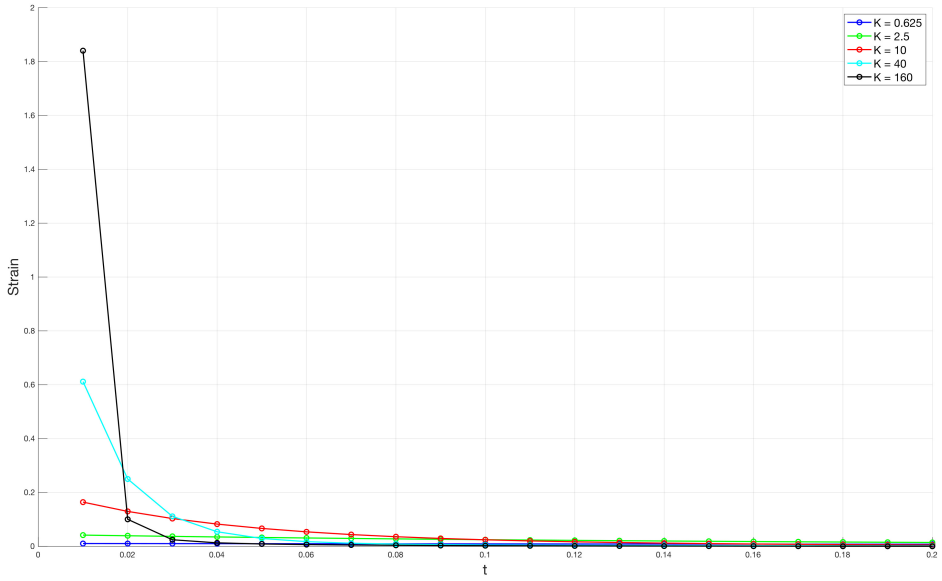


Figure 4.9: Stress functions for the viscoelastic network in the strain test while the spring constant of the Maxwell element is varied.

The next step is to calculate the apparent solvent and solution viscosities, as well as the elasticity, of the designed viscoelastic network. We derived a formula for the relationship between force and strain. According to the formula derived in Equation 4.3, there is a nonlinear relationship between force and strain. As explained previously, the coefficients α, β, and γ are functions of the solvent and solution viscosities and the elasticity of the network. To calculate the equivalent α, β, and γ for the designed viscoelastic network shown in Table 4.2, we apply a sinusoidal stress with a magnitude and frequency of 1 to the top surface of the viscoelastic network in the numerical model developed and explained at the beginning of this section in the x direction, and then measure the average strain on the nodes of the top surface of the network. We then do the same for Equation 4.3, where the force F on the LHS of the equation is the sinusoidal and oscillating force applied to the network in our simulation. We solve the ODE and calculate the strain on the RHS of the equation. For different combinations of α, β, and γ, the obtained strain varies. Therefore, employing a genetic algorithm, we optimized the three parameters α, β, and γ such that the objective function,

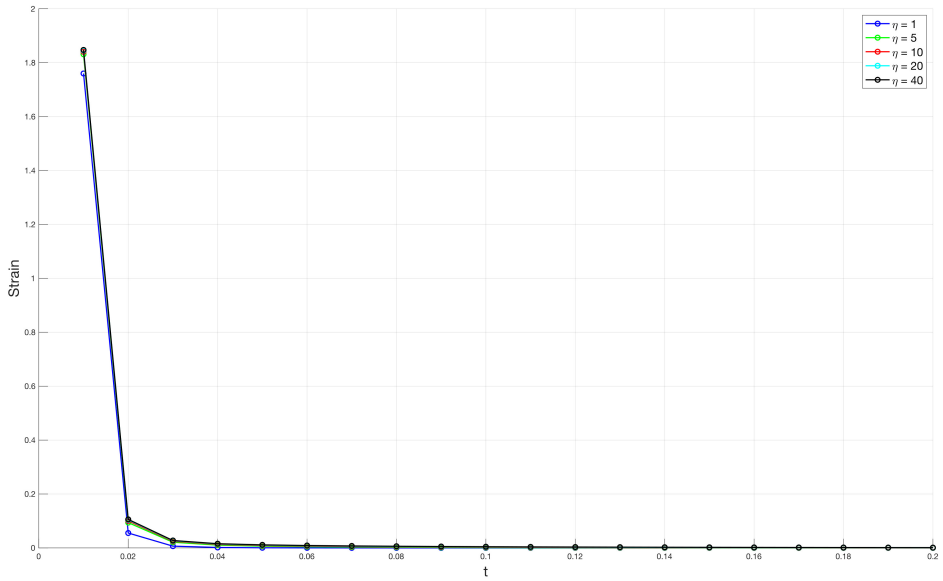


Figure 4.10: Stress functions for the viscoelastic network in the strain test while the dash-pot constant of the Maxwell element is varied.

which is the root mean square (RMS) difference in strain values obtained over time from the analytical expression and the numerical simulation, is minimized. The objective function is given by:

$$\text{Objective function} = \sqrt{\frac{\sum_{i=1}^{N_t} \left(\epsilon_{\text{analytical}}(t_i) - \epsilon_{\text{simulation}}(t_i)\right)^2}{N_t}},$$

where N_t is the number of time steps. Using the genetic algorithm (GA), the three parameters α, β, and γ were obtained for each fluid case shown in Table 4.2, ensuring the best agreement between the simulation results and the analytical solution based on the ODE in Equation 4.3. Finally, the results demonstrated that the ODE can predict the behavior of the viscoelastic network accurately. Thus, based on the obtained values of α, β, and γ for each viscoelastic network, the equivalent solvent and solution viscosities and the elasticity of the network were determined and summarized in Table 4.2. So far, we have utilized creep tests and strain tests to calculate the stress and strain relaxation times of the viscoelastic network. Subsequently, by applying a sinusoidal stress, we characterized the viscoelastic network, and using

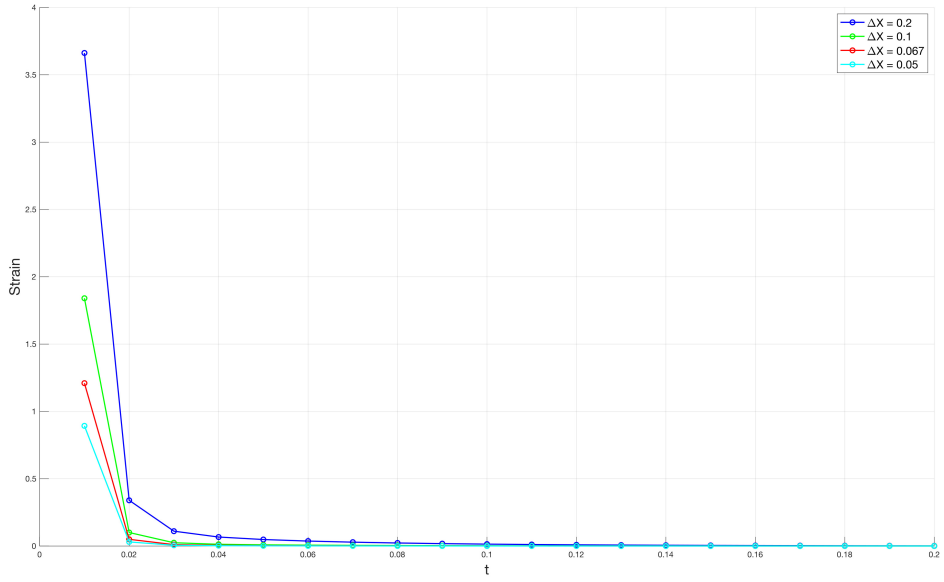


Figure 4.11: Stress functions for the viscoelastic network in the strain test while the spacing between the viscoelastic nodes is varied.

the derived analytical equation 4.3, we obtained the equivalent viscosities η_1 and η_2, as well as the elasticity of the viscoelastic network E. Since the properties of the viscoelastic network do not change with variations in the applied stress on its top surface, it raises the question of whether applying different stress functions to the top surface would yield the same equivalent viscoelastic properties. If this holds true, it would provide stronger evidence that the derived analytical formula accurately describes the behavior of the viscoelastic network. To investigate this, we tested five different stress functions. We used the values of η_1, η_2, and E previously obtained by fitting based on oscillation tests with frequency 1 and compared the behavior of the analytical solution with that of the full numerical simulation of the discrete network under the different testing conditions. This comparison helps to determine whether the derived formula truly represents an accurate differential equation for describing the behavior of the viscoelastic network.

Case	K	η	ΔX	ΔY	ΔZ	α	β	γ	η_1	η_2	E	RMS error
1	0.625	10	0.1	0.1	0.1	5.83	11.78	28	6.98	4.81	1.2	0.033
2	2.5	10	0.1	0.1	0.1	3.37	16.6	17.2	11.51	5.1	3.4	0.0243
3	10	10	0.1	0.1	0.1	1.25	19.5	7.84	13.2	6.27	10.6	0.011
4	40	10	0.1	0.1	0.1	0.495	20.0585	3.9005	12.2	7.88	24.6	0.0043
5	160	10	0.1	0.1	0.1	0.1406	20.028	1.475	9.54	10.5	67.8	0.0026
6	160	1	0.1	0.1	0.1	0.04	9.75	0.34	12.5	8.5	31.3	0.0077
7	160	5	0.1	0.1	0.1	0.1011	17.511	1.1366	6.27	11.2	62	0.0033
8	160	10	0.1	0.1	0.1	0.1409	25.695	1.48	15.2	10.5	108	0.0026
9	160	20	0.1	0.1	0.1	0.2643	41.566	2.655	31.5	10	119	0.0022
10	160	40	0.1	0.1	0.1	0.5202	73	5.1167	63.2	9.84	121	0.0022
11	160.00	10	0.2	0.2	0.2	0.1395	30.0915	1.5792	18.8	11.3	135	0.0022
12	160	10	0.1	0.1	0.1	0.1409	25.695	1.48	15.2	10.5	108	0.0026
13	160	10	0.067	0.067	0.067	0.1406	24.6571	1.4469	14.4	11.03	106.7	0.0018
14	160	10	0.05	0.05	0.05	0.1436	24.3038	1.4814	14	10.74	97.4	0.0007

Table 4.2: Characterizing the fluid and obtaining the apparent solvent and solution viscosities and the elasticity of the viscoelastic network using the oscillation test and comparing the results with the formula derived in Equation 4.3.

As stress creep functions, three sinusoidal forces were applied using the same formula, but with three different frequencies. The sinusoidal equation used is $\sin(2\pi ft)$, where f represents the frequency. In generating table 4.2, a frequency of 1 was employed. Additionally, the new creep functions tested included frequencies of 2, 4, and 8. Furthermore, a linear function $0.1t$ and a constant stress of 0.1 for a duration of time 1 were applied. It is worth noting that for the linear and constant functions, as the force is not sinusoidal and there is a high possibility of significant deformation of the network, the stress functions were applied for a limited time of 1 unit. Figure 4.12 presents the creep functions for all the sinusoidal stress functions with different frequencies, as well as for the linear and constant functions. The results obtained from the simulation of the developed viscoelastic network were compared with the creep functions derived from the analytical equation 4.3. As can be observed, with the values of η_1, η_2, and E obtained and presented in Table 4.2 for the equivalent viscosities and elasticity, the analytical equation accurately predicts the behavior of the developed viscoelastic network.

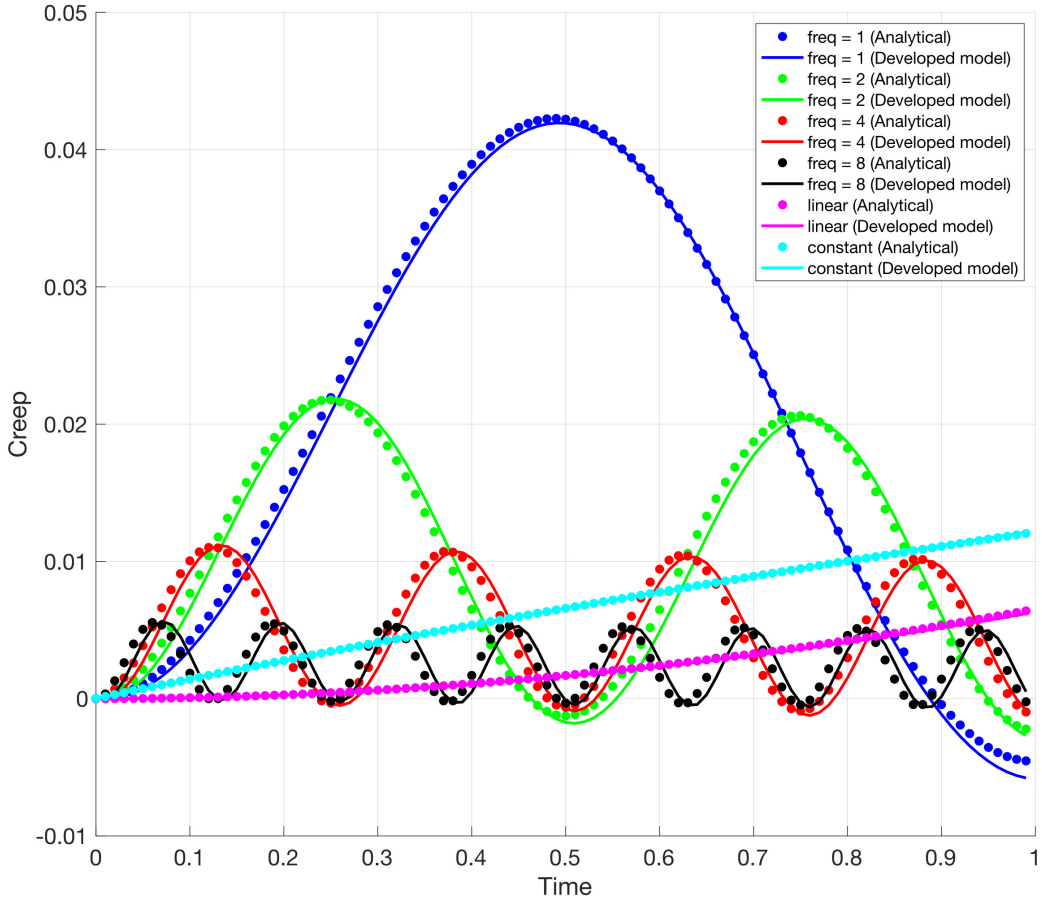


Figure 4.12: Comparison of the creep functions obtained from the simulation of the viscoelastic network and those derived from the analytical equation 4.3. The comparison includes sinusoidal stress functions with frequencies of 1, 2, 4, and 8, as well as linear and constant stress functions.

4.3 Modifying the developed viscoelastic network

In the previous section, a viscoelastic network was created using the Maxwell element and embedded within a Newtonian fluid to impart viscoelastic properties to the resulting fluid. This viscoelastic network was further characterized through creep and strain tests to gain a comprehensive understanding of the influence of the spring and dashpot constants in the Maxwell element, as well as the concentration of the viscoelastic network on the fluid's viscoelastic properties. However, the viscoelastic network model was found to be uniform and homogeneous. In contrast, the network depicted in Figure 4.13 is ultra-structured and heterogeneous. In this section, an ultra-structured and heterogeneous viscoelastic network is proposed, and the relaxation time of strain is obtained for different spring stiffnesses and dashpot constants. This approach aims to provide a more realistic representation of the complex and heterogeneous nature of viscoelastic networks observed in biological systems, thereby enhancing the predictive capability and applicability of the simulated fluid models. To incorporate the viscoelastic properties into the fluid, we utilize the viscoelastic network generated and characterized in the previous section. This network is also employed to evaluate the performance and physics of a helical micro-robot inside the viscoelastic fluid. However, to better mimic the heterogeneous and ultra-structured properties of the viscoelastic fluid, some modifications are applied to the previous network. As shown previously in Figure 4.13, polymer fibers in biological fluid are heterogeneous, forming networks that create void spaces allowing the robot to navigate through. The length of the fibers in these networks is relatively large compared to the void space between them.

To simulate the behavior of these networks accurately, we must ensure the network is heterogeneous and that each pair of nodes in the viscoelastic network is connected via multiple intermediary nodes. This approach accounts for the bending and deformation of the links connecting the nodes, as illustrated in Figure 4.13. To modify the network shown in Figure 4.4 to better mimic the behavior depicted in Figure 4.13, we implemented three key modifications: making the network heterogeneous, ensuring the links between nodes are deformable, and varying the concentration of the viscoelastic network to reflect the diversity encountered by microorganisms moving through biological fluids. To create the modified viscoelastic network based on these

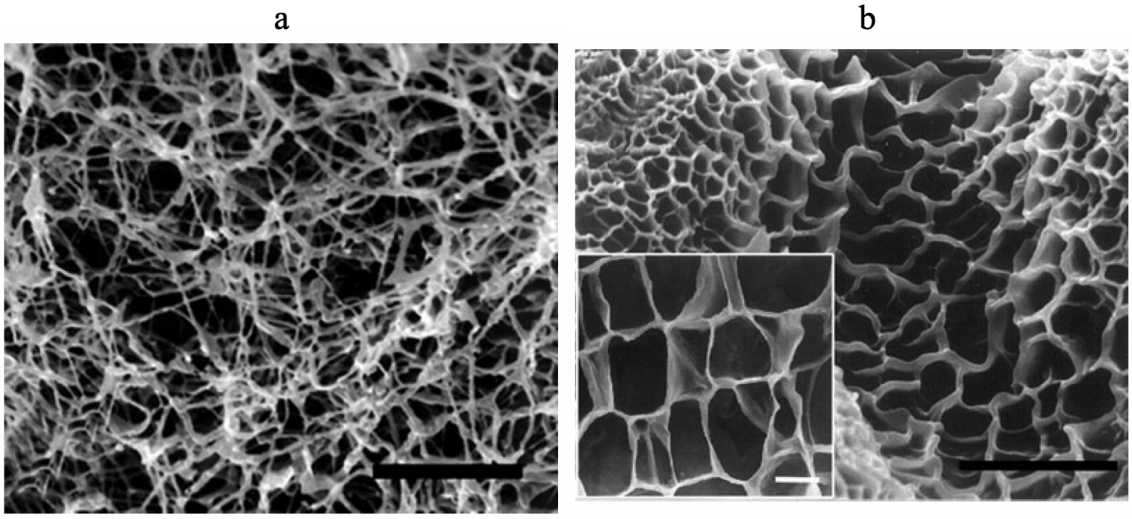


Figure 4.13: a) Scanning electron micrograph of a freeze-dried bovine vaginal fluid sample. Scale bar = $5\mu m$. b) Scanning electron micrograph of a freeze-dried bovine vaginal fluid sample considered to be an artifact. Scale bar = $25\mu m$, and insert $7.5\mu m$. Both figures adapted from Ref [14].

requirements, we first generate the initial network shown in Figure 4.4. A fraction of the links is then randomly removed to adjust the polymer concentration, ensuring heterogeneity. For example, in one scenario, 40% of the links were removed randomly. The nodes are randomly removed to ensure the heterogeneity of the final network. To make the remaining links deformable, five intermediary nodes are added between each pair of connected nodes, and all nodes are connected through a spring and dashpot (Maxwell element). This process allows us to control the polymer concentration by varying the percentage of links removed, while the addition of intermediary nodes ensures the deformability of the links.

We studied four different concentrations by removing 40%, 50%, 60%, and 70% of the links. A network with dimensions 1 (width) by 1 (depth) by 3 (length) along the x, y, and z axes was created. The minimum distance between neighboring nodes in the x, y, and z directions is 0.05. Thus, the network size is $45\mu m \times 45\mu m \times 135\mu m$, with the distance between neighboring nodes being $2.25\mu m$. In Figure 4.14, we present one of the created viscoelastic networks where 50% of the links are removed.

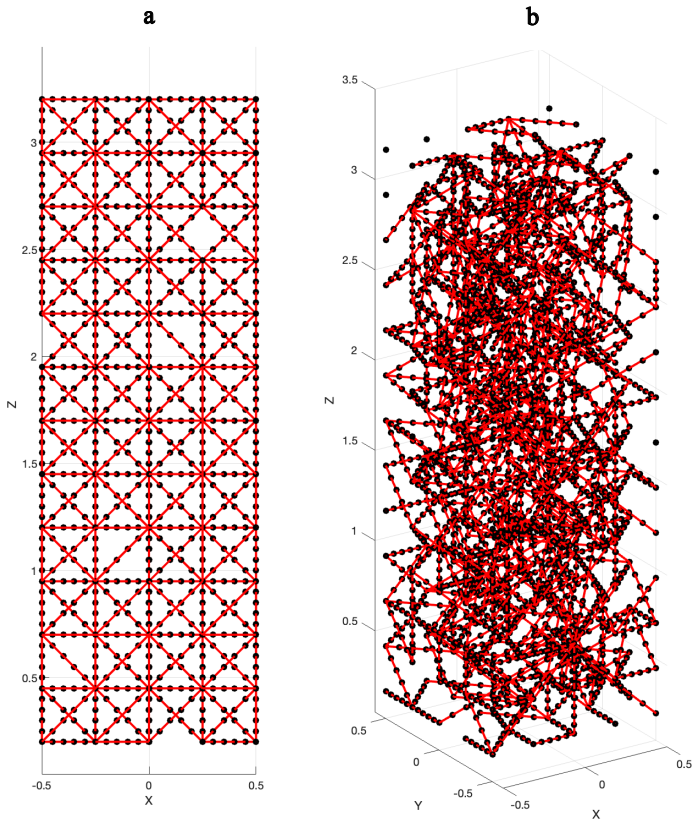


Figure 4.14: Viscoelastic network with 50% of the links removed, showing the heterogeneity of the network from two different views.

This is the size of the network we utilized to simulate the motion of a helical micro-robot through a viscoelastic fluid. Subsequently, we characterized the created viscoelastic fluid using a creep test. As described in the previous chapter, we first created a cube with a side length of 1. To maintain the same spacing between the nodes as in our viscoelastic network illustrated in Figure 4.14, the network was initially generated with $5 \times 5 \times 5$ nodes, and all neighboring nodes were connected through links. A percentage of the links were then randomly selected and removed. For the remaining links, five intermediary nodes were added, and all nodes were connected through springs and dashpots (Maxwell elements).

We aimed to study the effect of the stiffness of the spring, the dashpot constant, and the concentration of the viscoelastic network on the relaxation

time of the strain in the creep test. Therefore, a 0.1 non-dimensional stress was applied to the top surface of the unit cube while the bottom of the cube was fixed for a duration of 1 non-dimensional time. The stress was then removed, as in the creep test described in the previous section, and the relaxation time of the network was estimated using the fitting exponential function as explained in the previous section. To study the effect of spring stiffness, we tested springs with stiffness values of 0.625, 2.5, 10, 40, and 160 and obtained and compared the relaxation times. Then, the dashpot constant was varied with values of 1, 5, 10, 20, and 40, and the relaxation time was obtained and compared for each case. For all these simulations, the fraction of removed links was kept constant at 50%, and the viscosity of the fluid was set to 1. Finally, to investigate the effect of the concentration of the viscoelastic network on the relaxation time of the strain, we removed 40%, 50%, 60%, and 70% of the links in different simulations. The following figures show the creep function plotted versus time for different spring stiffnesses, dashpot constants, and concentrations of the viscoelastic network. Figures 4.15, 4.16, and 4.17 show the effect of the stiffness of the spring, the dashpot constant in the Maxwell element, and the fraction of the removed links on the creep function in the creep test. It is worth noting that a smaller fraction of removed links means a higher concentration of the viscoelastic network.

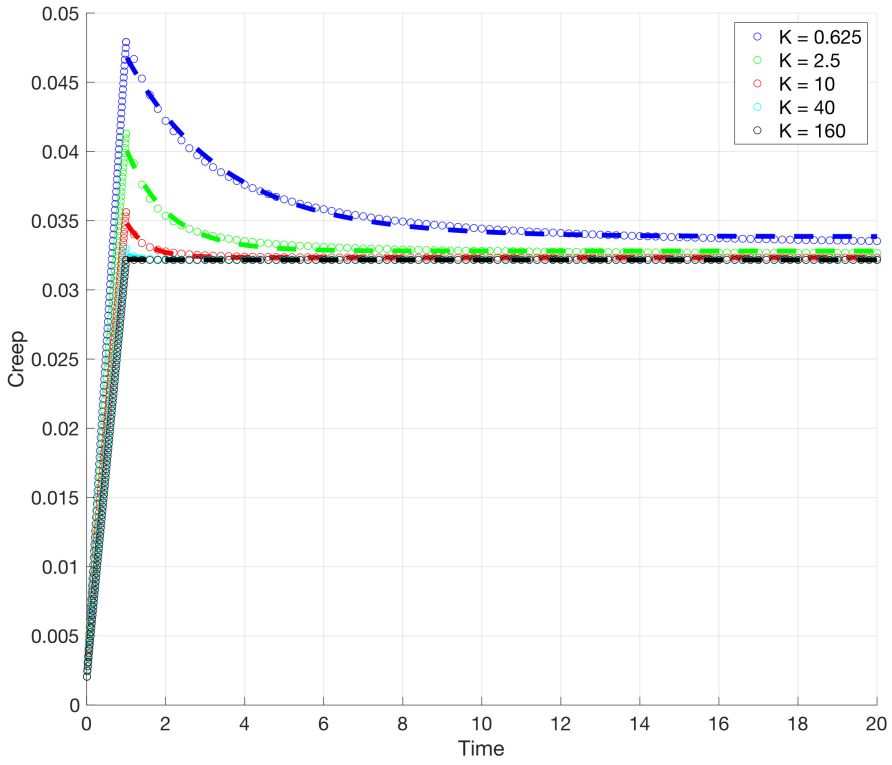


Figure 4.15: Creep functions for the viscoelastic network whose top surface is subjected to a 0.1 stress while the spring constant of the Maxwell element is varied. The dashed line represents the exponential curve fitted to the decreasing section of the plot to estimate the relaxation time.

As shown in Figures 4.15, 4.16, and 4.17, for a duration of 1 non-dimensional time, the stress is applied and then removed, allowing the cube to reach its steady-state situation. During the application of stress, the creep function increases non-linearly, and upon removal of the stress, the creep function decreases. Table 4.3 presents the relaxation time for all the cases discussed above. As interpreted from Table 4.3, increasing the stiffness of the spring results in a decrease in relaxation time, while increasing the dashpot constant in the Maxwell element results in a decrease in relaxation time. Additionally, increasing the concentration of the viscoelastic network by reducing the fraction of removed links increases the relaxation time.

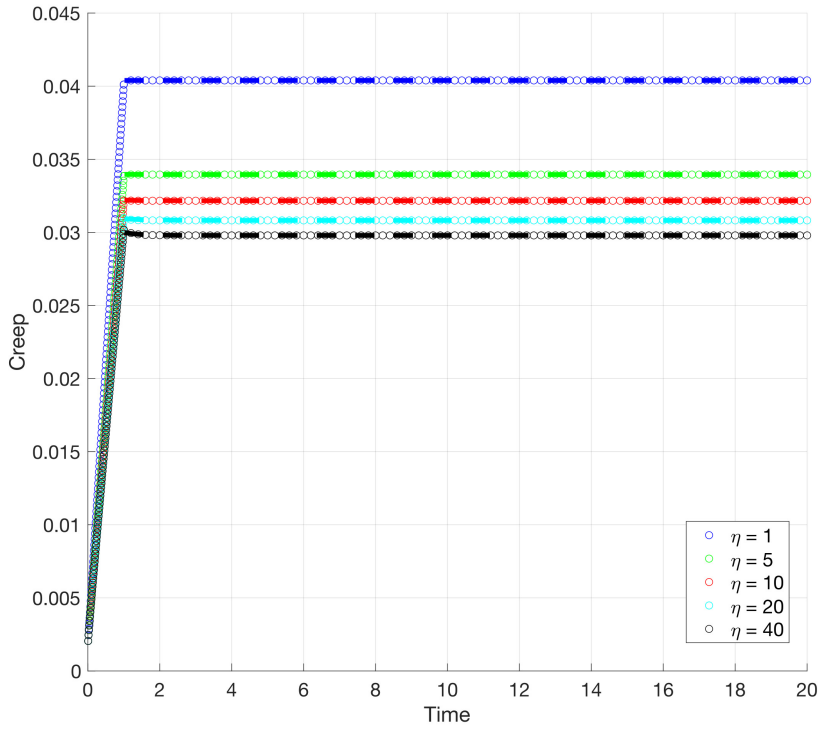


Figure 4.16: Creep functions for the viscoelastic network whose top surface is subjected to a 0.1 stress while the dashpot constant of the Maxwell element is varied. The dashed line represents the exponential curve fitted to the decreasing section of the plot to estimate the relaxation time.

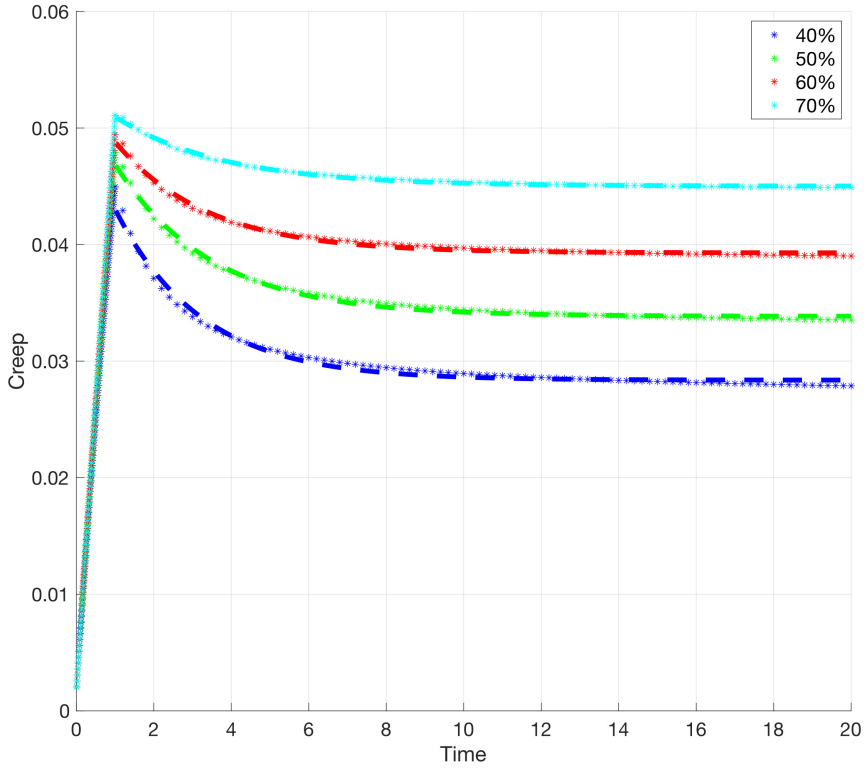


Figure 4.17: Creep functions for the viscoelastic network whose top surface is subjected to a 0.1 stress while the concentration of the viscoelastic network is varied by changing the fraction of links removed. The dashed line represents the exponential curve fitted to the decreasing section of the plot to estimate the relaxation time.

Case	K	η	Fraction of removed links	Relaxation time (τ)
1	0.625	10	50%	3.5
2	2.5	10	50%	1.6
3	10	10	50%	0.6
4	40	10	50%	0.05
5	160	10	50%	0.03
6	160	1	50%	0.05
7	160	5	50%	0.04
8	160	10	50%	0.03
9	160	20	50%	0.02
10	160	40	50%	0.02
11	0.625	10	40%	4.5
12	0.625	10	50%	3.5
13	0.625	10	60%	2.8
14	0.625	10	70%	2.3

Table 4.3: Relaxation time (τ) for different cases with varying spring stiffness (K), dashpot constant (η), and fraction of removed links in the viscoelastic network.

As the next step, similar to the previous section, we aimed to calculate the equivalent flexibility and viscosity of the viscoelastic network using the cyclic test and by comparing it with the analytical solution provided in Equation 4.3. However, the analytical equation was derived under the assumption that the viscoelastic network is fully connected. When a fraction of the links is removed and additional nodes are introduced to create a heterogeneous network, the system's behavior under cyclic force application changes. Consequently, determining the desired parameters α, β, and γ to achieve a close agreement with the simulation results proved to be unsuccessful.

In Figure 4.18b, the creep function of a viscoelastic network is plotted as a function of time, with $K = 0.625$, $\eta = 10$, and 40% of the links removed. The cyclic force $\sin(2\pi t)$ is applied to the top surface of the network, and the creep function is represented by the orange line. The parameters α, β, and γ were optimized to minimize the error between the creep function derived from Equation 4.3 and the one obtained from the simulation. However, as illustrated in Figure 4.18b, there is a significant discrepancy between the two curves, indicating that the analytical formula cannot accurately predict the behavior of the heterogeneous viscoelastic network. The prediction error in this case was 0.24. In contrast, Figure 4.18a shows the application of the analytical equation to predict the behavior of a fully connected viscoelastic network, resulting in a prediction error of 0.033. This demonstrates that while the analytical equation is highly effective in predicting the behavior of a fully connected network, its accuracy diminishes when a significant fraction of links is removed and additional viscoelastic nodes and links are added, depending on the extent of network modification. Thus, using the method from the previous section to find the equivalent viscosity and elasticity for these cases is not feasible.

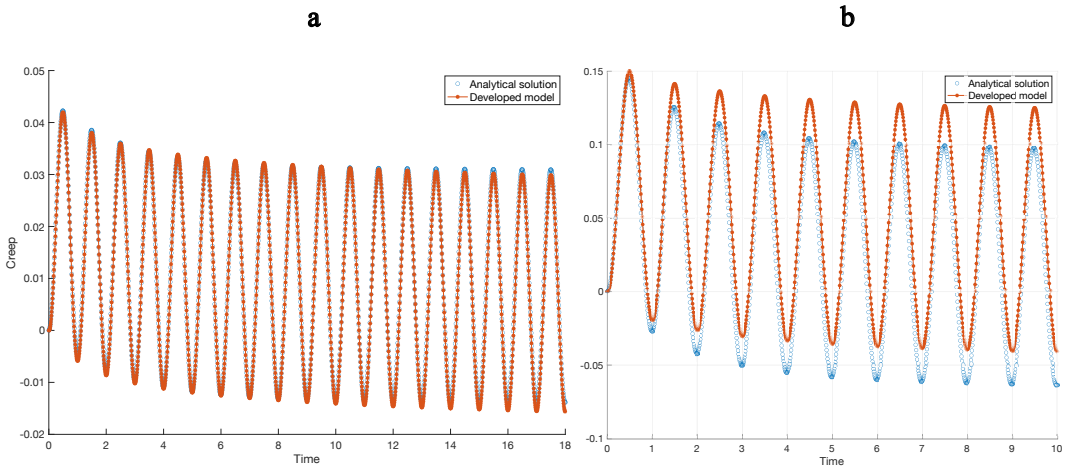


Figure 4.18: Creep functions for a viscoelastic network with $K = 0.625$ and $\eta = 10$ under a cyclic force $\sin(2\pi t)$ applied to the top surface: (a) fully connected network and (b) heterogeneous network with 40% of the links randomly removed.

Chapter 5

Motion of micro-robot in a viscoelastic fluid

5.1 Introduction

Microorganisms typically move through complex biological environments which contain high-molecular-weight polymeric material. Examples include mammalian spermatozoa swimming in viscoelastic mucus in the cervix or along the fallopian tubes [64], the bacterium Helicobacter pylori moving through the mucus layer covering the stomach and causing ulcers [68], the Lyme disease spirochete Borrelia burgdorferi penetrating the connective tissues in our skin [70], and bacteria producing extracellular polymeric substances (EPS) and forming biofilms [136]. Most biological fluids such as cervical mucus and vitreous humor are viscoelastic due to the presence of high-molecular-weight polymeric materials.

As shown in Figure 4.1a, viscoelastic fluids such as cervical mucus exhibit complex microstructural properties that influence microorganism motility. The movement of microorganisms and sperm cells within these viscoelastic fluids plays a pivotal role in numerous biological functions, including fertilization, infection, and the development of biofilms. As explained in the introduction section, to simulate microswimming in a viscoelastic fluid, various approaches, including continuum and non-continuum models, have been proposed. Depending on the Knudsen number (Kn), as defined earlier in the introduction section (equation 1.11), which captures the non-continuum as-

pects of the medium, and considering the size of dispersed phases relative to the swimming flow length scale, different approaches can be employed. For instance, $\mathrm{Kn}_f \ll 1$ indicates that the fluid can be modeled as a continuum; otherwise, the microstructural details become significant.

In the continuum approach, the viscoelastic properties are considered homogeneous at the microscale size and the scale size of the microswimmer. When the continuum approach is chosen, different constitutive equation models can be employed to model microswimming in polymeric fluids, including Oldroyd-B, Giesekus, and FENE models [137, 138, 139]. While many studies model complex fluids as continuum media, it is important to realize that most biological examples are highly heterogeneous at the microscopic scale [91]. Many microorganisms experience a biological environment of entangled fibers around 10–100 nm in diameter and pores ranging in size from 0.1 to 1 μm [92].

In this study, the motion of a micro-robot designed for transporting immotile sperm is being investigated. As discussed in Chapter 3, the size of designed micro-robot is based on the length and diameter of sperm, and the cervical mucus through which the sperm is swimming is a non-continuum fluid based on the pore size between the polymer fibers [14]. According to the study by Rutllant et al. on the ultrastructural and rheological properties of bovine vaginal fluid, the structure of polymers within bovine vaginal fluid, particularly the filamentous and fibrous components, reveals a complex and dynamic arrangement critical for sperm transport [14]. The vaginal fluid is primarily composed of mucins, which form a three-dimensional network that provides the gel-like properties of the fluid. These mucins are macromolecular glycoproteins secreted by the cervical epithelium, with a structure consisting of a polypeptide backbone and numerous heterosaccharide side chains. The filamentous network in bovine vaginal fluid varies significantly in size and structure depending on the phase of the ovarian cycle. During the estrogenic (follicular) phase, the network features larger intermicellar spaces, averaging 1–10 micrometers (μm), which facilitate sperm movement. In contrast, during the luteal phase under progestational influence, these spaces reduce to fractions of 1 μm, creating a denser network that impedes sperm penetration. Therefore, for the designed helical micro-robot discussed in Chapter 3, the viscoelastic fluid inside the vaginal fluid is considered non-continuum.

5.2 Geometry and mechanical/viscoelastic properties of the helical micro-robot and viscoelastic network fluid

In Chapter 3, the transportation of filamentous micro-cargo using a designed helical micro-robot was simulated in a Newtonian fluid. However, the biological fluid in which most microorganisms swim is a viscoelastic fluid. Therefore, in this chapter, the motion of the designed micro-robot in viscoelastic fluid is studied. One of the primary reasons for designing this micro-robot was to transport immotile sperm. Hence, it is essential to ensure that, firstly, the sizes of the designed micro-robot are consistent with those described in Chapter 3 and, secondly, that the viscoelastic fluid properties are compatible with cervical mucus.

Similar to Chapter 3, we non-dimensionalize all variables throughout this chapter using the characteristic length scale $\hat{l} = 45$ µm, the viscosity of water $\mu = 0.001$ Pa s, and the density scale $\rho = 1000$ kg m^{-3}, corresponding to the density of water. Additionally, in most of the simulations performed in this study, the rotational frequency, as represented by Equation 3.6, is fixed at $f = 0.15$ in dimensionless units. With our non-dimensionalization, this corresponds to 50 Hz, a frequency used in past experiments by Medina-Sánchez et al.[4]. We set the maximum magnitude of the non-dimensional magnetic torque to $T|\vec{m}| = 65$, which corresponds to 3×10^{-12} N $\cdot$ m. This value is selected based on the structural properties and materials of the micro-helices, as well as experimentally achievable magnetic field strengths. Additionally, the frequency is fixed at $f = 0.15$, and the magnetic field is held constant throughout.

Two different helical micro-robots are tested in this simulation: one with single handedness and one with three helices of alternating handedness, similar to Chapter 3. The micro-robot with three helices is particularly functional for the contactless transportation of filamentous micro-cargo. For the micro-robot with single handedness, we use $N_\lambda = 8$ windings, pitch $\lambda = 0.15$, radius $R = 0.08$, and cross-sectional radius $r = 0.005$ for the helix. For the micro-robot with three helices, we use $N_\lambda = 10$ windings, pitch $\lambda = 0.15$, radius $R = 0.08$, and cross-sectional radius $r = 0.005$ for the helix. Figure 5.1 shows the two micro-robots. As shown previously in Figure 4.13, polymer fibers in biological fluid are heterogeneous, forming networks that

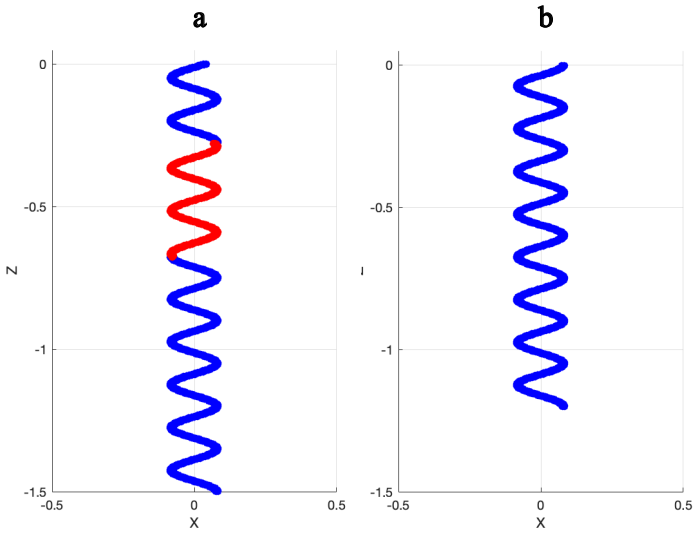


Figure 5.1: Helical micro-robots used in the simulation: (a) Micro-robot with single handedness, (b) Micro-robot with three helices of alternating handedness.

create void spaces allowing the robot to navigate through. The length of the fibers in these networks is relatively large compared to the void space between them. In Section 4.3, a viscoelastic network inspired by the heterogeneous structure of bovine vaginal fluid was developed to better mimic the heterogeneous and ultra-structured properties of the viscoelastic fluid. This network is employed to evaluate the performance and physics of a helical micro-robot inside the viscoelastic fluid.

To mimic the behavior of the non-continuum viscoelastic network, we ensured that the modified viscoelastic network incorporates three key features: heterogeneity, deformable links between nodes, and variable concentration to reflect the diversity encountered by microorganisms in biological fluids. In the following sections, we evaluate the performance of the designed micro-robot (Figure 5.1) as it navigates the heterogeneous viscoelastic network, previously described in Section 4.3.

5.3 Locomotion of helical magnetic micro-robot in a viscoelastic network

In this section, the locomotion of a helical magnetic micro-robot in a viscoelastic fluid is studied. In Chapter 3, we improved the design of the helical micro-robot by adding a pushing micro-helix to the middle of the micro-robot to enable the transport of filamentous microcargo without any contact. As discussed in Chapter 3, the novel micro-robot design with two different handedness can carry filamentous microcargo, such as immotile sperm or bacteria, in the fluid without contact, preventing adhesion and making the release of the microcargo at the final destination easier. However, in most biological fluids where sperm and bacteria must be transported, the fluid is viscoelastic. Therefore, it is crucial to understand how the helical magnetic micro-robot moves in a viscoelastic fluid and how the novel helical micro-robot with two different handedness performs in the viscoelastic fluid compared to the helical micro-robot with a single handedness. Additionally, we compare the performance of both micro-robots (with single and double handedness) in viscoelastic fluid to their performance in Newtonian fluid.

In this section, a finite piece of heterogeneous ultra-structured viscoelastic network, as introduced in Section 5.2, is generated with different concentrations of the viscoelastic network, and the locomotion of the helical micro-robot through the network is studied. We perform simulations with the helical micro-robot starting outside the viscoelastic network and analyze the processes of entering, swimming through, and exiting the network. All of these stages are important and physically relevant.

We first characterize the behaviour of the two micro-robots shown in Figure 5.1 as they separately swim through the viscoelastic network, focusing on their z-velocities as a measure of their performance. Subsequently, we examine the influence of various properties of the network by varying the fraction of the removed links in the network, the stiffness of the spring in the Maxwell element, and the dashpot constant.

5.3.1 Behaviour of helical micro-robots passing through a viscoelastic network

In this section, we examine the motion of two helical micro-robots, introduced in Figure 5.1, within a viscoelastic network. Initially, the micro-robots are positioned outside of the network, as shown in Figure 5.2. Using a magnetic field, the robots are rotated and move in the z-direction through the viscoelastic network.

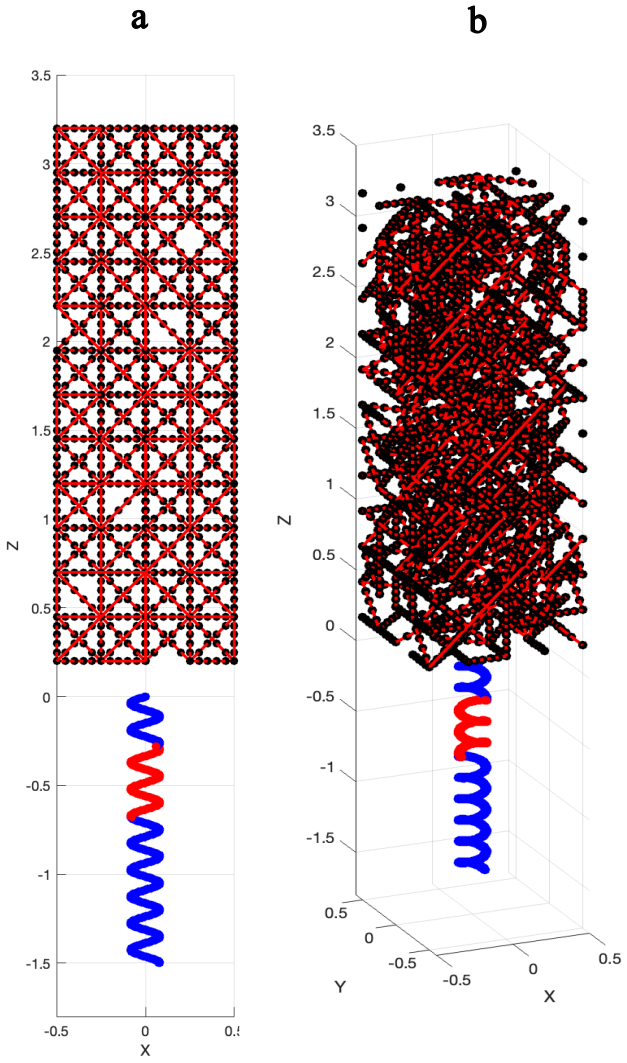


Figure 5.2: Two views of the initial configuration of the viscoelastic network and location of the micro-robot before entering the viscoelastic network.

We do not alter the viscoelastic properties of the network for this analysis. For a specific set of viscoelastic properties listed in Table 4.3, both micro-robots are tested. We study the pattern of the viscoelastic network nodes and links surrounding the micro-robots, comparing their performance to that in a Newtonian fluid and to each other. As an initial step, we examine the ve-

locity of the micro-robots in the z-direction, normalized by their Newtonian velocity over time. The viscoelastic network that is studied in this section has a spring stiffness of 0.625, a dashpot constant of 10, and 50% of the links removed. In Figures 5.3 and 5.4, the normalized velocity of the micro-robots with single handedness and with three helices with two handedness, relative to their velocity in Newtonian fluid, is plotted versus time. Initially, as both micro-robots start their motion from outside the viscoelastic network, the normalized velocity is very close to 1, indicating that the velocity is almost the same as in Newtonian fluid, showing that the viscoelastic network has not yet influenced the micro-robots. The red vertical lines indicate where the micro-robots enter and exit the viscoelastic network. Upon approaching and entering the viscoelastic network, the velocity of the micro-robot with single handedness increases, while the velocity of the micro-robot with three helices decreases. As the viscoelastic network is finite, initial end effects are observed, but when the micro-robot is at the center of the viscoelastic network, the velocity reaches an almost steady value. Although the velocity never completely stops oscillating due to the heterogeneous nature of the viscoelastic network, an average velocity can still be reported. This steady value is more observable for the micro-robot with single handedness. For the micro-robot with single handedness, when it exits the viscoelastic network, the velocity returns to 1. As the micro-robot approaches the exit, the velocity decreases, and finally, when the micro-robot exits the network, the normalized velocity returns to 1, indicating that the effect of the viscoelastic network has disappeared. However, for the micro-robot with three helices, the situation is different. The velocity of the micro-robot decreases, with this decrease slowing when the micro-robot is at the center of the viscoelastic network. When the micro-robot exits the network, the velocity does not return to 1 as it did for the micro-robot with single handedness. This shows that even after exiting the viscoelastic network, the effect of the viscoelastic network persists. The reason for this, as shown in Figure 5.8, is that the micro-robot with three helices transports some of the viscoelastic nodes with it, so even after exiting the viscoelastic region, the effect of the viscoelastic network remains. For this viscoelastic network, the velocity of the micro-robot with single handedness reaches 1.25 times its velocity in Newtonian fluid, while the velocity of the micro-robot with three helices and two different handedness reaches 0.4 times its velocity in Newtonian fluid.

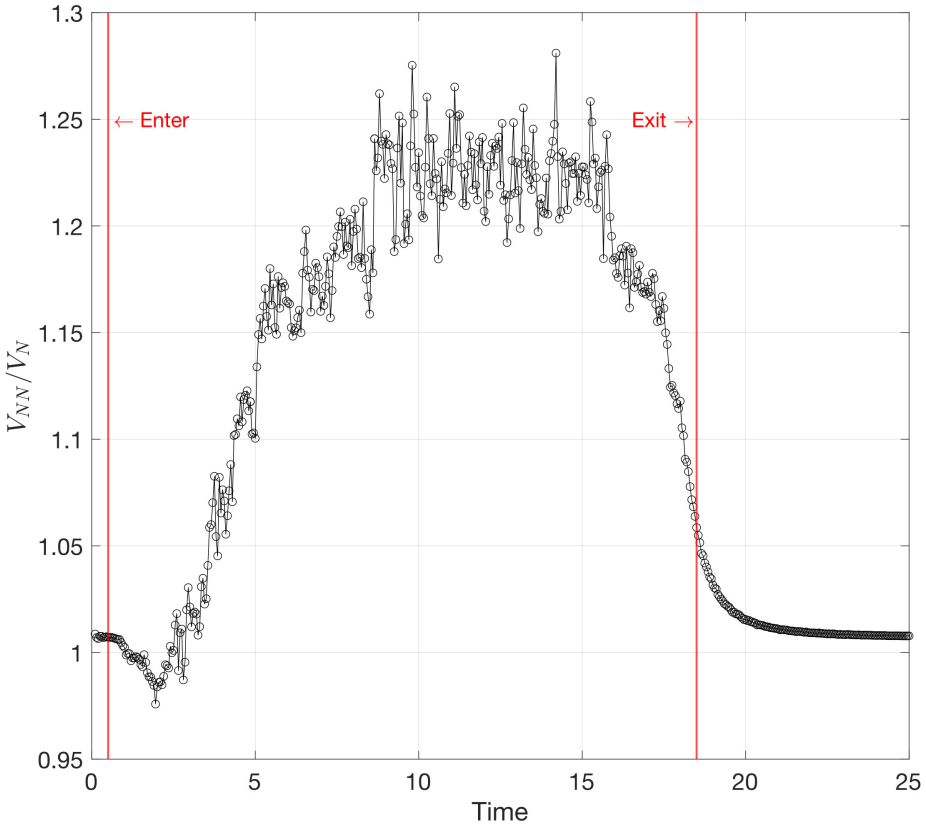


Figure 5.3: Normalized velocity of the micro-robot with single handedness in a viscoelastic fluid compared to its velocity in a Newtonian fluid versus time. Red vertical lines indicate where the micro-robots enter and exit the viscoelastic network.

The observed increase in the velocity of a single-handedness micro-robot in viscoelastic fluid, compared to Newtonian fluid, is consistent with the existing literature. As discussed in Sections 1.5.1 and 1.5.2, the behavior of a micro-swimmer in viscoelastic fluids varies based on its shape and propulsion method. While some cases show a decrease in velocity, others show an increase. However, Mahdy et al. found that the velocity of a magnetic helical micro-robot propelled by a rotating magnetic field increases with the fluid's viscoelasticity, which aligns with the results of this thesis[140]. To improve our understanding of the physics of helical micro-robots in a viscoelastic net-

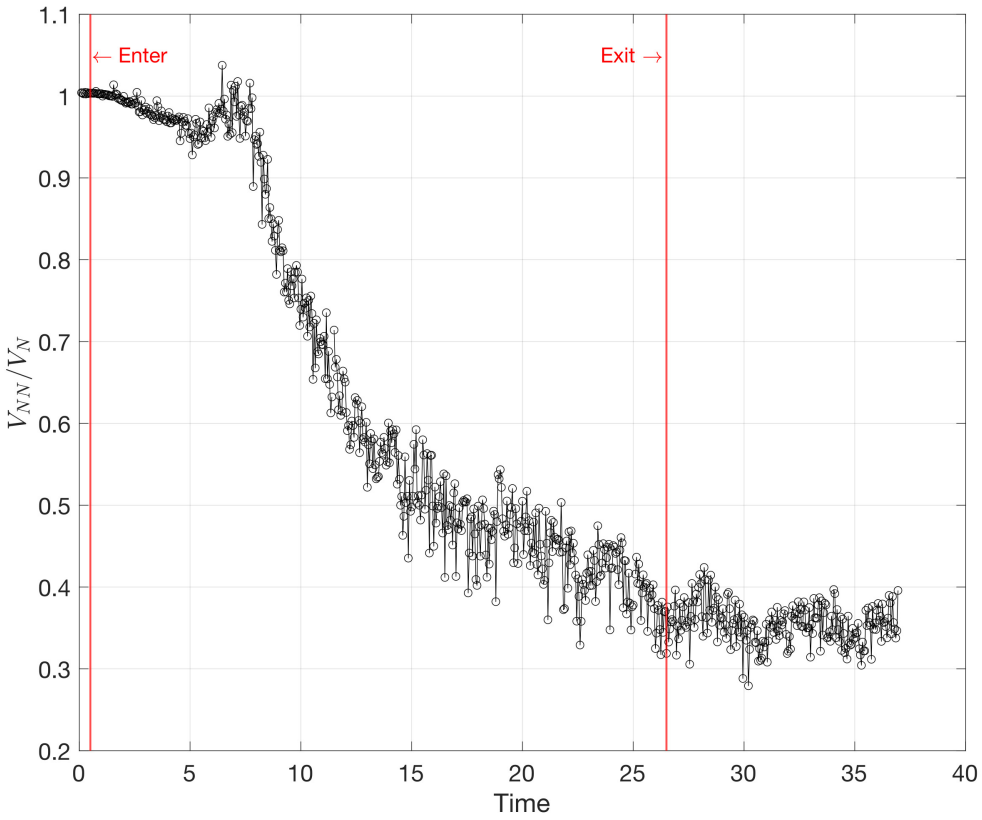


Figure 5.4: Normalized velocity of the micro-robot with three helices and two different handedness in a viscoelastic fluid compared to its velocity in a Newtonian fluid versus time. Red vertical lines indicate where the micro-robots enter and exit the viscoelastic network.

work, the streamline of the fluid around the micro-robot while it is inside and at the middle of the viscoelastic network is plotted in Figures 5.5 and 5.6.

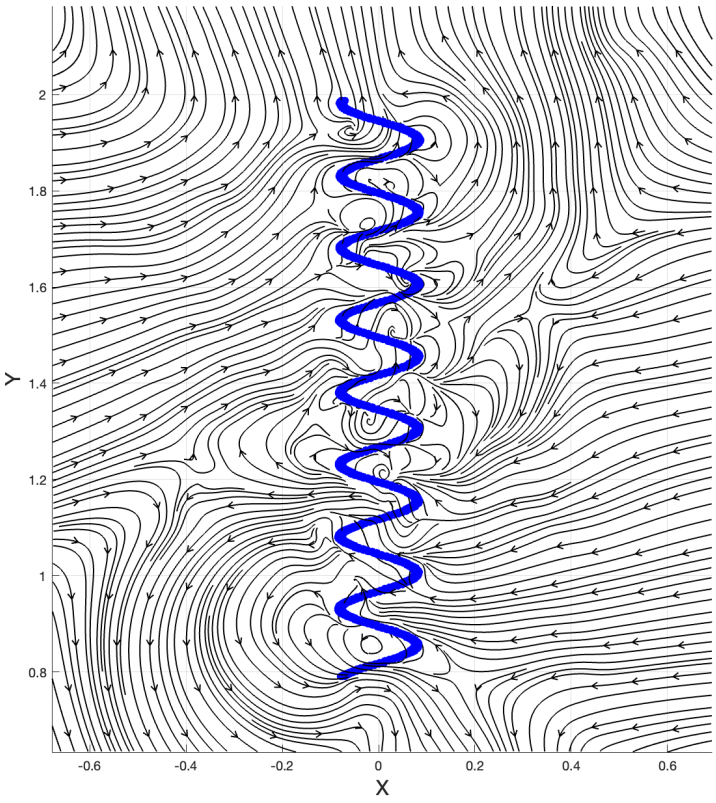


Figure 5.5: Streamline of the fluid around the micro-robot with single handedness while the micro-robot is at the middle of the viscoelastic network.

As shown in Figures 5.5 and 5.6, the streamline and the velocity field around the micro-robot in a viscoelastic network is very similar to the velocity field in Newtonian fluid, as shown in Chapter 3. As discussed before in Chapter 3, adding the pushing micro-helix to the middle of the micro-robot with three helices creates a zone inside the micro-robot that pushes the fluid forward rather than backward, as in a micro-robot with three handedness. This specific feature, as discussed in Chapter 3, helped us transport filamentous micro-cargo without contact. This feature also causes different behavior in the micro-robot with three helices compared to the micro-robot with single handedness. We further explain how this feature causes the velocity of the micro-robot with three helices and two different handedness to decrease in the viscoelastic network compared to its velocity in Newtonian fluid, while

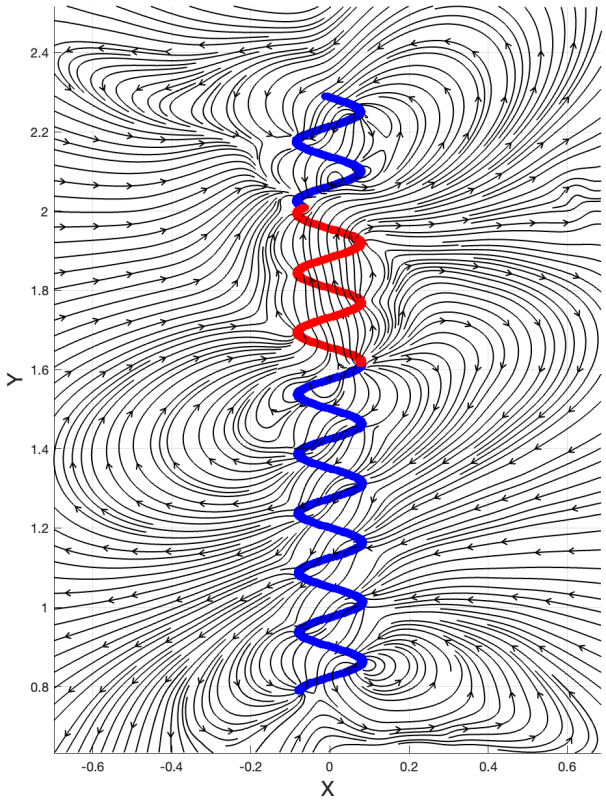


Figure 5.6: Streamline of the fluid around the micro-robot with three helices and two different handedness while the micro-robot is at the middle of the viscoelastic network.

the velocity of the micro-robot with single handedness increases.

To better understand the increase in velocity of the micro-robot with single handedness in a viscoelastic network compared to Newtonian fluid, and the decrease in velocity of the micro-robot with three helices and two different handedness, we examine two different times during the micro-robot's motion through the viscoelastic network: when the micro-robot is inside the network and when it is exiting the network.

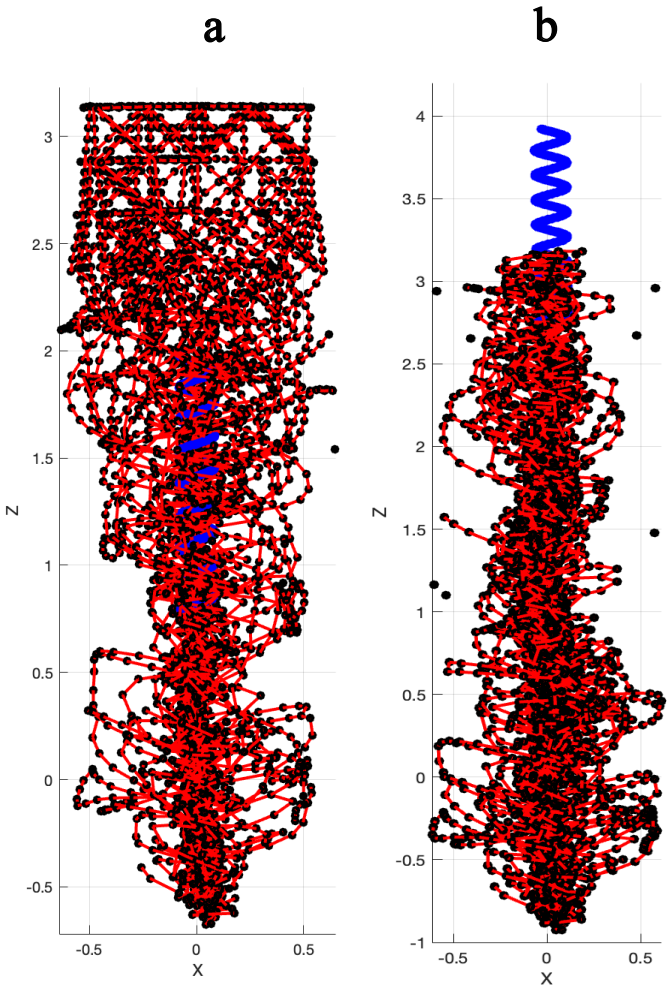


Figure 5.7: Helical micro-robot with single handedness a) inside the viscoelastic network and b) while it is exiting the network.

In Figures 5.7a and 5.8a, the micro-robots are at the center of the viscoelastic network. The main difference observed here is that for the micro-robot with single handedness, the network is more dragged towards the micro-robot compared to the micro-robot with three helices. For both cases, the viscoelastic network and the links and fibers connecting nodes are rotated around the micro-robot, and the network is twisted around the robot. Another difference is observed in Figures 5.7b and 5.8b, where the micro-

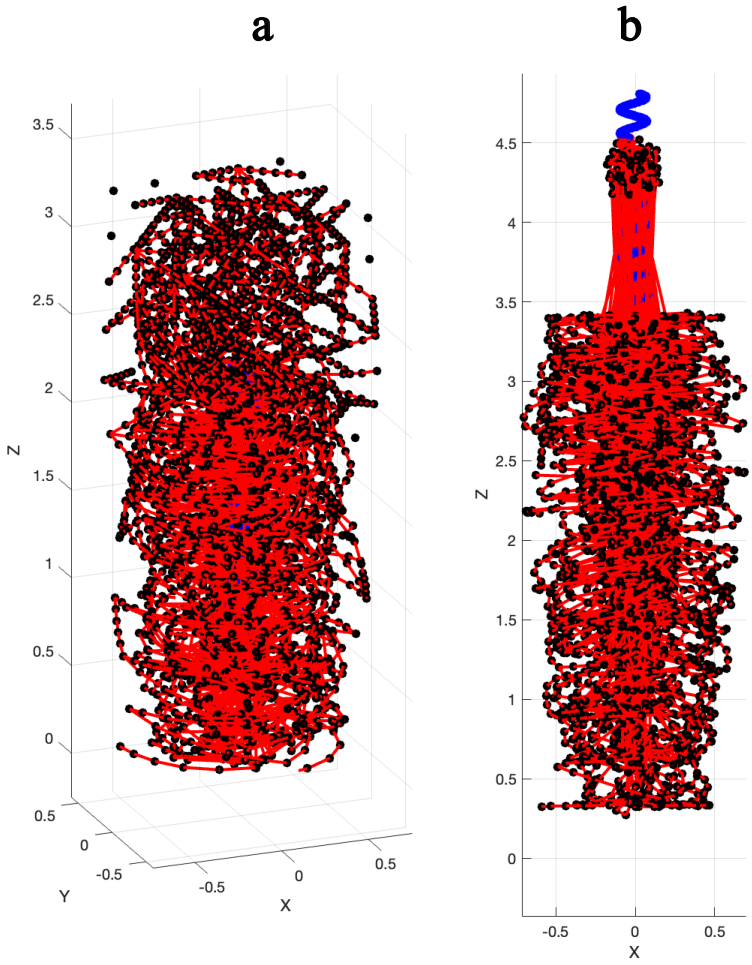


Figure 5.8: Helical micro-robot with three helices and two different handedness a) inside the viscoelastic network and b) while it is exiting the network.

robot is exiting the viscoelastic network. In Figure 5.7b, half of the robot is outside the viscoelastic network zone, and although the network in the XY plane is twisted and deformed significantly, the network is not dragged and relocated in the Z direction with the micro-robot's movement. However, in Figure 5.8b, it is observed that while the micro-robot is outside the viscoelastic network, some of the viscoelastic nodes are dragged and relocated with the micro-robot in the z-direction. All these nodes are around the middle section of the micro-robot where the pushing micro-helix is lo-

cated. As discussed in Chapter 3 and shown in Figure 5.6, the fluid inside the pushing micro-helix is in the forward direction, causing the viscoelastic nodes to be dragged with the micro-robot as it moves forward. Therefore, as shown in Figure 5.8b, the links connected to these viscoelastic nodes are also stretched. Stretching of those nodes causes a force in the backward direction to be applied to the micro-robot, pulling it backward. This behavior also occurs when the micro-robot is inside the viscoelastic network. Nodes in the z-direction are located at different layers, and when a micro-robot with a pushing micro-helix moves through the network, nodes at different layers are pulled forward with the micro-robot, and their links are stretched in the z-direction. This phenomenon causes the micro-robot with a pushing micro-helix to be pushed backward, reducing its velocity in the z-direction compared to the Newtonian fluid. This behavior is not observed for the micro-robot with single handedness, as it does not have a pushing micro-helix, so its velocity increases compared to the Newtonian fluid. For the micro-robot with single handedness, the viscoelastic nodes and the fibers are rotated around the micro-robot, providing a duct for the micro-robot to move forward.

To better understand how the viscoelastic network is arranged around the micro-robot as it moves through the network, we plot the radial distribution of the viscoelastic nodes around the robot. For each micro-robot, we create a cylindrical binning system centered around the micro-robot. Specifically, around the axis of the micro-robot, we create $N_r \times N_z$ bins, where N_r is the number of bins in the radial direction (r), and N_z is the number of bins in the axial direction (z). The average density of the viscoelastic nodes in each bin is then calculated for one complete rotation of the micro-robot. We select two levels in the z direction, denoted as Z_1 and Z_2, and sum the number of the viscoelastic nodes located in the bins between Z_1 and Z_2, and from $\theta = 0$ to 2π. The radial distribution of the viscoelastic nodes is then plotted. To better understand the distribution, the radial position of the bins is normalized by the radius of the micro-robot. Thus, distances greater than 1 indicate a position outside the micro-robot, while distances less than 1 indicate a position inside the micro-robot. For the micro-robot with a single helix, Z_1 and Z_2 are chosen such that Z_1 corresponds to the minimum z value of the micro-robot, and Z_2 to the maximum value. For the micro-robot with three helices, Z_1 and Z_2 are selected at the bottom and top of the middle micro-helix (pushing micro-helix), and at the bottom and top of

the pulling micro-helix at the back. Two separate radial distributions of the viscoelastic nodes are plotted for these cases. Figures 5.9 and 5.10 display these radial distributions. The normalized density shown in these figures is calculated as the number of viscoelastic nodes divided by the volume of the bin where those nodes are located, and then normalized by the average density of the viscoelastic nodes at the initial time. Initially, the viscoelastic network contains 3293 nodes with a total volume of 3, giving an average node density of 1097. Therefore, to normalize the density of the viscoelastic nodes around the micro-robot, the calculated density is divided by 1097.

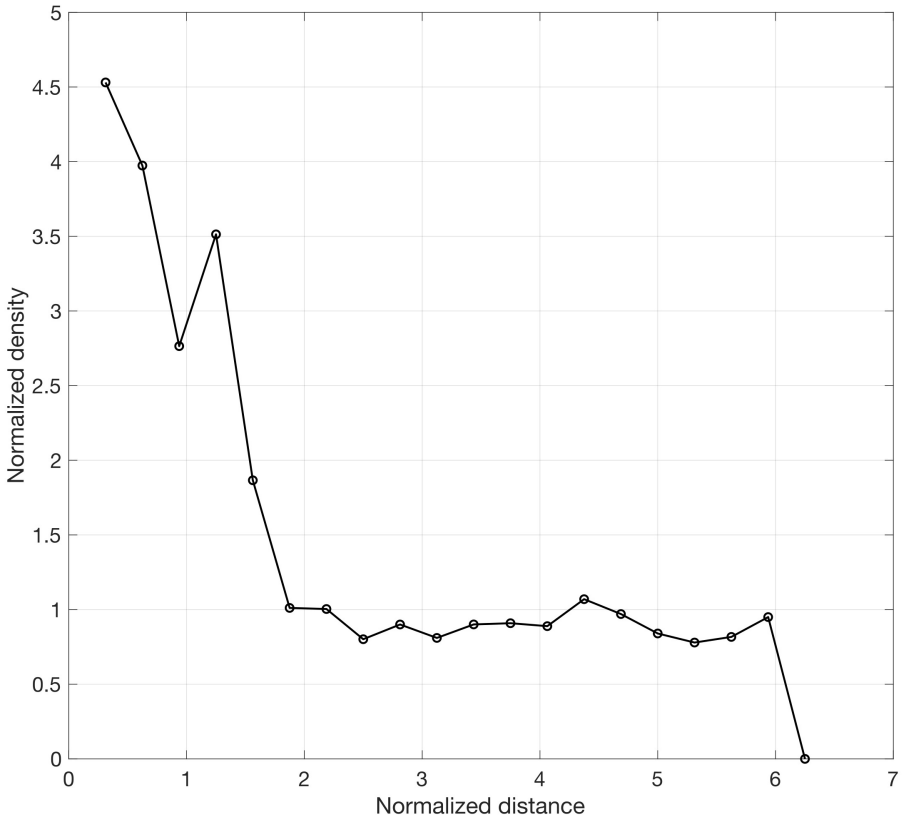


Figure 5.9: Normalized density of the viscoelastic nodes around the micro-robot with single handedness.

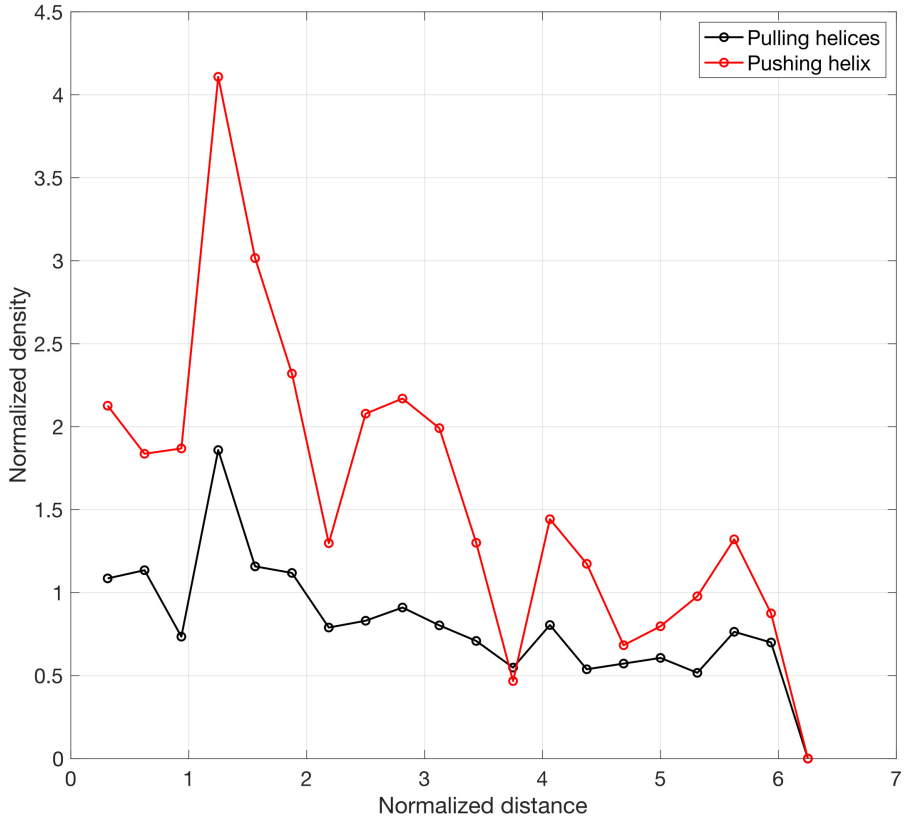


Figure 5.10: Normalized density of the viscoelastic nodes around the pushing micro-helix of the micro-robot with three helices and two different handedness.

As shown in Figure 5.9, compared to the micro-robot with three helices, the micro-robot with single handedness drags more nodes towards itself. This was also observed in Figure 5.7. Moreover, Figure 5.10 shows that the overall normalized density of the viscoelastic nodes around the pushing micro-helix is higher than that around the pulling micro-helices. The reason, as discussed before, is that the pushing micro-helix also drags some viscoelastic nodes from the previous layer of viscoelastic nodes in the z-direction. This is the main reason that the velocity of the micro-robot with three helices reduces in a viscoelastic network compared to a Newtonian fluid. In the next section, we will study the effect of the properties of the viscoelastic network

on the velocity of the micro-robot, including the stiffness of the spring in the Maxwell element, the dashpot constant in the Maxwell element, and the concentration of the viscoelastic nodes.

5.3.2 Studying the effect of viscoelastic properties on the performance of the helical micro-robots

In the preceding section, we discussed the performance of two different micro-robots in a viscoelastic network. The viscoelastic properties of the network were kept constant in the previous analysis. It was observed that the speed of micro-robots with three sections of alternating handedness in a viscoelastic network reduces compared to a Newtonian fluid. However, the micro-robot with single handedness demonstrated better performance in the viscoelastic network. This was attributed to the fluid flow around the micro-robot and the pattern and distribution of the viscoelastic nodes around it.

In this section, we evaluate the effect of spring stiffness, dash-pot constant, and the concentration of viscoelastic nodes in the network. These parameters, as examined in the previous chapter and characterized in this chapter, can alter the viscoelastic properties of the fluid. To assess the impact of these three parameters on the performance of the two micro-robots, we conducted multiple simulations for each micro-robot.

Firstly, we varied the spring stiffness of the Maxwell elements to four different values: 0.625, 10, 40, and 160. Next, keeping the spring stiffness constant at 160, we varied the dash-pot constant to values of 1, 5, 10, and 20. For all these simulations, the fraction of removed links was set to 50%, as previously discussed, to affect the concentration of the viscoelastic network. Setting the fraction of removed links to 50% generated 3293 nodes in the viscoelastic network.

Finally, we altered the concentration of the viscoelastic network by varying the fraction of removed links to 50%, 60%, and 70%, which generated 3293, 2173, and 1385 nodes, respectively. These nodes are connected to their neighboring nodes through multiple Maxwell elements. Figure 5.2 illustrates the viscoelastic network with the maximum concentration of viscoelastic components, comprising 3293 nodes.

Tables 5.1 and 5.2 summarize the effect of the viscoelastic network on the normalized velocity of the two micro-robots: one with single handedness

and the other with three helices and different handedness. In what follows, we examine each effect and study the velocity profile of the fluid and the distribution of the viscoelastic nodes around the micro-robot to understand why these effects occur.

Case	K	η	**Fraction of removed links**	V_{NN}/V_N
1	0.625	10	50%	1.25
2	10	10	50%	1.29
3	40	10	50%	1.33
4	160	10	50%	1.37
5	160	1	50%	1.07
6	160	5	50%	1.1
7	160	10	50%	1.37
8	160	20	50%	1.6
9	0.625	10	50%	1.25
10	0.625	10	60%	1.07
11	0.625	10	70%	1.03

Table 5.1: Effect of viscoelastic properties on the normalized velocity of the micro-robot with single handedness. (Velocity is normalized with the velocity of the micro-robot in Newtonian fluid.)

Case	K	η	Fraction of removed links	V_{NN}/V_N
1	0.625	10	50%	0.4
2	10	10	50%	0.32
3	40	10	50%	0.108
4	160	10	50%	-0.029
5	160	1	50%	0.58
6	160	5	50%	0.5
7	160	10	50%	-0.029
8	160	20	50%	-0.1
9	0.625	10	50%	0.4
10	0.625	10	60%	0.75
11	0.625	10	70%	0.91

Table 5.2: Effect of viscoelastic properties on the normalized velocity of the micro-robot with three helices. (Velocity is normalized with the velocity of the micro-robot in Newtonian fluid.)

Effect of elastic component of maxwell element on the performance of the micro-robots

As shown in Tables 5.1 and 5.2, increasing the stiffness of the Maxwell element in the viscoelastic network structure results in an increase in the velocity of the micro-robot with single handedness and a decrease in the velocity of the micro-robot with three helices. To better understand the effects of increased stiffness of the Maxwell element, we first examine the viscoelastic nodes and links surrounding the micro-robot while it is located in the middle of the viscoelastic network region.

Figure 5.11 illustrates the viscoelastic network around the micro-robot with three helices and a pushing micro-helix positioned at the center of the network. In Figure 5.11a, the spring stiffness of the Maxwell element is 0.625, while in Figure 5.11b, the spring stiffness is 160. As depicted, the stiffer network is more wrapped around the robot, with more network nodes being dragged inside or around the network. This occurs because, as the micro-robot rotates, viscoelastic nodes around it are dragged inward due to the fluid flow. When the network stiffness is very high, nodes connected

to those dragged nodes with stiff Maxwell elements are also pulled toward the network, causing a large group of connected nodes to wrap around the micro-robot.

Previously, we explained that for a micro-robot with three helices, many viscoelastic nodes are transported with the pushing micro-helix located at the center. This transportation stretches the Maxwell elements connected to those nodes, resulting in a backward force applied to both the nodes and the micro-robot, thus decreasing the micro-robot's speed. Therefore, stiffer Maxwell elements generate a larger backward force, further reducing the micro-robot's speed.

For the micro-robot with single handedness, nodes surrounding it create a channel that facilitates forward movement, increasing its speed. When the Maxwell element is stiffer, more nodes are dragged toward the micro-robot, amplifying this effect and increasing its speed.

Figure 5.12 shows the normalized density of viscoelastic nodes around the micro-robot with three helices. Two key observations can be made from this figure. First, compared to Figure 5.10 more viscoelastic nodes are pulled toward the micro-robot as the stiffness of the Maxwell element increases. Second, the normalized density of viscoelastic nodes around the pushing micro-helix is higher due to the pulling and transporting of some nodes from lower Z levels. Consequently, more nodes are transported with the micro-robot, making the reduction in its forward velocity more significant.

Figure 5.13 illustrates the fluid streamline around the micro-robot with three helices when the stiffness of the Maxwell element is 160. As previously reported in Table 5.2, the micro-robot does not move forward when the stiffness is very high. The streamline plot shows that the fluid inside the pushing micro-helix flows backward, indicating that the micro-robot is moving in the opposite direction. This backward movement is caused by the high density of transported viscoelastic nodes and the stiffness of the Maxwell element, which generates a backward force due to the extension of the connected Maxwell elements, as illustrated in Figure 5.11.

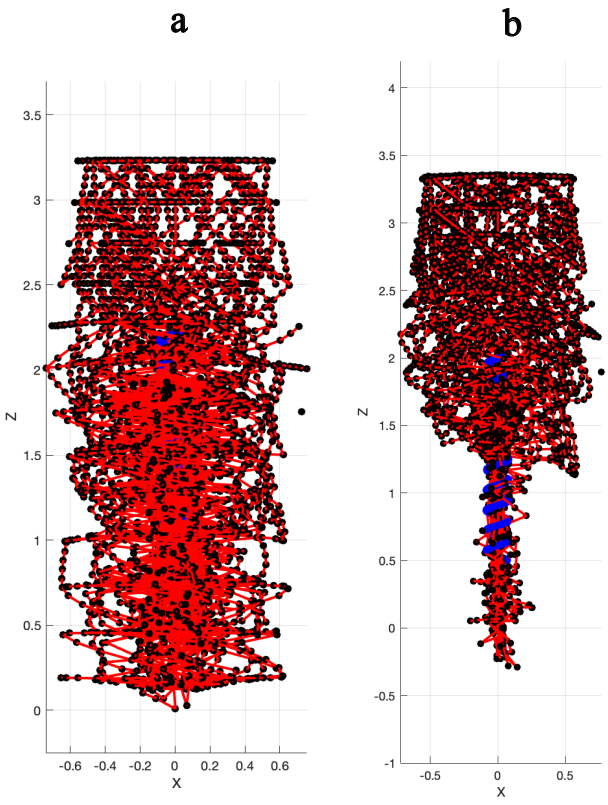


Figure 5.11: Viscoelastic network around the micro-robot with three helices and a pushing micro-helix at the center, with Maxwell element stiffness of a) 0.625 and b) 160.

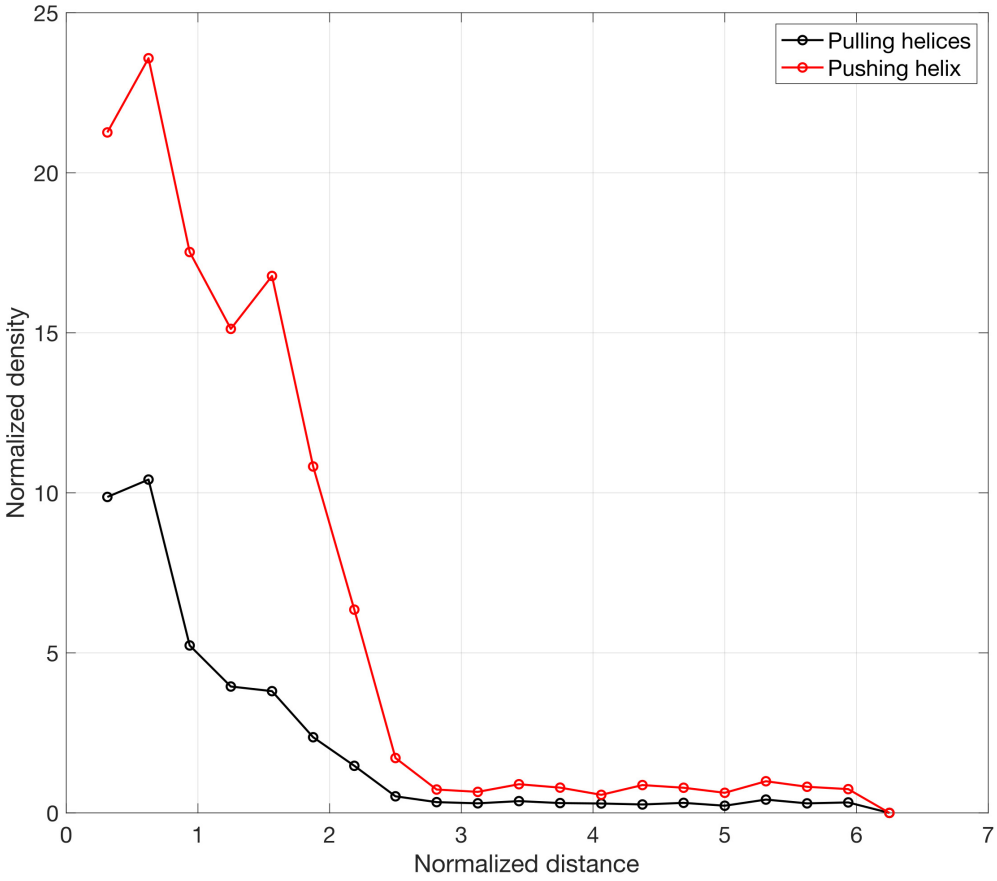


Figure 5.12: Normalized density of the viscoelastic nodes around the micro-robot close to the a) pushing micro-helix and b) back pulling micro-helix when the stiffness of the Maxwell element is 160.

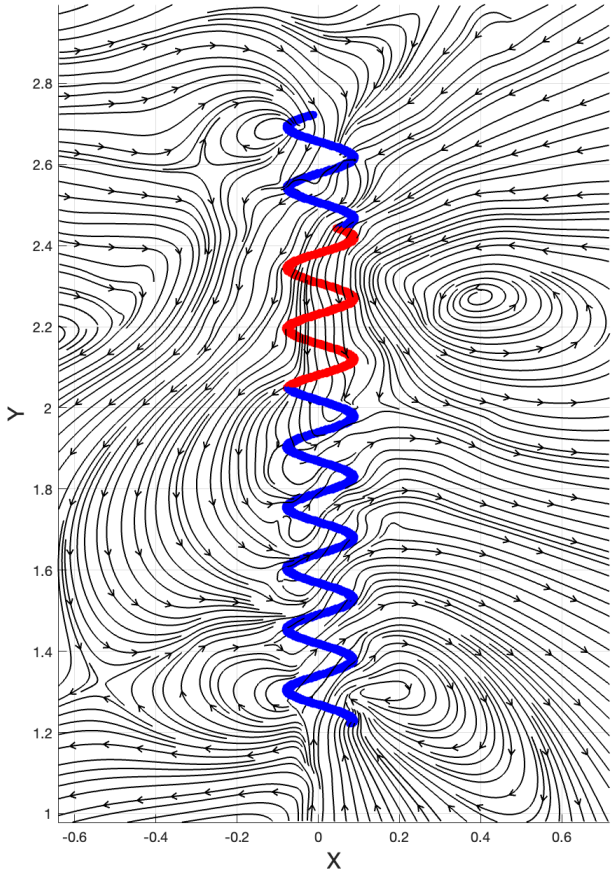


Figure 5.13: Streamline of the fluid around the micro-robot with three helices where the stiffness of the Maxwell element is 160.

For the single handedness micro-robot, it can also be observed from Figure 5.13 that the density of viscoelastic nodes around the micro-robot is higher compared to a network with lower stiffness, as shown in Figure 5.9. This increased density enhances the effect of the viscoelastic network, resulting in a higher velocity for the single handedness micro-robot in a stiff viscoelastic network.

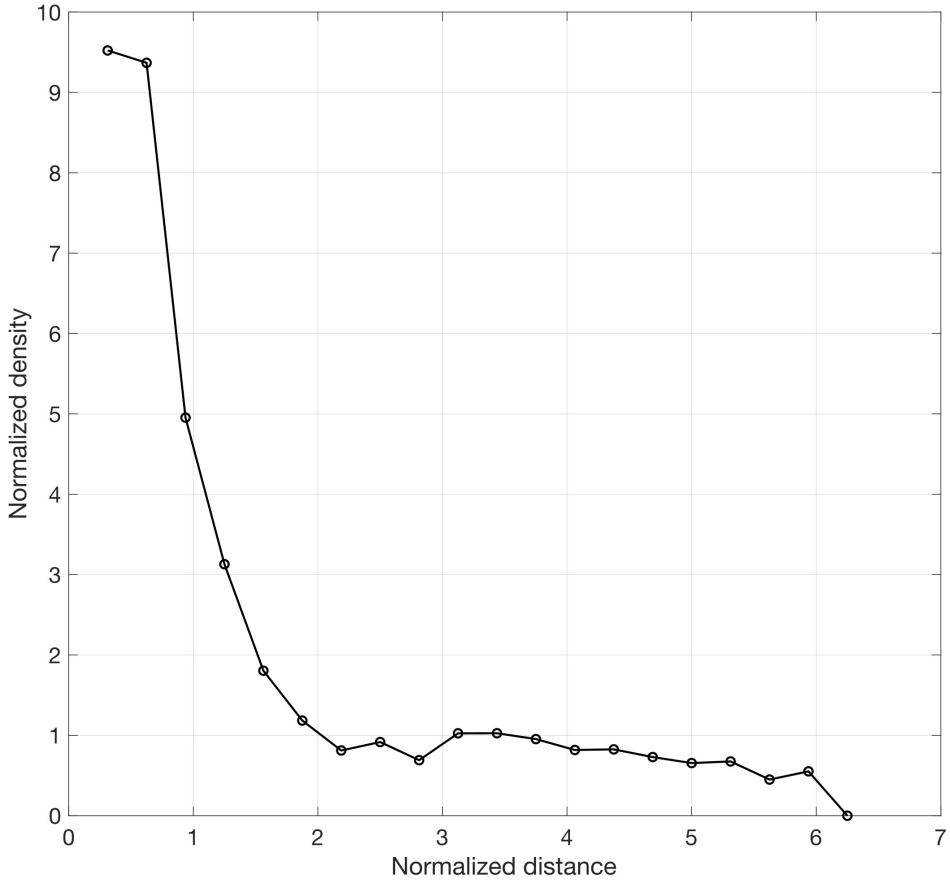


Figure 5.14: Normalized density of the viscoelastic nodes around the micro-robot with single handedness where the stiffness of the Maxwell element is 160.

Effect of viscous component of Maxwell element on the performance of the micro-robots

The influence of the viscous component of the Maxwell element can be observed in Tables 5.1 and 5.2. As shown, increasing the viscosity of the Maxwell element results in different outcomes for micro-robots with varying helices. For a micro-robot with three helices, increased viscosity reduces the forward velocity, whereas for a micro-robot with single handedness, it increases the forward velocity.

This phenomenon, similar to the effect of stiffness in the Maxwell element, occurs because higher viscosity makes it more difficult to change the length of the links connecting the nodes. Consequently, when the viscoelastic nodes near the micro-robot are dragged toward it, the nodes connected to them are also dragged closer, increasing the density of the viscoelastic nodes around the micro-robot. This heightened density enhances the effect of the viscoelastic network, resulting in an increased velocity for the micro-robot with single handedness and a decreased velocity for the micro-robot with three helices.

Furthermore, increasing the viscosity of the Maxwell element enhances the forces that pull back the transported viscoelastic nodes with the pushing micro-helix. This causes the micro-robot to be pulled back with greater force, reducing its forward velocity and sometimes even causing it to move backward instead of forward.

In Figure 5.15, it is evident that when the viscosity increases from 10 to 20, more viscoelastic nodes are pulled toward the micro-robot, resulting in an increased forward velocity for the micro-robot with single handedness.

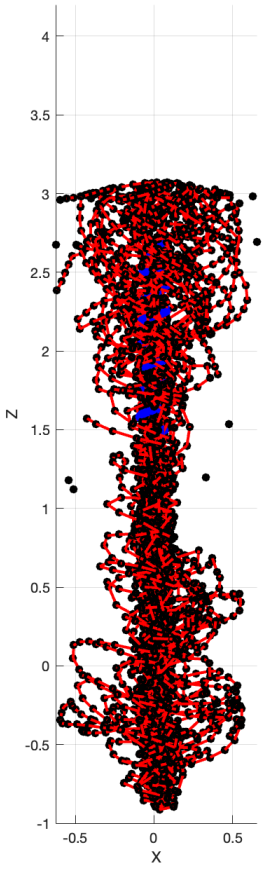


Figure 5.15: Viscoelastic network around a micro-robot with single handedness during its motion where the viscosity of the Maxwell element is 20.

Similarly, Figure 5.16 shows the viscoelastic network around a micro-robot with three helices and two different handedness. As the viscosity increases from 10 to 20, more viscoelastic nodes are pulled toward the micro-robot, resulting in a decreased forward velocity for the micro-robot with three helices and two different handedness.

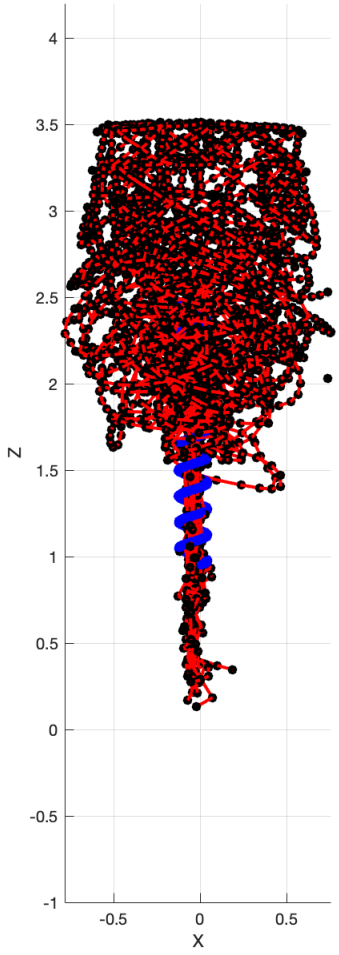


Figure 5.16: Viscoelastic network around a micro-robot with three helices during its motion where the viscosity of the Maxwell element is 20.

Effect of concentration of viscoelastic network on the performance of the micro-robots

Altering the concentration of viscoelastic nodes reduces the overall density of the nodes. Consequently, for a Maxwell element with consistent elasticity and viscosity, a network with lower concentration has fewer viscoelastic nodes surrounding the micro-robot. As the concentration of viscoelastic nodes decreases due to the increased fraction of removed links, the density of nodes around both types of micro-robots diminishes. This reduction in node density results in a decrease in the velocity of the micro-robot with single handedness, and increasing the velocity of the micro-robot with three helices and two different handedness. These effects are reported in Tables 5.1 and 5.2. Furthermore, to better illustrate how the velocity of the micro-robots changes with varying concentrations of the viscoelastic network and the viscoelastic properties of the fluid, we have plotted two different figures. Figures 5.17 and 5.18 illustrate the normalized velocity of the micro-robot inside the viscoelastic fluid, with the y-axis showing the velocity normalized by the velocity in Newtonian fluid. The x-axis indicates the concentration, calculated as 100 minus the percentage of removed links. Figure 5.17 plots various values of the stiffness (K) of the Maxwell element, while Figure 5.18 plots various values of the viscosity (η) of the Maxwell element. Both figures include separate curves for single-handedness micro-robots and micro-robots with three helices.

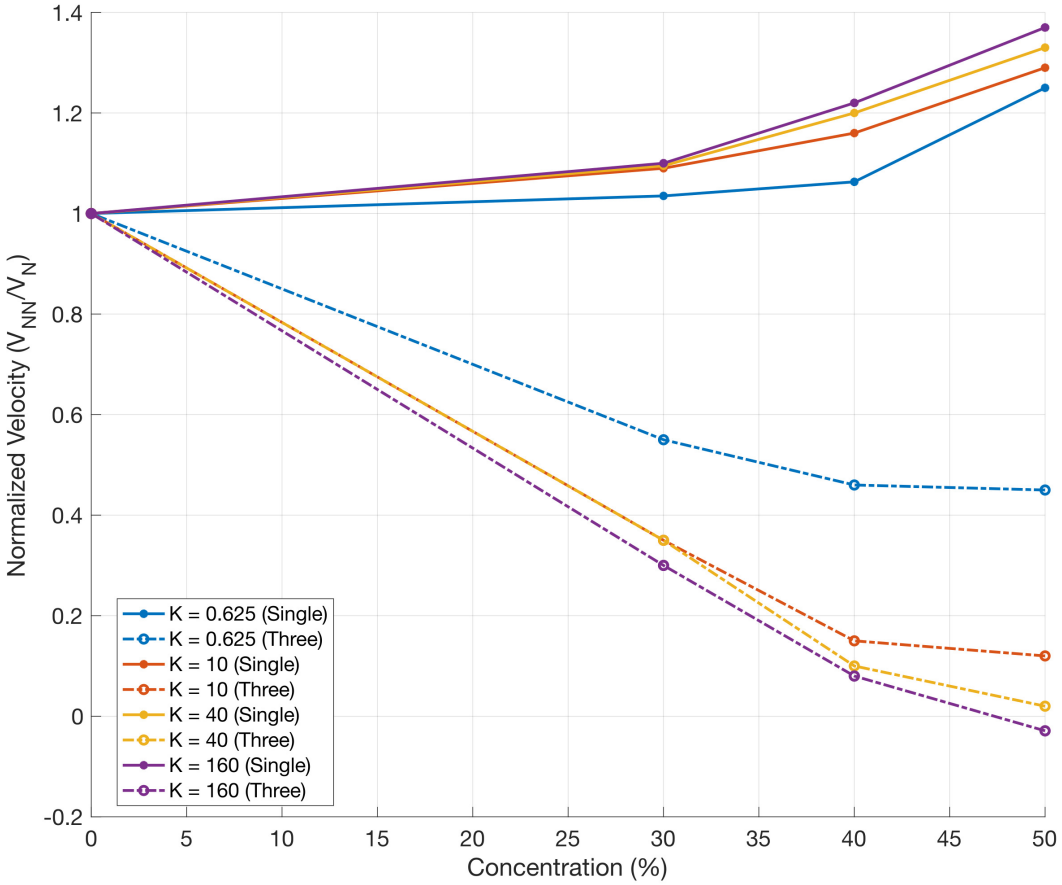


Figure 5.17: Normalized velocity of the micro-robot inside the viscoelastic fluid for different values of the stiffness (K) of the Maxwell element. The concentration is represented by 100 minus the percentage of removed links. The plot compares the performance of single-handedness micro-robots and micro-robots with three helices.

One important discussion remains. In Figures 5.17 and 5.18, as well as the data reported in Tables 5.1 and 5.2, some cases exhibit a negative velocity. For instance, when the concentration is 50% and the elasticity of the Maxwell element is 160, or when the concentration is 50% or 40% and the viscosity η is 20, the reported velocities are zero. This is unusual as we expect that the presence of the polymer resist the motion of the micro-robot but not completely and consistently reverse the direction of motion.

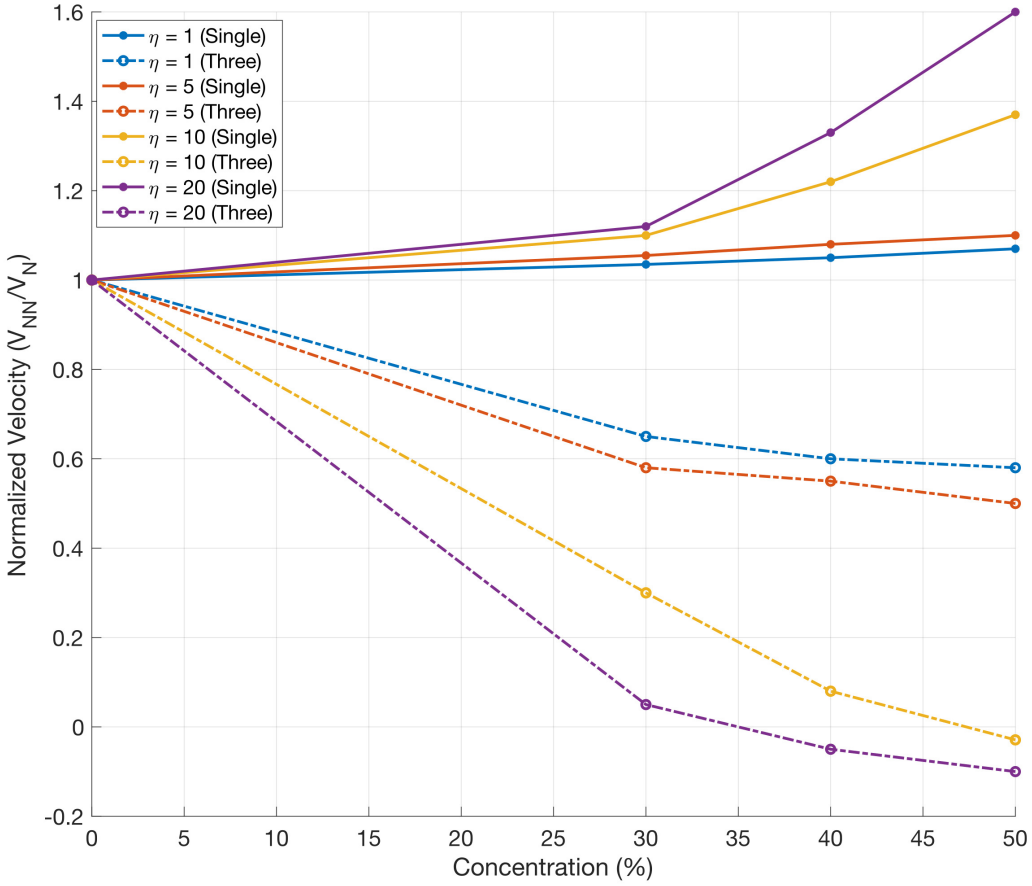


Figure 5.18: Normalized velocity of the micro-robot inside the viscoelastic fluid for different values of the viscosity (η) of the Maxwell element. The concentration is represented by 100 minus the percentage of removed links. The plot compares the performance of single-handedness micro-robots and micro-robots with three helices.

The reason for reporting negative velocities is that, in all cases except those with negative velocities, the velocity profile of the micro-robot over time follows a similar trend as shown in Figure 5.4. Here, the velocity decreases until it reaches a specific value, and as some viscoelastic nodes and their connected links are transported with the micro-robot, the normalized velocity never returns to 1. The effect of the viscoelastic network persists, and part of the network is carried along with the micro-robot until it reaches

an approximate steady velocity, which is then reported.

However, for cases where negative velocity is reported, the velocity profile trend differs. In Figure 5.19, where the concentration is 40% and the stiffness of the Maxwell element is 160, the velocity profile of the micro-robot in the z-direction (forward direction) is plotted. For cases where the concentration of viscoelastic nodes is high, and both the stiffness and viscosity of the Maxwell element are large, numerous viscoelastic links become wrapped around the micro-robot, causing it to move backward temporarily rather than forward. This backward movement helps to push away the viscoelastic nodes and links, freeing the micro-robot from being trapped in the network, which subsequently leads to an increase in velocity. Thus, the curve's main trend shows a decrease to negative values, followed by an increase to positive velocities, exceeding 1, and then a final decrease to values close to 1.

The negative velocities occur because many viscoelastic nodes wrap around the micro-robot, pushing it backward. However, eventually, the micro-robot pushes the nodes away, increasing its velocity and escaping the viscoelastic network. As the viscoelastic nodes are pushed away, the behavior previously observed with the three-helical micro-robot—where some nodes were inside the pushing helix and transported along with the micro-robot, slowing it down—is no longer observed. At this stage, the velocity of the micro-robot, similar to that of a single-handed micro-robot, exceeds the speed in a Newtonian fluid. Finally, when the micro-robot exits the viscoelastic network, and its influence is removed, the normalized velocity returns to 1. However, as can be seen, the velocity is not exactly 1, as we have for the single-handedness micro-robot, but it is very close when compared to other micro-robot with three helices. The velocity of the micro-robot reaches 0.86, indicating that a few viscoelastic nodes are still being transported with the micro-robot, even after it exits the viscoelastic network region.

In Figure 5.20, the normalized density of the viscoelastic nodes around the pushing and pulling sections of the micro-robot is plotted at two different times. In Figure 5.20a, the micro-robot exhibits negative velocity, and the viscoelastic links are tightly wrapped around it, hindering its forward motion. In contrast, in Figure 5.20b, the links have been pushed away from the micro-robot's surface, allowing it to move with a normalized speed slightly greater than 1. It can be observed that, unlike in Figure 5.20a, the maximum density of viscoelastic nodes in Figure 5.20b is located outside and away from the micro-robot's surface.

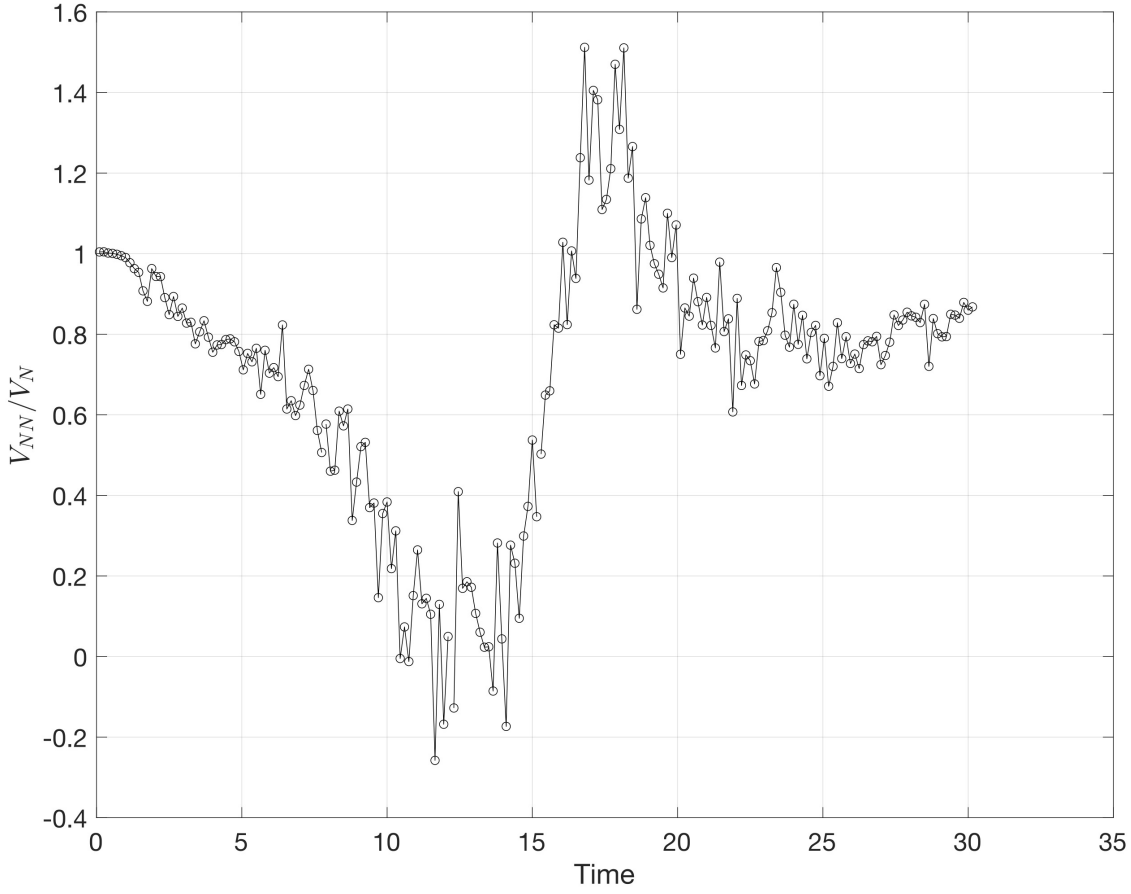


Figure 5.19: Normalized velocity of the micro-robot with three helices in the forward direction over time within a viscoelastic network with a concentration of 40%, Maxwell element stiffness of 160, and Maxwell element viscosity of 10.

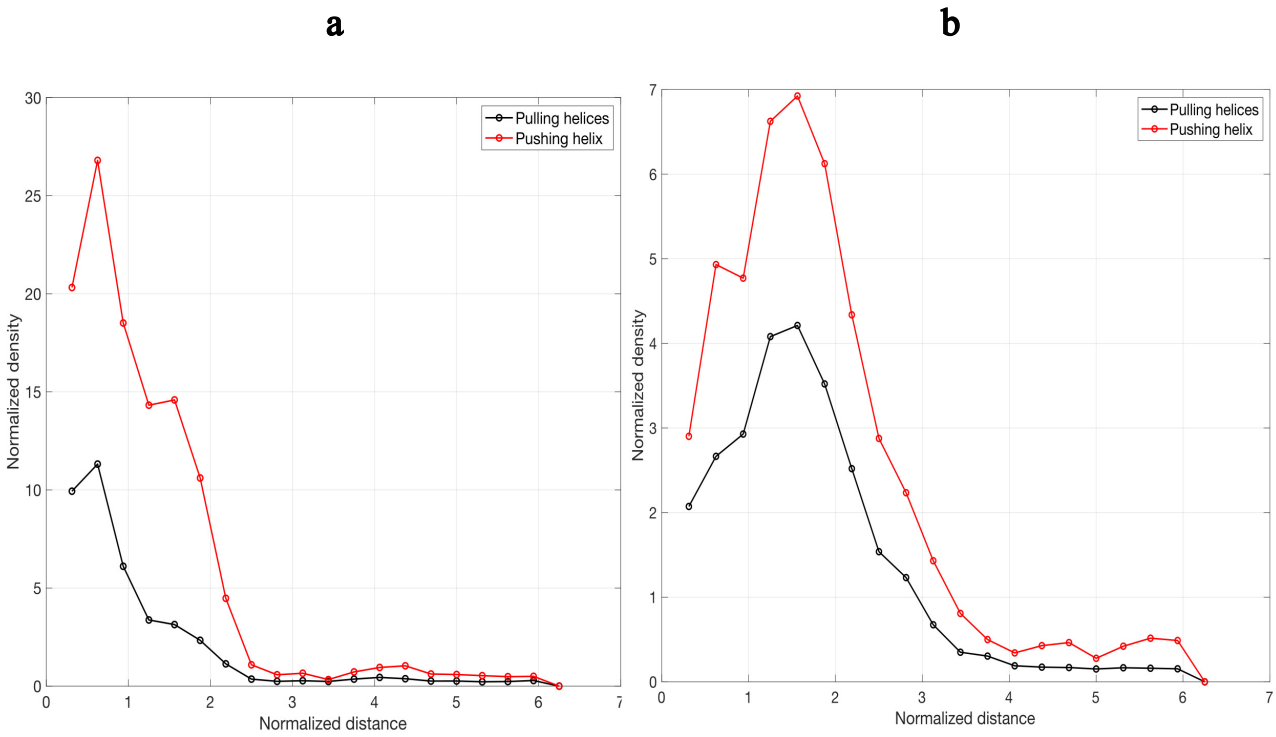


Figure 5.20: Normalized density of viscoelastic nodes around the micro-robot during the time robot has negative velocity and stuck inside the network (a) and after the viscoelastic links have been pushed away (b), where the micro-robot achieves a normalized speed greater than 1.

5.3.3 Studying the effect of breakpoints for links in the viscoelastic network on the performance of helical micro-robots

In the previous sections, we did not impose any limitations on the stretching of links within the viscoelastic networks. However, in real situations, polymer fibers in viscoelastic networks break when overstretched. Therefore, in this section, we study the effect of introducing breakpoints for the links connecting viscoelastic nodes. We vary the elasticity and viscosity of the Maxwell element as in previous sections, using a viscoelastic network where 60% of the links have been removed. At the end of each RK4 time step, links that have been stretched to more than three times their initial length are permanently removed from the remainder of the simulation. We expect that during the motion of micro-robots through the viscoelastic network, some links will break, and some nodes will become disconnected from the network. This phenomenon is similar to breaking polymer fibers into smaller sections.

As explained in Section 5.3.1, the primary reason for the reduced speed of the micro-robot with three helices in a viscoelastic network compared to a Newtonian fluid is the transport of viscoelastic nodes by the pushing micro-helix. The links connected to these transported nodes are stretched, resulting in a backward force that slows down the micro-robot. Therefore, we expect that the micro-robot with three helices will break more Maxwell elements than the single-handedness micro-robot. For the single-handedness micro-robot, although Maxwell elements are also deformed, fewer elements break because viscoelastic nodes are not transported with the micro-robot; they are just rotated and wrapped around it.

As shown in Figure 5.21, many viscoelastic nodes are disconnected from the network, and no Maxwell elements are connected to these nodes. Additionally, around the pushing micro-helix, many viscoelastic nodes are transported with the micro-robot, and their Maxwell elements are overstretched and disconnected. As this is the main reason for the reduced velocity of the three-helix micro-robot in a viscoelastic network, introducing a breakpoint for the Maxwell element results in a smaller reduction in the micro-robot's speed compared to a Newtonian fluid.

In Table 5.3, we vary the elasticity and viscosity of the Maxwell element

and calculate the percentage of broken elements and the normalized velocity of the micro-robot with three helices. As seen in the table, when 68% of the Maxwell elements are broken, the normalized velocity is close to 1, indicating that the micro-robot's velocity in a viscoelastic network is similar to that in a Newtonian fluid. Therefore, for the cases shown in Table 5.3 where more Maxwell elements are broken, the speed of the micro-robot is closer to that in a Newtonian fluid. Here in this study, we assume a 200% threshold for the stretching of the Maxwell element before breaking. Changing this threshold, or using more or less resistant fibers, will alter the fraction of broken Maxwell elements. Increasing the stiffness or viscosity of the Maxwell element decreases the fraction of broken elements because they stretch less, reaching the breaking threshold less frequently. However, there is an exception in Table 5.3 where increasing elasticity from 40 to 160 resulted in more broken elements. This is because stiffer Maxwell elements drag more viscoelastic nodes toward the micro-robot, increasing the number of potential elements for breaking.

For the single-handedness micro-robot, Table 5.4 shows significantly fewer broken Maxwell elements compared to the three-helix micro-robot. However, the trend is the same: higher fractions of broken Maxwell elements correspond to velocities closer to that in a Newtonian fluid because fewer fibers wrap around the micro-robot, creating a channel for the micro-robot to move forward. Figure 5.22 shows the viscoelastic nodes around the single-handedness micro-robot. The viscoelastic nodes are not transported with the micro-robot, resulting in fewer disconnected nodes.

In summary, in real situations, polymer fibers break when overstretched. The three-helix micro-robot causes more fiber stretching in the viscoelastic network, leading to more broken fibers. Breaking fibers makes the behavior of the viscoelastic fluid approach that of a Newtonian fluid. Depending on fiber resistance, the fraction of broken fibers changes, affecting the micro-robot's speed relative to that in a Newtonian fluid.

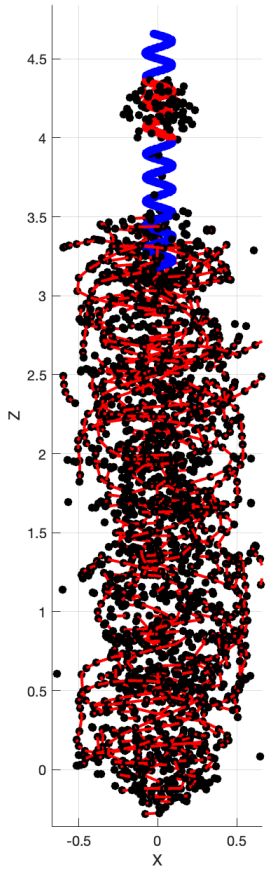


Figure 5.21: Viscoelastic network around a micro-robot with three helices during its motion. The viscosity of the Maxwell element is 20, the stiffness of the Maxwell element is 0.625, and breakpoints for the Maxwell element are considered.

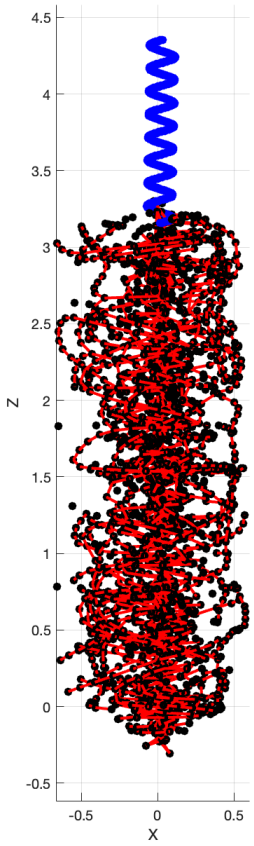


Figure 5.22: Viscoelastic network around a micro-robot with single handedness during its motion. The viscosity of the Maxwell element is 20, the stiffness of the Maxwell element is 0.625, and breakpoints for the Maxwell element are considered.

Case	K	eta	Broken Maxwell elements	V_{NN}/V_N
1	0.625	10	68%	0.98
2	10	10	46%	0.94
3	40	10	45%	0.84
4	160	10	50%	0.73
5	160	1	67%	0.93
6	160	5	56%	0.83
7	160	10	50%	0.73
8	160	20	33%	0.52

Table 5.3: Effect of having breakpoints for the Maxwell elements in the viscoelastic fluid on the performance of the three-helix micro-robot with 60% removed links.

Case	K	eta	Broken Maxwell elements	V_{NN}/V_N
1	0.625	10	48%	1.015
2	10	10	19%	1.06
3	40	10	10%	1.08
4	160	10	12%	1.12
5	160	1	41%	1.02
6	160	5	20%	1.07
7	160	10	12%	1.12
8	160	20	9.70%	1.2

Table 5.4: Effect of having breakpoints for the Maxwell elements in the viscoelastic fluid on the performance of the single handedness micro-robot with 60% removed links.

5.4 Summary and conclusion

This chapter delves into the intricate dynamics of a helical micro-robot operating within a viscoelastic fluid. The primary objective was to evaluate how the viscoelastic properties of the fluid influence the locomotion of the designed micro-robot, intended for applications in medical and biological fields. In Chapter 3, a new micro-robot with three helices of alternating handedness was designed and tested for its ability to improve the transportation of filamentous micro cargo such as sperm and bacteria. Given that most biological micro-swimmers, such as bacteria and sperm, move in viscoelastic fluids, it is crucial to evaluate the performance of the designed micro-robot in viscoelastic fluids and compare it with the conventional single-handed helical magnetic micro-robot.

The chapter began with an introduction to the geometry of the micro-robot and the viscoelastic network fluid. A viscoelastic network inspired by the network found in bovine vaginal fluid samples was designed and created. The micro-robot designs included single-handedness and three helices with alternating handedness, aimed at enhancing cargo transport capabilities. To assess the impact of different viscoelastic properties on the performance of the designed micro-robot, various viscoelastic networks were created by varying the flexibility of the Maxwell element, the viscosity of the Maxwell element, and the concentration of the viscoelastic network.

In the first section of assessing the performance of the helical magnetic micro-robot, the performance of the single-handed micro-robot and the three-helical alternating handedness micro-robot was compared, and their performances were also compared with that in a Newtonian fluid. It was observed that the single-handed micro-robot moved faster in a viscoelastic fluid, while the three-helical alternating handedness micro-robot moved slower in a viscoelastic fluid. After studying the pattern of the viscoelastic network around the micro-robot, the reason for the slower speed of the three-helical micro-robot compared to its speed in Newtonian fluid was revealed. Adding a pushing micro-helix to the middle of the three-helical micro-robot creates a zone inside the micro-robot that pushes the fluid forward rather than backward, as in a micro-robot with three helices of alternating handedness. This specific feature, as discussed in Chapter 3, helped transport filamentous micro-cargo without contact. This feature also causes different behavior in the three-helical micro-robot compared to the single-handed micro-robot. The fluid

inside the pushing micro-helix moves forward, causing the viscoelastic nodes to be dragged with the micro-robot as it moves forward. The links connected to these viscoelastic nodes are also stretched. Stretching of those nodes causes a backward force to be applied to the micro-robot, pulling it backward. Nodes in the z-direction are located at different layers, and when a micro-robot with a pushing micro-helix moves through the network, nodes at different layers are pulled forward with the micro-robot, and their links are stretched in the z-direction. This phenomenon causes the three-helical micro-robot to be pushed backward, reducing its velocity in the z-direction compared to its speed in Newtonian fluid. This behavior is not observed for the single-handed micro-robot, as it does not have a pushing micro-helix, so its velocity increases compared to its speed in Newtonian fluid. For the single-handed micro-robot, the viscoelastic nodes and fibers rotate around the micro-robot, providing a duct for the micro-robot to move forward.

Next, the effect of viscoelastic properties on the performance of the helical micro-robots was compared. Initially, the elasticity of the Maxwell element in the viscoelastic network was varied. It was observed that a stiffer network wraps more around the robot, with more network nodes being dragged inside or around the network. This occurs because, as the micro-robot rotates, viscoelastic nodes around it are dragged inward due to the fluid flow. When the network stiffness is very high, nodes connected to those dragged nodes with stiff Maxwell elements are also pulled toward the network, causing a large group of connected nodes to wrap around the micro-robot. This feature causes that for stiffer Maxwell elements, the single-handed micro-robot has more viscoelastic nodes providing the path to move forward and improve its performance and velocity. Conversely, for the three-helical alternating handedness micro-robot, many viscoelastic nodes are transported with the pushing micro-helix at the center. This transportation stretches the Maxwell elements connected to those nodes, resulting in a backward force applied to both the nodes and the micro-robot, thus decreasing the micro-robot's speed. Therefore, stiffer Maxwell elements generate a larger backward force, further reducing the micro-robot's speed. This behavior was also observed when the viscosity of the Maxwell element was varied. Increasing the viscosity of the Maxwell element has a similar effect to increasing its elasticity. This phenomenon occurs because higher viscosity makes it more difficult to change the length of the links connecting the nodes. Consequently, when the viscoelastic nodes near the micro-robot are dragged toward it, the nodes

connected to them are also dragged closer, increasing the density of the viscoelastic nodes around the micro-robot. This heightened density enhances the effect of the viscoelastic network, resulting in an increased velocity for the single-handed micro-robot and a decreased velocity for the three-helical micro-robot. Furthermore, increasing the viscosity of the Maxwell element enhances the forces that pull back the transported viscoelastic nodes with the pushing micro-helix. This causes the micro-robot to be pulled back with greater force, reducing its forward velocity and sometimes even causing it to move backward instead of forward.

Moreover, altering the concentration of viscoelastic nodes reduces the overall density of the nodes. Consequently, for a Maxwell element with consistent elasticity and viscosity, a network with lower concentration has fewer viscoelastic nodes surrounding the micro-robot. As the concentration of viscoelastic nodes decreases due to the increased fraction of removed links, the density of nodes around both types of micro-robots diminishes. This reduction in node density results in a decrease in the velocity of the single-handed micro-robot and an increase in the velocity of the three-helical alternating handedness micro-robot.

In the last section, the impact of overstretching-induced breakpoints in the viscoelastic network on micro-robot performance was analyzed. Unlike previous sections, this study introduced breakpoints for links exceeding 200% of their initial length, simulating the real-world breaking of polymer fibers. The analysis revealed that the micro-robot with three helices, which transports viscoelastic nodes and overstretches their connecting links, breaks more Maxwell elements than the single-handedness micro-robot. This increased breakage mitigates the backward force exerted by the stretched nodes, reducing the velocity differential between viscoelastic and Newtonian fluids for the micro-robot with three helices and alternate handedness. The study found that with a higher percentage of broken Maxwell elements, the normalized velocity of the micro-robot with three helices approaches that in a Newtonian fluid, demonstrating that the breaking of fibers shifts the viscoelastic fluid's behavior towards Newtonian-like characteristics. Conversely, for the single-handedness micro-robot, significantly fewer broken Maxwell elements compared to the micro-robot with three helices were detected. However, the trend is the same: higher fractions of broken Maxwell elements correspond to velocities closer to that in a Newtonian fluid because fewer fibers wrap around the micro-robot, creating a channel for the micro-robot to move

forward. This study highlights the critical role of fiber resistance and breakpoints in determining micro-robot performance in viscoelastic networks.

These findings provide a comprehensive understanding of the performance of helical micro-robots in viscoelastic fluids. While the micro-robot with three helices is effective in transporting filamentous cargo in Newtonian fluids, it faces challenges in viscoelastic environments and its speed can be reduced significantly and the possibility of getting stuck in the viscoelastic fluid is quite higher compared to the regular micro-robot with single handedness.

Chapter 6

Summary and conclusions

In recent years, there has been a notable surge in interest within the medical field towards minimally invasive procedures, with magnetic micro-robots emerging as a promising avenue. These micro-robots exhibit the capability to traverse various mediums, including viscoelastic and non-Newtonian fluids, facilitating targeted drug delivery and medical interventions. Many current designs, drawing inspiration from micro-swimmers found in biological systems such as bacteria and sperm, utilize a contact-based approach for transporting payloads. However, adhesion between the cargo and the carrier can complicate release at the intended site. This thesis investigated the potential of a helical micro-robot for non-contact delivery of drugs or cargo, focusing on its ability to transport passive filaments.

To design the helical micro-robot for capturing and carrying a passive filament, we first studied the streamline and pathline of fluid around the rotating helical micro-robot. Our calculations showed that confining the filament inside the micro-robot close to its axis maximized the forward hydrodynamic drag force. The geometrical parameters r/R and λ/R significantly affect the pathline of the fluid, and unsuitable choices can cause the fluid to escape the radial confinement of the micro-robot, resulting in backward fluid velocity. We simulated the motion of the helical micro-robot and the passive filament, examining the effects of filament flexibility, r/R, and λ/R. Increasing the flexibility of the filament and the ratio of r/R led to better coupling, while reducing λ/R improved the coupling as well. However, the forward velocity of the filament was lower than that of the micro-robot, causing it to surpass the filament and lose the coupling.

To address this issue, we added a pushing helix to the front of the micro-robot to apply a larger hydrodynamic thrust force to the filament and enhance its forward velocity. Despite this improvement, the flow field on the front of the micro-robot was in the forward direction, pushing the filament forward during the capturing process and making it difficult to capture. We then proposed a third design consisting of three helical sections: one pushing microhelix between two pulling microhelices of different lengths. The pulling helix at the back provided the main thrust for the micro-robot to move forward, while the front helix pulled fluid into the micro-robot to assist with capturing the filament. By optimizing the length ratio between the pushing and pulling microhelices and selecting appropriate helix parameters, we achieved effective filament capture and transportation.

Since biological and synthetic filaments are often curved, we conducted simulations with two different non-straight resting shapes: sinusoidal and circular arcs. Our micro-robot successfully captured and transported these filaments over a range of curvatures and amplitudes. Additionally, we demonstrated that the micro-robot could transport a straight filament with an attached head, similar to human sperm. By tuning the length ratio of the helical sections, we maintained a gap between the head of the cargo and the micro-robot, mitigating potential contact or adhesion issues.

We developed a theoretical model to estimate the length ratios that allow complete coupling between a filament and a micro-robot. The optimal length ratio from the model closely matched the numerically determined optimum, supporting our recommendation that the combined length of the front and middle sections be slightly longer than the intended filament cargo.

The second main part of the thesis focused on the dynamics of a helical micro-robot operating within a viscoelastic fluid. We evaluated how the viscoelastic properties of the fluid influence the locomotion of the designed micro-robot, which is crucial for applications in medical and biological fields. A viscoelastic network inspired by bovine vaginal fluid samples was designed and created. The performance of the single-handed micro-robot and the three-helical alternating handedness micro-robot was compared in both viscoelastic and Newtonian fluids. It was observed that the single-handed micro-robot moved faster in viscoelastic fluid, while the three-helical micro-robot moved slower.

The slower speed of the three-helical micro-robot was attributed to the

fluid inside the pushing micro-helix moving forward, causing the viscoelastic nodes to be dragged with the micro-robot, stretching the links and applying a backward force. This phenomenon was not observed in the single-handed micro-robot, as it did not have a pushing micro-helix, resulting in increased velocity compared to its speed in Newtonian fluid. The single-handed micro-robot's viscoelastic nodes and fibers rotated around it, providing a path for forward movement.

We also examined the impact of varying the viscoelastic properties on the micro-robot's performance. Increasing the elasticity and viscosity of the Maxwell element in the viscoelastic network caused more nodes to be dragged around the micro-robot, enhancing the single-handed micro-robot's performance but decreasing the three-helical micro-robot's speed due to the increased backward force. Altering the concentration of viscoelastic nodes affected the node density around the micro-robot, influencing its velocity accordingly.

The study also analyzed the impact of overstretching-induced breakpoints in the viscoelastic network. Breakpoints for links exceeding 300% of their initial length were introduced, simulating real-world breaking of polymer fibers. The three-helical micro-robot broke more Maxwell elements than the single-handed micro-robot, reducing the backward force and normalizing its velocity closer to that in a Newtonian fluid. This study highlights the critical role of fiber resistance and breakpoints in determining micro-robot performance in viscoelastic networks.

In conclusion, this thesis provides a comprehensive understanding of the design and performance of helical micro-robots in both Newtonian and viscoelastic fluids. The novel design of the micro-robot with three helices offers significant improvements in non-contact transport of filamentous cargo, with potential applications in medical procedures and drug delivery. However, challenges remain in viscoelastic environments, where the micro-robot's speed can be significantly reduced, and the risk of getting stuck is higher compared to a single-handed micro-robot. Future research should focus on further optimizing the micro-robot design and exploring additional strategies to overcome these challenges in viscoelastic fluids.

6.1 Recommendations for future works

In Chapter 3, we assessed the performance of the designed micro-robot in transporting filamentous microcargo by conducting all simulations with initial conditions that aligned the micro-robot with the filament. While it has been experimentally demonstrated that magnetic micro-robots are highly controllable and can be manipulated accurately, it is useful to investigate the extent of acceptable error in the micro-robot's alignment that still allows successful filament capture. When approaching a filament to capture and transport it, one must first determine the filament's orientation using a camera, then approach the filament for capture. There are two sources of error: finding the exact orientation and location of the filament, and the change in filament orientation due to fluid motion as the micro-robot approaches. Therefore, perfect alignment of the micro-robot and the filament is impossible. It is important to test how much alignment error is acceptable to ensure successful filament capture and transport.

Another parameter that can be studied in the future is the assumption that the filament is passive. Even immotile sperm are not completely passive; they are just less motile. Additionally, many micro-swimmers are active. Therefore, it is important to assess the performance of the designed micro-robot in capturing and transporting active filamentous micro-cargo.

Moreover, future projects could expand on the work in Chapter 5. In Chapter 5, we simulated a Newtonian fluid in which a viscoelastic network is suspended. However, some biological fluids are shear-thinning or shear-thickening, meaning the viscosity of the fluid is not constant but a function of the shear and strain rate. Future studies should investigate the performance of the micro-robot in such non-Newtonian fluids where the viscoelastic network is suspended in shear-dependent fluids.

Finally, in the last project, we observed that although the designed micro-robot is very successful in transporting filamentous micro-cargo without any contact, its speed can be significantly reduced in viscoelastic fluids where a multitude of polymer fibers are suspended. One other potential direction for future studies is to improve the design of the micro-robot to ensure it re-

mains effective in both Newtonian and viscoelastic fluids for the non-contact transport of filamentous micro-cargo.

Appendix I: Detailed calculations for deriving the analytical equation of developed viscoelastic Network

The calculations used for deriving the analytical force-strain relationship in the developed viscoelastic network model, as discussed in Chapter 4, are presented here in detail.

The viscoelastic network model used in this study is based on the structure proposed by Wróbel et al. [13, 117]. As depicted in Figure 4.1, this network consists of multiple nodes arranged within a cubic lattice, with each node connected to its 26 neighboring nodes. The connections between nodes are represented by a combination of springs and dashpots, forming the basis of the viscoelastic network. Therefore, the more accurate element connecting two nodes is a dashpot and spring in series in parallel with another dashpot, as shown in Figure 1: Next, the relationships between force, strain, and the

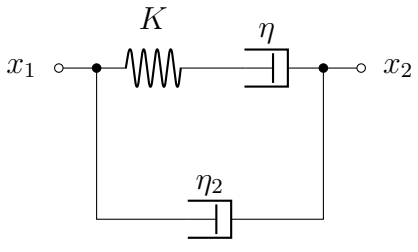


Figure 1: Schematic of the element connecting two nodes in the viscoelastic network.

velocity of nodes x_1 and x_2 are examined.

$$F_1 = K\epsilon_1 \quad \Rightarrow \quad \frac{F_1}{k} = \epsilon_1. \tag{1}$$

$$F_1 = \eta\dot{\epsilon}_1 \quad \Rightarrow \quad \frac{\dot{F}_1}{\eta} = \dot{\epsilon}_1. \tag{2}$$

$$F_2 = \eta_2\dot{\epsilon}. \tag{3}$$

$$F = F_1 + F_2. \tag{4}$$

$$\epsilon = \epsilon_1 + \epsilon_2. \tag{5}$$

where ϵ_1 is the strain of the spring and ϵ_2 is the strain of the dashpot η. F_1 is the force applied to the series of the spring and dashpot, and F_2 is the force applied to the dashpot η_2. F and ϵ are the forces and strain applied between nodes x_1 and x_2 which are connected. Using Equations (1) to (5), we derive the following equation relating the force F and the strain ϵ:

$$\frac{\eta}{K}\dot{F} + F = (\eta + \eta_2)\dot{\epsilon} + \frac{\eta\eta_2}{K}\ddot{\epsilon}. \tag{6}$$

By defining $\alpha = \frac{\eta}{K}$, $\beta = \eta + \eta_2$, and $\gamma = \frac{\eta\eta_2}{K}$, we obtain the following ODE relationship between F and ϵ:

$$\alpha\dot{F} + F = \beta\dot{\epsilon} + \gamma\ddot{\epsilon}. \tag{7}$$

To characterize the viscoelastic fluid, several tests can be conducted, including the creep test and strain test, where a strain or force is applied to the viscoelastic fluid and the system's behavior is observed. Assume the previously described network, consisting of multiple nodes arranged within a cubic lattice where each node is connected to its 26 neighboring nodes, extends infinitely in the x, y, and z directions. To analyze the system, we focus on a single representative cube containing eight nodes, which forms one unit of the periodic lattice. Since the network is periodic, all cubes are assumed to be identical, with edges and nodes shared between adjacent cells. By studying the behavior of a single cube, we can infer the behavior of the entire infinite viscoelastic network. Applying a shear force in the x-direction to the top surface ABCD, as shown in Figure 2, and an equal and opposite force to the bottom surface OPMN allows us to calculate the displacement of the nodes in the x-direction. The ODE equation relating the displacement of the nodes in the x direction to the force applied to the ABCD surface

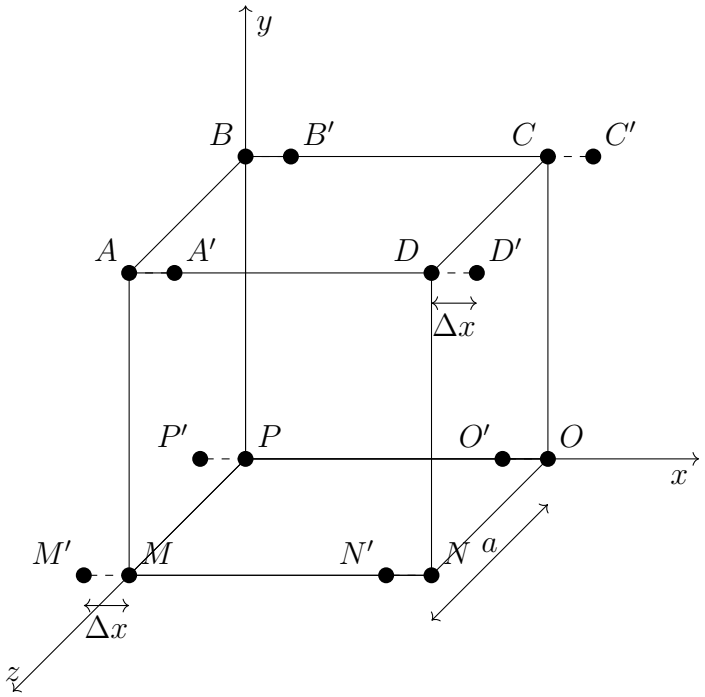


Figure 2: A cube within the viscoelastic network, where the nodes are connected by the elements shown in Figure 1.

is derived, providing a general formula for the viscoelastic fluid's behavior. The strain parameter is defined as follows:

$$\epsilon = \frac{2\Delta x}{a}.$$

Based on the diagram provided and considering that a shear force is applied to the cube, it is observed that the top vertices A, B, C, and D are displaced by a magnitude of Δx to the right, while the bottom vertices M, N, O, and P are displaced by the same magnitude Δx to the left. From this, the following relationships are deduced. It is important to note that the cube represents a unit of the periodic lattice. Since the network is periodic and all cubes are identical, with edges and nodes shared between adjacent cells, the strain of shared edges is only counted once to avoid multiple counting across cubes. This assumption is applied throughout the rest of the calculations in this thesis. As we predict the behavior of the entire system based on the analysis of this single cube, we ensure that strains of shared edges are not

double-counted. Therefore, in the calculations and equations below, certain edges are marked as 'only one counted' to indicate that their strain is shared between adjacent cubes and included only once in the overall calculations.

$$\epsilon_{AD} = \epsilon_{BC} = \epsilon_{MN} = \epsilon_{OP} = 0$$

$$\epsilon_{BD} = \epsilon_{AC} = \epsilon_{OM} = \epsilon_{NP} = 0$$

$$\epsilon_{CD} = \epsilon_{AB} = \epsilon_{ON} = \epsilon_{MP} = 0$$

$$\epsilon_{MD} = \epsilon_{CP} \quad \text{(only one counted)}$$

$$\epsilon_{AN} = \epsilon_{OB} \quad \text{(only one counted)}$$

$$\epsilon_{AM} = \epsilon_{DN} = \epsilon_{BP} = \epsilon_{OC} \quad \text{(only one counted)}$$

$$\epsilon_{NC} = \epsilon_{OD} = \epsilon_{BM} = \epsilon_{AP} \quad \text{(two are counted)}$$

$$\epsilon_{BN} = \epsilon_{OA} \quad \text{(two are counted)}$$

$$\epsilon_{CM} = \epsilon_{DP} \quad \text{(two are counted)}$$

The strains for each case are computed as follows:

$$\epsilon_{AD} = \epsilon_{BC} = \epsilon_{MN} = \epsilon_{OP} = 0$$

$$\epsilon_{BD} = \epsilon_{AC} = \epsilon_{OM} = \epsilon_{NP} = 0$$

$$\epsilon_{CD} = \epsilon_{AB} = \epsilon_{ON} = \epsilon_{MP} = 0$$

$$\epsilon_{MD} = \epsilon_{CP} \quad \text{(just one counted)}$$

$$\epsilon_{AN} = \epsilon_{OB} \quad \text{(just one counted)}$$

$$\epsilon_{AM} = \epsilon_{DN} = \epsilon_{BP} = \epsilon_{OC} \quad \text{(Just one counted)}$$

$$\epsilon_{NC} = \epsilon_{OD} = \epsilon_{BM} = \epsilon_{AP} \quad \text{(two are counted)}$$

$$\epsilon_{BN} = \epsilon_{OA} \quad \text{(two are counted)}$$

$$\epsilon_{CM} = \epsilon_{DP} \quad \text{(two are counted)}$$

These equations describe the strain relationships within the viscoelastic network when subjected to a shear force. This detailed analysis forms the basis for understanding the mechanical behavior of the network under various loading conditions. In what follows, the strain parameter ϵ for each of these links and their respective angles with the x-axis are calculated. The

purpose of determining these angles is to ultimately express the force in the x-direction, denoted as F, and establish its relationship with ϵ. Therefore, for all these terms, the components of force and strain in the x-direction are of primary importance. Term 1:

$$\epsilon_{MD} = \frac{\sqrt{a^2 + (a + 2\Delta x)^2} - a\sqrt{2}}{a\sqrt{2}}$$

$$\therefore \epsilon_{MD} = \sqrt{\frac{1}{2}(1 + \left(1 + \frac{2\Delta x}{a}\right)^2)} - 1 = \sqrt{\frac{1}{2}(1 + (1 + \epsilon)^2)} - 1$$

$$\cos_{\theta_{MD}} = \frac{a + 2\Delta x}{\sqrt{a^2 + (a + 2\Delta x)^2}} = \frac{1 + \epsilon}{\sqrt{1 + (1 + \epsilon)^2}}$$

Term 2:

$$\epsilon_{AN} = \frac{\sqrt{a^2 + (a - 2\Delta x)^2} - a\sqrt{2}}{a\sqrt{2}}$$

$$\therefore \epsilon_{AN} = \sqrt{\frac{1}{2}(1 + \left(1 - \frac{2\Delta x}{a}\right)^2)} - 1 = \sqrt{\frac{1}{2}(1 + (1 - \epsilon)^2)} - 1$$

$$\cos_{\theta_{AN}} = -\frac{a - 2\Delta x}{\sqrt{a^2 + (a - 2\Delta x)^2}} = -\frac{1 - \epsilon}{\sqrt{1 + (1 - \epsilon)^2}}$$

Term 3:

$$\epsilon_{AM} = \frac{\sqrt{a^2 + (2\Delta x)^2} - a}{a} = \sqrt{1 + \epsilon^2} - 1$$

$$\therefore \epsilon_{AM} = (\sqrt{1 + \epsilon^2} - 1)$$

$$\cos_{\theta_{AM}} = \frac{2\Delta x}{\sqrt{a^2 + (2\Delta x)^2}} = \frac{\epsilon}{\sqrt{1 + \epsilon^2}}$$

Term 4:

$$\epsilon_{NC} = \frac{\sqrt{2a^2 + (2\Delta x)^2} - a\sqrt{2}}{a\sqrt{2}} \times 2 \text{ (two of them are counted)}$$

$$\therefore \epsilon_{NC} = (\sqrt{1 + \frac{1}{2}\epsilon^2} - 1) \times 2$$

$$\cos_{\theta_{NC}} = \frac{2\Delta x}{\sqrt{2a^2 + (2\Delta x)^2}} = \frac{\epsilon}{\sqrt{2+\epsilon^2}}$$

Term 5:

$$\epsilon_{BN} = \frac{\sqrt{2a^2 + (a - 2\Delta x)^2} - a\sqrt{3}}{a\sqrt{3}} \times 2 \text{ (two of them are counted)}$$

$$\therefore \epsilon_{BN} = (\sqrt{\frac{2}{3} + \frac{1}{3}(1-\epsilon)^2} - 1) \times 2$$

$$\cos_{\theta_{BN}} = \frac{a - 2\Delta x}{\sqrt{2a^2 + (a - 2\Delta x)^2}} = \frac{1-\epsilon}{\sqrt{2 + (1-\epsilon)^2}} \times (-1)$$

Term 6:

$$\epsilon_{CM} = \frac{\sqrt{2a^2 + (a + 2\Delta x)^2} - a\sqrt{3}}{a\sqrt{3}} \times 2 \text{ (two of them are counted)}$$

$$\therefore \epsilon_{CM} = (\sqrt{\frac{2}{3} + \frac{1}{3}(1+\epsilon)^2} - 1) \times 2$$

$$\cos_{\theta_{CM}} = \frac{a + 2\Delta x}{\sqrt{2a^2 + (a + 2\Delta x)^2}} = \frac{1+\epsilon}{\sqrt{2 + (1+\epsilon)^2}}$$

Next, the Taylor series expansions for each term are derived up to the second order:

Term 1:

$$\epsilon_{MD} = \sqrt{\frac{1}{2}(1 + (1+\epsilon)^2)} - 1 = \frac{\epsilon^2}{8} + \frac{\epsilon}{2}$$

$$\cos\theta_{MD} = \frac{1+\epsilon}{\sqrt{1 + (1+\epsilon)^2}} = -\frac{3\sqrt{2}\epsilon^2}{16} + \frac{\sqrt{2}\epsilon}{4} + \frac{\sqrt{2}}{2}$$

Term 2:

$$\epsilon_{AN} = \sqrt{\frac{1}{2}(1 + (1-\epsilon)^2)} - 1 = \frac{\epsilon^2}{8} - \frac{\epsilon}{2}$$

$$\cos\theta_{AN} = -\frac{1-\epsilon}{\sqrt{1+(1-\epsilon)^2}} = \frac{3\sqrt{2}\epsilon^2}{16} + \frac{\sqrt{2}\epsilon}{4} - \frac{\sqrt{2}}{2}$$

Term 3:

$$\epsilon_{AM} = (\sqrt{1+\epsilon^2} - 1) \times 2 = \frac{\epsilon^2}{2}$$

$$\cos\theta_{AM} = \frac{\epsilon}{\sqrt{1+\epsilon^2}} = \epsilon$$

Term 4:

$$\epsilon_{NC} = (\sqrt{1+\frac{1}{2}\epsilon^2} - 1) \times 2 = \frac{\epsilon^2}{2} + 1$$

$$\cos_{\theta_{NC}} = \frac{\epsilon}{\sqrt{2+\epsilon^2}} = \frac{\sqrt{2}}{2}\epsilon$$

Term 5:

$$\epsilon_{BN} = (\sqrt{\frac{2}{3} + \frac{1}{3}(1-\epsilon)^2} - 1) \times 2 = \frac{2\epsilon^2}{9} - \frac{2\epsilon}{3}$$

$$\cos_{\theta_{BN}} = \frac{2\cdot\sqrt{3}\cdot\epsilon}{9} - \frac{\sqrt{3}}{3} + \frac{(\sqrt{3}\cdot\epsilon^2)}{9}$$

Term 6:

$$\epsilon_{CM} = (\sqrt{\frac{2}{3} + \frac{1}{3}(1+\epsilon)^2} - 1) \times 2 = \frac{2\epsilon^2}{9} + \frac{2\epsilon}{3}$$

$$\cos_{\theta_{CM}} = \frac{2\cdot\sqrt{3}\cdot\epsilon}{9} + \frac{\sqrt{3}}{3} - \frac{(\sqrt{3}\cdot\epsilon^2)}{9}$$

If a shear force F is applied to the system in the x-direction, each viscoelastic component, which consists of a spring and a dashpot in series, paralleled by

an additional dashpot, contributes to the system's overall behavior in the x-direction. The total response of the system in this direction is therefore the sum of the responses of all these components. Specifically, the term $\beta\dot{\epsilon} + \gamma\ddot{\epsilon}$ for each component projected onto the x-direction represents the cumulative effect of these components. Consequently, this sum is equivalent to the total stress $F + \alpha\dot{F}$ applied to the system. Thus, we have:

$$\begin{aligned} F + \alpha\dot{F} = &\cos_{\theta_{MD}}(\beta\dot{\epsilon}_{MD} + \gamma\ddot{\epsilon}_{MD}). \\ &+ \cos_{\theta_{AN}}(\beta\dot{\epsilon}_{AN} + \gamma\ddot{\epsilon}_{AN}). \\ &+ \cos_{\theta_{AM}}(\beta\dot{\epsilon}_{AM} + \gamma\ddot{\epsilon}_{AM}). \\ &+ \cos_{\theta_{NC}}(\beta\dot{\epsilon}_{NC} + \gamma\ddot{\epsilon}_{NC}). \\ &+ \cos_{\theta_{BN}}(\beta\dot{\epsilon}_{BN} + \gamma\ddot{\epsilon}_{BN}). \\ &+ \cos_{\theta_{CM}}(\beta\dot{\epsilon}_{CM} + \gamma\ddot{\epsilon}_{CM}) \end{aligned}$$

Upon substituting the strains from the previously derived equations, it is important to note that the Taylor series expansions up to the second order are considered. Therefore, in the calculations of the above equations, terms up to the second order of ϵ are included.

Term 1 + Term 2 of the RHS:

$$\text{Term1+Term2} = \beta(\frac{\sqrt{2}}{2}\dot{\epsilon} - \frac{\sqrt{2}}{16}\epsilon^2\dot{\epsilon}) + \gamma(\frac{\sqrt{2}}{2}\ddot{\epsilon} + \frac{\sqrt{2}}{2}\dot{\epsilon}^2\epsilon - \frac{\sqrt{2}}{16}\epsilon^2\ddot{\epsilon})$$

Term 3 of the RHS:

$$\text{Term3} = \beta(\epsilon^2\dot{\epsilon}) + \gamma(\epsilon^2\ddot{\epsilon} + 2\epsilon\dot{\epsilon}^2)$$

Term 4 of the RHS:

$$\text{Term4} = \beta(\frac{\sqrt{2}}{2}\epsilon^2\dot{\epsilon}) + \gamma(\epsilon^2\ddot{\epsilon} + \epsilon\dot{\epsilon}^2)$$

Term 5 + Term 6 of the RHS:

$$\text{Term5+Term6} = \beta(\frac{4\sqrt{3}}{9}\dot{\epsilon} - \frac{4\sqrt{3}}{81}\epsilon^2\dot{\epsilon}) + \gamma(\frac{4\sqrt{3}}{9}\ddot{\epsilon} + \frac{8\sqrt{3}}{81}\dot{\epsilon}^2\epsilon - \frac{4\sqrt{3}}{81}\epsilon^2\ddot{\epsilon})$$

By calculating the summation of all terms on the right-hand side (RHS), we obtain:

$$F + \alpha\dot{F} = \beta(1.4769\dot{\epsilon} + 1.5332\epsilon^2\dot{\epsilon}) + \gamma(1.4769\ddot{\epsilon} + 3.8782\dot{\epsilon}^2\epsilon + 1.8261\epsilon^2\ddot{\epsilon}). \tag{8}$$

Appendix II: Genetic Algorithm

The Genetic Algorithm (GA) is an optimization technique inspired by the process of natural selection in biology. Developed by John Holland in the 1970s [141], it belongs to the broader class of evolutionary algorithms, where a population of candidate solutions evolves over time toward an optimal solution. The algorithm is commonly used to solve complex optimization problems where traditional methods might struggle, especially when the solution space is large or poorly understood.

The genetic algorithm works by simulating the survival of the fittest. Initially, a population of potential solutions, called individuals or chromosomes, is generated. These individuals are typically represented as strings of binary values (bit strings), though other forms of representation, such as real numbers or more complex structures, can also be used depending on the problem at hand.

Each individual in the population is evaluated using a fitness function, which quantifies the quality of the solution. The fitness function is problem-specific, and it represents how close a given solution is to the optimal solution. In a minimization problem, for example, lower fitness values indicate better solutions, while in a maximization problem, higher fitness values are desirable.

Once the fitness of each individual has been assessed, the algorithm proceeds to select individuals for reproduction. The likelihood of an individual being selected is generally proportional to its fitness—fitter individuals have a higher chance of being chosen to pass their genes (solutions) on to the next generation. Several methods exist for selecting individuals, with roulette wheel selection and tournament selection being the most common.

In roulette wheel selection, each individual is given a slice of a wheel that is proportional to its fitness, and the wheel is spun to select individuals for reproduction. Tournament selection involves randomly selecting a group of individuals and choosing the fittest one from this group.

After selecting individuals, the next step in the GA is crossover (recombination). Crossover mimics biological reproduction by combining genetic material from two parent individuals to create offspring. The most common type of crossover is single-point crossover, where a crossover point is randomly chosen on the chromosome, and the genetic material from the two parents is swapped at that point. This results in offspring that carry traits from both parents, potentially combining the strengths of both. Another type of crossover is two-point crossover, where two crossover points are selected, and the genetic material between these points is swapped. Additionally, uniform crossover can be used, where each gene in the offspring is randomly selected from either parent with equal probability.

Mutation is another key process in GAs, and it serves to introduce random changes to the chromosomes. While crossover allows for the combination of good solutions, mutation ensures genetic diversity in the population and helps the algorithm explore new areas of the solution space. In the case of binary chromosomes, mutation involves flipping bits (changing 0s to 1s and vice versa). The mutation rate, typically a small probability, determines how often mutation occurs. A balance must be struck in setting the mutation rate: if the rate is too high, the algorithm behaves like a random search, while if it is too low, the population may converge prematurely to suboptimal solutions due to lack of diversity.

The final step of the GA is replacement, where the new population, consisting of the offspring, replaces the old population. In some cases, a technique known as elitism is used, where the best-performing individuals from the current generation are carried over to the next generation without any modification. This ensures that the best solutions are not lost during the evolutionary process. The GA repeats this process of selection, crossover, mutation, and replacement over many generations until a termination criterion is met. Common stopping criteria include reaching a predefined number of generations, achieving a satisfactory fitness level, or observing that the population has converged, meaning that most individuals have become very similar and further evolution is unlikely to yield significant improvements.

One of the key advantages of genetic algorithms is their ability to explore large and complex solution spaces without requiring gradient information or specific problem structures. Unlike traditional optimization methods, GAs do not require the objective function to be differentiable or continuous, making them suitable for a wide range of problems, including those with discontinuous or noisy objective functions. Additionally, because GAs maintain a population of solutions, they are less likely to get stuck in local optima compared to single-point optimization methods.

Another strength of GAs is their flexibility. They can be adapted to solve a wide variety of optimization problems by simply adjusting the representation of individuals, the fitness function, and the genetic operators. This makes GAs applicable to problems in diverse fields such as engineering, machine learning, scheduling, bioinformatics, and game development.

However, genetic algorithms are not without their drawbacks. One of the main disadvantages is their computational cost. Because GAs evaluate many individuals in each generation, and because they often require many generations to converge to a good solution, they can be computationally expensive, especially for problems where evaluating the fitness function is time-consuming. This makes GAs less practical for problems where real-time solutions are needed.

Additionally, GAs can suffer from premature convergence, where the population quickly becomes homogeneous and the algorithm gets stuck in a local optimum. This can happen if the mutation rate is too low or if the selection pressure is too high, causing only the fittest individuals to dominate the population early in the process. Careful tuning of the algorithm's parameters, such as mutation rate, crossover probability, and population size, is crucial to ensure that the GA performs well.

Another challenge is that GAs often require significant fine-tuning to perform effectively on specific problems. The performance of a GA can be highly sensitive to its parameters, and finding the right balance between exploration (searching new areas of the solution space) and exploitation (refining known good solutions) can be difficult. Hybrid approaches, where GAs are combined with other optimization techniques like local search, can help mitigate some of these issues, but they add complexity to the algorithm.

In conclusion, the genetic algorithm is a powerful and flexible optimization tool that can handle complex and challenging optimization problems.

Its ability to explore large solution spaces and avoid getting trapped in local optima makes it particularly useful for problems where traditional optimization methods struggle. However, its computational cost and the need for careful parameter tuning are important factors to consider when choosing whether to apply a GA to a particular problem. Despite these challenges, GAs remain a popular choice for many real-world optimization problems, thanks to their versatility and robustness.

For a more in-depth understanding of genetic algorithms, please refer to [134, 135].

References

[1] Michael Eisenbach and Laura C Giojalas. Sperm guidance in mammals—an unpaved road to the egg. *Nature reviews Molecular cell biology*, 7(4):276–285, 2006.

[2] Reza Nosrati. *Microfluidics for Sperm Selection and Male Infertility Diagnostics*. PhD thesis, University of Toronto (Canada), 2016.

[3] Tian-Yun Huang, Famin Qiu, Hsi-Wen Tung, Xue-Bo Chen, Bradley J Nelson, and Mahmut Selman Sakar. Generating mobile fluidic traps for selective three-dimensional transport of microobjects. *Applied Physics Letters*, 105(11):114102, 2014.

[4] Mariana Medina-Sánchez, Lukas Schwarz, Anne K Meyer, Franziska Hebenstreit, and Oliver G Schmidt. Cellular cargo delivery: Toward assisted fertilization by sperm-carrying micromotors. *Nano letters*, 16(1):555–561, 2016.

[5] Famin Qiu and Bradley J Nelson. Magnetic helical micro-and nanorobots: Toward their biomedical applications. *Engineering*, 1(1):021–026, 2015.

[6] Eamonn A Gaffney, Hermes Gadêlha, David J Smith, John R Blake, and Jackson C Kirkman-Brown. Mammalian sperm motility: observation and theory. *Annual Review of Fluid Mechanics*, 43:501–528, 2011.

[7] JM Krishnan, AP Deshpande, and PS Kumar. *Rheology of Complex Fluids*. Springer, New York, NY, USA, 2010.

[8] HY Gan and YC Lam. Viscoelasticity. In *Encyclopedia of Microfluidics and Nanofluidics*. Springer, 2014.

[9] DL Chen, PF Yang, and YS Lai. A review of three-dimensional viscoelastic models with an application to viscoelasticity characterization using nanoindentation. *Microelectronics Reliability*, 52(3):541–558, 2012.

[10] Y. Zhang, G. Li, and A.M. Ardekani. Reduced viscosity for flagella moving in a solution of long polymer chains. *Physical Review Fluids*, 3(2):023101, 2018.

[11] G. Li, E. Lauga, and A.M. Ardekani. Microswimming in viscoelastic fluids. *Journal of Non-Newtonian Fluid Mechanics*, 297:104655, 2021.

[12] A. Zöttl and J.M. Yeomans. Enhanced bacterial swimming speeds in macromolecular polymer solutions. *Nature Physics*, 15(6):554–558, 2019.

[13] JK Wróbel, S Lynch, A Barrett, L Fauci, and R Cortez. Enhanced flagellar swimming through a compliant viscoelastic network in stokes flow. *Journal of Fluid Mechanics*, 792:775–797, 2016.

[14] J Rutllant, M López-Béjar, and F López-Gatius. Ultrastructural and rheological properties of bovine vaginal fluid and its relation to sperm motility and fertilization: A review. *Reproduction in Domestic Animals*, 40(2):79–86, 2005.

[15] H. Shum, E.A. Gaffney, and D.J. Smith. Modelling bacterial behaviour close to a no-slip plane boundary: The influence of bacterial geometry. *Proceedings of the Royal Society A: Mathematical, Physical and Engineering Sciences*, 466(2118):1725–1748, 2010.

[16] Kim Tien Nguyen, Gwangjun Go, Zhen Jin, Bobby Aditya Darmawan, Ami Yoo, Seokjae Kim, Minghui Nan, Sang Bong Lee, Byungjeon Kang, and et al. Chang-Sei Kim. A magnetically guided self-rolled micro-robot for targeted drug delivery, real-time x-ray imaging, and micro-robot retrieval. *Advanced Healthcare Materials*, 10(6):2001681, 2021.

[17] Bradley J Nelson, Ioannis K Kaliakatsos, and Jake J Abbott. Microrobots for minimally invasive medicine. *Annual Review of Biomedical Engineering*, 12:55–85, 2010.

[18] Kathrin E Peyer, Li Zhang, and Bradley J Nelson. Bio-inspired magnetic swimming microrobots for biomedical applications. *Nanoscale*, 5(4):1259–1272, 2013.

[19] Ajay Vikram Singh and Metin Sitti. Targeted drug delivery and imaging using mobile milli/microrobots: A promising future towards theranostic pharmaceutical design. *Current pharmaceutical design*, 22(11):1418–1428, 2016.

[20] Kim Tien Nguyen, Manh Cuong Hoang, Eunpyo Choi, Byungjeon Kang, Jong-Oh Park, and Chang-Sei Kim. Medical micro-robot—a drug delivery capsule endoscope with active locomotion and drug release mechanism: Proof of concept. *International Journal of Control, Automation and Systems*, 18:65–75, 2020.

[21] Haifeng Xu, Mariana Medina-Sánchez, Manfred F Maitz, Carsten Werner, and Oliver G Schmidt. Sperm micromotors for cargo delivery through flowing blood. *ACS Nano*, 14(3):2982–2993, 2020.

[22] Haifeng Xu, Mariana Medina-Sánchez, Veronika Magdanz, Lukas Schwarz, Franziska Hebenstreit, and Oliver G Schmidt. Sperm-hybrid micromotor for targeted drug delivery. *ACS Nano*, 12(1):327–337, 2018.

[23] Seungmin Lee, Soyeun Kim, Sangwon Kim, Jin-Young Kim, Cheil Moon, Bradley J Nelson, and Hongsoo Choi. A capsule-type microrobot with pick-and-drop motion for targeted drug and cell delivery. *Advanced Healthcare Materials*, 7(9):1700985, 2018.

[24] Stephen Ornes. Medical microrobots have potential in surgery, therapy, imaging, and diagnostics. *Proceedings of the National Academy of Sciences*, 114(47):12356–12358, 2017.

[25] Franziska Ullrich, Christos Bergeles, Juho Pokki, Olgac Ergeneman, Sandro Erni, George Chatzipirpiridis, Salvador Pané, Carsten Framme, and Bradley J Nelson. Mobility experiments with microrobots for minimally invasive intraocular surgery. *Investigative Ophthalmology & Visual Science*, 54(4):2853–2863, 2013.

[26] Antonello Forgione. In vivo microrobots for natural orifice transluminal surgery. current status and future perspectives. *Surgical Oncology*, 18(2):121–129, 2009.

[27] Hakan Ceylan, Joshua Giltinan, Kristen Kozielski, and Metin Sitti. Mobile microrobots for bioengineering applications. *Lab on a Chip*, 17(10):1705–1724, 2017.

[28] Christine K Schmidt, Mariana Medina-Sánchez, Richard J Edmondson, and Oliver G Schmidt. Engineering microrobots for targeted cancer therapies from a medical perspective. *Nature Communications*, 11(1):5618, 2020.

[29] Susan S Suarez and AA Pacey. Sperm transport in the female reproductive tract. *Human reproduction update*, 12(1):23–37, 2006.

[30] Kiyoshi Miki and David E Clapham. Rheotaxis guides mammalian sperm. *Current Biology*, 23(6):443–452, 2013.

[31] Tatjana Smiljaković, Slavko Josipović, Olga Kosovac, Nikola Delić, S Aleksić, and Milan M Petrović. The role of ph values in porcine reproductive tracts of male and female individuals. *Biotechnology in Animal Husbandry*, 24(3-4):101–108, 2008.

[32] Tracey Bushnik, Jocelynn L Cook, A Albert Yuzpe, Suzanne Tough, and John Collins. Estimating the prevalence of infertility in canada. *Human reproduction*, 27(3):738–746, 2012.

[33] Naina Kumar and Amit Kant Singh. Trends of male factor infertility, an important cause of infertility: A review of literature. *Journal of human reproductive sciences*, 8(4):191, 2015.

[34] Gianpiero Palermo, Hubert Joris, Paul Devroey, and André C Van Steirteghem. Pregnancies after intracytoplasmic injection of single spermatozoon into an oocyte. *The Lancet*, 340(8810):17–18, 1992.

[35] Laura A Schieve, Herbert B Peterson, Susan F Meikle, Gary Jeng, Isabella Danel, Nancy M Burnett, and Lynne S Wilcox. Live-birth rates and multiple-birth risk using in vitro fertilization. *Jama*, 282(19):1832–1838, 1999.

[36] Bart CJM Fauser, Paul Devroey, and Nick S Macklon. Multiple birth resulting from ovarian stimulation for subfertility treatment. *The Lancet*, 365(9473):1807–1816, 2005.

[37] Carol Coughlan and William L Ledger. In-vitro fertilisation. *Obstetrics, Gynaecology & Reproductive Medicine*, 18(11):300–306, 2008.

[38] Gabor Huszar, Attila Jakab, Denny Sakkas, Ciler-Celik Ozenci, Sevil Cayli, Elena Delpiano, and Sinan Ozkavukcu. Fertility testing and icsi sperm selection by hyaluronic acid binding: clinical and genetic aspects. *Reproductive biomedicine online*, 14(5):650–663, 2007.

[39] Ralf R Henkel and Wolf-Bernhard Schill. Sperm preparation for art. *Reproductive Biology and Endocrinology*, 1(1):1–22, 2003.

[40] Savas Tasoglu, Hooman Safaee, Xiaohui Zhang, James L Kingsley, Paolo N Catalano, Umut Atakan Gurkan, Aida Nureddin, Emre Kayaalp, Raymond M Anchan, and et al. Richard L Maas. Exhaustion of racing sperm in nature-mimicking microfluidic channels during sorting. *Small*, 9(20):3374–3384, 2013.

[41] Stephanie M Knowlton, Magesh Sadasivam, and Savas Tasoglu. Microfluidics for sperm research. *Trends in Biotechnology*, 33(4):221–229, 2015.

[42] Tijana Maric, Muhammad Zafir Mohamad Nasir, Nur Farhanah Rosli, Maja Budanović, Richard D Webster, Nam-Joon Cho, and Martin Pumera. Microrobots derived from variety plant pollen grains for efficient environmental clean up and as an anti-cancer drug carrier. *Advanced Functional Materials*, 30(19):2000112, 2020.

[43] Beatriz Jurado-Sánchez, Marta Pacheco, Jaime Rojo, and Alberto Escarpa. Magnetocatalytic graphene quantum dots janus micromotors for bacterial endotoxin detection. *Angewandte Chemie International Edition*, 56(24):6957–6961, 2017.

[44] Gwangjun Go, Van Du Nguyen, Zhen Jin, Jong-Oh Park, and Sukho Park. A thermo-electromagnetically actuated micro-robot for the targeted transport of therapeutic agents. *International Journal of Control, Automation and Systems*, 16:1341–1354, 2018.

[45] Yue Dong, Lu Wang, Ke Yuan, Fengtong Ji, Jinhong Gao, Zifeng Zhang, Xingzhou Du, Yuan Tian, Qianqian Wang, and Li Zhang. Magnetic microswarm composed of porous nanocatalysts for targeted elimination of biofilm occlusion. *ACS Nano*, 15(3):5056–5067, 2021.

[46] Lisi Xie, Xin Pang, Xiaohui Yan, Qixuan Dai, Huirong Lin, Jing Ye, Yi Cheng, Qingliang Zhao, Xing Ma, and et al. Xianzhong Zhang. Photoacoustic imaging-trackable magnetic microswimmers for pathogenic bacterial infection treatment. *ACS Nano*, 14(3):2880–2893, 2020.

[47] Katherine Villa and Martin Pumera. Fuel-free light-driven micro/nanomachines: artificial active matter mimicking nature. *Chemical Society Reviews*, 48(19):4966–4978, 2019.

[48] Mengyue Li, Junfeng Wu, Daojing Lin, Jia Yang, Niandong Jiao, Yuechao Wang, and Lianqing Liu. A diatom-based biohybrid microrobot with a high drug-loading capacity and ph-sensitive drug release for target therapy. *Acta Biomaterialia*, 154:443–453, 2022.

[49] Wei Gao, Xiaomiao Feng, Allen Pei, Christopher R Kane, Ryan Tam, Camille Hennessy, and Joseph Wang. Bioinspired helical microswimmers based on vascular plants. *Nano Letters*, 14(1):305–310, 2014.

[50] Dandan Li, Moonkwang Jeong, Eran Oren, Tingting Yu, and Tian Qiu. A helical micro-robot with an optimized propeller-shape for propulsion in viscoelastic biological media. *Robotics*, 8(4):87, 2019.

[51] Hyoryong Lee, Dong in Kim, Su hyun Kwon, and Sukho Park. Magnetically actuated drug delivery helical micro-robot with magnetic nanoparticle retrieval ability. *ACS Applied Materials & Interfaces*, 13(17):19633–19647, 2021.

[52] Ugur Bozuyuk, Oncay Yasa, I Ceren Yasa, Hakan Ceylan, Seda Kizilel, and Metin Sitti. Light-triggered drug release from 3d-printed magnetic chitosan microswimmers. *ACS Nano*, 12(9):9617–9625, 2018.

[53] Laurent Arcese, Matthieu Fruchard, and Antoine Ferreira. Adaptive controller and observer for a magnetic micro-robot. *IEEE Transactions on Robotics*, 29(4):1060–1067, 2013.

[54] SM Jeon, GH Jang, HC Choi, SH Park, and JO Park. Magnetic navigation system for the precise helical and translational motions of a micro-robot in human blood vessels. *Journal of Applied Physics*, 111(7):07E702, 2012.

[55] Tinotenda Gwisai, Nima Mirkhani, Michael G Christiansen, Thuy Trinh Nguyen, V Ling, and S Schuerle. Magnetic torque-driven living microrobots for increased tumor infiltration. *Science Robotics*, 7(71):eabo0665, 2022.

[56] Masoud Yousefi and Hossein Nejat Pishkenari. Independent position control of two identical magnetic microrobots in a plane using rotating permanent magnets. *Journal of Micro-Bio Robotics*, 17:59–67, 2021.

[57] Dominik J Bell, Stefan Leutenegger, KM Hammar, Lixin X Dong, and Bradley J Nelson. Flagella-like propulsion for microrobots using a nanocoil and a rotating electromagnetic field. In *Proceedings 2007 IEEE International Conference on Robotics and Automation*, pages 1128–1133, 2007.

[58] Edward M Purcell. The efficiency of propulsion by a rotating flagellum. *Proceedings of the National Academy of Sciences*, 94(21):11307–11311, 1997.

[59] AT Chwang and Th Y Wu. A note on the helical movement of micro-organisms. *Proceedings of the Royal Society of London. Series B. Biological Sciences*, 178(1052):327–346, 1971.

[60] SMH Andrabi. Mammalian sperm chromatin structure and assessment of dna fragmentation. *Journal of assisted reproduction and genetics*, 24(12):561–569, 2007.

[61] K. A. Schmitz-Lesich and C. B. Lindemann. Direct measurement of the passive stiffness of rat sperm and implications to the mechanism of the calcium response. *Cell Motility and the Cytoskeleton*, 59(3):169–179, 2004.

[62] Charles B Lindemann and KS Kanous. Regulation of mammalian sperm motility. *Archives of andrology*, 23(1):1–22, 1989.

[63] R.P. Chhabra. Non-newtonian fluids: An introduction. In *Rheology of Complex Fluids*, pages 3–4. Springer, 2010.

[64] DF Katz, RN Mills, and TR Pritchett. The movement of human spermatozoa in cervical mucus. *Reproduction*, 53(2):259–265, 1978.

[65] DF Katz and SA Berger. Flagellar propulsion of human sperm in cervical mucus. *Biorheology*, 17(1-2):169–175, 1980.

[66] DF Katz, TD Bloom, and RH Bondurant. Movement of bull spermatozoa in cervical mucus. *Biology of Reproduction*, 25(5):931–937, 1981.

[67] SS Suarez and X Dai. Hyperactivation enhances mouse sperm capacity for penetrating viscoelastic media. *Biology of Reproduction*, 46(4):686–691, 1992.

[68] C Montecucco and R Rappuoli. Living dangerously: How helicobacter pylori survives in the human stomach. *Nature Reviews Molecular Cell Biology*, 2(6):457–466, 2001.

[69] JP Celli, BS Turner, NH Afdhal, S Keates, I Ghiran, CP Kelly, RH Ewoldt, GH McKinley, P So, S Erramilli, and R Bansil. Helicobacter pylori moves through mucus by reducing mucin viscoelasticity. *Proceedings of the National Academy of Sciences*, 106(34):14321–14326, 2009.

[70] TJ Moriarty, MU Norman, P Colarusso, T Bankhead, P Kubes, and G Chaconas. Real-time high resolution 3d imaging of the lyme disease spirochete adhering to and escaping from the vasculature of a living host. *PLoS Pathogens*, 4(6):e1000090, 2008.

[71] RB Kimsey and A Spielman. Motility of lyme disease spirochetes in fluids as viscous as the extracellular matrix. *Journal of Infectious Diseases*, 162(5):1205–1208, 1990.

[72] LJ Fauci and R Dillon. Biofluidmechanics of reproduction. *Annual Review of Fluid Mechanics*, 38:371–394, 2006.

[73] C O'Callaghan, K Sikand, and MA Chilvers. Analysis of ependymal ciliary beat pattern and beat frequency using high speed imaging:

Comparison with the photomultiplier and photodiode methods. *Cilia*, 1(1):1–7, 2012.

[74] EM Purcell. Life at low reynolds number. *American Journal of Physics*, 45(1):3–11, 1977.

[75] D Bray. *Cell Movements*. Garland Publishing, New York, NY, 2000.

[76] NC Keim, M Garcia, and PE Arratia. Fluid elasticity can enable propulsion at low reynolds number. *Physics of Fluids*, 24(8):081703, 2012.

[77] T Qiu, TC Lee, AG Mark, KI Morozov, R Münster, O Mierka, S Turek, AM Leshansky, and P Fischer. Swimming by reciprocal motion at low reynolds number. *Nature Communications*, 5(1):1–8, 2014.

[78] AE Patteson, A Gopinath, M Goulian, and PE Arratia. Running and tumbling with e. coli in polymeric solutions. *Scientific Reports*, 5:15761, 2015.

[79] B Qin, A Gopinath, J Yang, JP Gollub, and PE Arratia. Flagellar kinematics and swimming of algal cells in viscoelastic fluids. *Scientific Reports*, 5:9190, 2015.

[80] HC Ho and SS Suarez. Hyperactivation of mammalian spermatozoa: Function and regulation. *Reproduction*, 122(4):519–526, 2001.

[81] S. Ishijima, S. Oshio, and H. Mohri. Flagellar movement of human spermatozoa. *Gamete Research*, 13(3):185–197, 1986.

[82] D.J. Smith, E.A. Gaffney, H. Gadêlha, N. Kapur, and J.C. Kirkman-Brown. Bend propagation in the flagella of migrating human sperm, and its modulation by viscosity. *Cell Motility and the Cytoskeleton*, 66(4):220–236, 2009.

[83] C. Tung, C. Lin, B. Harvey, A.G. Fiore, F. Ardon, M. Wu, and S.S. Suarez. Fluid viscoelasticity promotes collective swimming of sperm. *Scientific Reports*, 7(1):1–9, 2017.

[84] P. Stoodley, R. Cargo, C.J. Rupp, S. Wilson, and I. Klapper. Biofilm material properties as related to shear-induced deformation and detachment phenomena. *Journal of Industrial Microbiology and Biotechnology*, 29(6):361–367, 2002.

[85] B.W. Towler, C.J. Rupp, A.L.B. Cunningham, and P. Stoodley. Viscoelastic properties of a mixed culture biofilm from rheometer creep analysis. *Biofouling*, 19(5):279–285, 2003.

[86] A.M. Vinogradov, M.T. Winston, C.J. Rupp, and P. Stoodley. Rheology of biofilms formed from the dental plaque pathogen streptococcus mutans. *Biofilms*, 1(1):49–56, 2004.

[87] C.J. Rupp, C.A. Fux, and P. Stoodley. Viscoelasticity of staphylococcus aureus biofilms in response to fluid shear allows resistance to detachment and facilitates rolling migration. *Applied and Environmental Microbiology*, 71(4):2175–2178, 2005.

[88] T. Shaw, M. Winston, C.J. Rupp, I. Klapper, and P. Stoodley. Commonality of elastic relaxation times in biofilms. *Physical Review Letters*, 93(9):098102, 2004.

[89] M. Litt, M.A. Khan, and D.P. Wolf. Mucus rheology: relation to structure and function. *Biorheology*, 13(1):37–48, 1976.

[90] S.K. Lai, Y.-Y. Wang, D. Wirtz, and J. Hanes. Micro-and macrorheology of mucus. *Advanced Drug Delivery Reviews*, 61(2):86–100, 2009.

[91] P.S. Stewart and M.J. Franklin. Physiological heterogeneity in biofilms. *Nature Reviews Microbiology*, 6(3):199–210, 2008.

[92] S.K. Lai, Y.-Y. Wang, K. Hida, R. Cone, and J. Hanes. Nanoparticles reveal that human cervicovaginal mucus is riddled with pores larger than viruses. *Proceedings of the National Academy of Sciences USA*, 107(2):598–603, 2010.

[93] D. De Beer, P. Stoodley, F. Roe, and Z. Lewandowski. Effects of biofilm structures on oxygen distribution and mass transport. *Biotechnology and Bioengineering*, 43(11):1131–1138, 1994.

[94] W.R. Schneider and R.N. Doetsch. Effect of viscosity on bacterial motility. *Journal of Bacteriology*, 117(2):696–701, 1974.

[95] H.C. Berg and L. Turner. Movement of microorganisms in viscous environments. *Nature*, 278(5702):349–351, 1979.

[96] E.P. Greenberg and E. Canale-Parola. Relationship between cell coiling and motility of spirochetes in viscous environments. *Journal of Bacteriology*, 131(3):960–969, 1977.

[97] E.P. Greenberg and E. Canale-Parola. Motility of flagellated bacteria in viscous environments. *Journal of Bacteriology*, 132(1):356–358, 1977.

[98] F. Ullrich, F. Qiu, J. Pokki, T. Huang, S. Pané, and B.J. Nelson. Swimming characteristics of helical microrobots in fibrous environments. In *6th IEEE International Conference on Biomedical Robotics and Biomechatronics (BioRob)*, pages 470–475, 2016.

[99] Y. Magariyama and S. Kudo. A mathematical explanation of an increase in bacterial swimming speed with viscosity in linear-polymer solutions. *Biophysical Journal*, 83(2):733–739, 2002.

[100] V.A. Martinez, J. Schwarz-Linek, M. Reufer, L.G. Wilson, A.N. Morozov, and W.C.K. Poon. Flagellated bacterial motility in polymer solutions. *Proceedings of the National Academy of Sciences USA*, 111(50):17771–17776, 2014.

[101] H.C. Fu, C.W. Wolgemuth, and T.R. Powers. Swimming speeds of filaments in nonlinearly viscoelastic fluids. *Physics of Fluids*, 21(3):033102, 2009.

[102] L. Li and S.E. Spagnolie. Swimming and pumping by helical waves in viscous and viscoelastic fluids. *Physics of Fluids*, 27(2):021902, 2015.

[103] S.E. Spagnolie, B. Liu, and T.R. Powers. Locomotion of helical bodies in viscoelastic fluids: enhanced swimming at large helical amplitudes. *Physical Review Letters*, 111(6):068101, 2013.

[104] B. Liu, T.R. Powers, and K.S. Breuer. Force-free swimming of a model helical flagellum in viscoelastic fluids. *Proceedings of the National Academy of Sciences USA*, 108(49):19516–19520, 2011.

[105] A.K. Balin, A. Zöttl, J.M. Yeomans, and T.N. Shendruk. Biopolymer dynamics driven by helical flagella. *Physical Review Fluids*, 2(11):113102, 2017.

[106] A.M. Leshansky. Enhanced low-reynolds-number propulsion in heterogeneous viscous environments. *Physical Review E*, 80(5):051911, 2009.

[107] H.C. Fu, V.B. Shenoy, and T.R. Powers. Low-reynolds-number swimming in gels. *Europhysics Letters*, 91(2):24002, 2010.

[108] P. Lee and C.W. Wolgemuth. An immersed boundary method for two-phase fluids and gels and the swimming of caenorhabditis elegans through viscoelastic fluids. *Physics of Fluids*, 28(1):011901, 2016.

[109] O Malaspinas, N Fiétier, and M Deville. Lattice boltzmann method for the simulation of viscoelastic fluid flows. *Journal of Non-Newtonian Fluid Mechanics*, 165(23-24):1637–1653, 2010.

[110] J Su, J Ouyang, X Wang, B Yang, and W Zhou. Lattice boltzmann method for the simulation of viscoelastic fluid flows over a large range of weissenberg numbers. *Journal of Non-Newtonian Fluid Mechanics*, 194:42–59, 2013.

[111] MF Tomé, N Mangiavacchi, JA Cuminato, A Castelo, and S McKee. A finite difference technique for simulating unsteady viscoelastic free surface flows. *Journal of Non-Newtonian Fluid Mechanics*, 106(2-3):61–106, 2002.

[112] MF Tomé, MS de Araujo, MA Alves, and FT Pinho. Numerical simulation of viscoelastic flows using integral constitutive equations: A finite difference approach. *Journal of Computational Physics*, 227(8):4207–4243, 2008.

[113] TN Phillips and AJ Williams. Viscoelastic flow through a planar contraction using a semi-lagrangian finite volume method. *Journal of Non-Newtonian Fluid Mechanics*, 87(2-3):215–246, 1999.

[114] J Rutllant, M López-Béjar, P Santolaria, J Yániz, and F López-Gatius. Rheological and ultrastructural properties of bovine vaginal fluid obtained at oestrus. *Journal of Anatomy*, 201(1):53–60, 2002.

[115] DA Gagnon, XN Shen, and PE Arratia. Undulatory swimming in fluids with polymer networks. *Europhysics Letters*, 104(1):14004, 2013.

[116] R Ledesma-Aguilar and JM Yeomans. Enhanced motility of a microswimmer in rigid and elastic confinement. *Physical Review Letters*, 111(13):138101, 2013.

[117] JK Wróbel, R Cortez, and L Fauci. Modeling viscoelastic networks in stokes flow. *Physics of Fluids*, 26(11):2889–2893, November 2014.

[118] B. Bird. *Dynamics of Polymeric Liquids: Kinetic Theory*. Wiley, New York, 1987.

[119] R. Cortez. The method of regularized stokeslets. *SIAM Journal on Scientific Computing*, 23(4):1204–1225, 2001.

[120] Ricardo Cortez, Lisa Fauci, and Alexei Medovikov. The method of regularized stokeslets in three dimensions: Analysis, validation, and application to helical swimming. *Physics of Fluids*, 17(3):031504, 2005.

[121] R. Cortez, L. Fauci, and A. Medovikov. The method of regularized stokeslets in three dimensions: Analysis, validation, and application to helical swimming. *Physics of Fluids*, 17(3), 2005.

[122] Hermes Gadêlha and Eamonn A Gaffney. Flagellar ultrastructure suppresses buckling instabilities and enables mammalian sperm navigation in high-viscosity media. *Journal of The Royal Society Interface*, 16(152):20180668, 2019.

[123] MeDhont JK and Briels WJ. Rod-like brownian particles in shear flow. In *Soft Matter: Complex Colloidal Suspensions*. Gompper G, Schick M, 2006.

[124] Frank TM Nguyen and Michael D Graham. Impacts of multiflagellarity on stability and speed of bacterial locomotion. *Physical Review E*, 98(4):042419, 2018.

[125] Jake J Abbott, Kathrin E Peyer, Marco Cosentino Lagomarsino, Li Zhang, Lixin Dong, Ioannis K Kaliakatsos, and Bradley J Nelson. How should microrobots swim? *The International Journal of Robotics Research*, 28(11-12):1434–1447, 2009.

[126] T.S. Yu, E. Lauga, and A.E. Hosoi. Experimental investigations of elastic tail propulsion at low reynolds number. *Physics of Fluids*, 18(9), 2006.

[127] X. Xu and A. Nadim. Deformation and orientation of an elastic slender body sedimenting in a viscous liquid. *Physics of Fluids*, 6(9):2889–2893, 1994.

[128] L. Li, H. Manikantan, D. Saintillan, and S.E. Spagnolie. The sedimentation of flexible filaments. *Journal of Fluid Mechanics*, 735:705–736, 2013.

[129] S Tottori, L Zhang, F Qiu, KK Krawczyk, A Franco-Obregón, and BJ Nelson. Magnetic helical micromachines: Fabrication, controlled swimming, and cargo transport. *Advanced Materials*, 24(6):811–816, 2012.

[130] Y Dong, L Wang, V Iacovacci, X Wang, L Zhang, and BJ Nelson. Magnetic helical micro-/nanomachines: Recent progress and perspective. *Matter*, 5(1):77–109, 2022.

[131] R Menkveld, CA Holleboom, and JP Rhemrev. Measurement and significance of sperm morphology. *Asian Journal of Andrology*, 13(1):59, 2011.

[132] James Gray and GJ Hancock. The propulsion of sea-urchin spermatozoa. *Journal of Experimental Biology*, 32(4):802–814, 1955.

[133] Bruce Rodenborn, Chih-Hung Chen, Harry L Swinney, Bin Liu, and HP Zhang. Propulsion of microorganisms by a helical flagellum. *Proceedings of the National Academy of Sciences*, 110(5):E338–E347, 2013.

[134] M. Mitchell. *An introduction to genetic algorithms*. MIT Press, 1998.

[135] G. Zames. Genetic algorithms in search, optimization and machine learning. *Information Technology Journal*, 3(1):301, 1981.

[136] S. Yazdi and A.M. Ardekani. Bacterial aggregation and biofilm formation in a vortical flow. *Biomicrofluidics*, 6(4):044114, 2012.

[137] T. Kobayashi, G. Jung, Y. Matsuoka, Y. Nakayama, J.J. Molina, and R. Yamamoto. Direct numerical simulations of a microswimmer in a viscoelastic fluid. *Soft Matter*, 19(37):7109–7121, 2023.

[138] K.D. Housiadas, J.P. Binagia, and E.S. Shaqfeh. Squirmers with swirl at low weissenberg number. *Journal of Fluid Mechanics*, 911:A16, 2021.

[139] M. Zhang, Z. Yu, Z. Ouyang, Y. Xia, and Z. Lin. Numerical study of collective motion of microswimmers in giesekus viscoelastic fluids. *Journal of Non-Newtonian Fluid Mechanics*, 329:105245, 2024.

[140] D. Mahdy, A. Mohamed, A. Klingner, A. Tammam, A. Wahdan, M. Serry, and I.S. Khalil. Experimental characterization of helical propulsion in newtonian and viscoelastic mediums. In *IEEE International Conference on Manipulation, Manufacturing and Measurement on the Nanoscale (3M-NANO)*, pages 311–314, 2017.

[141] J.R. Sampson. Adaptation in natural and artificial systems (john h. holland). page 529, 1976.

[142] Willem Ombelet, Ian Cooke, Silke Dyer, Gamal Serour, and Paul Devroey. Infertility and the provision of infertility medical services in developing countries. *Human reproduction update*, 14(6):605–621, 2008.

[143] David Lai, Joyce Han-Ching Chiu, Gary D Smith, Shuichi Takayama, A van den Berg, and L Segernik. Microfluidics for assisted reproductive technologies. In *Microfluidics for Medical Applications*, pages 131–150. Royal Society of Chemistry, 2014.

[144] JAM Hamilton, M Cissen, M Brandes, JMJ Smeenk, JP De Bruin, JAM Kremer, WLDM Nelen, and CJCM Hamilton. Total motile sperm count: a better indicator for the severity of male factor infertility than the who sperm classification system. *Human Reproduction*, 30(5):1110–1121, 2015.

[145] Charles B Lindemann. The geometric clutch as a working hypothesis for future research on cilia and flagella. *Annals of the New York Academy of Sciences*, 1101(1):477–493, 2007.

[146] Bart CJM Fauser, Paul Devroey, and Nick S Macklon. Multiple birth resulting from ovarian stimulation for subfertility treatment. *The Lancet*, 365(9473):1807–1816, 2005.

[147] Ralf R Henkel and Wolf-Bernhard Schill. Sperm preparation for art. *Reproductive biology and endocrinology*, 1(1):1–22, 2003.

[148] Savas Tasoglu, Hooman Safaee, Xiaohui Zhang, James L Kingsley, Paolo N Catalano, Umut Atakan Gurkan, Aida Nureddin, Emre Kayaalp, Raymond M Anchan, and et al. Richard L Maas. Exhaustion of racing sperm in nature-mimicking microfluidic channels during sorting. *Small*, 9(20):3374–3384, 2013.

[149] Stephanie M Knowlton, Magesh Sadasivam, and Savas Tasoglu. Microfluidics for sperm research. *Trends in biotechnology*, 33(4):221–229, 2015.

[150] Meisam Zaferani, Farhad Javi, Amir Mokhtare, Peilong Li, and Alireza Abbaspourrad. Rolling controls sperm navigation in response to the dynamic rheological properties of the environment. *Elife*, 10:e68693, 2021.

[151] Ricardo Cortez. The method of regularized stokeslets. *SIAM Journal on Scientific Computing*, 23(4):1204–1225, 2001.

[152] N. Narinder, C. Bechinger, and J.R. Gomez-Solano. Memory-induced transition from a persistent random walk to circular motion for achiral microswimmers. *Physical Review Letters*, 121(7):078003, 2018.

[153] J.R. Gomez-Solano, A. Blokhuis, and C. Bechinger. Dynamics of self-propelled janus particles in viscoelastic fluids. *Physical Review Letters*, 116(13):138301, 2016.

[154] K. Qi, E. Westphal, G. Gompper, and R.G. Winkler. Enhanced rotational motion of spherical squirmer in polymer solutions. *Physical Review Letters*, 124(6):068001, 2020.

[155] Y. Du, H. Jiang, and Z. Hou. Study of active brownian particle diffusion in polymer solutions. *Soft Matter*, 15(9):2020–2031, 2019.